January 1996 • NREL/TP-442-7819

Effects of Grit Roughness and Pitch Oscillations on the LS(1)-0417MOD Airfoil

Airfoil Performance Report, Revised (12/99)

J. M. Janiszewska
R. Reuss Ramsay
M. J. Hoffmann
G.M. Gregorek
The Ohio State University
Columbus, Ohio

National Renewable Energy Laboratory
1617 Cole Boulevard
Golden, Colorado 80401-3393
A national laboratory of the U.S. Department of Energy
Managed by Midwest Research Institute
for the U.S. Department of Energy
under contract No. DE-AC36-83CH10093

Foreword

Airfoils for wind turbines have been selected by comparing data from different wind tunnels, tested under different conditions, making it difficult to make accurate comparisons. Most wind tunnel data sets do not contain airfoil performance in stall commonly experienced by turbines operating in the field. Wind turbines commonly experience extreme roughness for which there is very little data. Finally, recent tests have shown that dynamic stall is a common occurrence for most wind turbines operating in yawed, stall or turbulent conditions. Very little dynamic stall data exists for the airfoils of interest to a wind turbine designer. In summary, very little airfoil performance data exists which is appropriate for wind turbine design.

Recognizing the need for a wind turbine airfoil performance data base, the National Renewable Energy Laboratory (NREL), funded by the U.S. Department of Energy, awarded a contract to Ohio State University (OSU) to conduct a wind tunnel test program. Under this program OSU tested a series of popular wind turbine airfoils. A standard test matrix was developed to assure that each airfoil was tested under the same conditions. The test matrix was developed in partnership with industry and is intended to include all of the operating conditions experienced by wind turbines. These conditions include airfoil performance at high angles of attack, rough leading edge (bug simulation), steady and unsteady angles of attack.

Special care has been taken to report as much of the test conditions and raw data as practical so that designers can make their own comparisons and focus on details of the data relevant to their design goals. Some of the airfoil coordinates are proprietary to NREL or an industry partner. To protect the information which defines the exact shape of the airfoil, the coordinates have not been included in the report. Instructions on how to obtain these coordinates may be obtained by contacting C.P. (Sandy) Butterfield at NREL.

C. P. (Sandy) Butterfield
Wind Technology Division
National Renewable Energy Laboratory
1617 Cole Blvd.
Golden, Colorado, 80401 USA
Internet Address: Sandy_Butterfield@NREL.GOV
Phone 303-384-6902
FAX 303-384-6901

Preface

The Ohio State University Aeronautical and Astronautical Research Laboratory is conducting a series of steady state and unsteady wind tunnel tests on a set of airfoils which have been or will be used for horizontal axis wind turbines. The purpose is to investigate the effect of pitch oscillations and leading edge grit roughness on airfoil performance. The study of pitch oscillation effects can help to understand the behavior of horizontal axis wind turbines in yaw. The results of these tests will aid in the development of new airfoil performance codes which account for unsteady behavior and also aid in the design of new airfoils for wind turbines. The application of leading edge grit roughness simulates surface irregularities that occur on wind turbines. These irregularities on the blades are due to the accumulation of insect debris, ice, and/or the aging process and can significantly reduce the power output of the horizontal axis wind turbines. The experimental results from the application of LEGR will help the development of airfoils which are less sensitive to this kind of roughness.

This work was made possible by the efforts and financial support of the National Renewable Energy Laboratory which provided major funding and technical monitoring, the U.S. Department of Energy is credited for its funding of this document through the National Renewable Energy Laboratory under contract number DE-AC36-83CH10093 and KENETECH, U.S. Windpower Incorporated which provided technical assistance. The staff of The Ohio State University Aeronautical and Astronautical Research Laboratory appreciate the contributions made by personnel from both organizations. In addition the authors would like to recognize the efforts of the following student research assistants, Fernando Falasca and Monica Angelats i Coll.

Summary

A LS(1)-0417MOD airfoil model was tested in The Ohio State University Aeronautical and Astronautical Research Laboratory 3x5 subsonic wind tunnel under steady state and unsteady conditions. The test defined baseline conditions for steady state angles of attack from -20° to +40° and examined unsteady behavior by oscillating the model about its pitch axis for three mean angles, three frequencies, and two amplitudes. For all cases, Reynolds numbers of 0.75, 1, 1.25, and 1.5 million were used. In addition, the above conditions were repeated after the application of leading edge grit roughness (LEGR) to determine contamination effects on the airfoil performance.

Steady state results of the LS(1)-0417MOD testing at Reynolds number of 1 million showed a baseline maximum lift coefficient of 1.55 at 15.3° angle of attack. The application of LEGR reduced the maximum lift coefficient by as much as 27% and increased the minimum drag coefficient by more than 42%. The zero lift pitching moment of -0.0748 showed a 15% reduction in magnitude to -0.0634 with LEGR applied.

Data were also obtained for two pitch oscillation amplitudes: ±5.5° and ±10°. The larger amplitude consistently gave a higher maximum lift coefficient than the smaller amplitude, and both unsteady maximum lift coefficients were greater than the steady state values. Stall is delayed on the airfoil while the angle of attack is increasing, thereby causing an increase in maximum lift coefficient. A hysteresis behavior was exhibited for all the unsteady test cases. The hysteresis loops were larger for the higher reduced frequencies and for the larger amplitude oscillations. As in the steady case, the effect of LEGR in the unsteady case was to reduce the lift coefficient at high angles of attack. In addition, with LEGR, the hysteresis behavior persisted into lower angles of attack than in the clean case. The application of LEGR also increased the size of the hysteresis loops.

In general, the unsteady maximum lift coefficient was from 9% to 119% higher than the steady state maximum lift coefficient, and variation in the quarter chord pitching moment coefficient magnitude was from 3% to 1059% relative to steady state values at high angles of attack. These findings indicate the importance of considering the unsteady flow behavior occurring in wind turbine operation in order to obtain accurate loads estimates.

Table of Contents Page

List of Figures Page

List of Tables Page

List of Symbols

AOA	Angle of attack
A/C, a.c.	Alternating current
c	Model chord length
C_d	Drag coefficient
C_{dmin}	Minimum drag coefficient
C_{dp}	Pressure drag coefficient
C_{dw}	Wake drag coefficient
C_{du}	Uncorrected drag coefficient
C_l	Lift coefficient
C_{lmax}	Maximum lift coefficient
$C_{l\ dec}$	Lift coefficient at angle of maximum lift, but with angle of attack decreasing
C_{lu}	Uncorrected lift coefficient
C_m, $C_{m¼}$	Pitching moment coefficient about the quarter chord
$C_{m\ dec}$	Pitching moment coefficient at angle of maximum lift, but with angle of attack decreasing
$C_{m\ inc}$	Pitching moment coefficient at angle of maximum lift, but with angle of attack increasing
C_{mo}	Pitching moment coefficient about the quarter chord, at zero lift
$C_{m¼u}$	Uncorrected pitching moment coefficient about the quarter chord
C_p	Pressure coefficient, $(p- p_\infty)/q_\infty$
C_{pmin}	Minimum pressure coefficient
f	Frequency
h	Wind tunnel test section height
hp, Hp, HP	Horsepower
Hz	Hertz
k	Grit particle size
k/c	Grit particle size divided by airfoil model chord length
p	Pressure
q	Dynamic pressure
q_u	Uncorrected dynamic pressure
q_w	Dynamic pressure through the model wake
q_∞	Free stream dynamic pressure
Re	Reynolds number
Re_u	Uncorrected Reynolds number
t	Time
U_∞	Corrected free stream velocity
V	Velocity
V_u	Uncorrected velocity
x	Axis parallel to model reference line
y	Axis perpendicular to model reference line

α	Angle of attack
α_{dec}	Decreasing angle of attack
α_{inc}	Increasing angle of attack
α_{m}	Median angle of attack
α_{mean}	Mean angle of attack
α_{u}	Uncorrected angle of attack
ϵ	Tunnel solid wall correction scalar
ϵ_{sb}	Solid blockage correction scalar
ϵ_{wb}	Wake blockage correction scalar
Λ	Body-shape factor
π	3.1416
σ	Tunnel solid wall correction parameter
ω_{red}, $\omega_{reduced}$	Reduced frequency, $\pi fc/U_{\infty}$

Introduction

Horizontal axis wind turbine rotors experience unsteady aerodynamics due to wind shear when the rotor is yawed, when the rotor blades pass through the support tower wake, and when the wind is gusting. An understanding of this unsteady behavior is necessary to assist in the calculation of rotor performance and loads. The rotors also experience performance degradation caused by surface roughness. These surface irregularities are due to the accumulation of insect debris, ice, and/or the aging process. Wind tunnel studies that examine both the steady and unsteady behavior of airfoils can help define the flow phenomena, and the resultant data can be used to validate analytical computer codes.

An LS(1)-0417MOD airfoil model was tested in The Ohio State University Aeronautical and Astronautical Research Laboratory (OSU/AARL) 3x5 subsonic wind tunnel (3x5) under steady flow and stationary model conditions, as well as with the model undergoing pitch oscillations. To study the possible extent of performance loss due to surface roughness, a standard grit pattern (LEGR) was used to simulate leading edge contamination. After baseline cases were completed, the LEGR was applied for both steady state and model pitch oscillation cases. The Reynolds numbers for steady state conditions were 0.75, 1, 1.25, and 1.5 million, while the angle of attack ranged from -20° to +40°. With the model undergoing pitch oscillations, data were acquired at Reynolds numbers of 0.75, 1, 1.25, and 1.5 million, at frequencies of 0.6, 1.2, and 1.8 Hz. Two sine wave forcing functions were used; ±5.5° and ±10° amplitude, at mean angles of attack of 8°, 14°, and 20°. For purposes herein, any reference to unsteady conditions means the airfoil model was in pitch oscillation about the quarter chord.

Experimental Facility

Wind Tunnel

The OSU/AARL 3×5 was used to conduct tests on the LS(1)-0417MOD airfoil section. Schematics of the top and side views of the tunnel are shown in figures 1 and 2. This open-circuit tunnel has a velocity range of 0 - 55 m/s (180-ft/sec) produced by a 2.4-meter (8-ft) diameter, six-bladed fan. The fan is belt driven by

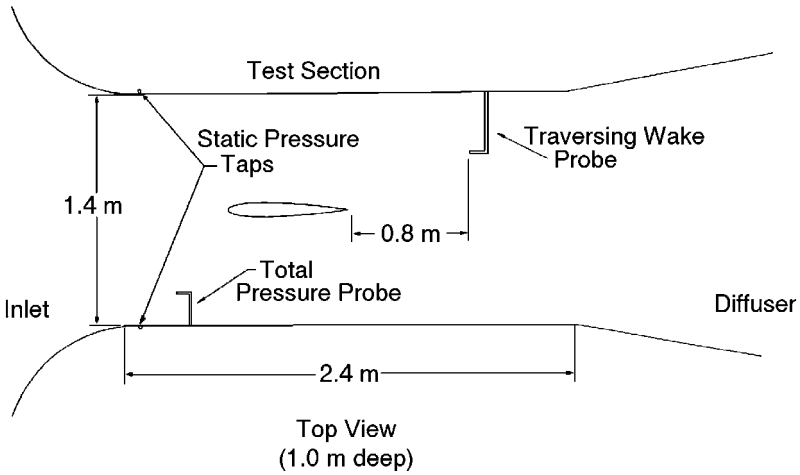

Figure 1. 3x5 subsonic wind tunnel, top view.

a 93.2-kw (125-hp) three phase a.c. motor connected to a variable frequency motor controller. Nominal test section dimensions are 1.0-m (39-inches) high by 1.4-m (55-inches) wide by 2.4-m (96-inches) long. The 457-mm (18-inch) chord airfoil model was mounted vertically in the test section. A steel tube through the

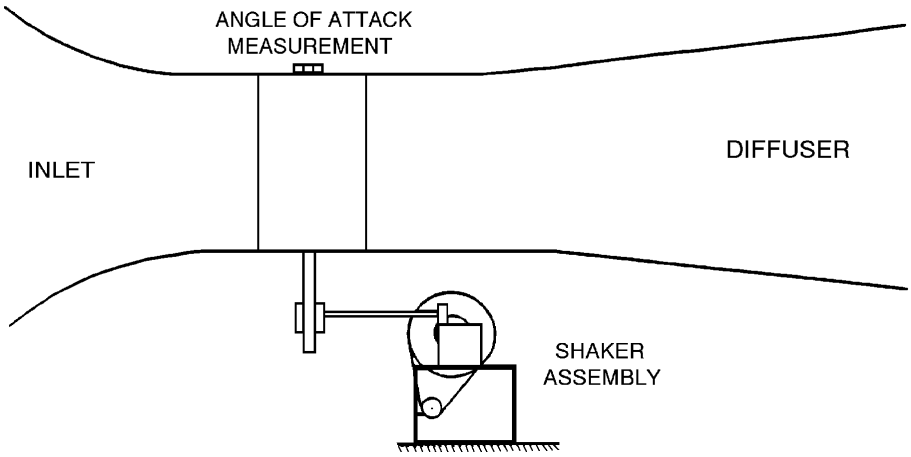

Figure 2. 3x5 subsonic wind tunnel, side view.

quarter chord of the model attached the model to the tunnel during testing. An angle of attack potentiometer was fastened to the model at the top of the tunnel, as shown in figure 2. The steady state angle of attack was adjusted with a worm gear drive attached to the model strut below the tunnel floor.

Oscillation System

Portions of the airfoil model testing required the use of a reliable model pitch oscillation system. The OSU/AARL "shaker" system incorporated a face cam and follower arm attached to the model support tube below the wind tunnel floor, shown in figure 3. The choice of cam governed the type and amplitude of the wave form produced. Sine wave forms with amplitudes of ±5.5° and ±10° were used for these tests. The wave form is defined by the equation

$$\alpha = \alpha_m + A\sin(2\pi ft)$$

where A is the respective amplitude. The shaker system was powered by a 5 hp a.c. motor with variable line frequency controller. The useable oscillating frequency range was 0.1 to 2.0 Hz, with three frequencies used for this test: 0.6, 1.2, and 1.8 Hz.

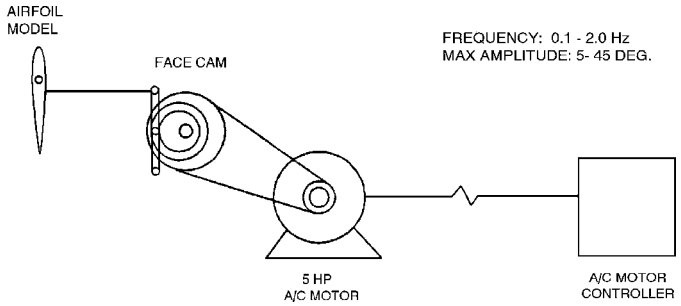

Figure 3. 3x5 wind tunnel oscillation system.

Model Details

A 457-mm (18-inch) constant chord LS(1)-0417MOD airfoil model was designed by OSU/AARL personnel and manufactured by others. Figure 4 shows the airfoil section; while the model measured coordinates are given in Appendix A. The model was manufactured with a carbon composite skin over ribs and foam. The

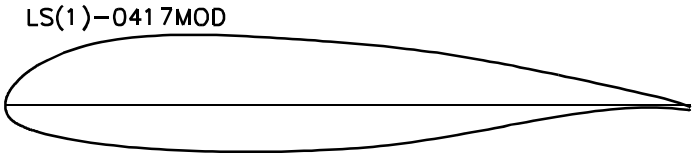

Figure 4. LS(1)-0417MOD airfoil section.

main load-bearing member was a 38-mm (1.5-inch) diameter steel tube passed through the model quarter chord station. Ribs and end plates were used to transfer loads from the composite skin to the steel tube. The final surface was hand worked using templates to attain given coordinates within a requested tolerance of ±0.25-mm (±0.01-inch). The completed model was measured at three spanwise locations using a Sheffield-Cordax coordinate measurement machine. Measurements were made in English units and later

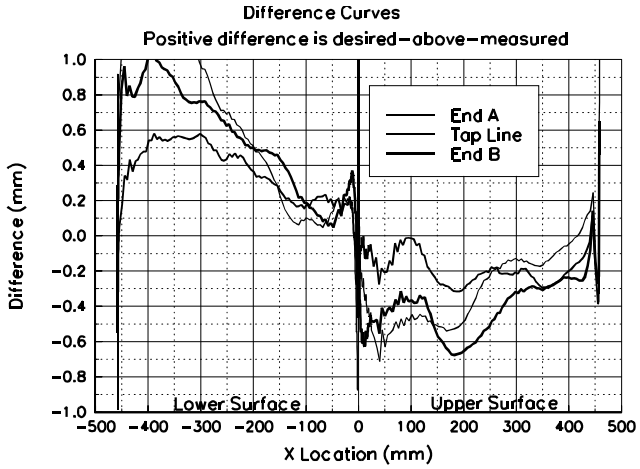

Figure 5. Measured-to-desired model coordinates difference curves..

converted to metric. Figure 5 shows the results of comparing measured-to-desired coordinates by calculating differences normal to the profiled surface at three stations on the model. The "spikes" apparent near the trailing edge are due to the numerical methods used and are not real.

To minimize pressure response times, which is important for the unsteady testing, the surface pressure tap lead-out lines had to be as short as possible. Consequently, a compartment was built into the model so pressure scanning modules could be installed inside the model. This compartment was accessed through a panel door fitted flush with the model contour on the lower (pressure) surface.

For test cases involving roughness, a standard, repeatable pattern with grit as roughness elements was desired. The roughness pattern used was jointly developed by OSU/AARL and KENETECH, Windpower personnel with a molded insect pattern taken from a wind turbine in the field by personnel at the University

of Texas Permian Basin. The particle density was 5 particles per cm^2 (32 particles per square inch) in the middle of the pattern, thinning to 1.25 particles per cm^2 (8 particles per square inch) at the edge of the pattern. Figure 6 shows the pattern. To make a usable template, the pattern was repeatedly cut into a steel sheet 102-mm (4-inch) wide and 91-cm (3-ft) long with holes just large enough for one piece of grit. Based on average particle size from the field specimen, standard #40 lapidary grit was chosen for the roughness elements, giving k/c=0.0019 for a 457-mm (18-inch) chord model.

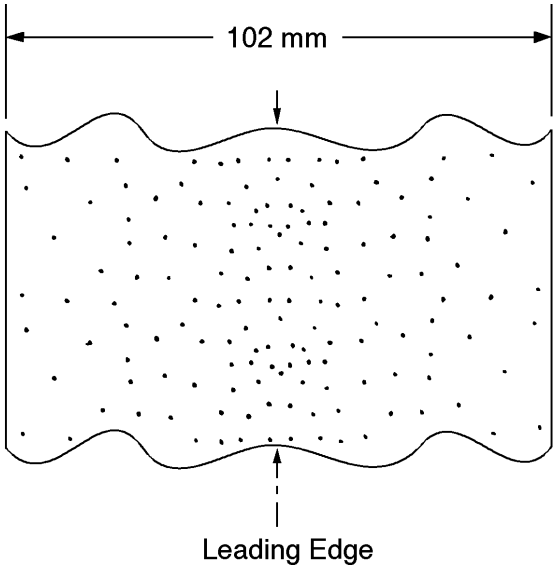

Figure 6. Roughness pattern.

To use the template, 102-mm (4-inch) wide double-tack tape was applied to one side of the template and grit was poured and brushed from the opposite side. The tape was then removed from the template and transferred to the model. This method allowed the same roughness pattern to be replicated for any test.

Test Equipment and Procedures

Data Acquisition

Data were acquired and processed from 52 surface pressure taps, four individual tunnel pressure transducers, an angle of attack potentiometer, a wake probe position potentiometer, and a tunnel thermocouple. The data acquisition system included an IBM PC compatible 80486-based computer connected to a Pressure Systems Incorporated (PSI) data scanning system. The PSI system included a 780B Data Acquisition and Control Unit (DACU), 780B Pressure Calibration Unit (PCU), 81-IFC scanning module interface, two 2.5-psid pressure scanning modules (ESPs), one 20-inch water column range pressure scanning module, and a 30-channel Remotely Addressed Millivolt Module (RAMM-30). Figure 7 shows the data acquisition system schematic.

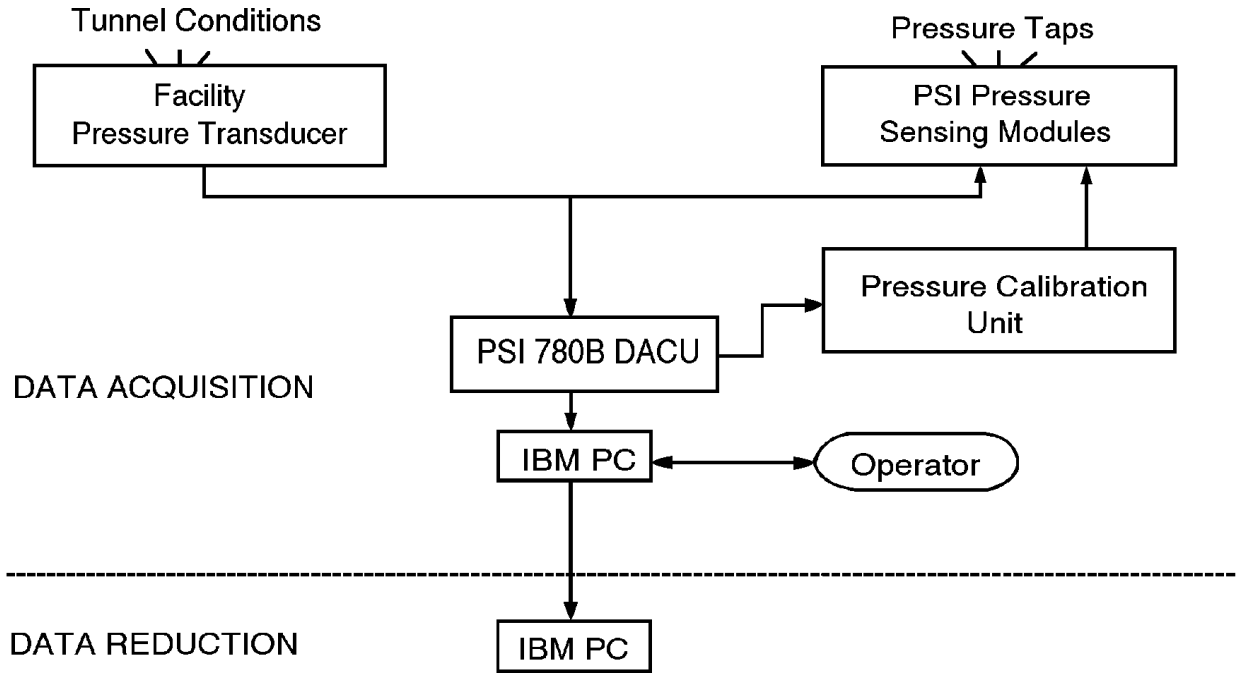

Figure 7. Data acquisition schematic.

Four individual pressure transducers read tunnel total pressure, tunnel north static pressure, tunnel south static pressure, and wake dynamic pressure. Before the test began, these transducers were bench calibrated using a water manometer to determine their sensitivities and offsets. Related values were entered into the data acquisition and reduction program so the transducers could be shunt resistor calibrated before each series of wind tunnel runs.

The rotary angle of attack potentiometer of 0.5% linearity was regularly calibrated during the tunnel pressure transducers shunt calibration. The angle of attack calibration was accomplished by taking voltage readings at known values of set angle of attack. This calibration method gave angle of attack readings within ±0.25° over the entire angle range. The wake probe position potentiometer was also a linear potentiometer and it was regularly calibrated during the shunt calibration of the tunnel pressure transducers.

Calibration of the three ESPs was done simultaneously using the DACU and PCU. At operator request, the DACU commanded the PCU to apply known regulated pressures to the ESPs and read the output voltages from each integrated pressure sensor. From these values, the DACU calculated the calibration coefficients and stored them internally until the coefficients were requested by the controlling computer. This calibration

was done several times during a run set because the ESPs were installed inside the model and their outputs tended to drift with temperature changes during a test sequence. Frequent on-line calibrations minimized the effect.

For steady state cases, the model was set to angle of attack and the tunnel conditions were adjusted. At operator request, pressure measurements from the airfoil surface taps and all other channels of information were acquired and stored by the DACU and subsequently passed to the controlling computer for final processing. The angles of attack were always set in the same progression, from negative to positive values.

For model oscillating cases, the tunnel conditions were set while the model was stationary at the desired mean angle of attack. The "shaker" was started, and after approximately 10 seconds, the model surface pressure and tunnel condition data were acquired. Generally, 120 data scans were acquired over three model oscillation cycles. Since surface pressures were scanned sequentially, the data rate was set so the model rotated through less than 0.50° during any data burst. Finally, due to the unsteady and complex nature of the pitch oscillation cases, model wake surveys (for drag) were not conducted.

Data Reduction

The data reduction routine was included as a section of the data acquisition program. This combination of data acquisition and reduction routines allowed data to be reduced on-line during a test. By quickly reducing selected runs, integrity checks could be made to ensure the equipment was working properly and to allow timely decisions about the test matrix.

The ambient pressure was manually input into the computer and updated regularly. This value, along with the measurements from the tunnel pressure transducers and the tunnel thermocouple, were used to calculate tunnel airspeed. As a continuous check of readings, the tunnel total and static pressures were read by both the tunnel individual pressure transducers and the 20-inch water column ESP.

A typical steady state datum point was derived by acquiring ten data scans of all channels over a 10 second window at each angle of attack and tunnel condition. The reduction portion of the program processed each data scan to coefficient forms (C_p, C_l, $C_{m¼}$, and C_{dp}) using the measured surface pressure voltages, calibration coefficients, tap locations and wind tunnel conditions. Then, all scan sets for a given condition were ensemble averaged to provide one data set, and that data set was then corrected for the effects of solid tunnel walls. All data were saved in electronic form.

Corrections due to solid tunnel sidewalls were applied to the wind tunnel data. As described by Pope and Harper (1966), tunnel conditions are represented by the following equations:

$$q = q_u(1 + 2\epsilon)$$

$$V = V_u(1 + \epsilon)$$

$$R_e = R_{e_u}(1 + \epsilon)$$

Airfoil aerodynamic characteristics are corrected by:

$$\alpha = \alpha_u + \frac{57.3\sigma}{2\pi}(C_{l_u} + 4C_{m\frac{1}{4}_u})$$

$$C_l = C_{l_u}(1 - \sigma - 2\epsilon)$$

$$C_{m_{\frac{1}{4}}} = C_{m_{\frac{1}{4}_u}}(1-2\epsilon) + \frac{\sigma\, C_l}{4}$$

$$C_d = C_{d_u}(1-3\epsilon_{sb}-2\epsilon_{wb})$$

where

$$\sigma = \frac{\pi^2}{48}\left(\frac{c}{h}\right)^2$$

$$\epsilon = \epsilon_{sb} + \epsilon_{wb}$$

$$\epsilon_{sb} = \Lambda\sigma$$

$$\epsilon_{wb} = \frac{c}{h4} C_{d_u}$$

Model wake data were taken for steady state cases when the wake could be completely traversed. Pressures were acquired from a pitot-static probe which was connected to measure incompressible dynamic pressure through the wake. These pressure measurements were used to calculate drag coefficient using a form of the Jones equation derived from Schlichting (1979).

$$C_{dw} = \frac{2}{c}\int \sqrt{\frac{q_w}{q_\infty}}\left(1-\sqrt{\frac{q_w}{q_\infty}}\right)\, dy$$

This equation assumes that static pressure at the measurement site is the free-stream value. The integration was done automatically except the computer operator chose the end points of the integration from a plot of the wake survey displayed on the computer screen.

For pitch oscillation cases, model surface pressures were reduced to pressure coefficient form with subsequent integrations and angle of attack considerations giving lift, moment, and pressure drag coefficients. The wind tunnel was not calibrated for unsteady model pitch conditions; therefore, the unsteady pressure data were not corrected for any possible effects due to time-dependent pitching or solid tunnel walls. Also, for these cases, the wind tunnel contraction pressures (used for steady state cases) could not be used to calculate instantaneous freestream conditions due to slow response. The tunnel conditions were obtained from a total pressure probe and the average of opposing static pressure taps in the test section entrance, thereby giving near instantaneous flow pressure conditions for the pitching frequencies used.

Test Matrix

The test was designed to study steady state and unsteady pitch oscillation data. Steady state data were acquired at Reynolds numbers of 0.75, 1, 1.25, and 1.5 million with and without LEGR. Refer to the tabular data in Appendix B for the actual Reynolds number for each angle of attack for the steady state data. The angle of attack increment was two degrees when $-20° < \alpha < +10°$ or $+20° < \alpha < +40°$ and one degree when $+10° < \alpha < +20°$. Wake surveys were conducted to find total airfoil drag over an approximate angle of attack range of -10° to +10°. Unsteady data were taken for Reynolds numbers of 0.75, 1, 1.25, and 1.5 million. Sine wave cams with amplitudes ±5.5° and ±10° were used for pitch oscillations, and the mean angles for

both of these amplitudes were 8°, 14°, and 20°. For all these conditions, the frequencies were varied to 0.6, 1.2, and 1.8 Hz. All data points for the unsteady cases were acquired for both clean and LEGR cases.

Results and Discussion

The LS(1)-0417MOD airfoil model was tested under steady state and pitch oscillation conditions. A brief discussion of the results follows, beginning with a comparison of experimental data and computational predictions.

Comparison with Theory

Present wind tunnel steady state data were compared with the computed predictions made using the North Carolina State Airfoil Analysis Code. This analysis code has proven to be accurate for moderate angles of attack. The analysis was made with specifications set to allow for free transition from laminar to turbulent flow, and the pressure distribution comparisons were matched to the same angle of attack as the wind tunnel cases.

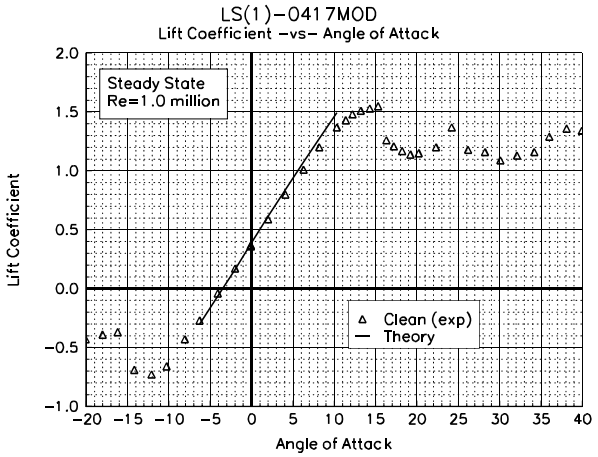

Figure 8. Comparison with theory, C_l vs α.

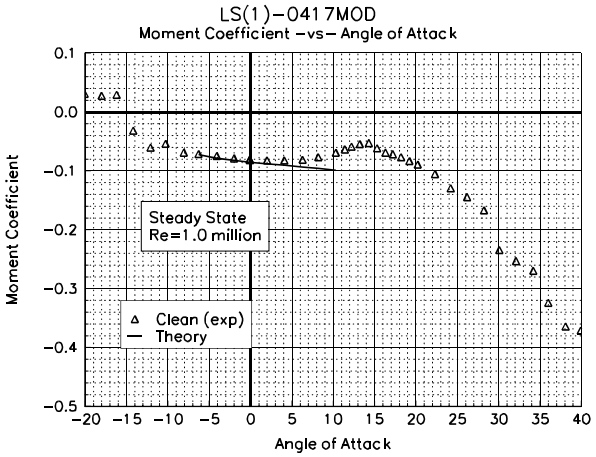

Figure 9. Comparison with theory, C_m vs α.

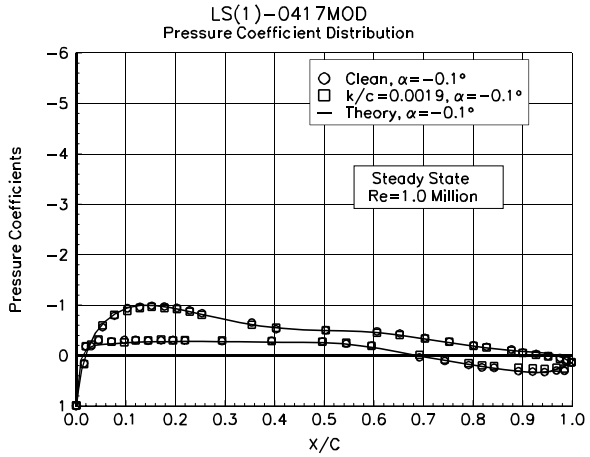

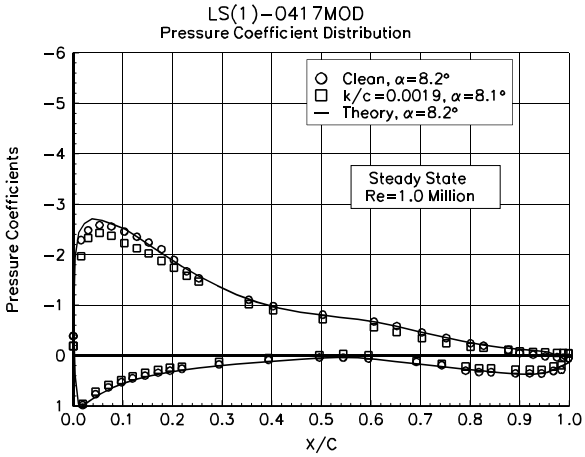

Figure 10. Comparison with theory, C_p vs x/c, α=-0.1°. **Figure 11. Comparison with theory, C_p vs x/c, α=8.2°.**

Figure 8 shows the lift coefficient versus angle of attack for the 1 million Reynolds number case. For moderate angles of attack, where the analysis code is valid, the comparison shows good agreement. The pitching moment about the quarter chord, in figure 9, also shows good agreement for angles of attack from -6° to +2°. The pressure distributions shown in figures 10 and 11, show angles of attack of -0.1° and 8.2°, respectively, and include clean and LEGR wind tunnel data as compared to computed, free transition pressure

distributions. For the -0.1° angle of attack, there is excellent correlation between the experimental and predicted values. For the 8.2° angle of attack, the agreement is good except there is some discrepancy near the upper (suction) surface leading edge; this can be attributed to the uneven surface around the tap holes.

Steady State Data

The LS(1)-0417MOD airfoil model was tested at four Reynolds numbers at nominal angles of attack from -20° to +40°. Figures 12 and 13 show lift coefficients for all the test Reynolds numbers both for a clean

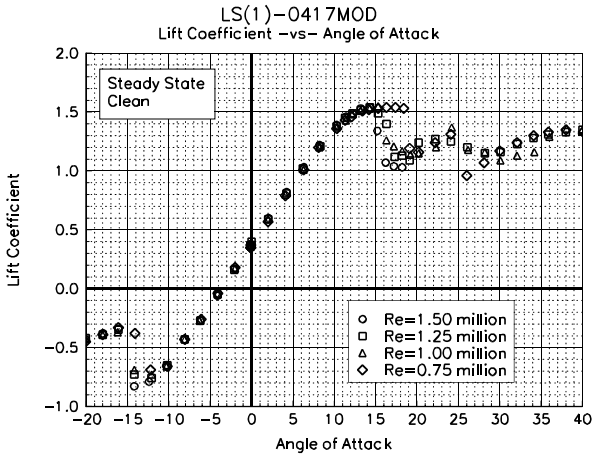

Figure 12. C_l vs α, clean.

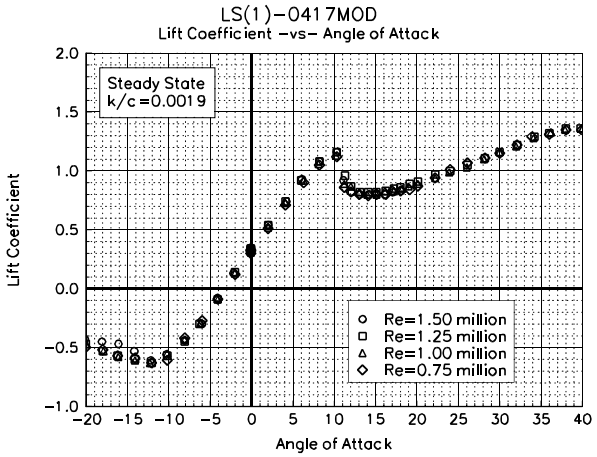

Figure 13. C_l vs α, LEGR, k/c=0.0019.

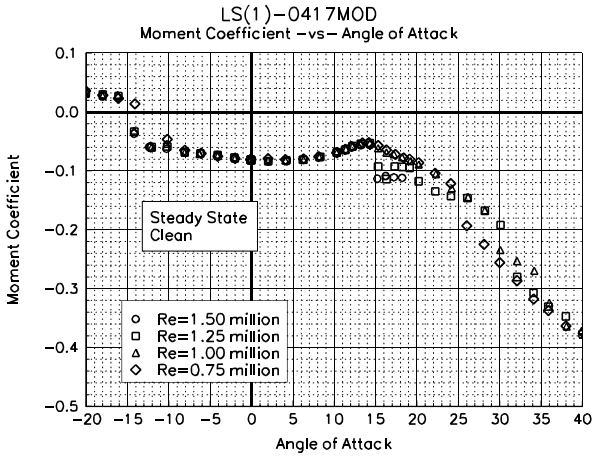

Figure 14. C_m vs α, clean.

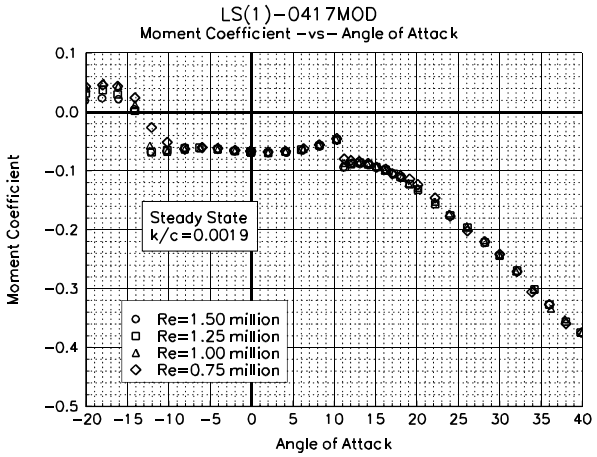

Figure 15. C_m vs α, LEGR, k/c=0.0019.

model and with LEGR applied, respectively. The maximum positive lift coefficient for the clean cases is about 1.55 and about 1.13 for the LEGR cases, a 27% reduction. Not only is the lift coefficient lower for the LEGR case, but the stall starts at a significantly lower angle of attack than for the clean case. Finally, the average lift curve slope for clean data is about 0.104; it is slightly lower for the LEGR case at 0.096. The associated average lift coefficients at zero angle of attack are 0.36 for the clean case and 0.31 for the LEGR case.

Figure 14 shows the pitching moment about the quarter chord for the clean cases and figure 15 shows the same for the LEGR cases. The LEGR data have slightly more positive pitching moment and a flatter curve

for angles of attack near zero lift. The pitching moment coefficient about the quarter chord for the 1 million Reynolds number, clean case is -0.0748 and -0.0634 for the LEGR case.

Total wake drag data were obtained for both the clean and LEGR cases over a nominal angle of attack range of -10° to +10°. A pitot-static probe was used to describe the wake profile. This method is reliable when

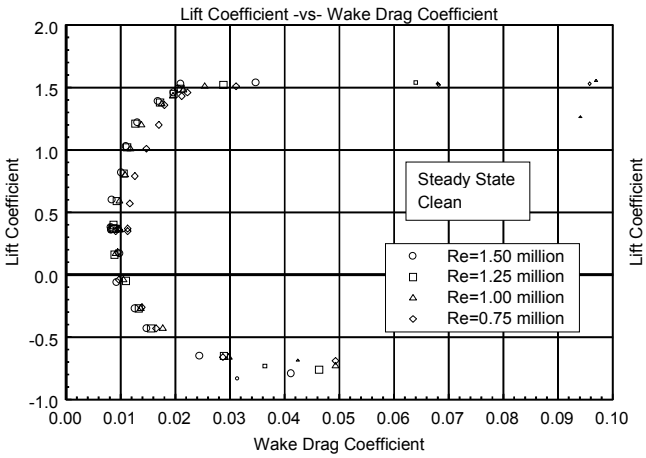

Figure 16. Drag polar, clean.

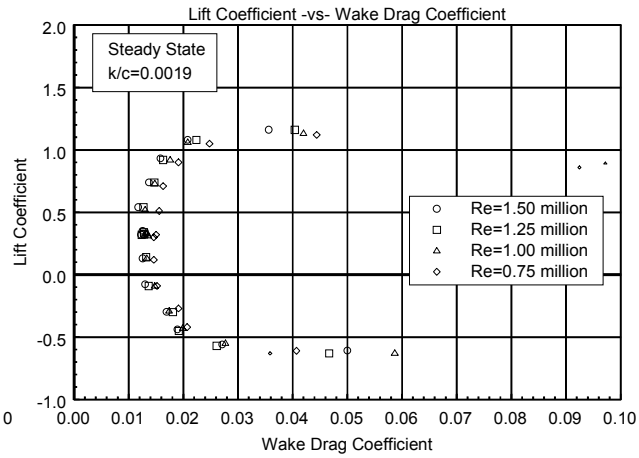

Figure 17. Drag polar, LEGR, k/c=0.0019.

there is relatively low turbulence in the wake flow; therefore, only moderate angles of attack have reliable total drag coefficient data. At angles of attack other than -10° to +10°, surface pressure data were integrated to give C_{dp} and are shown in the drag polars as small symbols. The model clean drag data are shown in figure 16 and the LEGR case is shown in figure 17. At 1 million Reynolds number, minimum drag coefficient for the clean cases was measured as 0.0091 and 0.0129 for LEGR, a 42% increase. The general effect of LEGR is to increase drag consistently through most angles of attack.

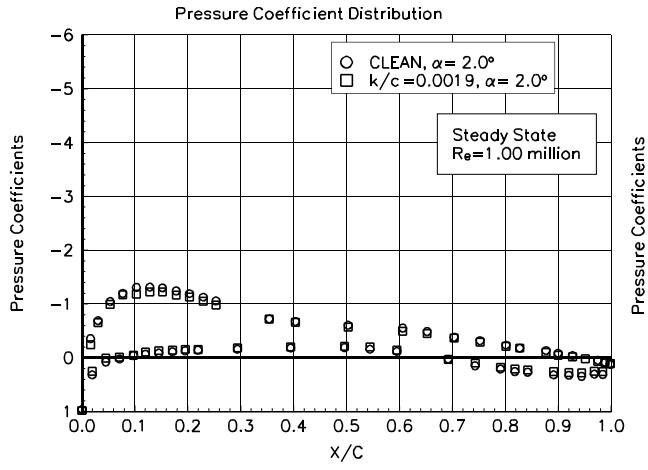

Figure 18. Pressure distribution, α=2.0°.

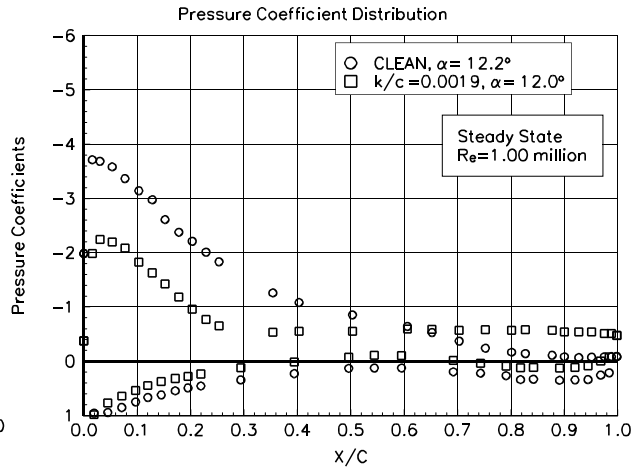

Figure 19. Pressure distribution, α=12.2°.

Two examples of the surface pressure distributions are shown in figures 18 and 19 for 2.0° and 12.2°, respectively, at 1 million Reynolds number. At the angles of attack close to zero degrees, the effect of LEGR does not appear to significantly affect the pressure distribution compared to the clean case distribution; however, there is an effect apparent in the lift coefficient with values of 0.59 for the clean case and 0.52 for the LEGR case. Another difference between the two cases, which cannot be observed from the pressure distribution, is that the drag increases from 0.0120 for the clean case to 0.0156 for the LEGR case. For the

higher angle of attack case, figure 19, the effect of LEGR is to reduce the magnitude of the pressure peak from -3.7 to -2.3 which contributes to a reduction in lift coefficient from 1.48 to 0.87, a 41% decrease. The pitching moment is affected at this angle of attack, the clean case is -0.0586 and the LEGR case is -0.0879.

Unsteady Data

Unsteady experimental data were obtained for the LS(1)-0417MOD airfoil model undergoing sinusoidal pitch oscillations. As mentioned earlier, no attempt was made to calibrate the wind tunnel for the unsteady oscillating model conditions. The steady state tunnel calibration was used to set flow conditions while the model was stationary at its mean angle of attack. The use of the unsteady data should be limited to comparisons with other models tested in this same facility and can be used to detect possible trends. A comprehensive set of test conditions was used to describe unsteady behavior of an airfoil, including two angle of attack amplitudes, ±5.5° and ±10°; four Reynolds numbers, 0.75, 1, 1.25, and 1.5 million; three pitch oscillation frequencies, 0.6, 1.2, and 1.8; and three mean angles of attack, 8°, 14°, and 20°.

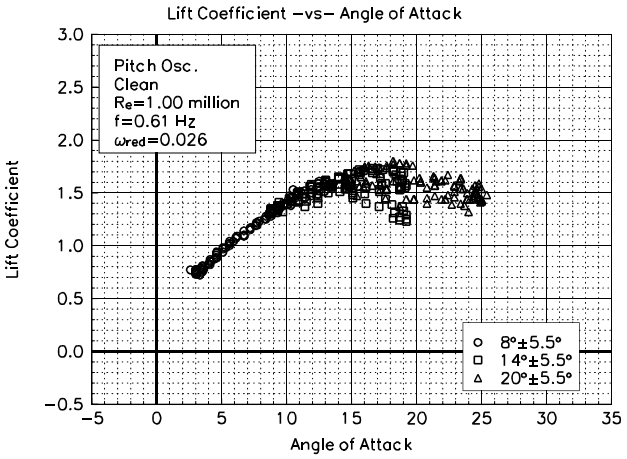

Figure 20. Clean, C_l vs α, ω_{red}=0.026, ±5.5°.

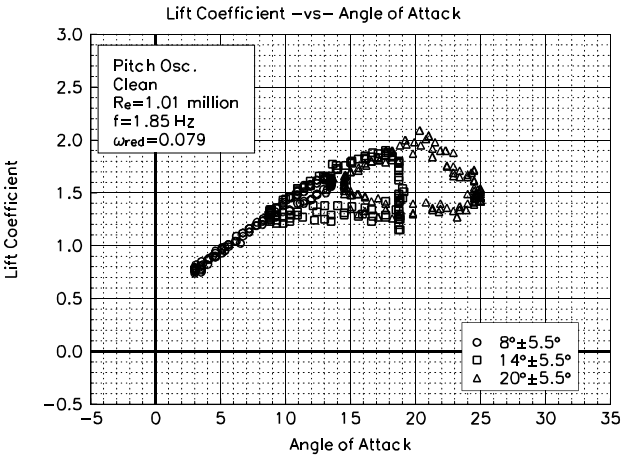

Figure 21. Clean, C_l vs α, ω_{red}=0.079, ±5.5°.

Figure 20 shows the lift coefficient versus angle of attack for the ±5.5° amplitude, model clean case, at reduced frequency of 0.026 and 1 million Reynolds number. Note that all three mean angles of attack are plotted on the same figure. The maximum pre-stall lift coefficient for this case is near 1.73 and occurs when the airfoil is traveling with the angle of attack increasing. In contrast, when the model is traveling through decreasing angles of attack, the stall recovery is delayed and a hysteresis behavior is exhibited in the lift coefficient that can be seen throughout all the unsteady data. In order to obtain some measure of this hysteresis behavior, the lift coefficient on the "return" portion of the curve, at the angle of attack where maximum lift coefficient occurs, can be used. For the case discussed here, the hysteresis or decreasing angle of attack lift coefficient is 1.37, a 21% decrease from the 1.73 unsteady maximum value. By comparison, the steady state maximum lift coefficient is 1.55. At higher reduced frequency of 0.079, the hysteresis behavior is more pronounced, as seen in figure 21. In addition to greater hysteresis, the maximum lift coefficient is increased to about 1.90, is a 23% increase over the steady state value. The corresponding hysteresis lift coefficient is 1.27. This difference between steady state behavior and unsteady hysteresis behavior is a main reason that unsteady testing should be required for airfoils used in wind turbine applications.

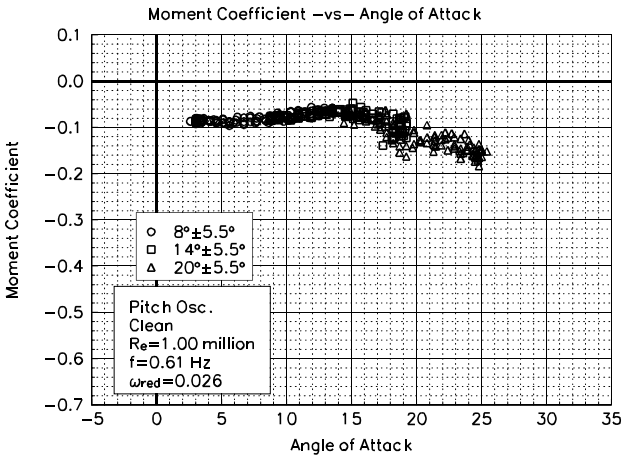

Figure 22. Clean, C_m vs α, ω_{red}=0.026, ±5.5°.

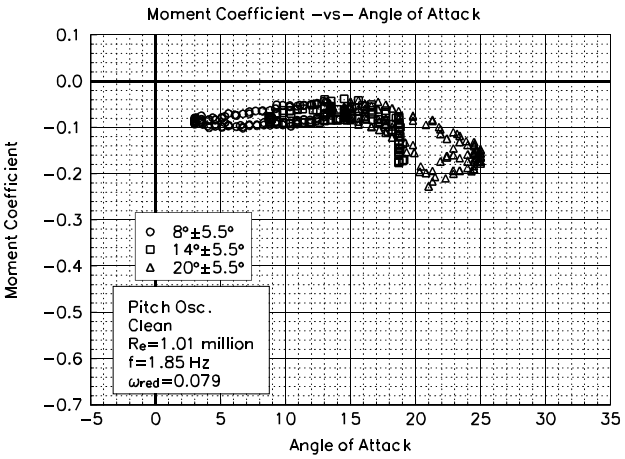

Figure 23. Clean, C_m vs α, ω_{red}=0.079, ±5.5°.

The pitching moment in figures 22 and 23 corresponds to the same conditions as the two lift coefficient plots previously discussed. Hysteresis behavior is present but it is not as apparent as in the lift coefficient plots. However, the higher reduced frequency case does show hysteresis more than the lower reduced frequency case. For reference, the steady state maximum lift occurs near 15° angle of attack and the steady state pitching moment at this maximum lift point is -0.0615. By comparison, when the airfoil is undergoing pitch oscillation for the lower frequency, pitching moment varies from -0.0932 to -0.0795 (at the angle of attack were maximum lift occurs), a 52% to 29% increase in magnitude from the steady state value. Note the angle of attack were the maximum lift coefficient occurs does not necessarily show the "greatest" hysteresis behavior but does give a relative indication of the effect.

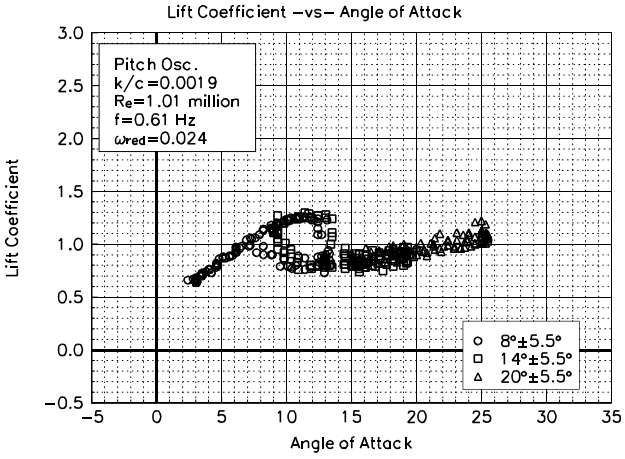

Figure 24. LEGR, C_l vs α, ω_{red}=0.024, ±5.5°.

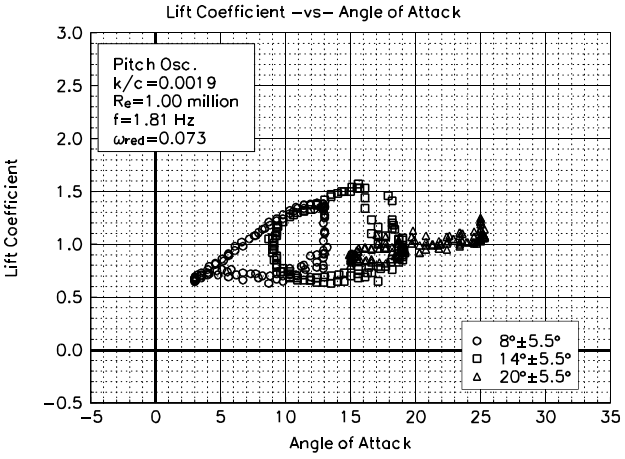

Figure 25. LEGR, C_l vs α, ω_{red}=0.073, ±5.5°.

In comparison to the clean data, the application of LEGR reduces the maximum lift coefficient in the pitch oscillation cases. Lift coefficient versus angle of attack with LEGR applied is shown in figure 24 for the 0.024 reduced frequency case. The 0.073 reduced frequency case is shown in figure 25. Both plots correspond to the same run conditions described earlier for the clean cases. For the lower reduced frequency, the maximum unsteady lift coefficient is reduced to 1.30 from the corresponding clean case of 1.73, a 25% decrease. Hysteresis behavior is apparent at this frequency, and the loops are slightly more apparent than in the clean case; the corresponding hysteresis lift coefficient is 0.80 when LEGR is applied. In comparison, the higher frequency, LEGR case has a maximum lift coefficient of 1.57 while the model is increasing in angle of attack and the corresponding decreasing angle of attack lift coefficient is 0.72. The application of

LEGR increased the hysteresis loop size when compared to the clean case at the same run conditions, and the hysteresis loop can be seen at the lower angles of attack for the LEGR case.

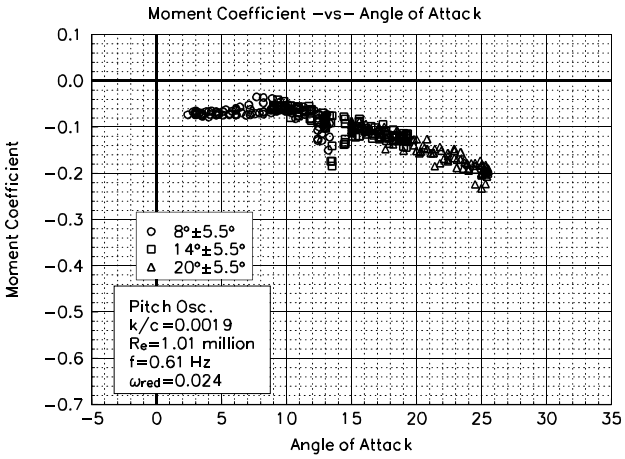

Figure 26. LEGR, C_m vs α, ω_{red}=0.024, ±5.5°.

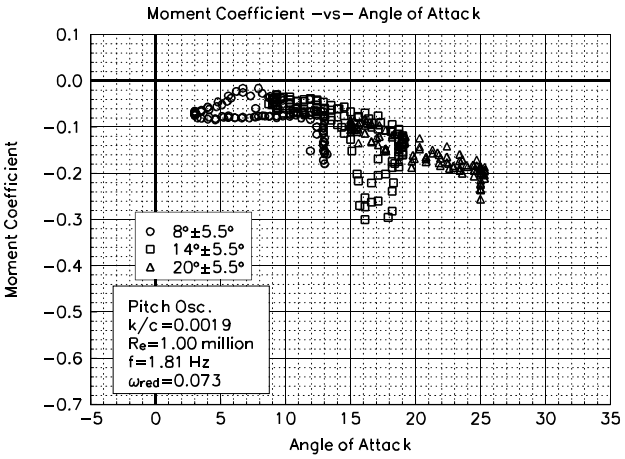

Figure 27. LEGR, C_m vs α, ω_{red}=0.073, ±5.5°.

The pitching moment coefficient shown in figure 26 is for 0.024 reduced frequency with LEGR applied. At the angle of unsteady maximum lift, the pitching moment ranges from -0.0652 to -0.0822; the steady state LEGR pitching moment is -0.0459 at the steady state stall angle of attack (10.2°). The higher reduced frequency of 0.073 with LEGR applied is shown in figure 27. As was seen with the lift coefficient, pitching moment hysteresis is also more apparent at the higher reduced frequency than the at lower reduced frequency. Unsteady maximum lift angle of attack for this reduced frequency occurs at 15.6°, and the pitching moment ranges from -0.2166 to -0.0769 at that angle. The effect of LEGR is more visible at the higher frequencies, where the stall is more abrupt and generates a drastic increase in the magnitude of the pitching moment. Throughout the higher angle of attack range, the magnitude of the unsteady pitching moment can be very different from the steady state, clean condition (steady state pitching moment at maximum lift is -0.0615). It seems these differences can have an impact on the fatigue life predictions of a wind turbine system.

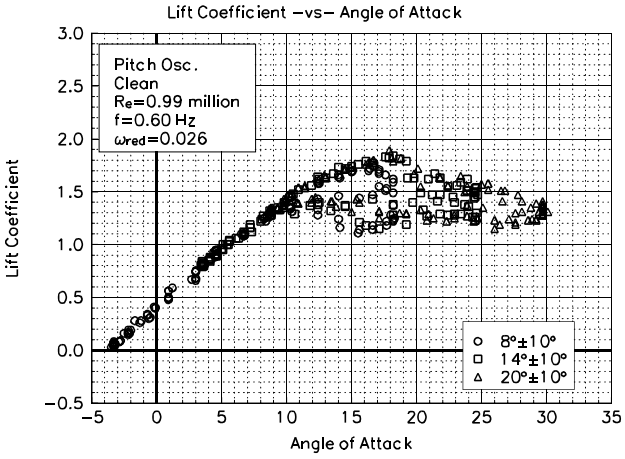

Figure 28. Clean, C_l vs α, ω_{red}=0.026, ±10°.

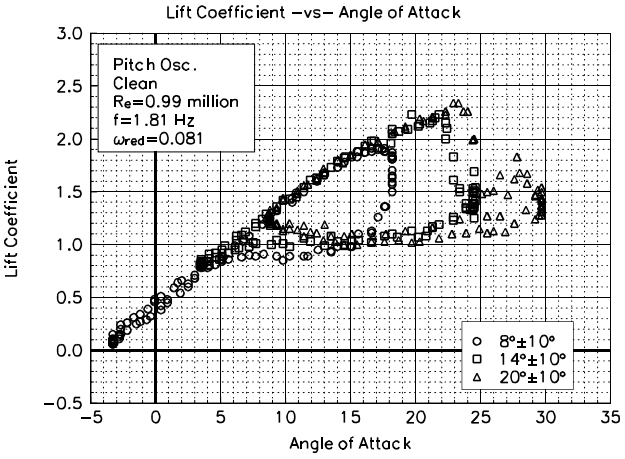

Figure 29. Clean, C_l vs α, ω_{red}=0.081, ±10°.

In addition to the ±5° unsteady experimental data, ±10° unsteady data were obtained with and without LEGR. The data were taken at 1 million Reynolds number using the same mean angle and frequencies as the 5.5° amplitude cases. Figures 28 and 29 show the ±10°, unsteady, clean, lift coefficient for the reduced frequencies of 0.026 and 0.081, respectively. The maximum lift coefficient for the lower frequency is 1.84

and occurs, as expected, when the airfoil is traveling through increasing angle of attack. The hysteresis lift coefficient (at 18.2°) is 1.28. At the higher reduced frequency, the maximum lift coefficient occurs at a higher angle of attack, 21.8°, and is 2.23. The corresponding hysteresis lift coefficient is 1.19. The difference between the maximum lift coefficient and the hysteresis lift coefficient indicates a much larger hysteresis response for the higher reduced frequency than for the lower reduced frequency. The steady state, clean, maximum lift coefficient is 1.55; therefore, the clean unsteady behavior created lift coefficients up to 44% higher than the steady state conditions.

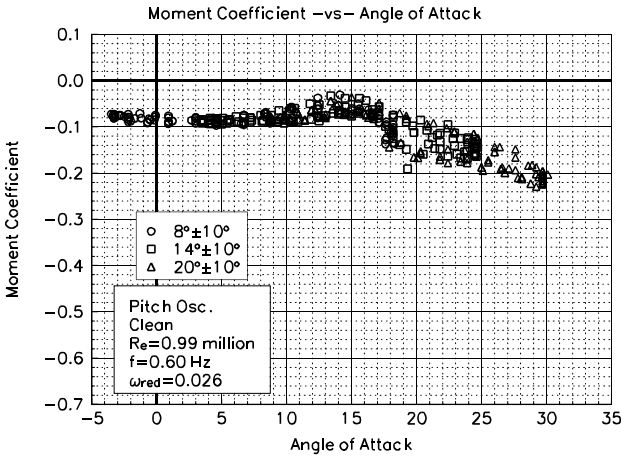

Figure 30. Clean, C_m vs α, ω_{red}=0.026, ±10°.

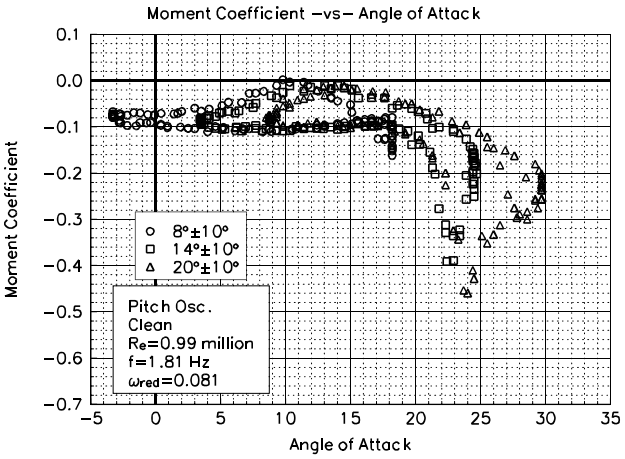

Figure 31. Clean, C_m vs α, ω_{red}=0.081, ±10°.

The quarter chord pitching moments with the same reduced frequencies as the lift coefficient cases are shown in figures 30 and 31. The hysteresis behavior observed in the lift coefficient plots is also reflected in this pitching moment data. Near the maximum lift angle of attack, 18.2°, for the lower frequency, the pitching moment coefficient ranges from -0.1250 to -0.0800; whereas the 0.081 reduced frequency case has maximum lift near 21.8° and pitching moment ranges from -0.2270 to -0.1009. The higher reduced frequency again shows large hysteresis loops for all three mean angles of attack. In comparison, the steady state pitching moment is -0.0615 near the steady state maximum lift coefficient angle of attack of 15.3°.

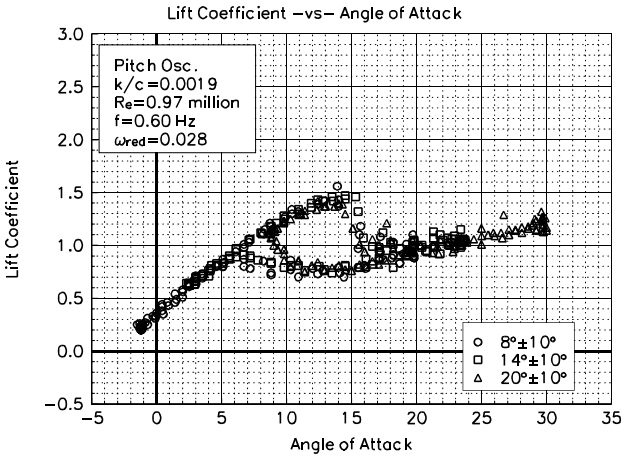

Figure 32. LEGR, C_l vs α, ω_{red}=0.028, ±10°.

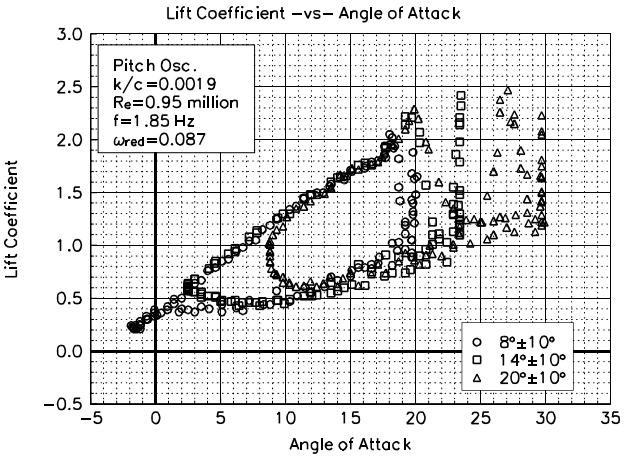

Figure 33. LEGR, C_l vs α, ω_{red}=0.087, ±10°.

The application of LEGR degrades the lift performance of the airfoil, as would be expected from the results discussed previously. The LEGR, lift coefficient data for reduced frequencies of 0.028 and 0.087 are shown in figures 32 and 33, respectively. The maximum lift coefficient is reduced to 1.47 from 1.84, for the low

frequency clean case. Although there is a reduction, this value is still significantly higher than the LEGR steady state case, which has a maximum lift coefficient of 1.13 at 10.2° angle of attack. The higher reduced frequency has a maximum lift coefficient of 2.22, which occurs near 19.2° angle of attack. The corresponding lift coefficient at 19.2° for the airfoil traveling with decreasing angle of attack is 0.74, or one third of the maximum. In the deep stall region for the higher frequencies cases, the lift coefficient data show an abrupt stall and sharp recovery, which is not necessarily evident in the graphs.

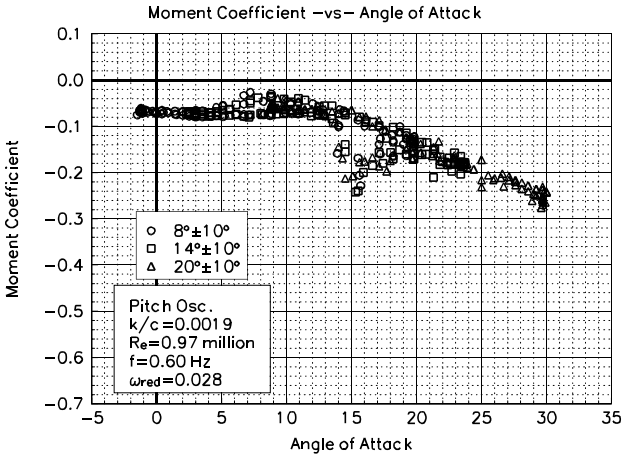

Figure 34. LEGR, C_m vs α, ω_{red}=0.028, ±10°.

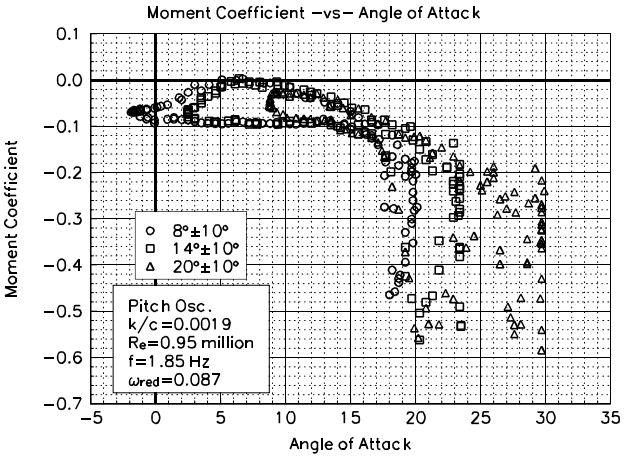

Figure 35. LEGR, C_m vs α, ω_{red}=0.087, ±10°.

Figures 34 and 35 show the corresponding pitching moment coefficients for the LEGR case at reduced frequencies of 0.028 and 0.087. For the 0.028 reduced frequency case, the pitching moment varies from -0.1393 to -0.0715 at 14.5° (were the maximum lift occurs). The hysteresis behavior is more pronounced for the higher reduced frequency case where the range of pitching moments at the maximum lift angle of 19.2° is from -0.4247 to -0.1046. These values are much higher in magnitude than the steady state LEGR value of -0.0459.

Although all the unsteady data were not discussed here, the previous discussion included typical examples of the wind tunnel data. The remaining cases of the ±5° and ±10° oscillation data for all the Reynolds numbers are included in Appendix C.

The following four unsteady pressure distributions show examples of the data used to calculate the lift, pressure drag, and pitching moment coefficients. Figure 36 shows the distribution for a clean model with reduced frequency of 0.053, 14° mean angle of attack, and ±10° pitch oscillation. For plotting clarity, the model pressures were "unwrapped" about the trailing edge. The upper surface pressures are depicted on the right of the surface plot; lower surface values are on the left. The trailing edge is at the midpoint of the x-axis with the leading edge at each extreme. The time scale corresponds to angle of attack. Separation areas are defined by the irregular, "rough" areas in the plot surface. The upper surface pressure peaks correspond to the maximum lift locations in the sweeps. For clarification of the irregularities in the pressure distribution, an equally spaced grid was used. The pressure coefficients were linearly interpolated to the specified number of evenly spaced x positions. For this case, during high angle of attack oscillations, much of the airfoil upper surface separated. The lower surface stays attached through all of the airfoil travel.

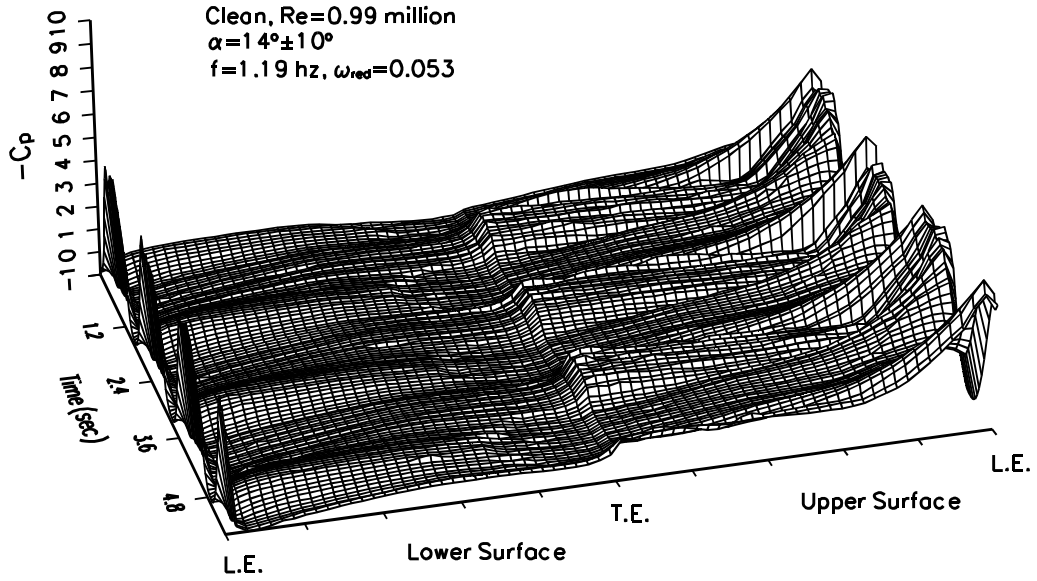

Figure 36. Unsteady pressure distribution, clean, ω_{red}=0.053, 14±10°.

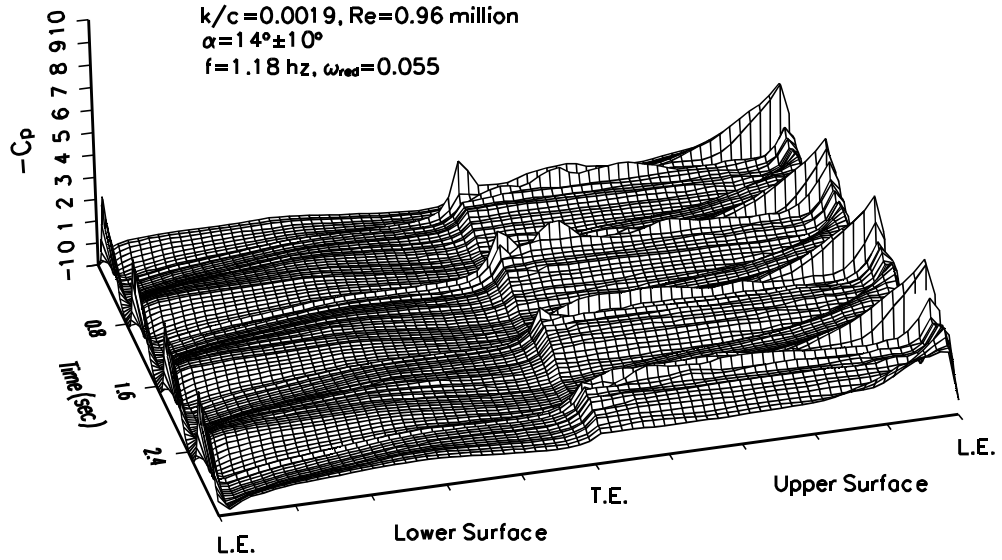

Figure 37. Unsteady pressure distribution, LEGR, ω_{red}=0.055, 14±10°.

Figure 37 shows the LEGR case for the same test conditions as the previous figure. In this case, the pressure peaks were not as high as for the clean case and the stall behavior becomes more noticeable as even more of the upper surface is separated.

Figure 38 shows the same clean run conditions as above except at a smaller oscillation angle. The structure is similar to the previous graphs; however, there is less flow separation on the upper surface, the consequence of lower angles of attack.

Figure 39 shows clean run conditions for a ±10° oscillation at a higher Reynolds number and 20° mean angle of attack. Because of the higher angles of attack, significant portions of the upper surface have separated. The pressure peaks seen emerging at the leading edge have pressure coefficient values up to -5.5.

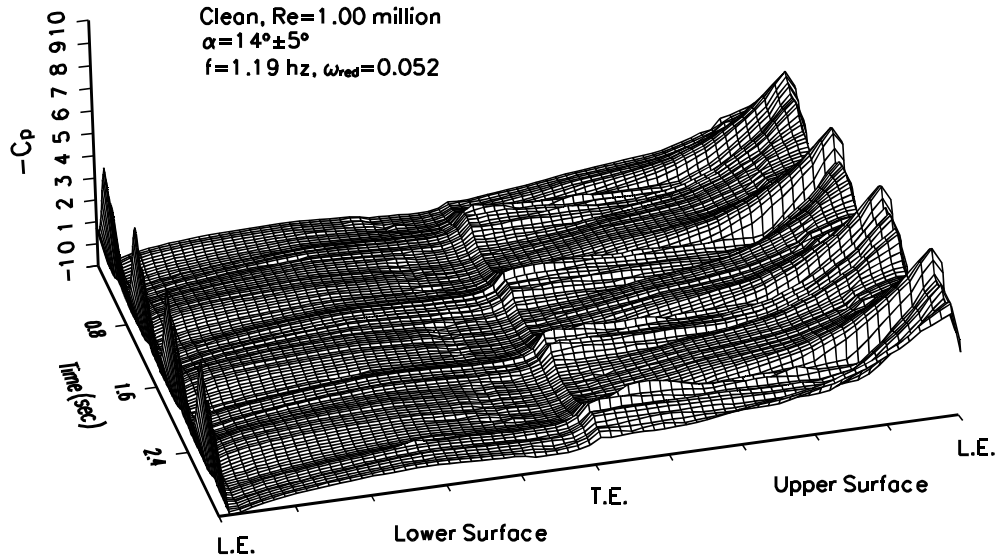

Figure 38. Unsteady pressure distribution, clean, ω_{red}=0.052, 14±5.5°.

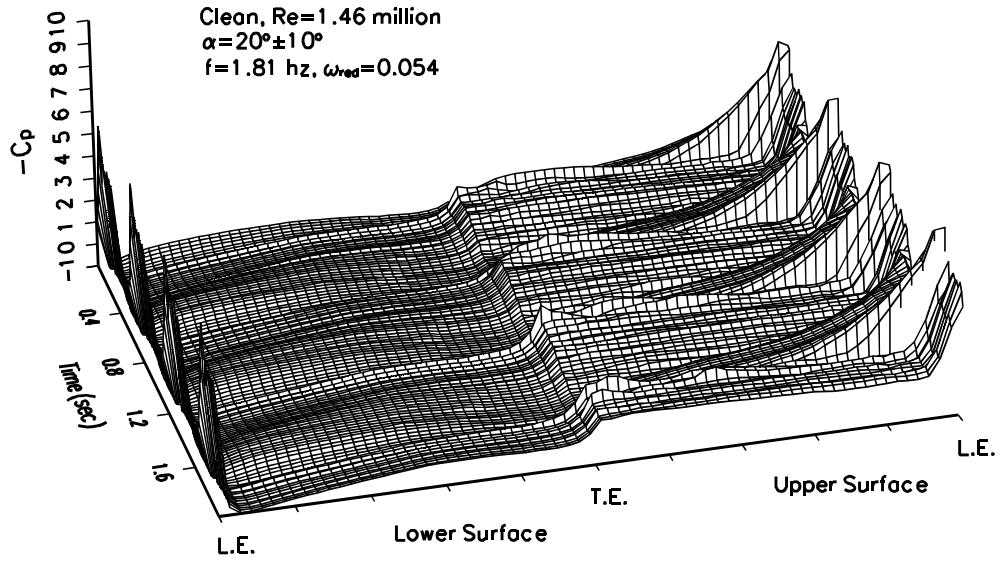

Figure 39. Unsteady pressure distribution, clean, ω_{red}=0.053, 20±10°.

Summary of Results

The LS(1)-0417MOD airfoil was tested under steady and pitch oscillation conditions. Baseline tests were made while the model was clean, and then corresponding tests were conducted with LEGR applied. A summary of the steady state aerodynamic parameters is shown in Table 1. As observed, the application of LEGR reduced the maximum lift of the airfoil up to 27% and the minimum drag coefficient increased by 42% to 46%. LEGR also affected the zero lift pitching moment coefficient, reducing the magnitude an average of 15%.

Table 1. LS(1)-0417MOD Aerodynamic Parameters Summary

Grit Pattern	Reynolds no.	C_{lmax}	C_{dmin}	C_{mo}
Clean	0.75×10^6	1.54 @ 16.3	0.0091	-0.0755
k/c=0.0019	0.75×10^6	1.12 @ 10.3	0.0132	-0.0621
Clean	1.00×10^6	1.55 @ 15.3	0.0091	-0.0748
k/c=0.0019	1.00×10^6	1.13 @ 10.2	0.0129	-0.0634
Clean	1.25×10^6	1.54 @ 14.3	0.0085	-0.0732
k/c=0.0019	1.25×10^6	1.16 @ 10.3	0.0124	-0.0631
Clean	1.50×10^6	1.54 @ 14.3	0.0082	-0.0727
k/c=0.0019	1.50×10^6	1.16 @ 10.3	0.0118	-0.0625

Table 2. LS(1)-0417MOD, Unsteady, Clean, ±5.5°

ω_{red}	$Rex10^{-6}$	f	C_{lmax}	α_{Clmax}	$C_{l\,dec}$	$C_{m\,inc}$	$C_{m\,dec}$
0.035	0.75	0.61	1.77	17.7	1.55	-0.1250	-0.0763
0.069	0.76	1.21	1.86	17.1	1.49	-0.0847	-0.0691
0.104	0.76	1.83	1.96	18.6	1.30	-0.1478	-0.0914
0.026	1.00	0.61	1.73	17.0	1.37	-0.0932	-0.0795
0.052	1.00	1.19	1.84	16.6	1.47	-0.0810	-0.0730
0.079	1.01	1.85	1.90	17.7	1.27	-0.0993	-0.0686
0.020	1.26	0.61	1.68	16.1	1.26	-0.0699	-0.0604
0.041	1.26	1.19	1.76	16.6	1.09	-0.0843	-0.0645
0.061	1.26	1.81	1.83	16.5	1.07	-0.0782	-0.0619
0.017	1.47	0.61	1.71	17.1	1.26	-0.1374	-0.1105
0.035	1.46	1.19	1.74	16.2	1.06	-0.0799	-0.0742
0.054	1.46	1.85	1.82	16.6	1.29	-0.0782	-0.0947

The pitch oscillation data can be divided into two groups, the ±5.5° amplitude and ±10° amplitude oscillations which show similar trends. For both ±5.5° and ±10°, the unsteady test conditions and some parameters are listed in Tables 2, 3, 4, and 5. As the reduced frequency, which takes oscillation and tunnel speed into account, is increased, maximum lift coefficient also increases. In addition, the hysteresis behavior becomes increasingly apparent with increased reduced frequency.

Table 3. LS(1)-0417MOD, Unsteady, LEGR, ±5.5°

ω_{red}	$Rex10^{-6}$	f	C_{lmax}	α_{Clmax}	$C_{l\,dec}$	$C_{m\,inc}$	$C_{m\,dec}$
0.032	0.76	0.60	1.34	13.5	0.72	-0.1066	-0.0713
0.066	0.75	1.21	1.52	15.0	0.76	-0.1853	-0.0783
0.100	0.76	1.85	1.72	16.6	0.72	-0.2408	-0.0800
0.024	1.01	0.61	1.30	11.4	0.80	-0.0652	-0.0822
0.048	1.00	1.18	1.42	14.0	0.76	-0.1343	-0.0689
0.073	1.00	1.81	1.57	15.6	0.72	-0.2166	-0.0769
0.019	1.25	0.61	1.29	12.4	0.80	-0.0871	-0.0718
0.039	1.25	1.21	1.43	13.9	0.77	-0.1535	-0.0810
0.059	1.25	1.83	1.50	14.8	0.76	-0.1830	-0.0736
0.018	1.34	0.61	1.30	12.4	0.73	-0.1061	-0.0808
0.037	1.33	1.21	1.41	12.4	0.76	-0.0840	-0.0782
0.056	1.34	1.85	1.49	14.5	0.77	-0.1649	-0.0700

Table 4. LS(1)-0417MOD, Unsteady, Clean, ±10°

ω_{red}	$Rex10^{-6}$	f	C_{lmax}	α_{Clmax}	$C_{l\,dec}$	$C_{m\,inc}$	$C_{m\,dec}$
0.035	0.75	0.60	1.87	18.0	1.48	-0.0994	-0.0717
0.072	0.74	1.21	2.18	21.3	1.17	-0.2014	-0.0927
0.109	0.74	1.83	2.48	23.4	1.22	-0.4590	-0.1363
0.026	0.99	0.60	1.84	18.2	1.28	-0.1250	-0.0800
0.053	0.99	1.19	2.05	19.8	1.07	-0.1770	-0.0669
0.081	0.99	1.81	2.23	21.8	1.19	-0.2770	-0.1009
0.021	1.24	0.61	1.77	16.8	1.27	-0.0945	-0.0807
0.042	1.23	1.19	1.92	18.2	1.21	-0.0937	-0.0765
0.065	1.23	1.85	2.14	20.8	1.01	-0.1724	-0.0829
0.018	1.46	0.61	1.75	17.0	1.35	-0.0968	-0.0918
0.035	1.46	1.18	1.90	18.2	1.19	-0.1048	-0.0839
0.054	1.46	1.81	2.04	20.3	1.09	-0.2200	-0.1002

As expected, the application of LEGR reduces the aerodynamic performance of the airfoil. The maximum lift coefficient is reduced by 12% to 25% for the ±5.5° case and 0% to 20% for the ±10° case. In addition to the following the same trends as the clean, unsteady data discussed previously, LEGR causes the hysteresis behavior to persist into lower angles of attack than in the clean cases. Overall, the unsteady wind tunnel data show hysteresis behavior that becomes more apparent with increased reduced frequency. The maximum unsteady lift coefficient can be up to 54% higher for the ±5.5° amplitude and up to 119% higher for the ±10° amplitude than the steady state maximum lift coefficient. Variation in the quarter chord pitching moment coefficient can be up to ten times greater than that indicated by steady state results. These findings indicate

that it is very important to consider the unsteady loading that will occur in wind turbine operation because steady state results can greatly underestimate the forces.

Table 5. LS(1)-0417MOD, Unsteady, LEGR, ±10°

ω_{red}	$Rex10^{-6}$	f	C_{lmax}	α_{Clmax}	$C_{l\,dec}$	$C_{m\,inc}$	$C_{m\,dec}$
0.037	0.74	0.60	1.55	15.6	0.77	-0.1470	-0.0825
0.074	0.73	1.19	2.00	19.2	0.76	-0.4691	-0.0956
0.115	0.72	1.83	2.45	21.3	1.51	-0.5229	-0.4117
0.028	0.97	0.60	1.47	14.5	0.80	-0.1393	-0.0715
0.055	0.96	1.18	1.81	16.6	0.92	-0.2555	-0.1136
0.087	0.95	1.85	2.22	19.2	0.74	-0.4247	-0.1046
0.022	1.23	0.60	1.41	13.5	0.75	-0.1048	-0.0757
0.044	1.23	1.19	1.75	16.6	0.76	-0.3621	-0.0781
0.067	1.22	1.83	2.04	17.8	0.75	-0.3243	-0.0837
0.018	1.46	0.60	1.41	13.5	0.75	-0.1149	-0.0766
0.037	1.46	1.21	1.63	15.6	0.71	-0.2148	-0.0739
0.057	1.45	1.83	1.86	17.2	0.84	-0.3556	-0.1048

References

Pope, A.; Harper, J.J. 1966. *Low Speed Wind Tunnel Testing*. New York, NY: John Wiley & Sons, Inc.

Schlichting, H. 1979. *Boundary Layer Theory*. New York, NY: McGraw-Hill Inc.

Smetana, F., Summey, D., et-al. 1975. *Light Aircraft Lift, Drag, Moment Prediction - a Review and Analysis.* North Carolina State University. NASA CR-2523.

Appendix A: Model and Surface Pressure Tap Coordinates

List of Tables Page

Table A1. LS(1)-0417MOD Measured Model Coordinates, 18-inch Desired Chord				
Chord Station (in)	Upper Ordinate (in)		Chord Station (in)	Lower Ordinate (in)
0.0000	0.0000		0.0000	0.0000
0.0024	0.0405		0.0006	-0.0514
0.0051	0.0627		0.0020	-0.0691
0.0077	0.0782		0.0036	-0.0849
0.0101	0.0922		0.0052	-0.0995
0.0124	0.1034		0.0068	-0.1103
0.0147	0.1138		0.0085	-0.1205
0.0170	0.1239		0.0102	-0.1299
0.0191	0.1329		0.0120	-0.1385
0.0214	0.1415		0.0137	-0.1470
0.0236	0.1494		0.0154	-0.1540
0.0257	0.1573		0.0171	-0.1613
0.0278	0.1643		0.0189	-0.1679
0.0300	0.1714		0.0206	-0.1742
0.0321	0.1781		0.0224	-0.1804
0.0343	0.1846		0.0241	-0.1864
0.0365	0.1912		0.0259	-0.1922
0.0387	0.1974		0.0277	-0.1977
0.0408	0.2033		0.0365	-0.2217
0.0430	0.2094		0.0457	-0.2428
0.0450	0.2148		0.0551	-0.2631
0.0556	0.2414		0.0640	-0.2807
0.0664	0.2662		0.0733	-0.2970
0.0766	0.2874		0.0824	-0.3117
0.0873	0.3083		0.0917	-0.3254
0.0976	0.3270		0.1010	-0.3382
0.1081	0.3454		0.1101	-0.3497
0.1183	0.3623		0.1196	-0.3607
0.1287	0.3787		0.1290	-0.3713
0.1392	0.3945		0.1385	-0.3812
0.1496	0.4100		0.1478	-0.3904
0.1601	0.4250		0.1576	-0.3996
0.1705	0.4395		0.1672	-0.4086
0.1809	0.4535		0.1767	-0.4173
0.1913	0.4674		0.1861	-0.4253

Table A1. LS(1)-0417MOD Measured Model Coordinates, 18-inch Desired Chord				
Chord Station (in)	Upper Ordinate (in)		Chord Station (in)	Lower Ordinate (in)
0.2016	0.4806		0.1956	-0.4331
0.2121	0.4942		0.2054	-0.4409
0.2223	0.5068		0.2148	-0.4482
0.2327	0.5197		0.2246	-0.4553
0.2429	0.5317		0.2342	-0.4622
0.2534	0.5440		0.2436	-0.4688
0.2636	0.5557		0.2528	-0.4747
0.2740	0.5673		0.2627	-0.4806
0.2844	0.5792		0.2729	-0.4871
0.2945	0.5904		0.2820	-0.4924
0.3049	0.6016		0.2920	-0.4980
0.3152	0.6125		0.3017	-0.5034
0.3255	0.6235		0.3116	-0.5090
0.3359	0.6343		0.3210	-0.5139
0.3463	0.6449		0.3308	-0.5189
0.3567	0.6557		0.3412	-0.5245
0.3669	0.6661		0.3504	-0.5291
0.3771	0.6762		0.3606	-0.5343
0.3875	0.6863		0.3704	-0.5394
0.3982	0.6969		0.3800	-0.5444
0.4078	0.7060		0.3892	-0.5482
0.4185	0.7160		0.4002	-0.5537
0.4287	0.7256		0.4096	-0.5584
0.4388	0.7349		0.4189	-0.5627
0.4492	0.7444		0.4291	-0.5673
0.4591	0.7532		0.4391	-0.5725
0.4697	0.7627		0.4481	-0.5763
0.4797	0.7717		0.4582	-0.5807
0.4900	0.7804		0.4686	-0.5858
0.5002	0.7892		0.4775	-0.5894
0.5105	0.7980		0.4879	-0.5939
0.5205	0.8061		0.4981	-0.5984
0.5311	0.8152		0.5078	-0.6026
0.5410	0.8229		0.5179	-0.6070
0.5515	0.8312		0.5279	-0.6113
0.5621	0.8399		0.5378	-0.6156

Table A1. LS(1)-0417MOD Measured Model Coordinates, 18-inch Desired Chord				
Chord Station (in)	Upper Ordinate (in)		Chord Station (in)	Lower Ordinate (in)
0.5714	0.8468		0.5475	-0.6196
0.5825	0.8553		0.5574	-0.6236
0.5925	0.8631		0.5674	-0.6278
0.6027	0.8707		0.5770	-0.6316
0.6130	0.8785		0.5871	-0.6355
0.6233	0.8860		0.5966	-0.6391
0.6339	0.8938		0.6068	-0.6431
0.6435	0.9008		0.6165	-0.6468
0.6538	0.9079		0.6262	-0.6504
0.6640	0.9150		0.6361	-0.6540
0.6741	0.9220		0.6459	-0.6575
0.6842	0.9289		0.6560	-0.6611
0.6944	0.9358		0.6657	-0.6645
0.7047	0.9426		0.6759	-0.6680
0.7148	0.9494		0.6856	-0.6713
0.7251	0.9562		0.6956	-0.6747
0.7354	0.9629		0.7054	-0.6779
0.7457	0.9696		0.7151	-0.6811
0.7560	0.9763		0.7253	-0.6843
0.7660	0.9827		0.7350	-0.6875
0.7764	0.9893		0.7453	-0.6908
0.7866	0.9956		0.7549	-0.6938
0.7968	1.0022		0.7649	-0.6969
0.8071	1.0086		0.7750	-0.6999
0.8176	1.0153		0.7846	-0.7031
0.8274	1.0212		0.7946	-0.7062
0.8376	1.0273		0.8046	-0.7093
0.8478	1.0334		0.8145	-0.7123
0.8581	1.0396		0.8238	-0.7151
0.8682	1.0458		0.8339	-0.7179
0.8781	1.0516		0.8441	-0.7207
0.8884	1.0575		0.8541	-0.7238
0.8986	1.0634		1.0521	-0.7772
0.9090	1.0695		1.2510	-0.8252
0.9191	1.0754		1.4497	-0.8692
1.1215	1.1831		1.6488	-0.9085

Table A1. LS(1)-0417MOD Measured Model Coordinates, 18-inch Desired Chord				
Chord Station (in)	Upper Ordinate (in)		Chord Station (in)	Lower Ordinate (in)
1.3239	1.2774		1.8477	-0.9443
1.5261	1.3611		2.0468	-0.9767
1.7278	1.4344		2.2463	-1.0065
1.9294	1.4990		2.4460	-1.0339
2.1309	1.5558		2.6456	-1.0590
2.3321	1.6057		2.8453	-1.0818
2.5333	1.6489		3.0451	-1.1029
2.7345	1.6859		3.2447	-1.1218
2.9355	1.7184		3.4448	-1.1388
3.1364	1.7461		3.6447	-1.1543
3.3372	1.7697		3.8445	-1.1689
3.5379	1.7890		4.0447	-1.1819
3.7386	1.8051		4.2447	-1.1938
3.9392	1.8180		4.4446	-1.2046
4.1397	1.8276		4.6450	-1.2137
4.3402	1.8349		4.8448	-1.2219
4.5405	1.8401		5.0451	-1.2289
4.7409	1.8427		5.2453	-1.2349
4.9411	1.8433		5.4455	-1.2397
5.1417	1.8417		5.6458	-1.2437
5.3417	1.8383		5.8462	-1.2471
5.5418	1.8333		6.0463	-1.2491
5.7422	1.8268		6.2464	-1.2502
5.9421	1.8192		6.4469	-1.2503
6.1422	1.8102		6.6472	-1.2498
6.3424	1.8002		6.8475	-1.2478
6.5423	1.7893		7.0480	-1.2449
6.7423	1.7781		7.2484	-1.2410
6.9424	1.7665		7.4489	-1.2360
7.1423	1.7547		7.6496	-1.2305
7.3423	1.7423		7.8499	-1.2242
7.5425	1.7295		8.0504	-1.2171
7.7423	1.7163		8.2510	-1.2091
7.9423	1.7023		8.4515	-1.2002
8.1424	1.6880		8.6519	-1.1899
8.3422	1.6736		8.8526	-1.1782

Table A1. LS(1)-0417MOD Measured Model Coordinates, 18-inch Desired Chord				
Chord Station (in)	Upper Ordinate (in)		Chord Station (in)	Lower Ordinate (in)
8.5422	1.6587		9.0532	-1.1649
8.7420	1.6434		9.2540	-1.1503
8.9418	1.6275		9.4547	-1.1339
9.1419	1.6111		9.6552	-1.1153
9.3416	1.5941		9.8561	-1.0946
9.5412	1.5762		10.0570	-1.0724
9.7411	1.5575		10.2579	-1.0489
9.9407	1.5374		10.4589	-1.0238
10.1403	1.5166		10.6599	-0.9969
10.3401	1.4949		10.8609	-0.9681
10.5397	1.4722		11.0622	-0.9378
10.7392	1.4482		11.2636	-0.9061
10.9388	1.4226		11.4646	-0.8731
11.1383	1.3957		11.6665	-0.8392
11.3377	1.3674		11.8677	-0.8044
11.5372	1.3375		12.0691	-0.7681
11.7368	1.3063		12.2709	-0.7312
11.9360	1.2738		12.4726	-0.6942
12.1354	1.2398		12.6741	-0.6568
12.3348	1.2048		12.8759	-0.6190
12.5342	1.1692		13.0777	-0.5811
12.7338	1.1335		13.2792	-0.5431
12.9331	1.0968		13.4811	-0.5048
13.1327	1.0591		13.6829	-0.4670
13.3320	1.0211		13.8845	-0.4295
13.5314	0.9825		14.0865	-0.3926
13.7308	0.9430		14.2882	-0.3569
13.9303	0.9029		14.4897	-0.3230
14.1297	0.8622		14.6916	-0.2906
14.3291	0.8208		14.8932	-0.2602
14.5284	0.7789		15.0947	-0.2315
14.7278	0.7369		15.2963	-0.2046
14.9270	0.6948		15.4977	-0.1787
15.1266	0.6519		15.6992	-0.1546
15.3258	0.6085		15.9008	-0.1329
15.5250	0.5648		16.1021	-0.1151

Table A1. LS(1)-0417MOD Measured Model Coordinates, 18-inch Desired Chord				
Chord Station (in)	Upper Ordinate (in)		Chord Station (in)	Lower Ordinate (in)
15.7246	0.5211		16.3032	-0.1008
15.9236	0.4771		16.5045	-0.0899
16.1229	0.4327		16.7055	-0.0829
16.3222	0.3881		16.9064	-0.0800
16.5213	0.3430		17.1074	-0.0816
16.7204	0.2974		17.3083	-0.0886
16.9198	0.2512		17.5088	-0.1011
17.1188	0.2045		17.7093	-0.1198
17.3175	0.1547		17.9097	-0.1450
17.5160	0.1005		17.9141	-0.1455
17.7142	0.0393		17.9189	-0.1460
17.9089	-0.0297		17.9237	-0.1465
17.9134	-0.0314		17.9287	-0.1470
17.9186	-0.0335		17.9337	-0.1475
17.9236	-0.0356		17.9383	-0.1479
17.9283	-0.0375		17.9433	-0.1484
17.9330	-0.0395		17.9482	-0.1488
17.9380	-0.0415		17.9529	-0.1492
17.9431	-0.0436		17.9575	-0.1494
17.9477	-0.0456		17.9620	-0.1496
17.9523	-0.0476		17.9664	-0.1497
17.9570	-0.0497		17.9709	-0.1496
17.9622	-0.0519		17.9747	-0.1493
17.9670	-0.0541		17.9774	-0.1485
17.9713	-0.0561		17.9794	-0.1475
17.9758	-0.0583		17.9816	-0.1459
17.9805	-0.0607		17.9840	-0.1434
17.9843	-0.0630		17.9854	-0.1389
17.9869	-0.0654		17.9891	-0.1319
17.9893	-0.0685			
17.9909	-0.0739			
17.9946	-0.0824			
End of Table A1				

Table A2. LS(1)-0417MOD Surface Pressure Taps, Non-Dimensional Coordinates		
Tap Number	Chord Station	Ordinate
1	0.9978	-0.0005
2	0.9839	-0.0063
3	0.9684	-0.0049
4	0.9444	-0.0041
5	0.9202	-0.0045
6	0.8909	-0.0064
7 *	0.8683	-0.0088
8	0.8422	-0.0121
9	0.8175	-0.0158
10	0.7909	-0.0201
11	0.7427	-0.0291
12	0.6922	-0.0386
13 *	0.6442	-0.0472
14	0.5950	-0.0550
15	0.5445	-0.0612
16	0.4960	-0.0653
17	0.3942	-0.0693
18	0.2943	-0.0689
19 *	0.2448	-0.0671
20	0.2193	-0.0656
21	0.1951	-0.0640
22	0.1710	-0.0618
23	0.1447	-0.0589
24	0.1198	-0.0556
25	0.0971	-0.0519
26	0.0714	-0.0467
27	0.0454	-0.0400
28	0.0195	-0.0297
29	-0.0001	0.0031
30	0.0162	0.0319
31	0.0300	0.0450
32	0.0530	0.0602
33	0.0766	0.0717
34	0.1030	0.0815
35	0.1284	0.0885
36	0.1524	0.0934

Table A2. LS(1)-0417MOD Surface Pressure Taps, Non-Dimensional Coordinates		
Tap Number	Chord Station	Ordinate
37	0.1784	0.0971
38	0.2028	0.0996
39	0.2286	0.1012
40	0.2529	0.1019
41 *	0.3031	0.1017
42	0.3537	0.0998
43	0.4029	0.0970
44 *	0.4544	0.0936
45	0.5027	0.0899
46 *	0.5513	0.0855
47	0.6056	0.0794
48	0.6517	0.0728
49	0.7026	0.0640
50	0.7516	0.0549
51	0.8008	0.0449
52	0.8273	0.0393
53 *	0.8551	0.0334
54	0.8772	0.0285
55	0.9001	0.0235
56	0.9268	0.0174
57	0.9515	0.0117
58	0.9754	0.0054
59	0.9880	0.0014
End of Table A2		

Taps marked with an * were unusable, because of weak response.

Appendix B: Steady State Data
Integrated Coefficients and Pressure Distributions

List of Tables Page

List of Figures Page

Table B1. LS(1)-0417MOD, Clean, Re = 0.75 x 10^6						
RUN	AOA	C_l	C_{dp}	$C_{m¼}$	Re x 10^{-6}	C_{dw}
113	-20.1	-0.45	0.2805	0.0361	0.76	--
112	-18.0	-0.39	0.2401	0.0286	0.75	--
111	-16.1	-0.33	0.2067	0.0233	0.76	--
110	-14.1	-0.38	0.1594	0.0141	0.73	--
109	-12.2	-0.69	0.0116	-0.0595	0.75	0.0493
108	-10.2	-0.66	0.0104	-0.0467	0.75	0.0287
107	-8.1	-0.43	0.0043	-0.0651	0.75	0.0165
106	-6.1	-0.26	-0.0008	-0.0701	0.75	0.0139
105	-4.1	-0.04	-0.0020	-0.0755	0.74	0.0097
104	-2.0	0.18	-0.0011	-0.0790	0.75	0.0095
103	-0.1	0.35	0.0027	-0.0814	0.75	0.0091
114	-0.1	0.35	0.0020	-0.0810	0.75	0.0113
140	-0.1	0.37	0.0004	-0.0799	0.75	0.0113
115	2.0	0.57	0.0080	-0.0788	0.75	0.0117
116	4.1	0.79	0.0158	-0.0807	0.75	0.0126
117	6.3	1.01	0.0242	-0.0796	0.75	0.0147
118	8.1	1.20	0.0256	-0.0757	0.74	0.0170
119	10.3	1.36	0.0361	-0.0690	0.74	0.0180
120	11.3	1.43	0.0405	-0.0636	0.74	0.0212
121	12.1	1.46	0.0459	-0.0584	0.74	0.0222
122	13.4	1.51	0.0526	-0.0522	0.74	0.0311
123	14.2	1.52	0.0682	-0.0521	0.75	--
124	15.3	1.53	0.0958	-0.0567	0.75	--
125	16.3	1.54	0.1266	-0.0645	0.75	--
126	17.4	1.54	0.1545	-0.0721	0.75	--
127	18.4	1.53	0.1806	-0.0780	0.75	--
128	19.1	1.19	0.1426	-0.0799	0.75	--
129	20.2	1.16	0.1627	-0.0863	0.75	--

Table B1. LS(1)-0417MOD, Clean, Re = 0.75 x 10^6						
RUN	AOA	C_l	C_{dp}	$C_{m¼}$	Re x 10^{-6}	C_{dw}
130	22.2	1.24	0.2191	-0.1039	0.74	--
131	24.1	1.31	0.2759	-0.1215	0.74	--
132	26.0	0.96	0.5257	-0.1932	0.72	--
133	28.1	1.07	0.6227	-0.2249	0.75	--
134	30.0	1.17	0.7195	-0.2560	0.74	--
135	32.1	1.24	0.8241	-0.2865	0.74	--
136	34.1	1.30	0.9302	-0.3179	0.75	--
137	35.9	1.33	1.0116	-0.3371	0.75	--
138	38.0	1.35	1.1111	-0.3635	0.74	--
139	40.1	1.33	1.1837	-0.3750	0.75	--
End of Table B1						

Table B2. LS(1)-0417MOD, Clean, Re = 1.0 x 10^6						
RUN	AOA	C_l	C_{dp}	$C_{m¼}$	Re x 10^{-6}	C_{dw}
49	-20.1	-0.43	0.2726	0.0309	1.00	--
48	-18.0	-0.39	0.2387	0.0277	1.00	--
47	-16.2	-0.37	0.2158	0.0294	1.00	--
46	-14.2	-0.69	0.0424	-0.0315	1.00	--
45	-12.1	-0.73	0.0041	-0.0605	1.00	0.0493
44	-10.3	-0.66	0.0030	-0.0537	1.00	0.0298
43	-8.1	-0.43	-0.0002	-0.0688	1.00	0.0177
42	-6.3	-0.27	-0.0035	-0.0713	1.00	0.0137
41	-4.1	-0.04	-0.0034	-0.0748	1.00	0.0105
40	-2.0	0.17	-0.0025	-0.0785	1.00	0.0091
39	-0.1	0.36	0.0010	-0.0807	1.00	0.0099
50	-0.1	0.37	0.0004	-0.0814	1.00	0.0097
76	-0.1	0.36	0.0007	-0.0806	1.00	0.0097
51	2.0	0.59	0.0065	-0.0823	1.00	0.0098
52	4.1	0.80	0.0148	-0.0821	1.00	0.0108
53	6.3	1.01	0.0220	-0.0809	1.00	0.0118
54	8.2	1.20	0.0253	-0.0764	1.00	0.0138
55	10.3	1.37	0.0353	-0.0691	1.00	0.0175
56	11.4	1.43	0.0391	-0.0632	1.00	0.0196
57	12.2	1.48	0.0427	-0.0586	1.00	0.0215
58	13.2	1.51	0.0554	-0.0543	1.00	0.0254
59	14.3	1.53	0.0680	-0.0524	1.00	--
60	15.3	1.55	0.0970	-0.0615	1.00	--
61	16.3	1.26	0.0941	-0.0688	1.02	--
62	17.2	1.21	0.1069	-0.0714	1.02	--
63	18.2	1.17	0.1269	-0.0768	1.00	--
64	19.2	1.14	0.1462	-0.0834	1.00	--
65	20.2	1.15	0.1678	-0.0893	1.00	--

Table B2. LS(1)-0417MOD, Clean, Re = 1.0 x 10^6						
RUN	AOA	C_l	C_{dp}	$C_{m¼}$	Re x 10^{-6}	C_{dw}
66	22.3	1.20	0.2214	-0.1054	0.99	--
67	24.2	1.37	0.3034	-0.1296	0.99	--
68	26.2	1.18	0.3305	-0.1444	0.99	--
69	28.2	1.16	0.3973	-0.1670	0.97	--
70	30.1	1.09	0.6750	-0.2343	0.98	--
71	32.1	1.13	0.7535	-0.2530	0.97	--
72	34.2	1.16	0.8307	-0.2700	0.98	--
73	36.0	1.29	0.9879	-0.3243	0.99	--
74	38.1	1.36	1.1175	-0.3645	0.98	--
75	39.9	1.34	1.1750	-0.3715	0.98	--
End of Table B2						

Table B3. LS(1)-0417MOD, Clean, Re = 1.25 x 10^6						
RUN	AOA	C_l	C_{dp}	$C_{m¼}$	Re x 10^{-6}	C_{dw}
11	-20.1	-0.42	0.2700	0.0319	1.24	--
10	-18.0	-0.39	0.2380	0.0297	1.25	--
9	-16.1	-0.35	0.2106	0.0271	1.25	--
8	-14.2	-0.73	0.0364	-0.0335	1.26	--
7	-12.1	-0.76	0.0006	-0.0596	1.25	0.0463
6	-10.2	-0.65	0.0015	-0.0586	1.26	0.0289
5	-8.1	-0.43	-0.0016	-0.0678	1.25	0.0156
4	-6.2	-0.27	-0.0029	-0.0701	1.25	0.0133
3	-4.1	-0.05	-0.0040	-0.0732	1.25	0.0110
2	-2.1	0.16	-0.0028	-0.0774	1.25	0.0089
12	-0.1	0.37	0.0000	-0.0813	1.25	0.0085
38	-0.1	0.37	0.0007	-0.0812	1.25	0.0087
1	0.0	0.40	-0.0004	-0.0820	1.26	0.0087
13	2.0	0.59	0.0068	-0.0837	1.25	0.0093
14	4.2	0.81	0.0143	-0.0824	1.25	0.0106
15	6.2	1.02	0.0198	-0.0811	1.25	0.0112
16	8.3	1.21	0.0271	-0.0760	1.25	0.0127
17	10.3	1.38	0.0327	-0.0688	1.24	0.0172
18	11.3	1.45	0.0385	-0.0644	1.25	0.0197
19	12.2	1.49	0.0390	-0.0578	1.25	0.0210
20	13.2	1.52	0.0514	-0.0542	1.25	0.0288
21	14.3	1.54	0.0640	-0.0530	1.25	--
22	15.3	1.49	0.1253	-0.0925	1.25	--
23	16.3	1.40	0.1632	-0.1140	1.25	--
24	17.3	1.12	0.1304	-0.0924	1.27	--
25	18.2	1.13	0.1477	-0.0931	1.25	--
26	19.1	1.09	0.1580	-0.0951	1.25	--
27	20.2	1.24	0.2211	-0.1178	1.25	--

Table B3. LS(1)-0417MOD, Clean, Re = 1.25 x 10^6						
RUN	AOA	C_l	C_{dp}	$C_{m¼}$	Re x 10^{-6}	C_{dw}
28	22.2	1.27	0.2818	-0.1347	1.24	--
29	24.1	1.25	0.3185	-0.1430	1.24	--
30	26.1	1.20	0.3476	-0.1463	1.23	--
31	28.2	1.15	0.4052	-0.1679	1.22	--
32	30.1	1.16	0.4721	-0.1919	1.22	--
33	32.1	1.23	0.8115	-0.2802	1.23	--
34	34.1	1.28	0.9128	-0.3071	1.22	--
35	35.9	1.31	0.9994	-0.3306	1.22	--
36	38.0	1.33	1.0845	-0.3473	1.21	--
37	40.0	1.35	1.1915	-0.3777	1.21	--
End of Table B3						

Table B4. LS(1)-0417MOD, Clean, Re = 1.5 x 10^6						
RUN	AOA	C_l	C_{dp}	$C_{m¼}$	Re x 10^{-6}	C_{dw}
87	-20.1	-0.43	0.2707	0.0316	1.45	--
86	-18.0	-0.38	0.2356	0.0268	1.46	--
85	-16.1	-0.34	0.2063	0.0242	1.47	--
84	-14.2	-0.83	0.0313	-0.0367	1.48	--
83	-12.4	-0.79	0.0008	-0.0596	1.51	0.0412
82	-10.3	-0.65	-0.0006	-0.0625	1.50	0.0244
81	-8.1	-0.43	-0.0020	-0.0686	1.51	0.0148
80	-6.2	-0.27	-0.0041	-0.0704	1.51	0.0126
79	-4.1	-0.06	-0.0046	-0.0727	1.51	0.0093
78	-2.0	0.17	-0.0031	-0.0773	1.50	0.0098
77	-0.1	0.38	-0.0008	-0.0808	1.51	0.0082
88	-0.1	0.36	0.0006	-0.0802	1.50	0.0083
89	2.0	0.60	0.0058	-0.0841	1.50	0.0084
90	4.2	0.82	0.0129	-0.0838	1.51	0.0101
91	6.3	1.03	0.0200	-0.0800	1.51	0.0110
92	8.2	1.22	0.0238	-0.0757	1.49	0.0131
93	10.3	1.39	0.0306	-0.0669	1.50	0.0168
94	11.4	1.46	0.0360	-0.0628	1.50	0.0197
95	12.2	1.49	0.0414	-0.0596	1.50	0.0206
96	13.2	1.53	0.0483	-0.0566	1.50	0.0210
97	14.3	1.54	0.0641	-0.0561	1.50	0.0347
98	15.2	1.34	0.1508	-0.1135	1.49	--
99	16.2	1.07	0.1381	-0.1088	1.50	--
100	17.2	1.04	0.1549	-0.1112	1.49	--
101	18.2	1.03	0.1705	-0.1118	1.48	--
End of Table B4						

Table B5. LS(1)-0417MOD, k/c = 0.0019, Re = 0.75 x 10^6						
RUN	AOA	C_l	C_{dp}	$C_{m¼}$	Re x 10^{-6}	C_{dw}
260	-20.1	-0.50	0.2700	0.0430	0.75	--
259	-18.0	-0.52	0.2405	0.0458	0.75	--
258	-16.2	-0.57	0.2053	0.0435	0.75	--
257	-14.1	-0.59	0.1412	0.0239	0.74	--
256	-12.1	-0.63	0.0359	-0.0260	0.74	--
255	-10.2	-0.61	0.0002	-0.0514	0.75	0.0407
254	-8.1	-0.42	-0.0031	-0.0630	0.76	0.0207
253	-6.0	-0.27	-0.0040	-0.0598	0.75	0.0191
252	-4.1	-0.09	-0.0017	-0.0621	0.75	0.0152
251	-2.0	0.12	-0.0013	-0.0651	0.75	0.0146
250	-0.1	0.32	0.0009	-0.0665	0.75	0.0150
261	-0.1	0.33	0.0007	-0.0671	0.76	0.0132
287	-0.1	0.30	0.0035	-0.0660	0.75	0.0146
262	2.0	0.51	0.0076	-0.0678	0.75	0.0156
263	4.1	0.71	0.0149	-0.0666	0.74	0.0163
264	6.3	0.90	0.0260	-0.0625	0.75	0.0191
265	8.2	1.05	0.0327	-0.0559	0.75	0.0248
266	10.3	1.12	0.0431	-0.0451	0.75	0.0444
267	11.2	0.86	0.0925	-0.0796	0.75	--
268	12.0	0.82	0.1062	-0.0822	0.75	--
269	13.0	0.80	0.1235	-0.0840	0.75	--
270	14.1	0.79	0.1399	-0.0874	0.75	--
271	15.1	0.80	0.1600	-0.0937	0.75	--
272	16.2	0.80	0.1788	-0.0971	0.75	--
273	17.0	0.83	0.2019	-0.1046	0.76	--
274	18.0	0.83	0.2207	-0.1084	0.75	--
275	19.1	0.84	0.2441	-0.1140	0.75	--
276	20.1	0.87	0.2740	-0.1234	0.75	--

Table B5. LS(1)-0417MOD, k/c = 0.0019, Re = 0.75 x 10^6						
RUN	AOA	C_l	C_{dp}	$C_{m¼}$	Re x 10^{-6}	C_{dw}
277	22.2	0.94	0.3409	-0.1458	0.76	--
278	24.0	1.01	0.4212	-0.1767	0.75	--
279	26.1	1.07	0.5010	-0.2018	0.75	--
280	28.2	1.11	0.5774	-0.2204	0.75	--
281	30.0	1.15	0.6568	-0.2419	0.74	--
282	32.1	1.22	0.7598	-0.2711	0.74	--
283	33.9	1.29	0.8666	-0.3059	0.74	--
284	36.0	1.31	0.9562	-0.3272	0.73	--
285	38.0	1.35	1.0650	-0.3597	0.73	--
286	39.9	1.35	1.1361	-0.3749	0.72	--
End of Table B5						

Table B6. LS(1)-0417MOD, k/c = 0.0019, Re = 1.0 x 10^6						
RUN	AOA	C_l	C_{dp}	$C_{m¼}$	Re x 10^{-6}	C_{dw}
222	-20.0	-0.47	0.2742	0.0400	1.00	--
221	-17.9	-0.53	0.2580	0.0498	1.00	--
220	-16.1	-0.58	0.2225	0.0437	1.01	--
219	-14.1	-0.61	0.1437	0.0122	1.01	--
218	-12.3	-0.63	0.0282	-0.0569	1.01	0.0587
217	-10.2	-0.55	0.0112	-0.0674	1.00	0.0277
216	-8.1	-0.43	0.0037	-0.0632	1.00	0.0199
215	-6.2	-0.29	-0.0007	-0.0615	1.00	0.0174
214	-4.1	-0.09	-0.0019	-0.0634	1.00	0.0148
213	-2.0	0.13	-0.0011	-0.0657	1.00	0.0133
212	-0.1	0.33	0.0012	-0.0686	1.00	0.0134
223	-0.1	0.31	0.0015	-0.0672	1.00	0.0135
249	-0.1	0.31	0.0020	-0.0673	1.00	0.0129
224	2.0	0.52	0.0074	-0.0687	1.00	0.0130
225	4.1	0.73	0.0132	-0.0665	1.00	0.0148
226	6.3	0.92	0.0216	-0.0624	1.00	0.0176
227	8.1	1.06	0.0260	-0.0554	1.00	0.0208
228	10.2	1.13	0.0377	-0.0459	1.00	0.0420
229	11.2	0.89	0.0972	-0.0865	1.00	--
230	12.0	0.87	0.1106	-0.0879	1.01	--
231	13.0	0.82	0.1230	-0.0865	1.00	--
232	14.0	0.80	0.1385	-0.0871	1.01	--
233	15.1	0.80	0.1580	-0.0924	1.01	--
234	16.1	0.83	0.1809	-0.0994	1.00	--
235	17.2	0.83	0.2014	-0.1037	1.00	--
236	18.2	0.85	0.2268	-0.1114	1.00	--
237	19.0	0.87	0.2510	-0.1212	1.00	--
238	20.1	0.89	0.2785	-0.1290	1.00	--

Table B6. LS(1)-0417MOD, k/c = 0.0019, Re = 1.0 x 10^6						
RUN	AOA	C_l	C_{dp}	$C_{m¼}$	Re x 10^{-6}	C_{dw}
239	22.2	0.94	0.3476	-0.1523	1.00	--
240	23.9	0.99	0.4113	-0.1723	1.00	--
241	26.0	1.03	0.4883	-0.1945	1.00	--
242	28.1	1.10	0.5695	-0.2173	1.00	--
243	30.0	1.16	0.6548	-0.2429	0.99	--
244	32.0	1.21	0.7547	-0.2709	0.99	--
245	34.1	1.28	0.8596	-0.3007	0.98	--
246	36.2	1.33	0.9708	-0.3338	0.97	--
247	37.9	1.35	1.0524	-0.3518	0.99	--
248	40.0	1.36	1.1427	-0.3741	0.98	--
End of Table B6						

Table B7. LS(1)-0417MOD, k/c = 0.0019, Re = 1.25 x 10^6						
RUN	AOA	C_l	C_{dp}	$C_{m¼}$	Re x 10^{-6}	C_{dw}
184	-20.1	-0.47	0.2704	0.0317	1.25	--
183	-18.0	-0.53	0.2492	0.0373	1.25	--
182	-16.2	-0.57	0.2092	0.0301	1.26	--
181	-14.1	-0.60	0.1321	0.0023	1.25	--
180	-12.1	-0.63	0.0228	-0.0684	1.25	0.0467
179	-10.2	-0.57	0.0135	-0.0647	1.25	0.0261
178	-8.1	-0.45	0.0039	-0.0618	1.26	0.0192
177	-6.3	-0.30	-0.0009	-0.0606	1.25	0.0181
176	-4.1	-0.09	-0.0022	-0.0631	1.25	0.0137
175	-2.0	0.14	-0.0018	-0.0662	1.25	0.0132
174	-0.1	0.33	0.0007	-0.0678	1.25	0.0129
185	-0.1	0.34	0.0007	-0.0678	1.25	0.0128
211	-0.1	0.32	0.0013	-0.0679	1.26	0.0124
186	2.0	0.54	0.0062	-0.0696	1.25	0.0127
187	4.1	0.74	0.0141	-0.0676	1.25	0.0147
188	6.0	0.92	0.0174	-0.0639	1.25	0.0163
189	8.2	1.08	0.0263	-0.0571	1.25	0.0224
190	10.3	1.16	0.0375	-0.0470	1.25	0.0404
191	11.3	0.96	0.1016	-0.0929	1.26	--
192	12.0	0.87	0.1112	-0.0886	1.25	--
193	13.1	0.82	0.1240	-0.0861	1.26	--
194	14.1	0.82	0.1419	-0.0890	1.25	--
195	15.1	0.82	0.1613	-0.0937	1.25	--
196	16.2	0.83	0.1810	-0.0981	1.26	--
197	17.2	0.85	0.2054	-0.1053	1.26	--
198	18.0	0.86	0.2243	-0.1104	1.25	--
199	19.1	0.89	0.2546	-0.1227	1.27	--
200	20.1	0.91	0.2815	-0.1319	1.25	--

Table B7. LS(1)-0417MOD, k/c = 0.0019, Re = 1.25 x 10^6						
RUN	AOA	C_l	C_{dp}	$C_{m¼}$	Re x 10^{-6}	C_{dw}
201	22.2	0.97	0.3539	-0.1567	1.26	--
202	24.0	1.00	0.4154	-0.1757	1.25	--
203	26.1	1.05	0.4883	-0.1962	1.24	--
204	28.2	1.11	0.5772	-0.2216	1.25	--
205	30.0	1.16	0.6537	-0.2442	1.25	--
206	32.1	1.22	0.7502	-0.2693	1.23	--
207	34.2	1.29	0.8619	-0.3017	1.22	--
208	36.0	1.32	0.9514	-0.3271	1.21	--
209	38.0	1.36	1.0557	-0.3562	1.19	--
210	39.8	1.36	1.1323	-0.3747	1.17	--
End of Table B7						

Table B8. LS(1)-0417MOD, k/c = 0.0019, Re = 1.5 x 10^6						
RUN	AOA	C_l	C_{dp}	$C_{m¼}$	Re x 10^{-6}	C_{dw}
151	-20.2	-0.43	0.2502	0.0191	1.41	--
150	-18.1	-0.45	0.2206	0.0232	1.43	--
149	-16.1	-0.47	0.1890	0.0217	1.44	--
148	-14.2	-0.53	0.1319	0.0045	1.46	--
147	-12.2	-0.61	0.0109	-0.0679	1.49	0.0501
146	-10.3	-0.56	0.0038	-0.0662	1.49	0.0272
145	-8.1	-0.44	-0.0017	-0.0606	1.51	0.0190
144	-6.0	-0.30	-0.0048	-0.0605	1.50	0.0170
143	-4.1	-0.08	-0.0022	-0.0625	1.51	0.0131
142	-2.2	0.13	-0.0018	-0.0660	1.50	0.0126
141	-0.1	0.32	0.0017	-0.0679	1.51	0.0123
152	-0.1	0.35	0.0001	-0.0686	1.50	0.0126
153	2.0	0.54	0.0082	-0.0697	1.50	0.0118
154	4.2	0.74	0.0164	-0.0692	1.50	0.0138
155	6.1	0.93	0.0203	-0.0655	1.50	0.0159
156	8.2	1.08	0.0293	-0.0585	1.50	0.0209
157	10.3	1.16	0.0390	-0.0480	1.49	0.0357
158	11.1	0.92	0.1034	-0.0941	1.47	--
159	12.1	0.82	0.1128	-0.0867	1.47	--
160	13.1	0.80	0.1291	-0.0883	1.47	--
161	14.2	0.80	0.1446	-0.0899	1.46	--
162	15.1	0.81	0.1625	-0.0946	1.46	--
163	16.1	0.80	0.1804	-0.0984	1.44	--
164	17.1	0.82	0.2025	-0.1052	1.44	--
165	18.1	0.83	0.2244	-0.1113	1.43	--
End of Table B8						

Steady State
Pressure Distributions
LS(1)-0417MOD

Re = 0.75 million

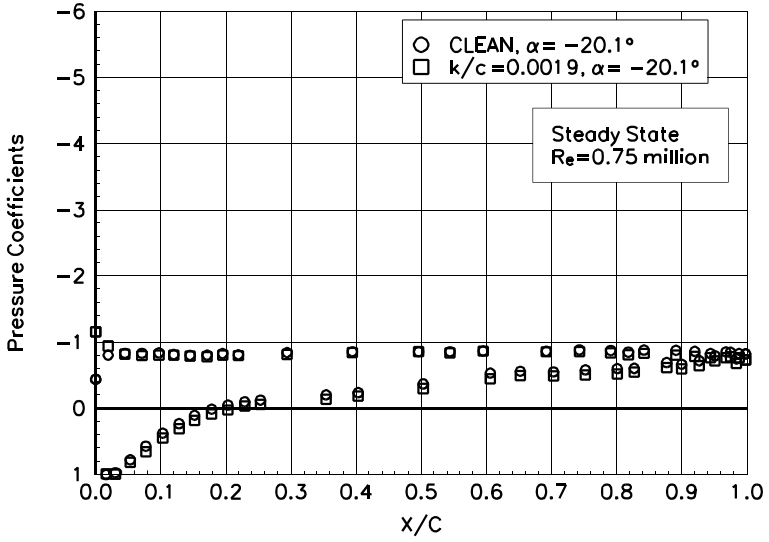

Figure B1. α = -20.1°

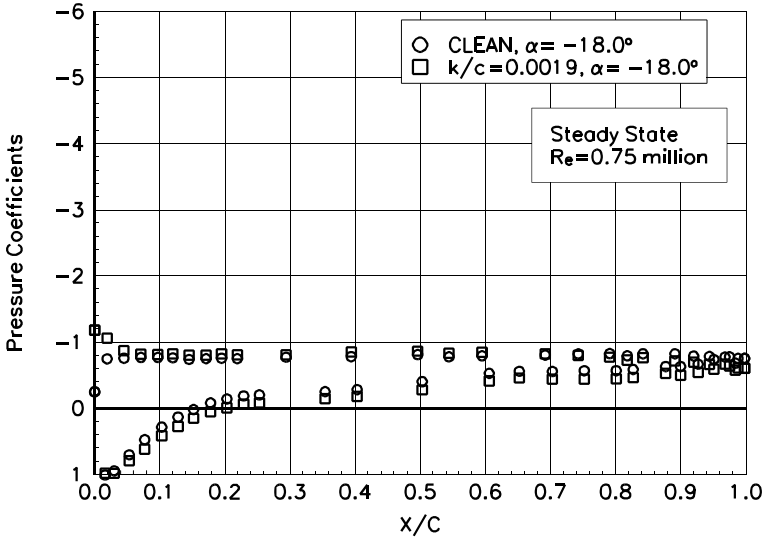

Figure B2. α = -18.0°

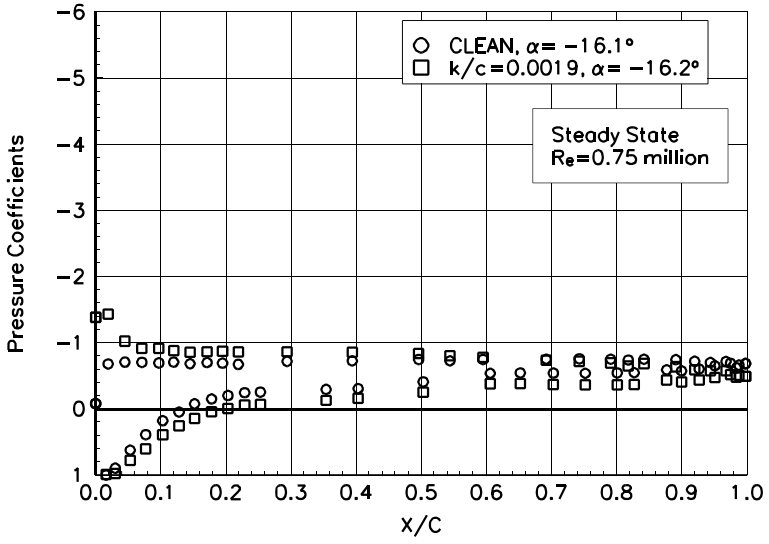

Figure B3. α = -16.1°

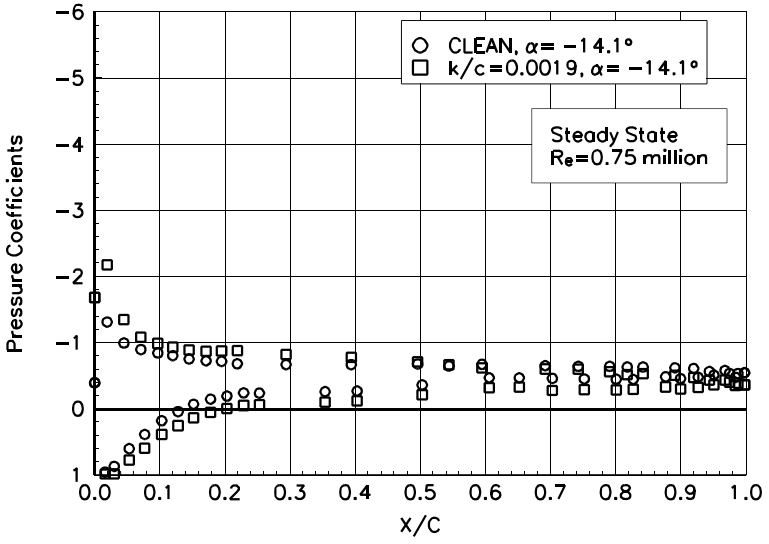

Figure B4. α = -14.1°

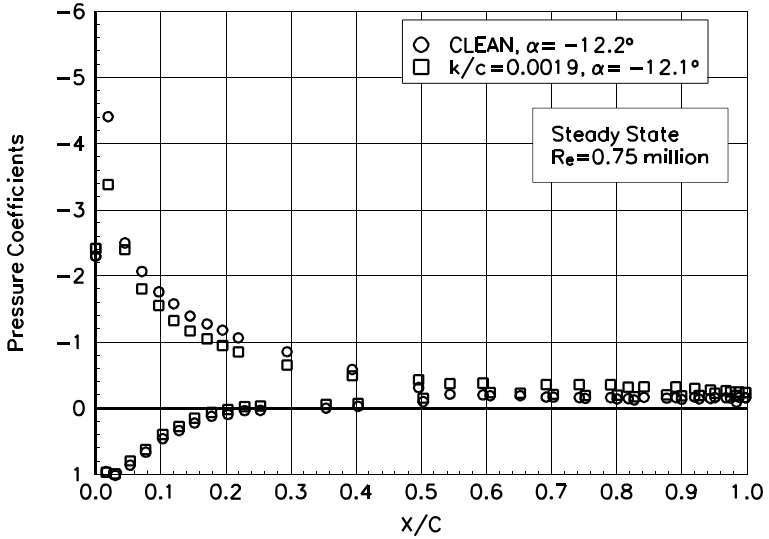

Figure B5. α = -12.2°

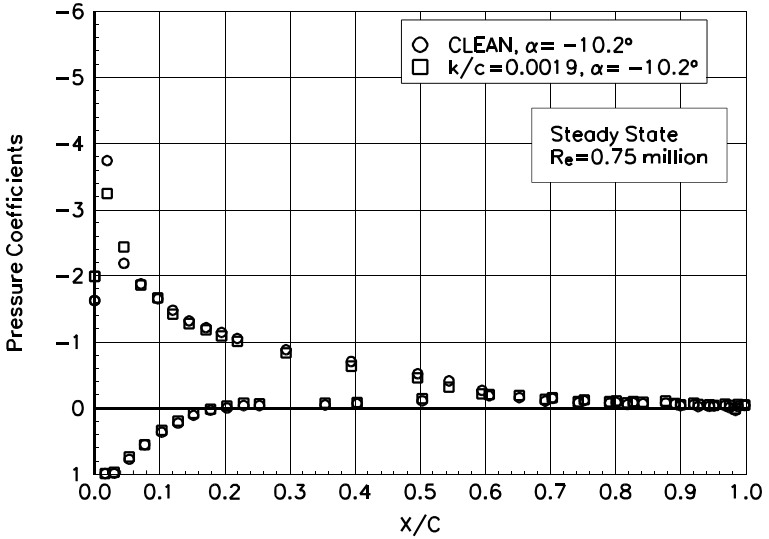

Figure B6. α = -10.2°

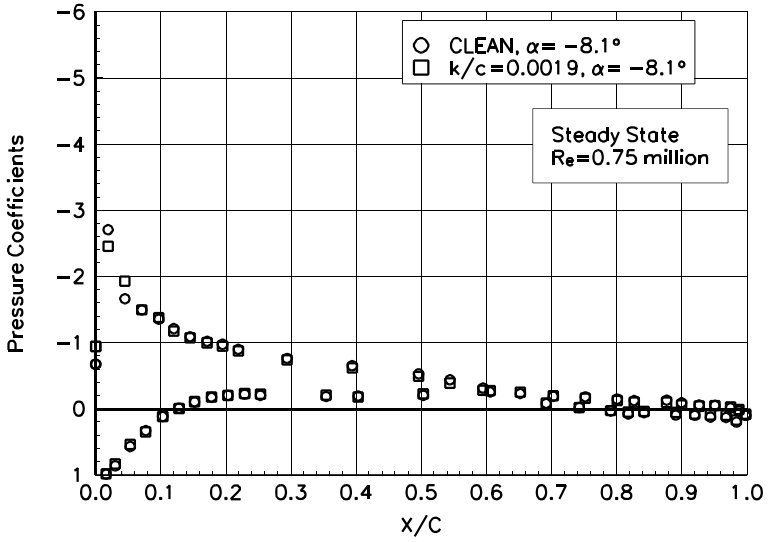

Figure B7. α = -8.1°

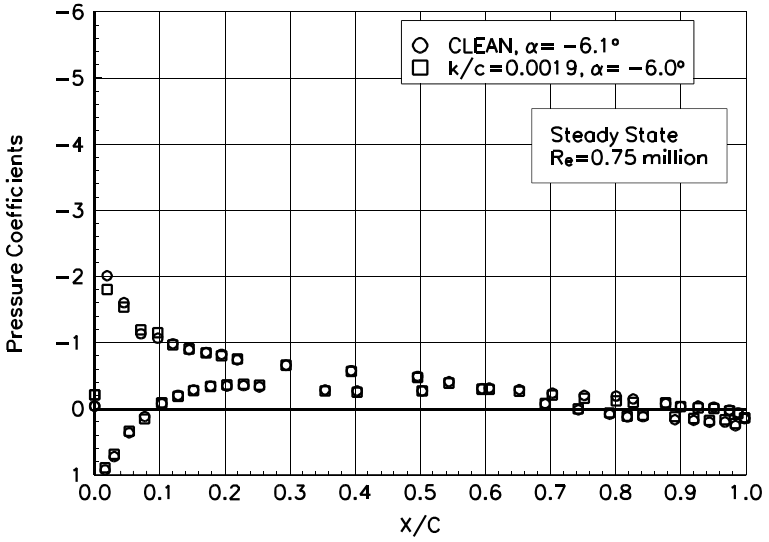

Figure B8. α = -6.1°

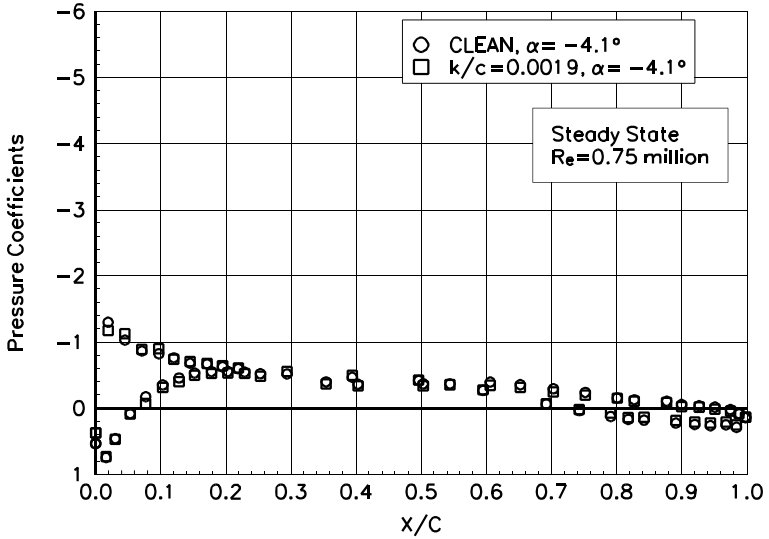

Figure B9. α = -4.1°

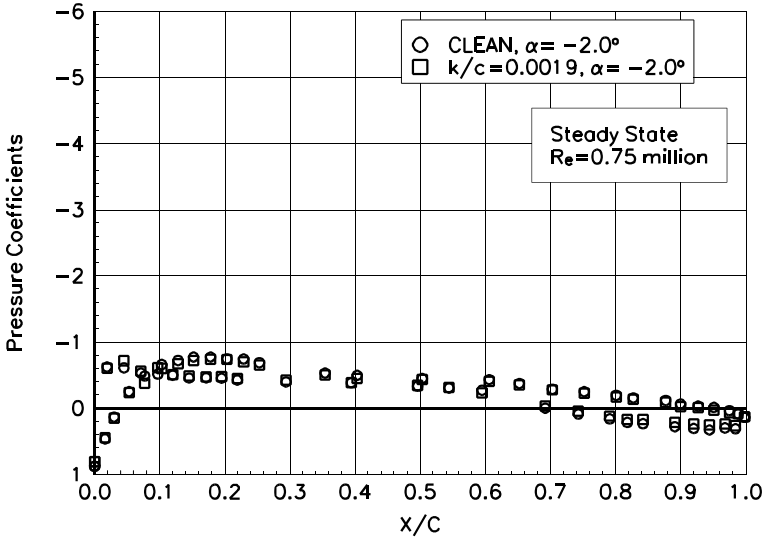

Figure B10. α = -2.0°

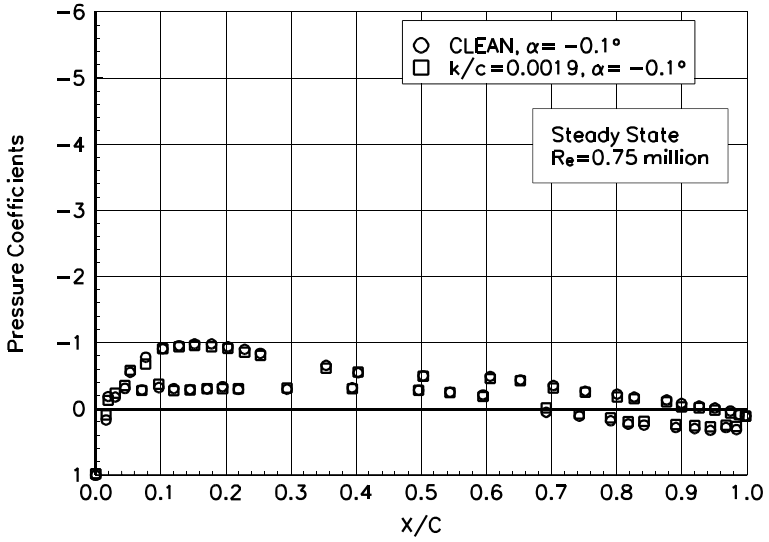

Figure B11. α = -0.1°

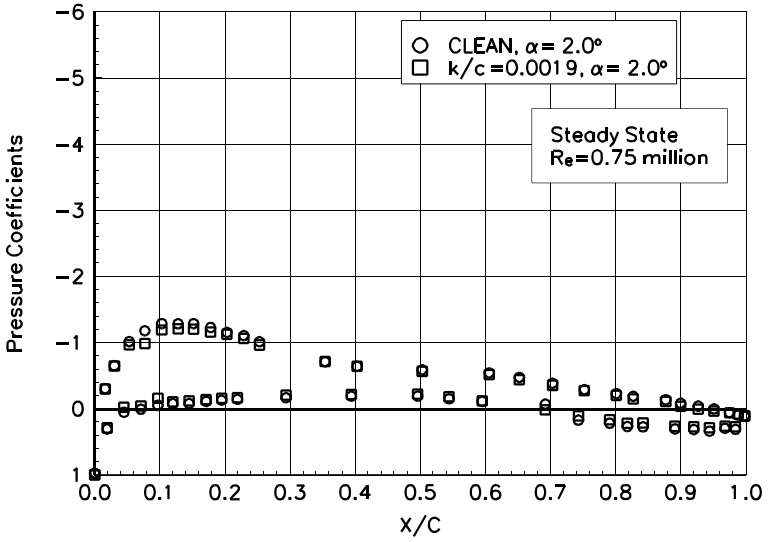

Figure B12. α = 2.0°

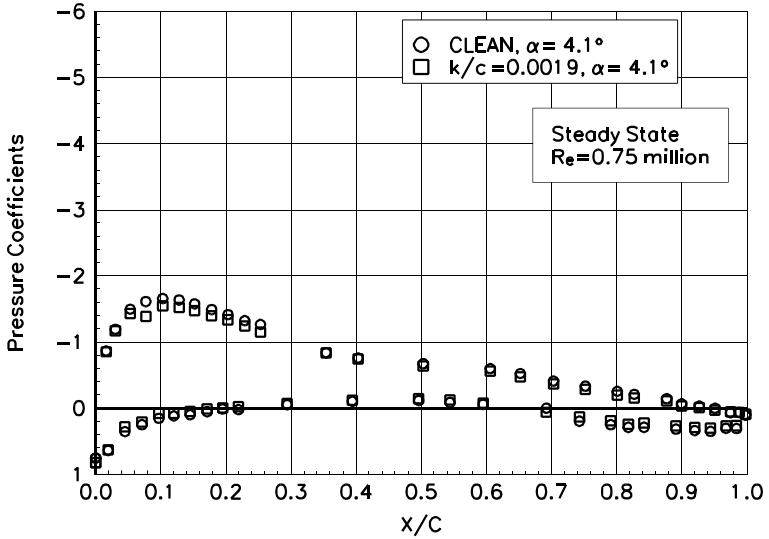

Figure B13. α = 4.1°

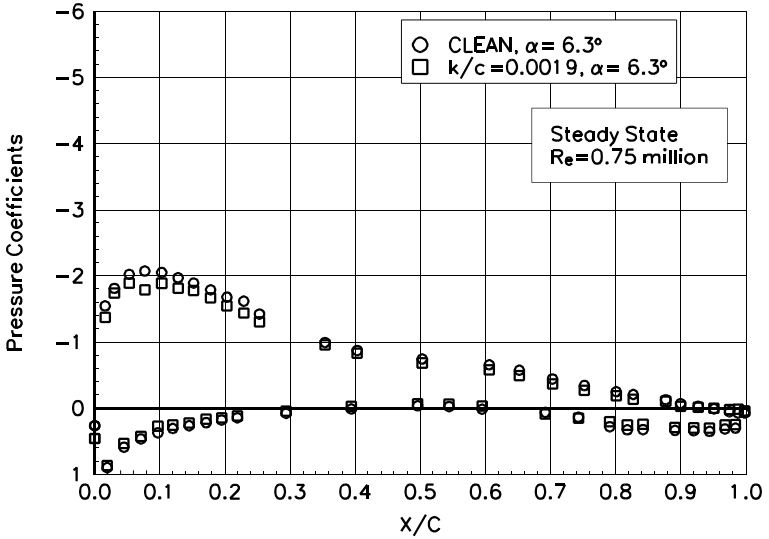

Figure B14. α = 6.3°

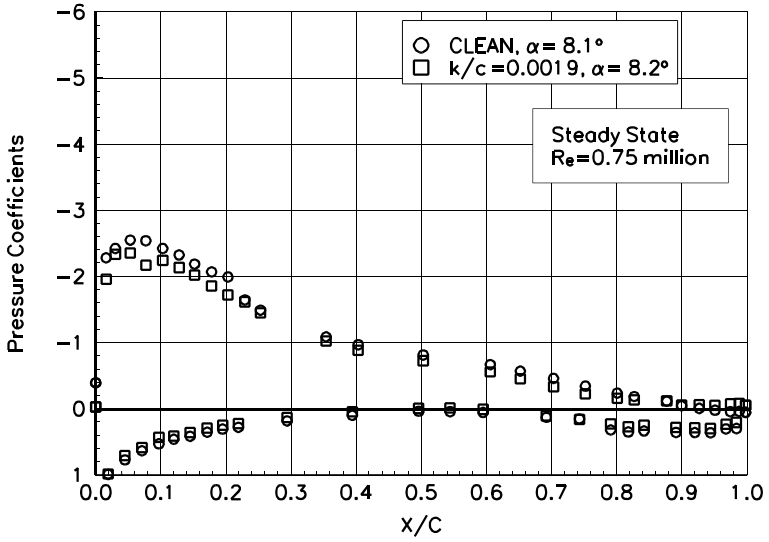

Figure B15. α = 8.1°

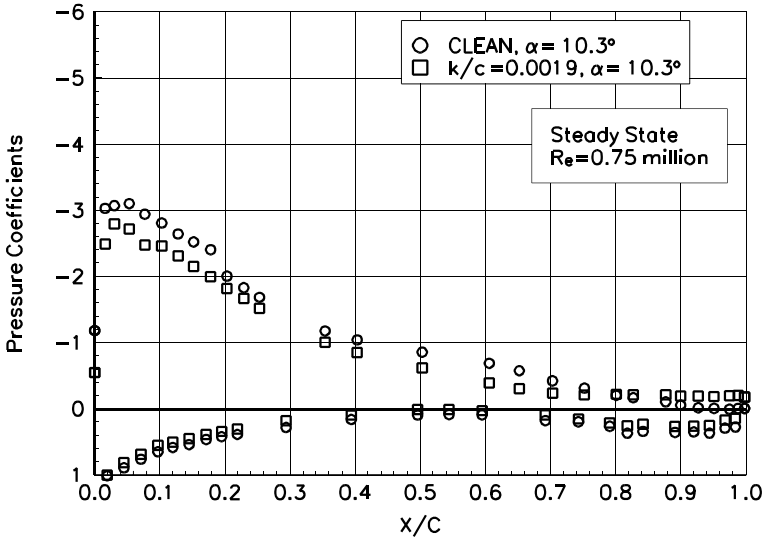

Figure B16. α = 10.3°

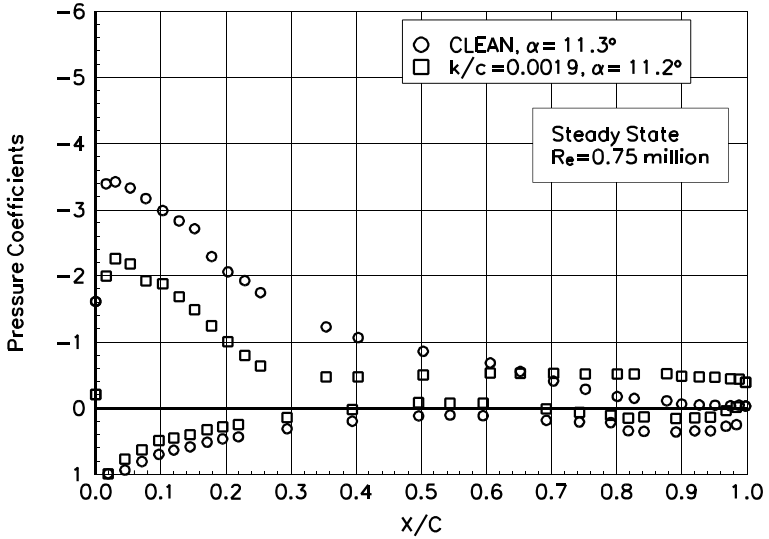

Figure B17. α = 11.3°

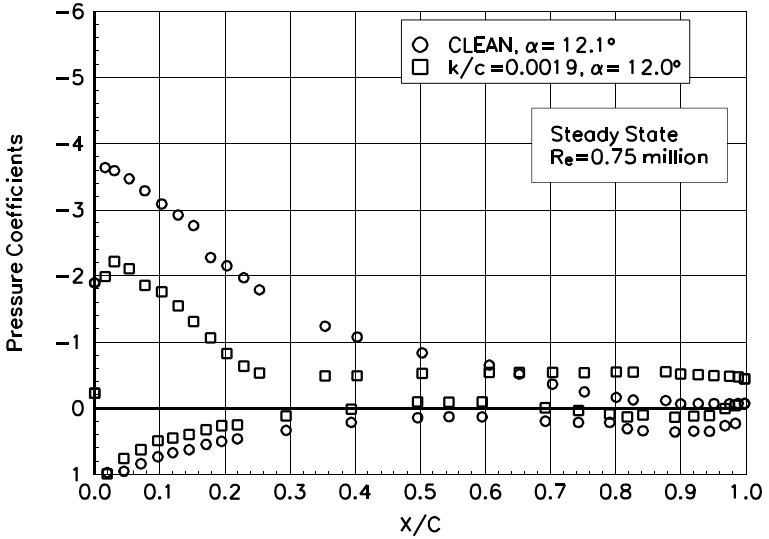

Figure B18. α = 12.1°

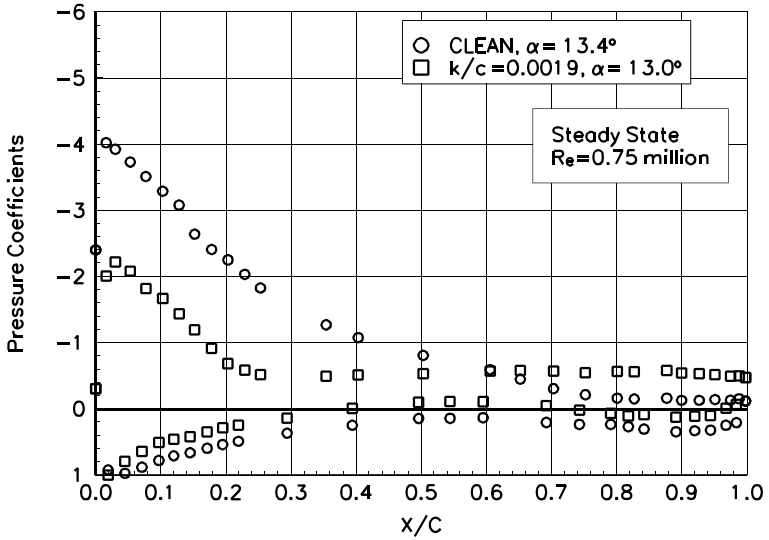

Figure B19. α = 13.4°

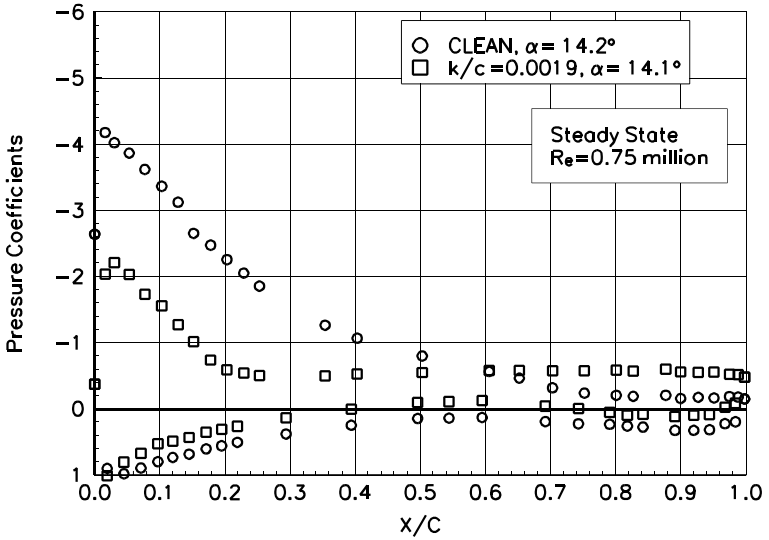

Figure B20. α = 14.2°

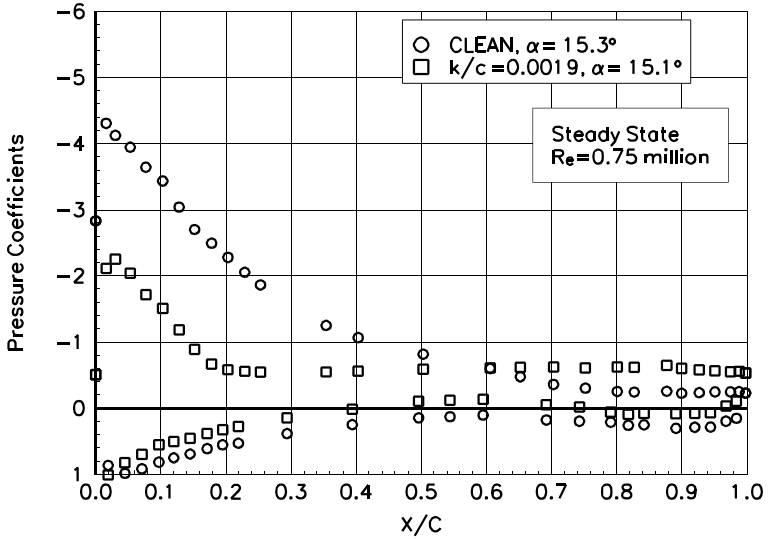

Figure B21. α = 15.3°

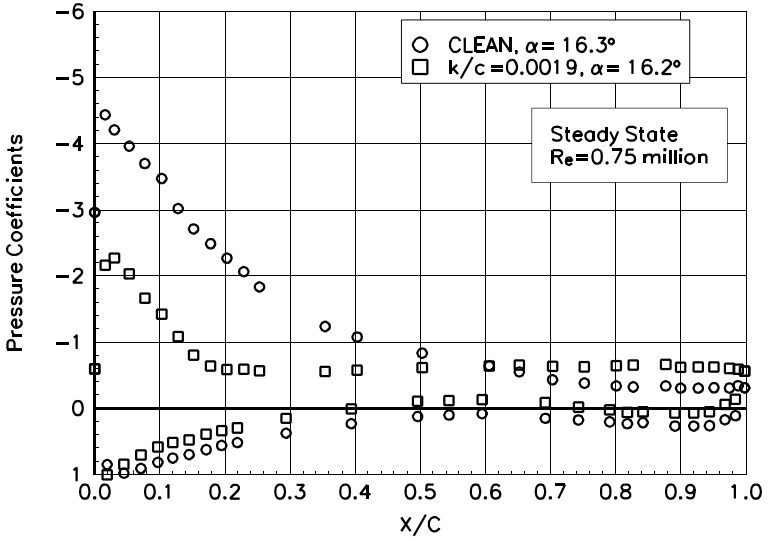

Figure B22. α = 16.3°

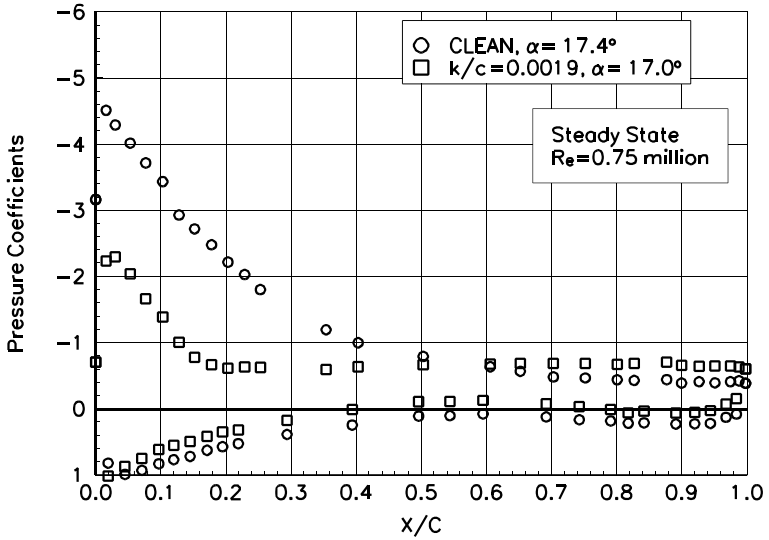

Figure B23. α = 17.4°

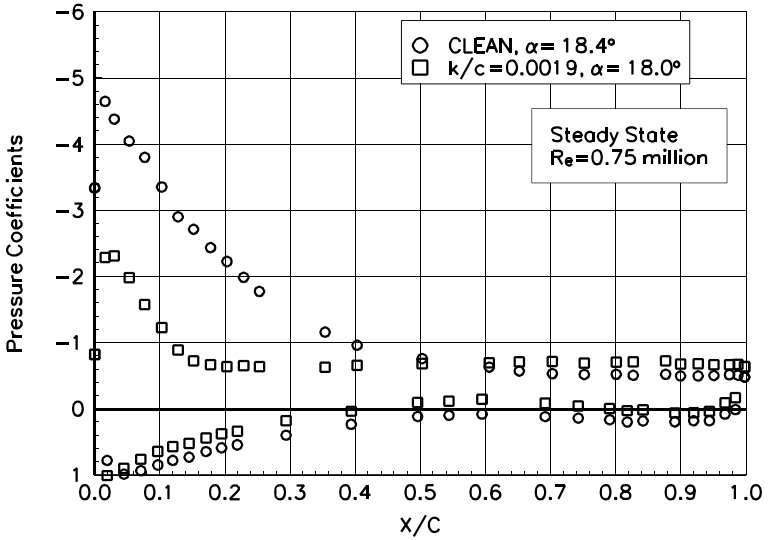

Figure B24. α = 18.4°

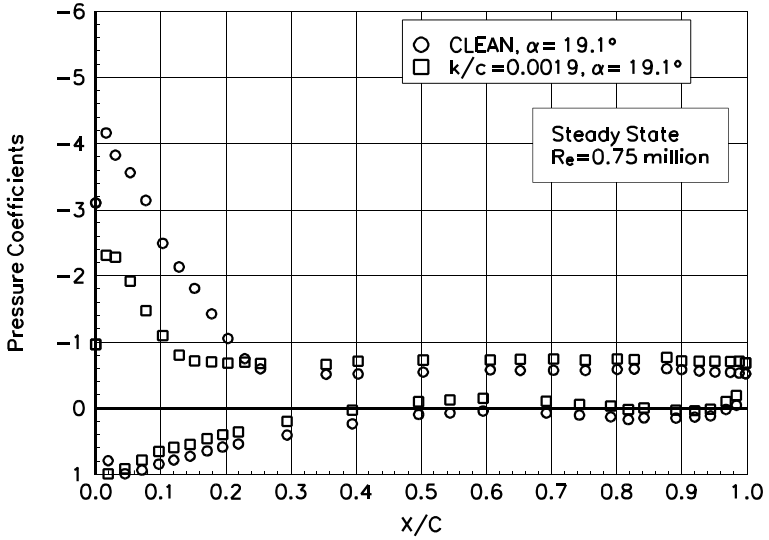

Figure B25. α = 19.1°

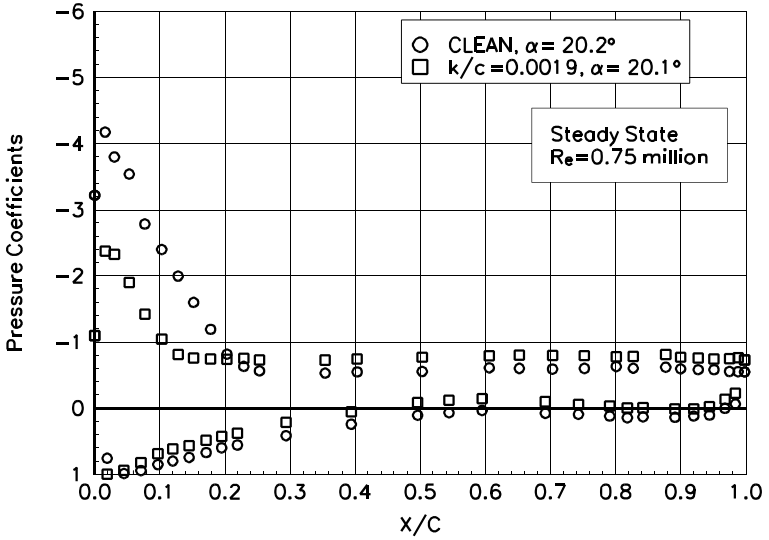

Figure B26. α = 20.2°

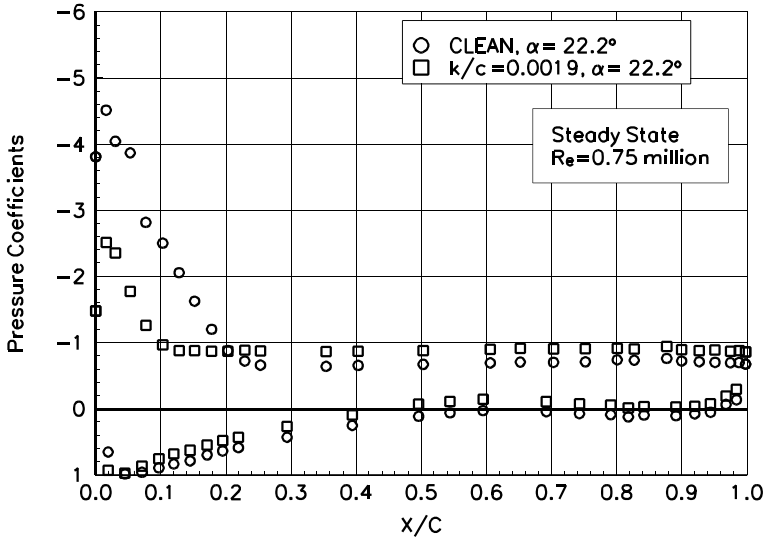

Figure B27. α = 22.2°

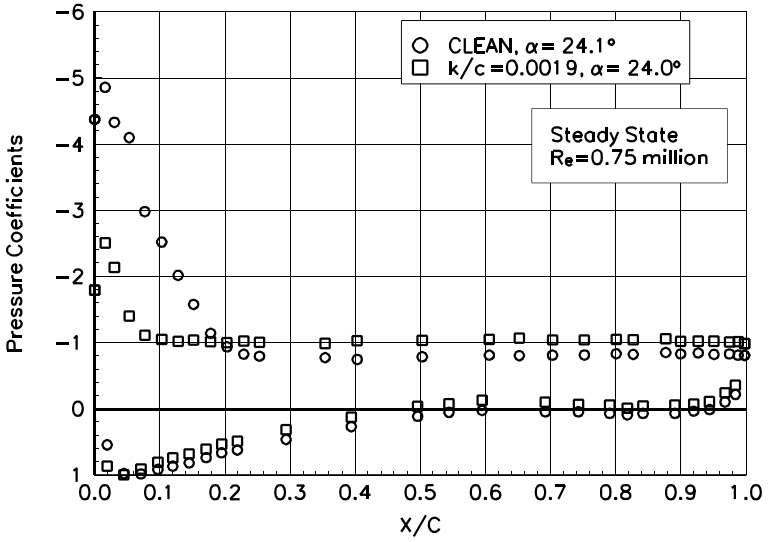

Figure B28. α = 24.1°

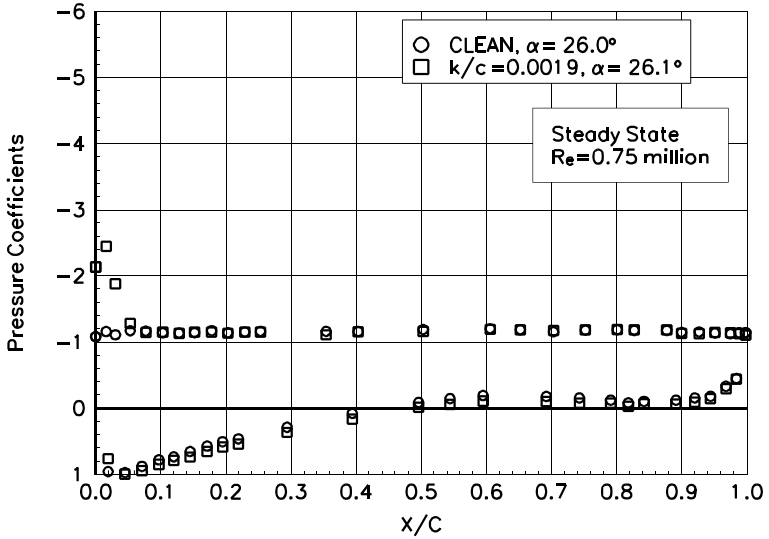

Figure B29. α = 26.0°

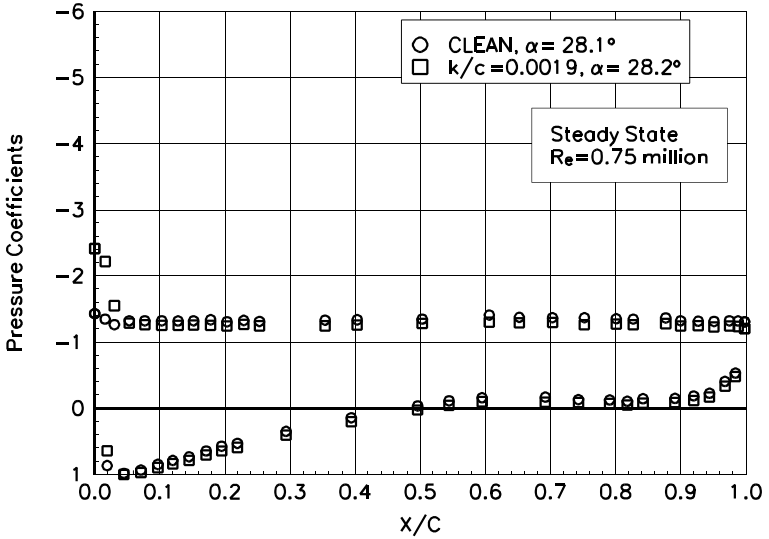

Figure B30. α = 28.1°

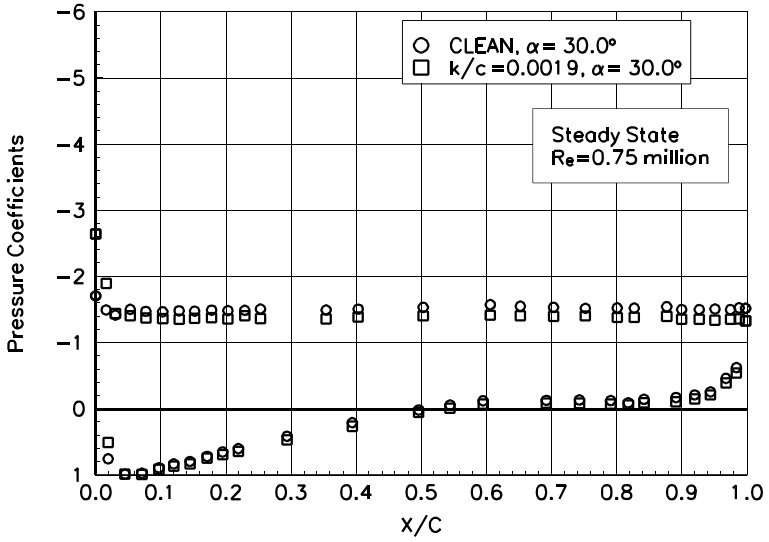

Figure B31. α = 30.0°

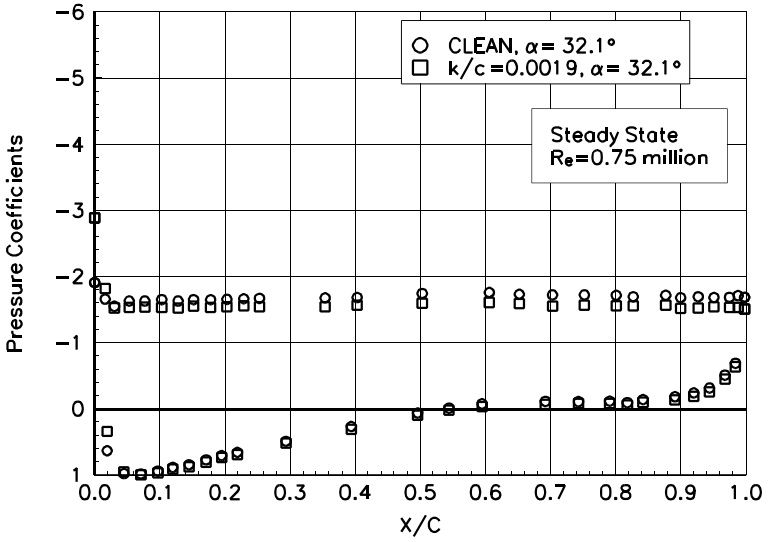

Figure B32. α = 32.1°

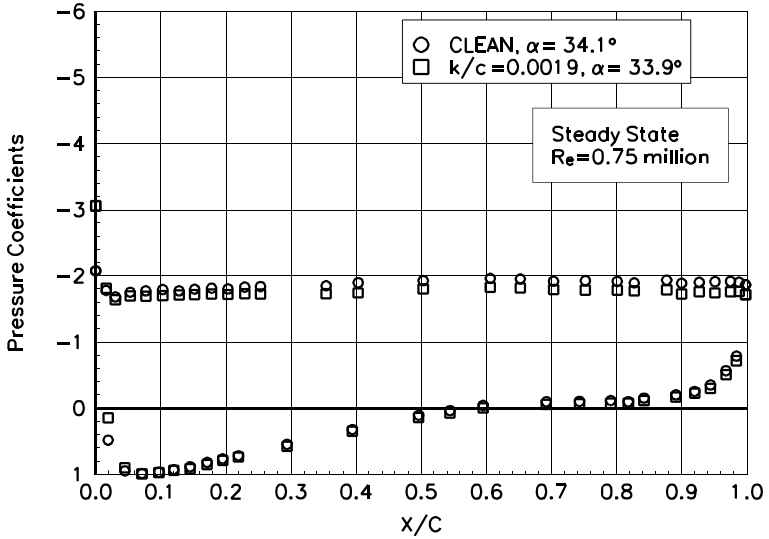

Figure B33. α = 34.1°

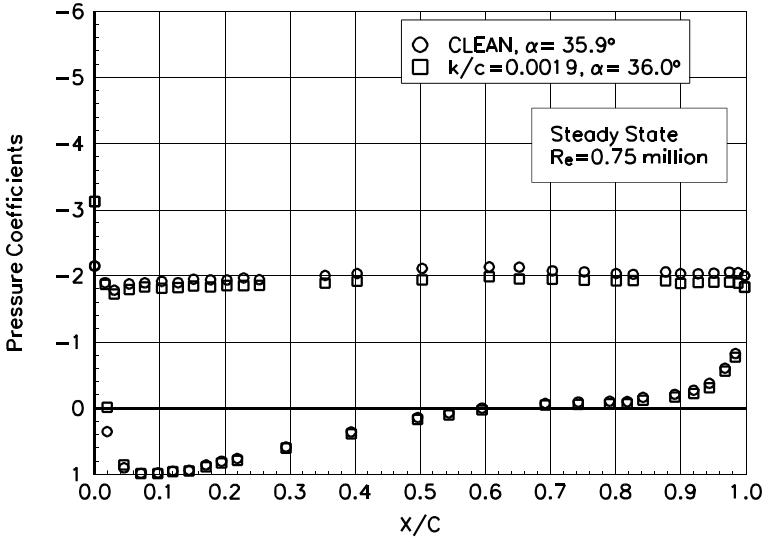

Figure B34. α = 35.9°

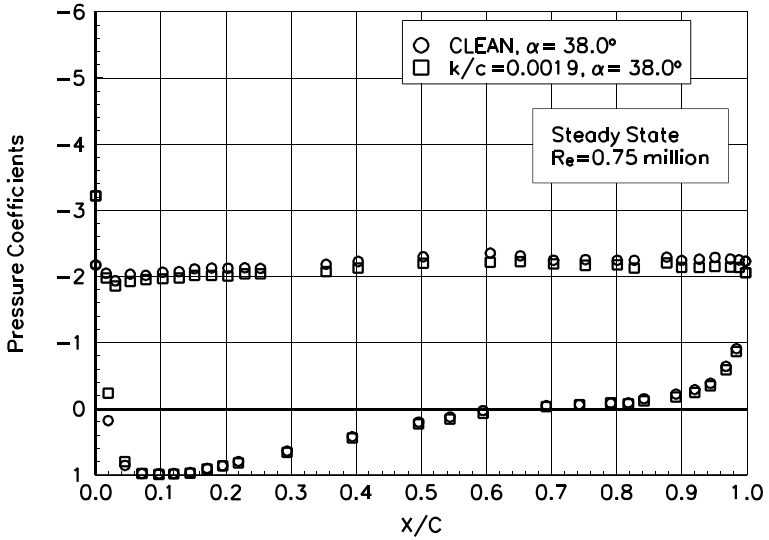

Figure B35. α = 38.0°

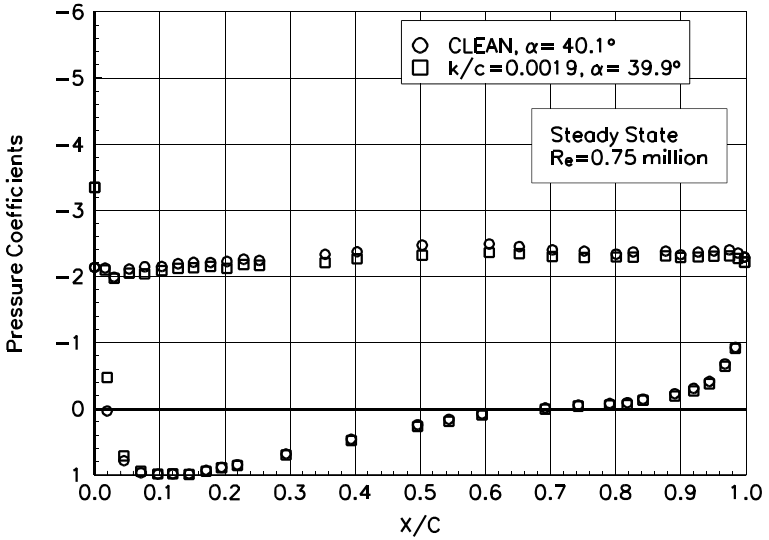

Figure B36. α = 40.1°

Steady State
Pressure Distributions
LS(1)-0417MOD

Re = 1 million

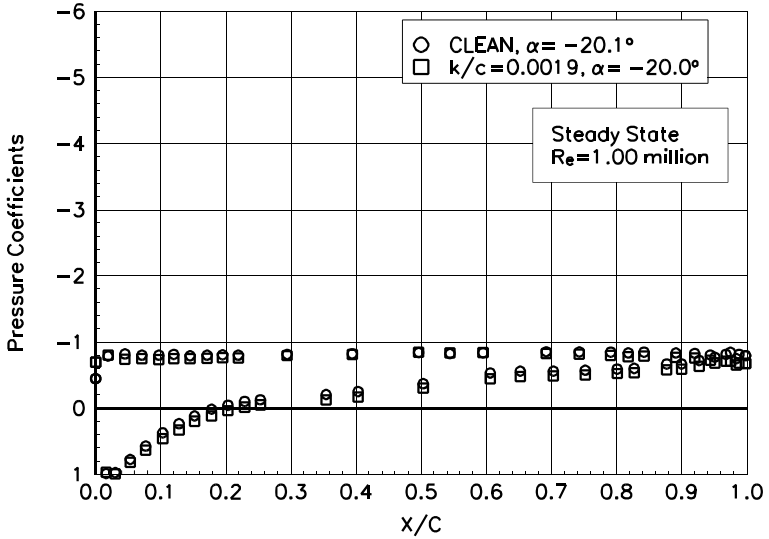

Figure B37. α = -20.1°

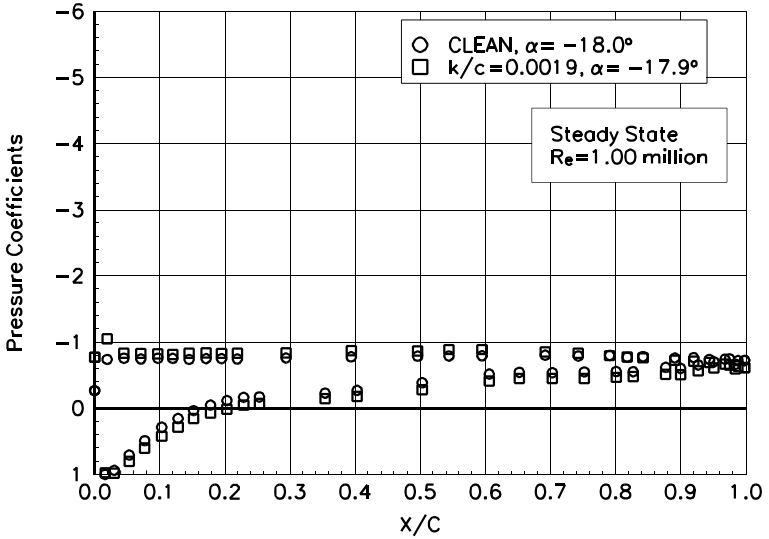

Figure B38. α = -18.0°

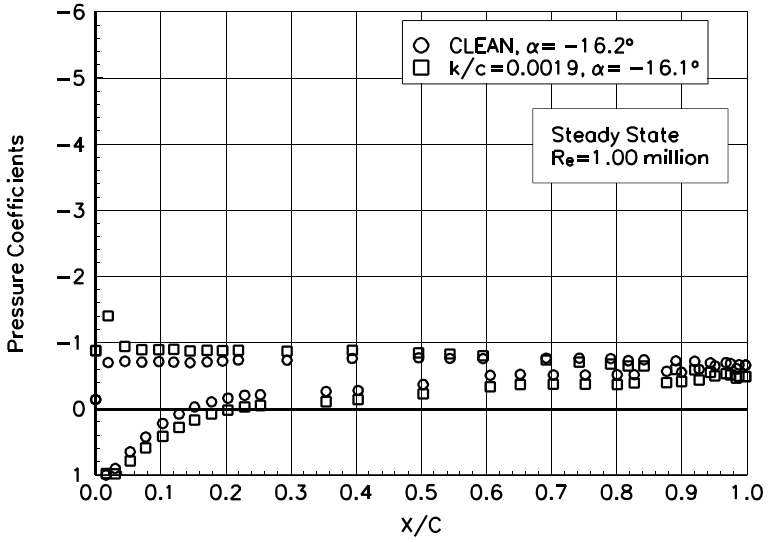

Figure B39. α = -16.2°

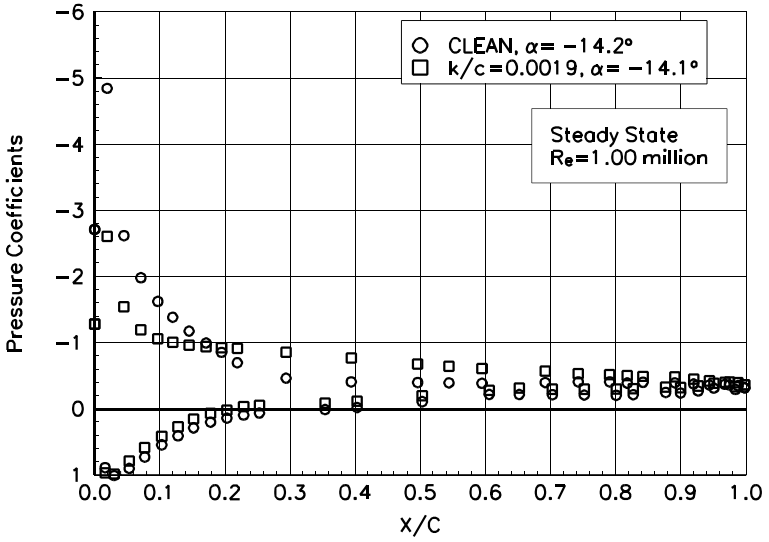

Figure B40. α = -14.2°

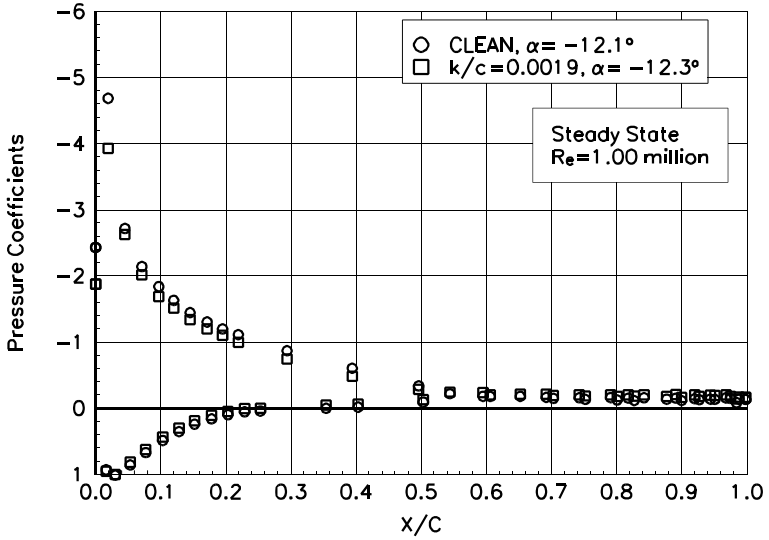

Figure B41. α = -12.1°

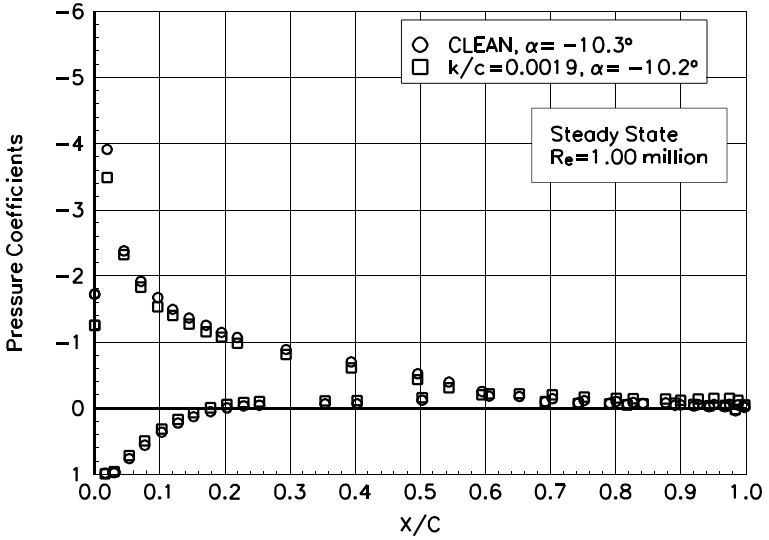

Figure B42. α = -10.3°

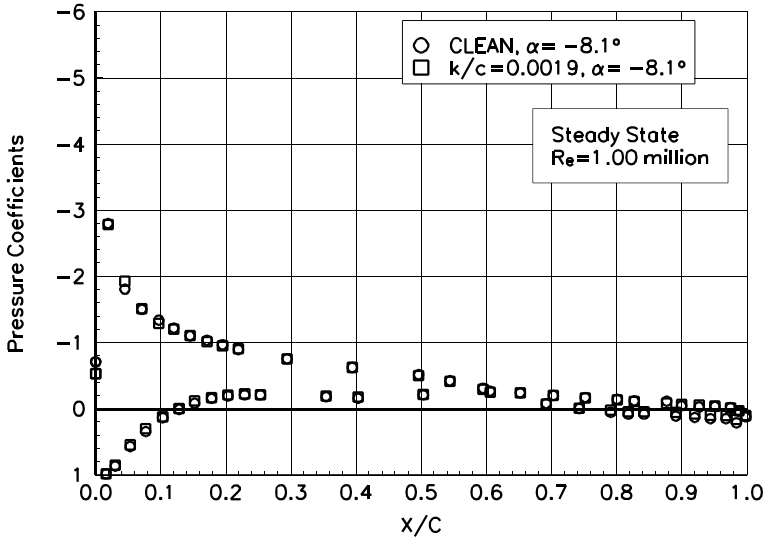

Figure B43. α = -8.1°

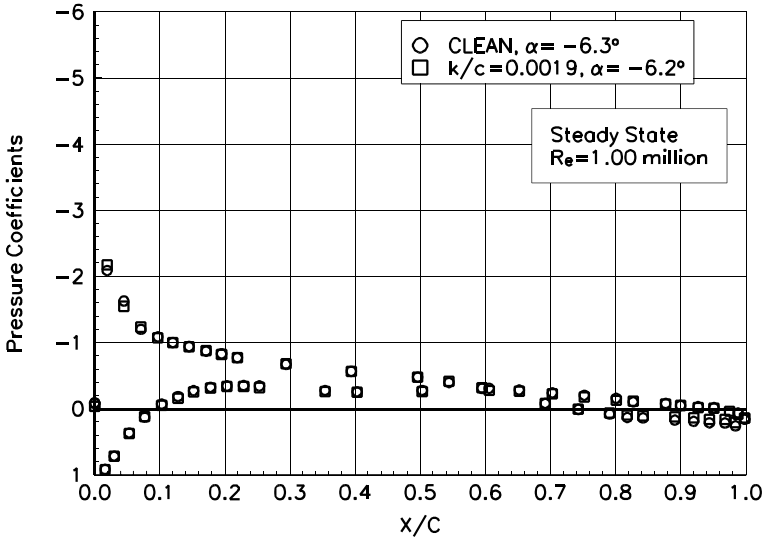

Figure B44. α = -6.3°

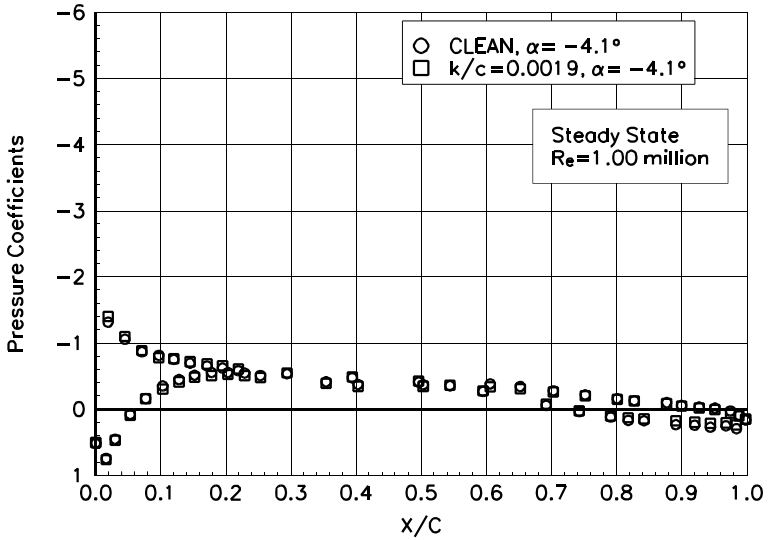

Figure B45. α = -4.1°

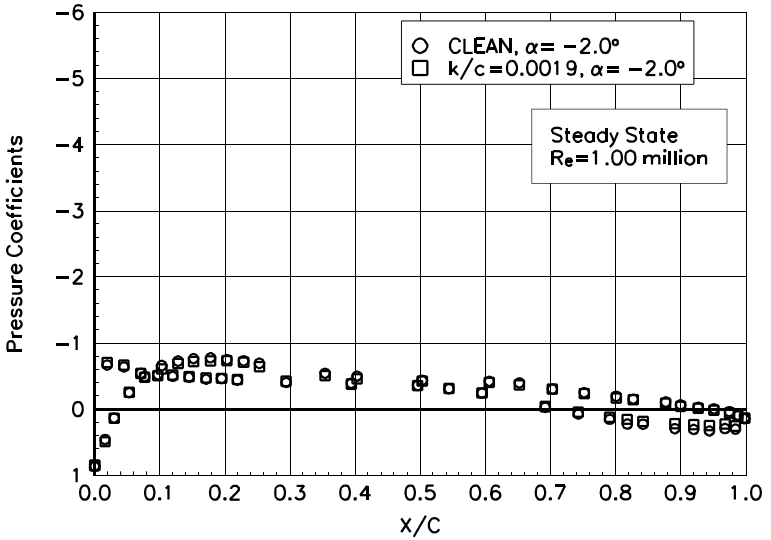

Figure B46. α = -2.0°

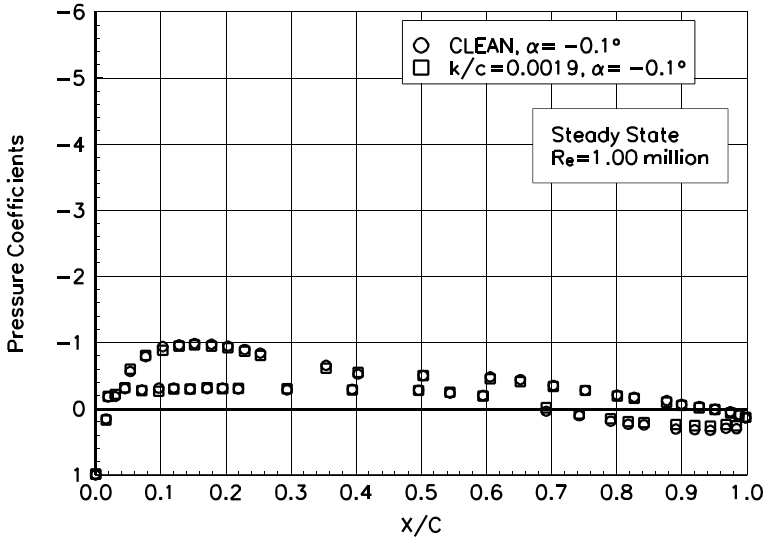

Figure B47. α = -0.1

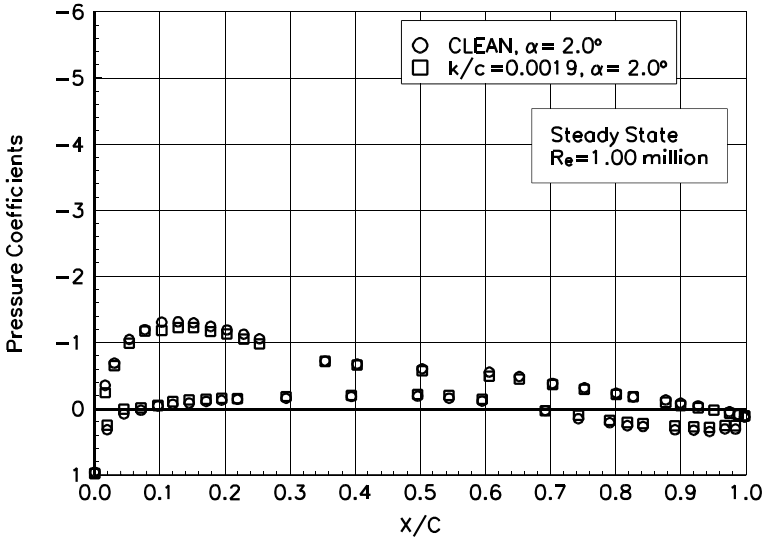

Figure B48. α = 2.0°

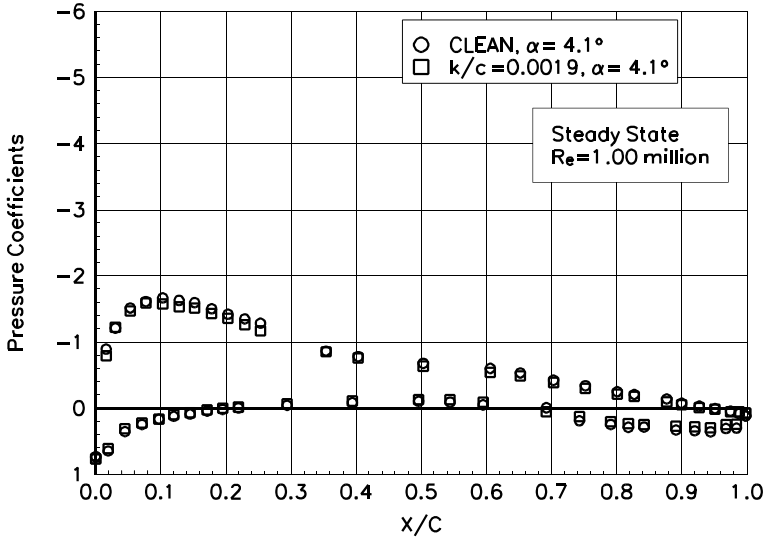

Figure B49. α = 4.1°

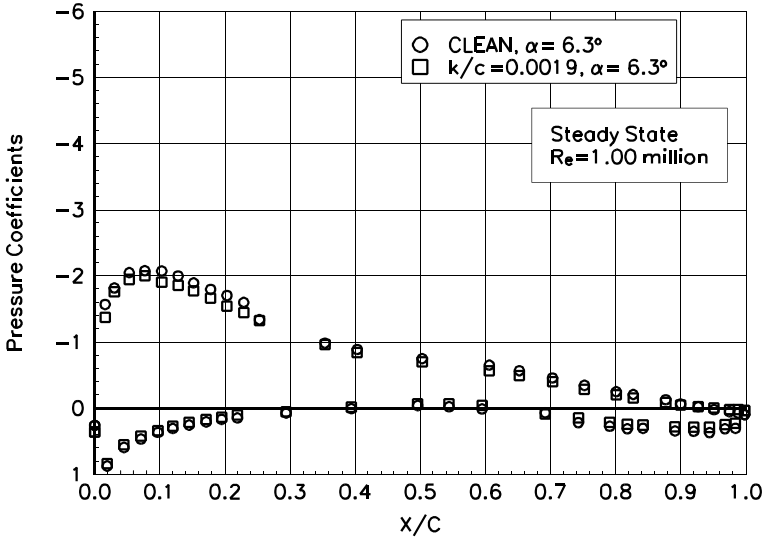

Figure B50. α = 6.3°

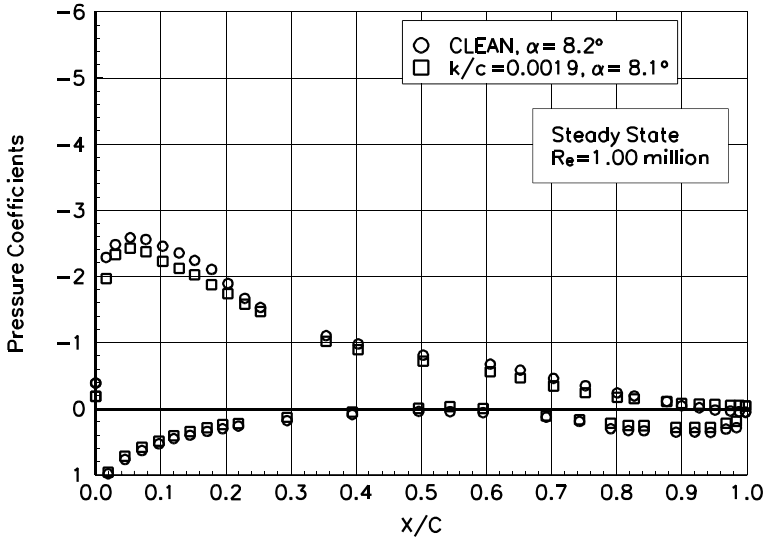

Figure B51. α = 8.2°

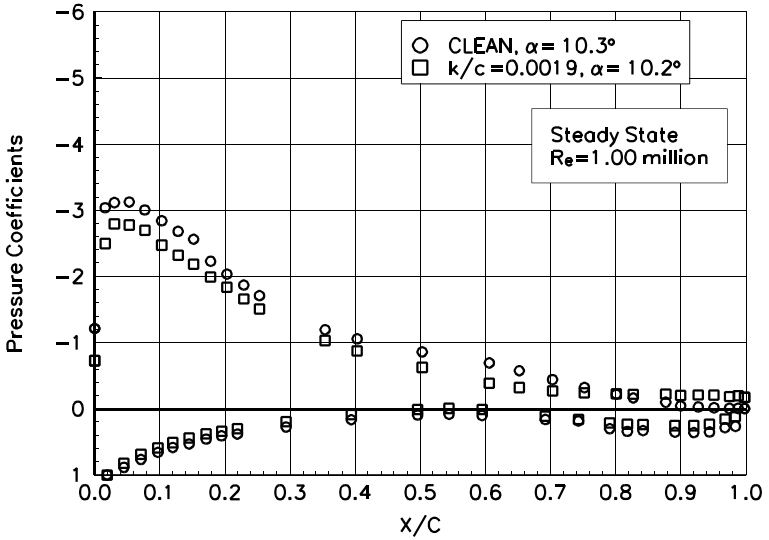

Figure B52. α = 10.3°

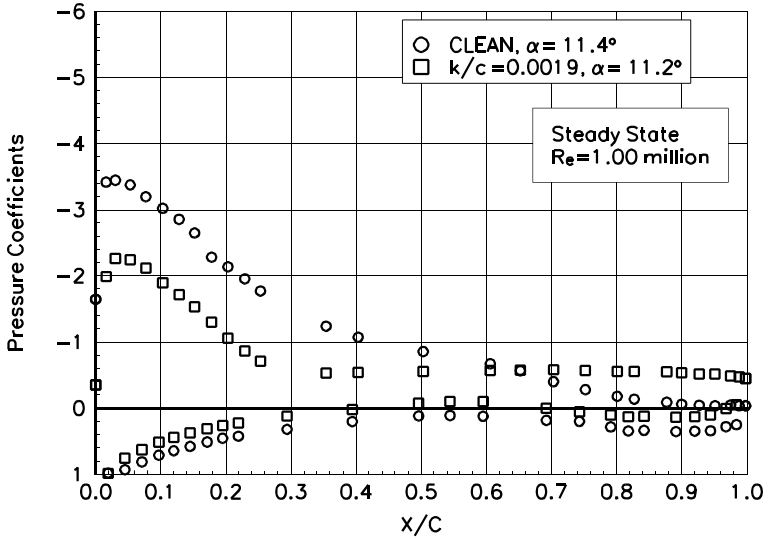

Figure B53. α = 11.4°

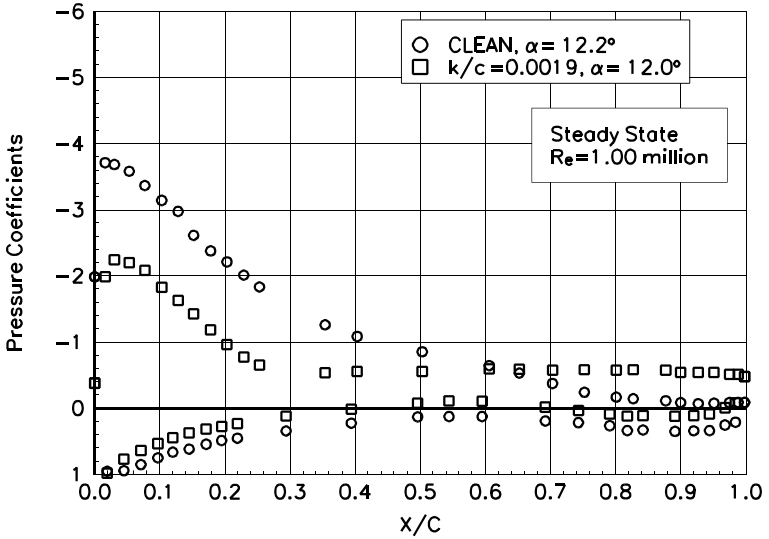

Figure B54. α = 12.2°

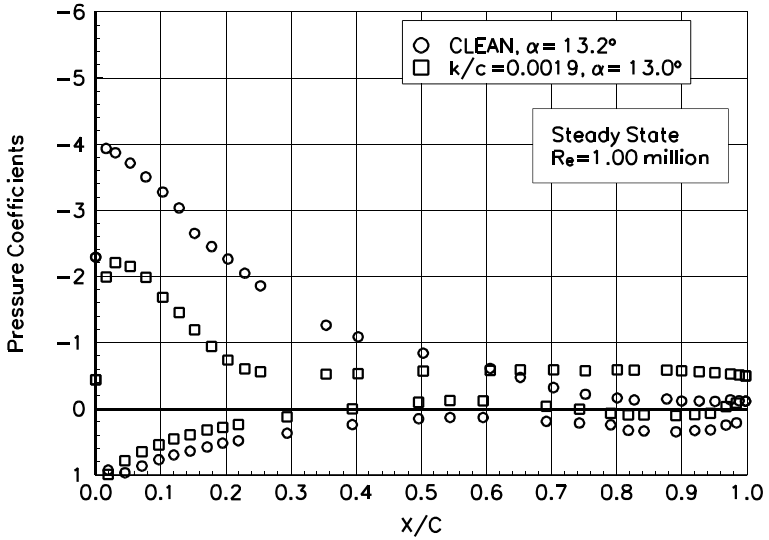

Figure B55. α = 13.2°

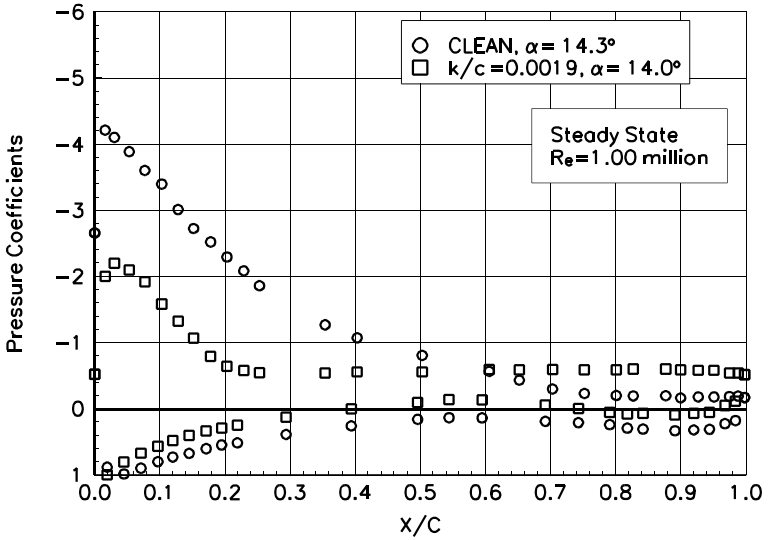

Figure B56. α = 14.3°

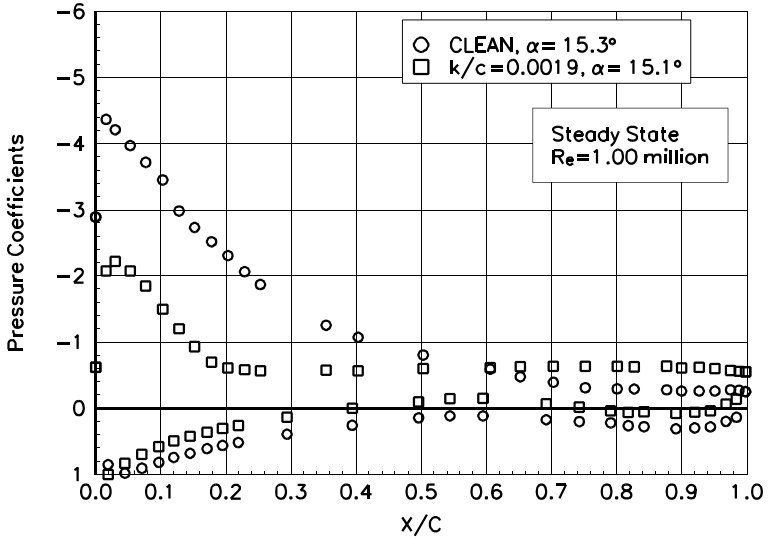

Figure B57. α = 15.3°

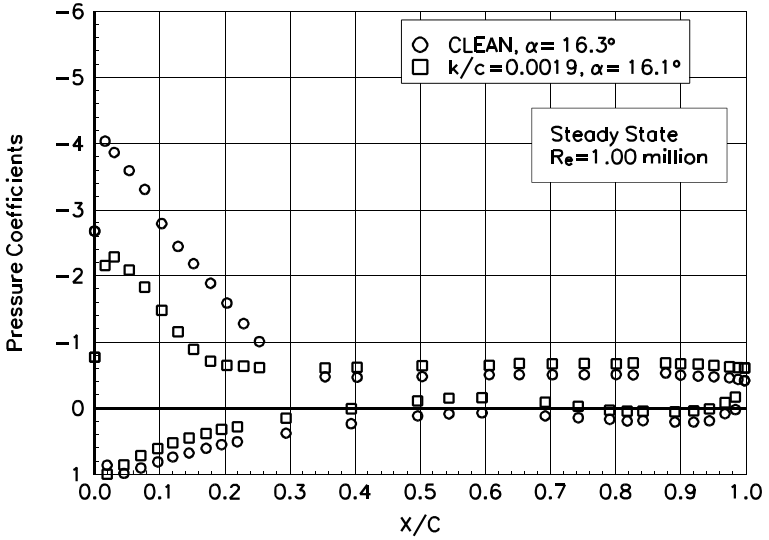

Figure B58. α = 16.3°

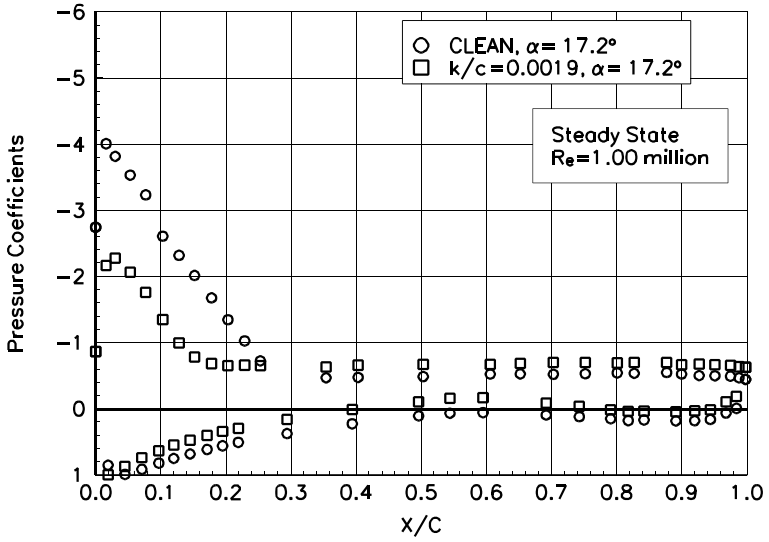

Figure B59. α = 17.2°

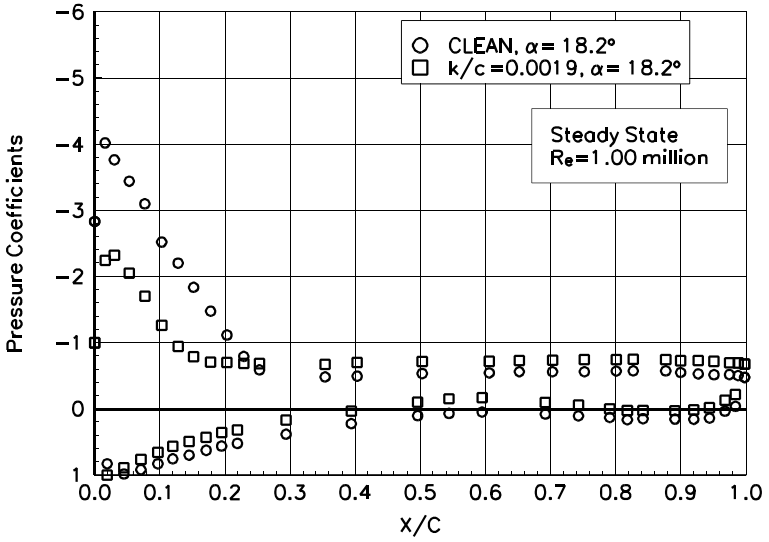

Figure B60. α = 18.2°

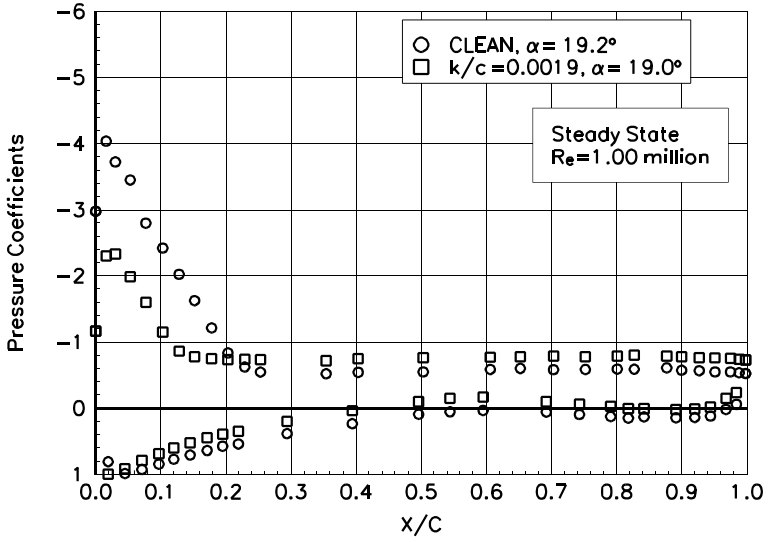

Figure B61. α = 19.2°

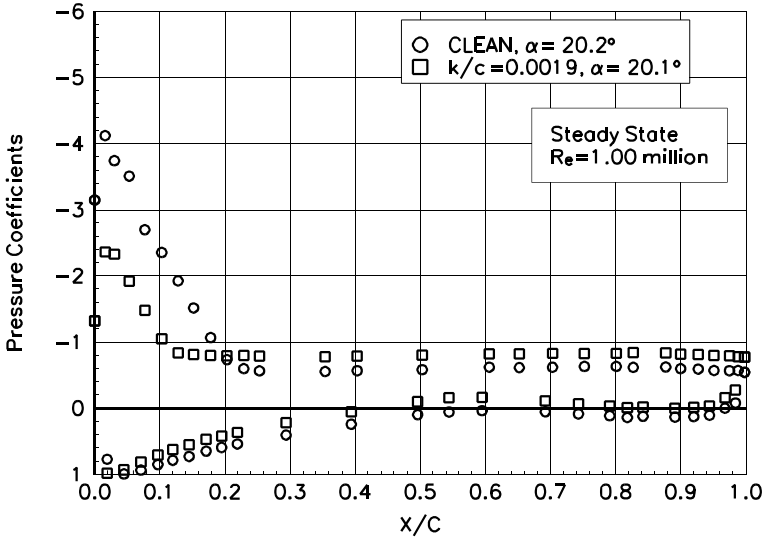

Figure B62. α = 20.2°

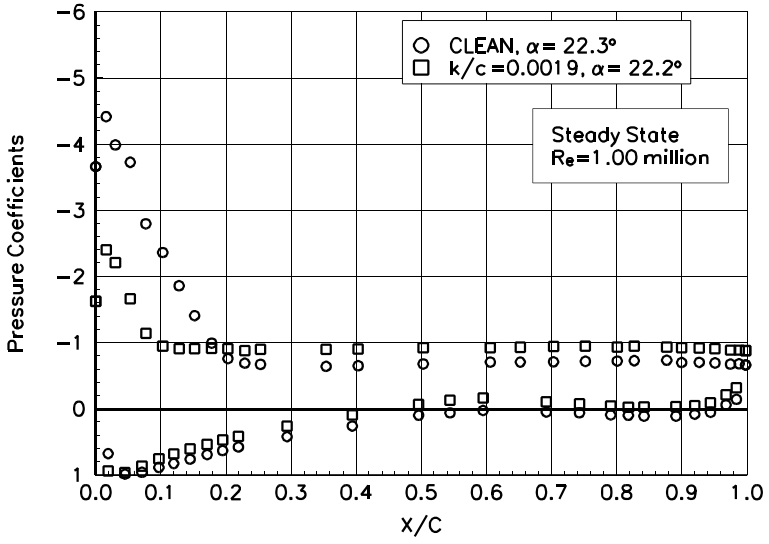

Figure B63. α = 22.3°

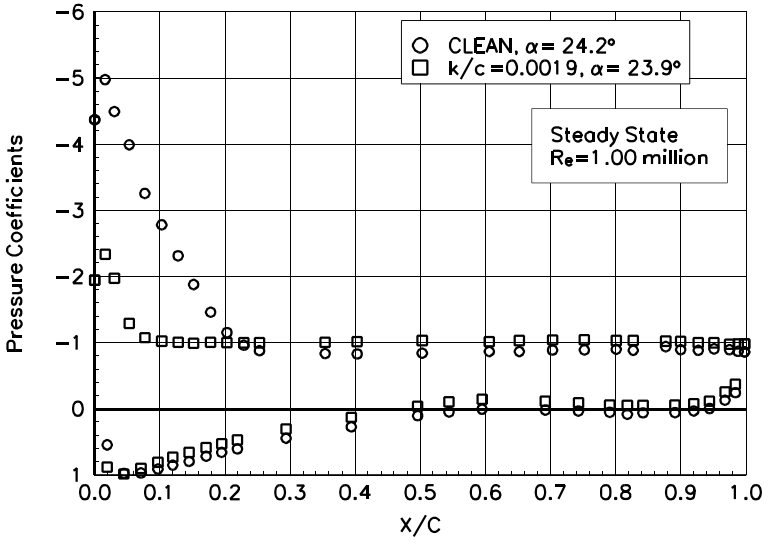

Figure B64. α = 24.2°

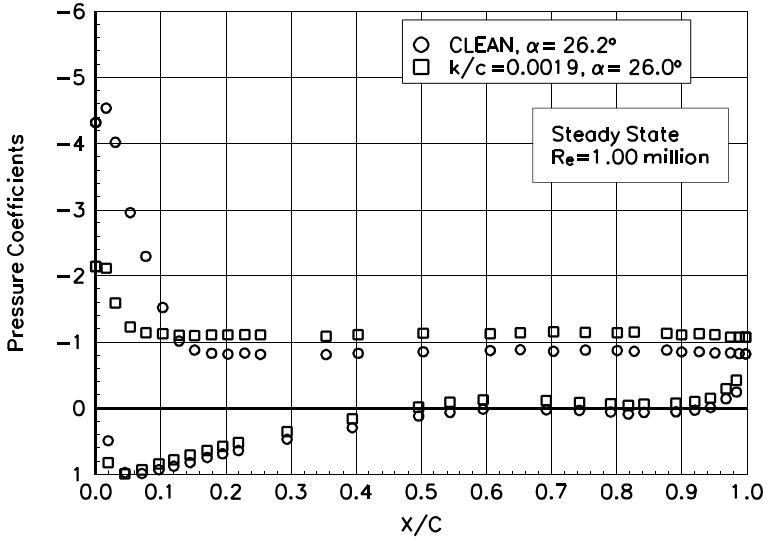

Figure B65. α = 26.2°

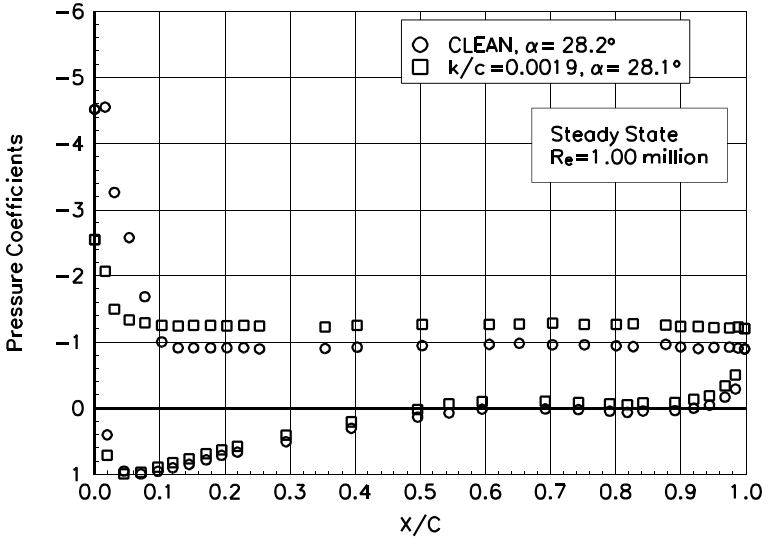

Figure B66. α = 28.2°

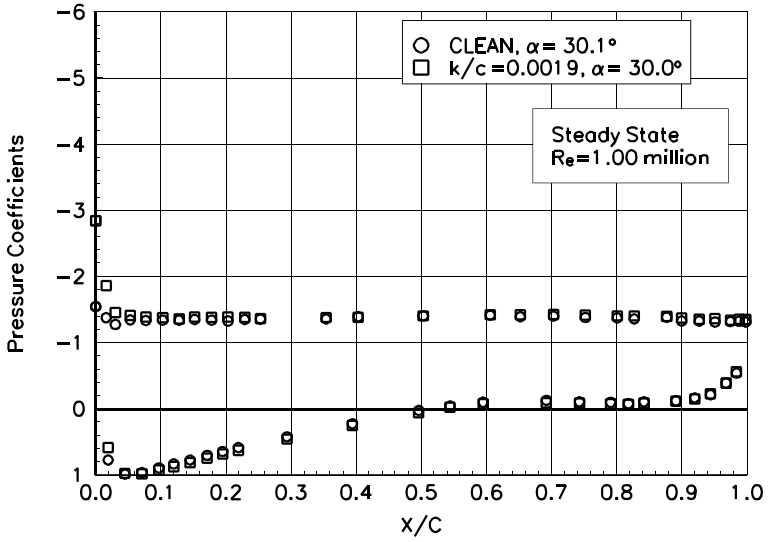

Figure B67. α = 30.1°

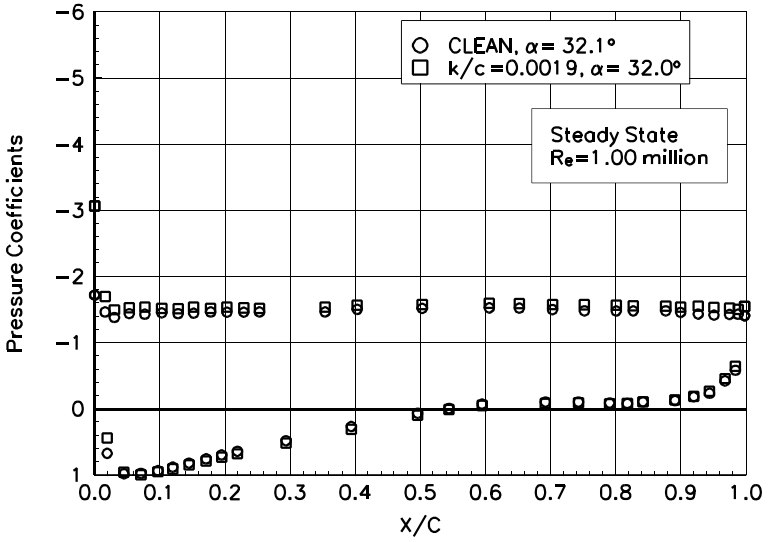

Figure B68. α = 32.1°

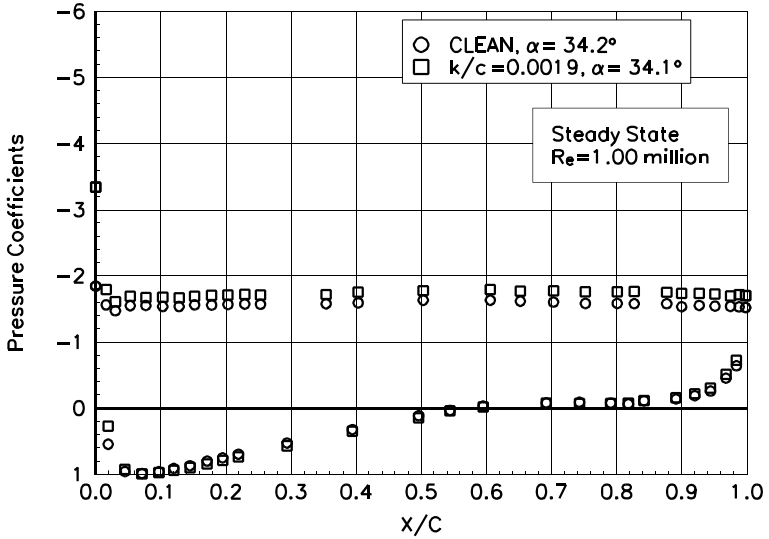

Figure B69. α = 34.2°

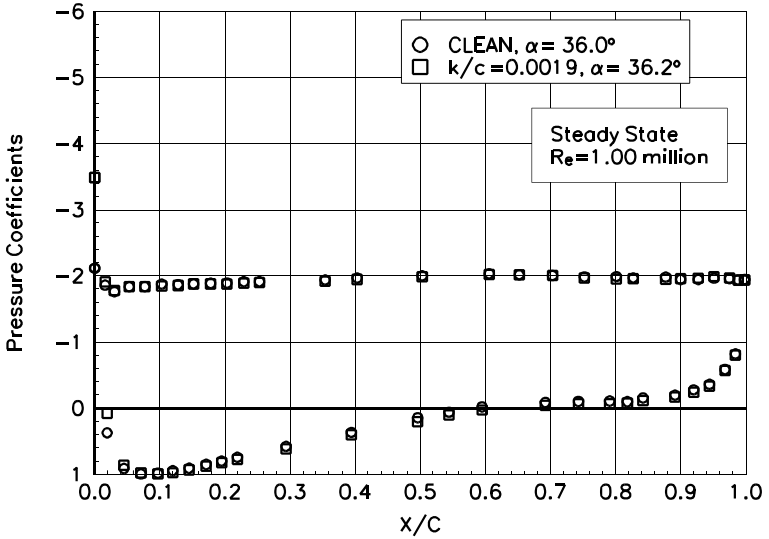

Figure B70. α = 36.0°

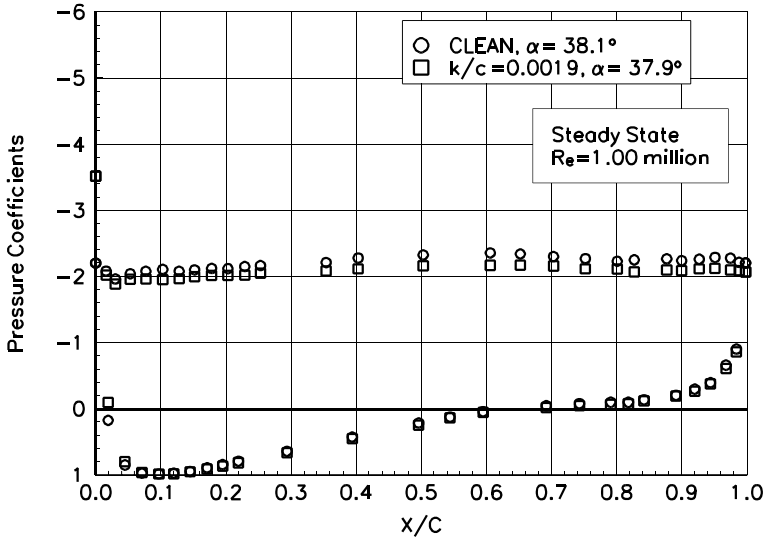

Figure B71. α = 38.1°

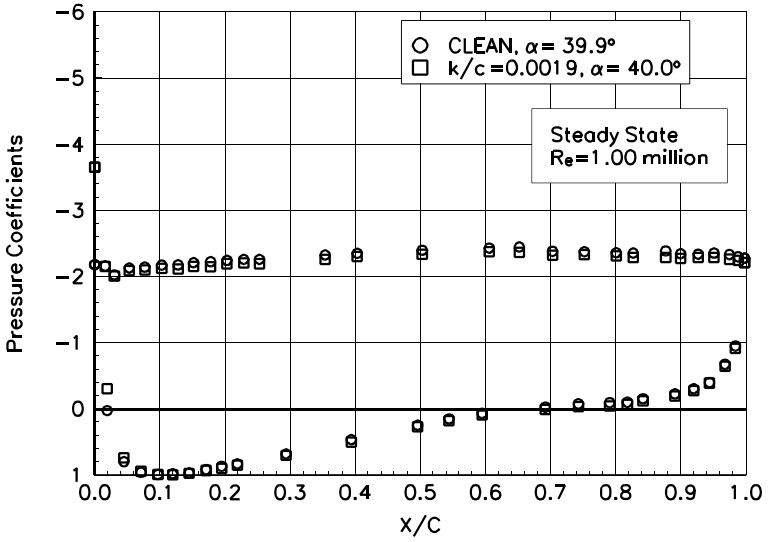

Figure B72. α = 39.9°

Steady State
Pressure Distributions
LS(1)-0417MOD

Re = 1.25 million

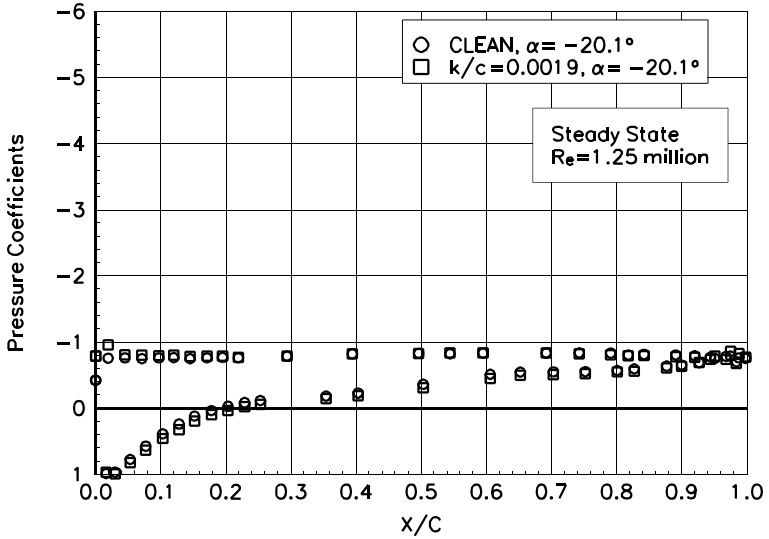

Figure B73. α = -20.1°

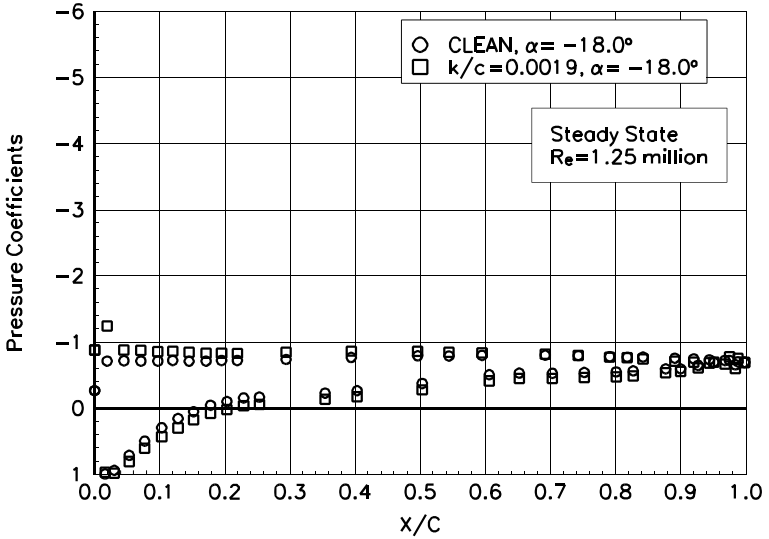

Figure B74. α = -18.0°

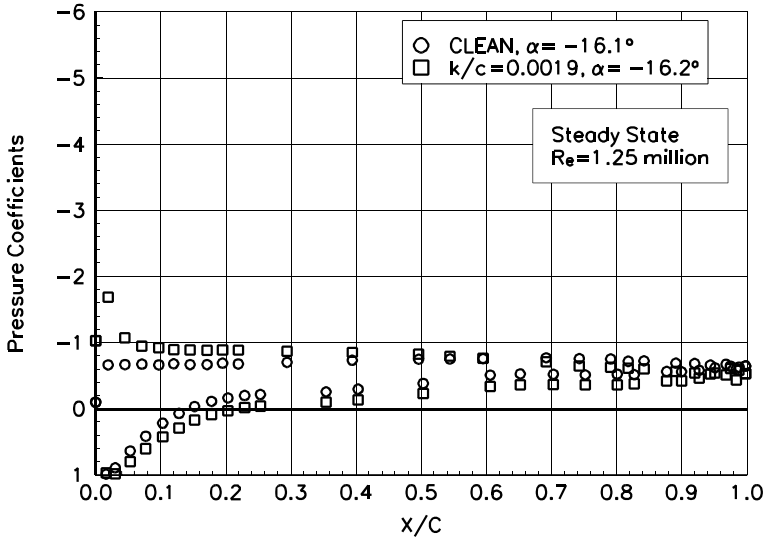

Figure B75. α = -16.1°

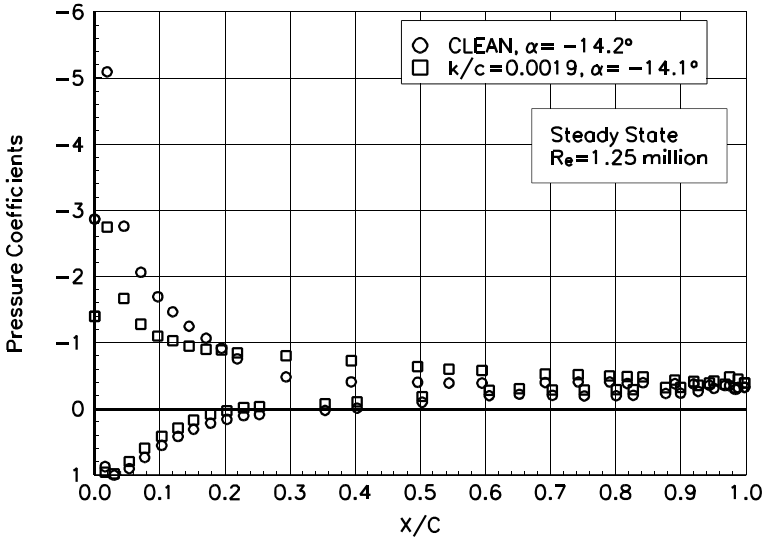

Figure B76. α = -14.2°

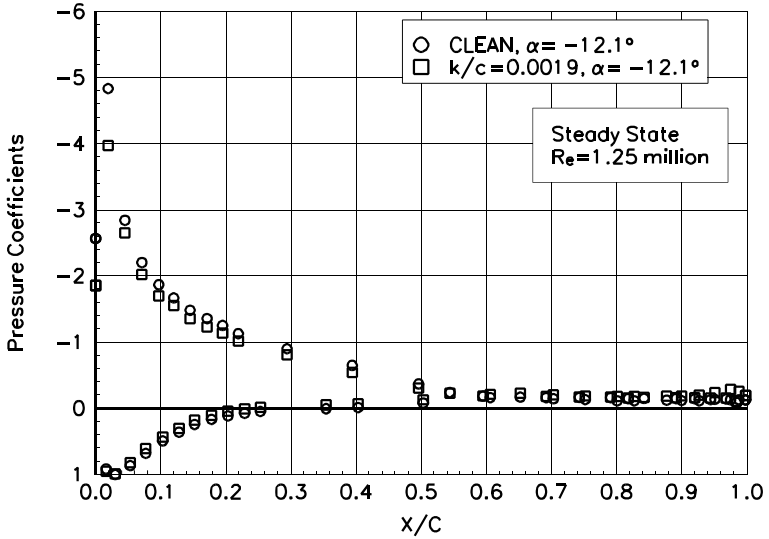

Figure B77. α = -12.1°

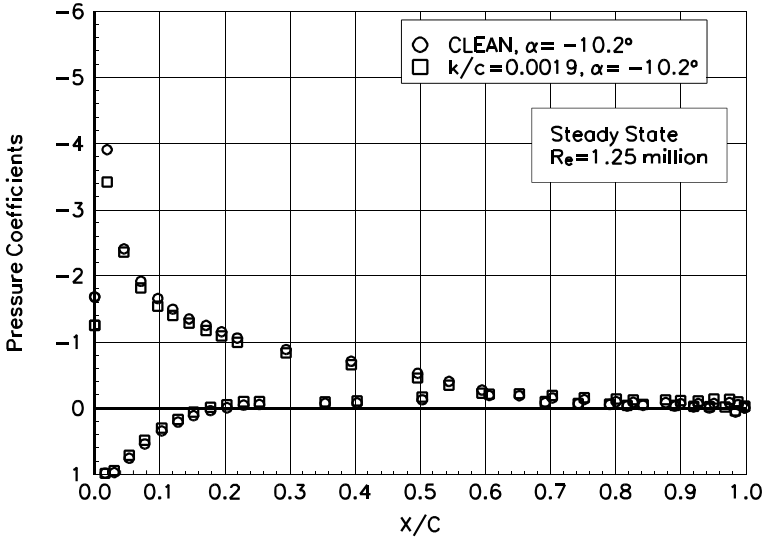

Figure B78. α = -10.2°

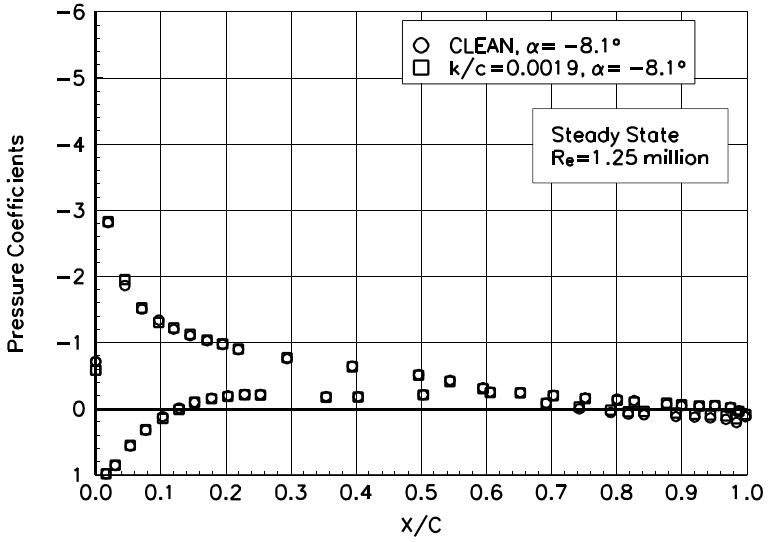

Figure B79. α = -8.1°

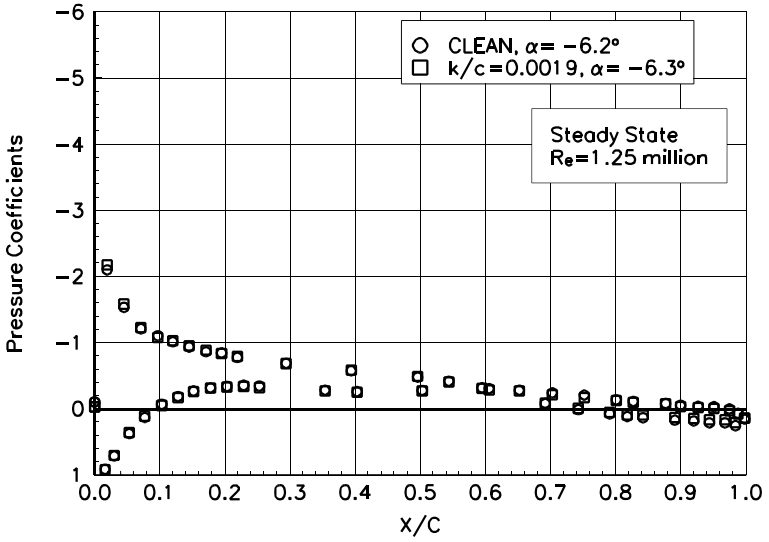

Figure B80. α = -6.2°

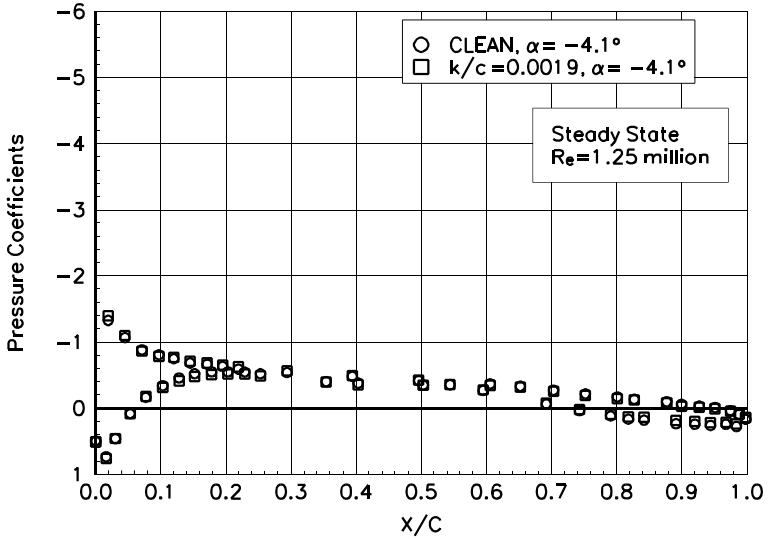

Figure B81. α = -4.1°

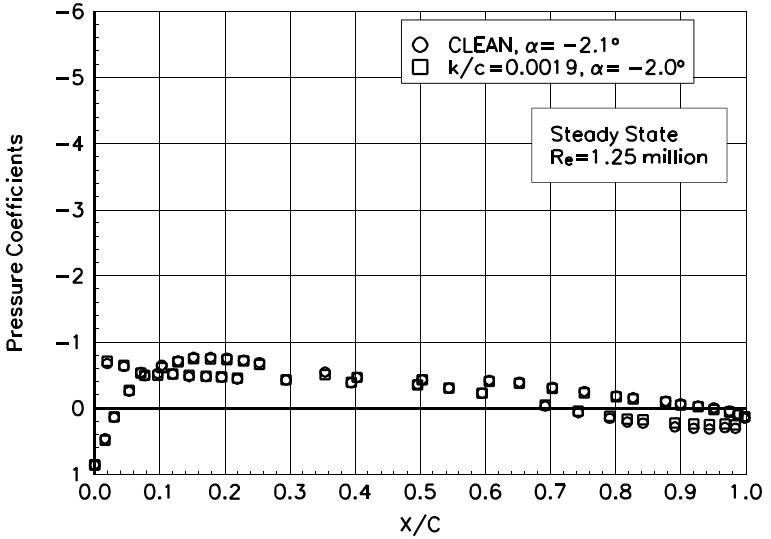

Figure B82. α = -2.1°

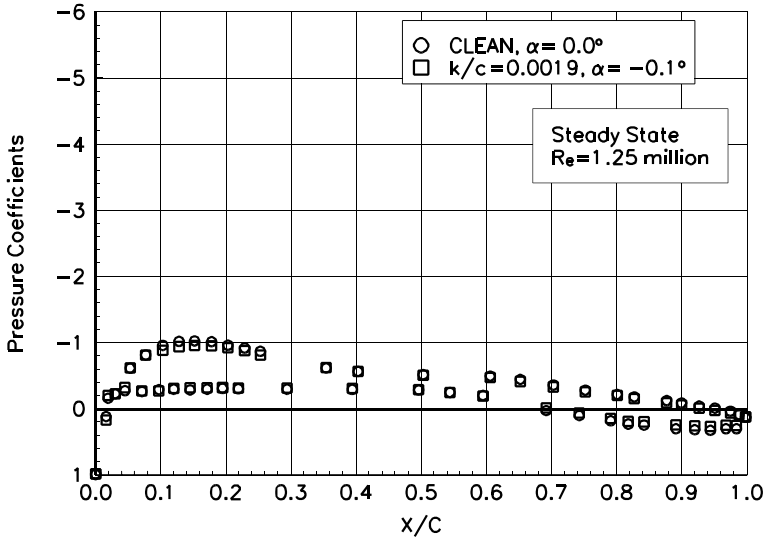

Figure B83. α = 0.0°

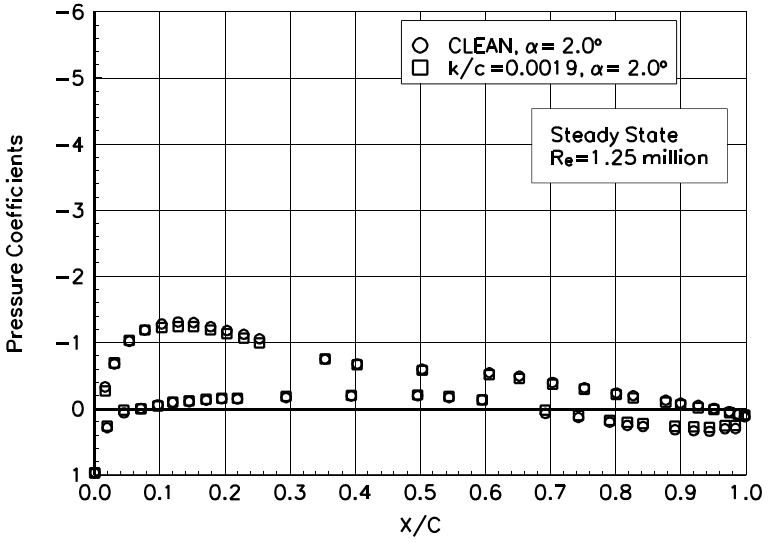

Figure B84. α = 2.0°

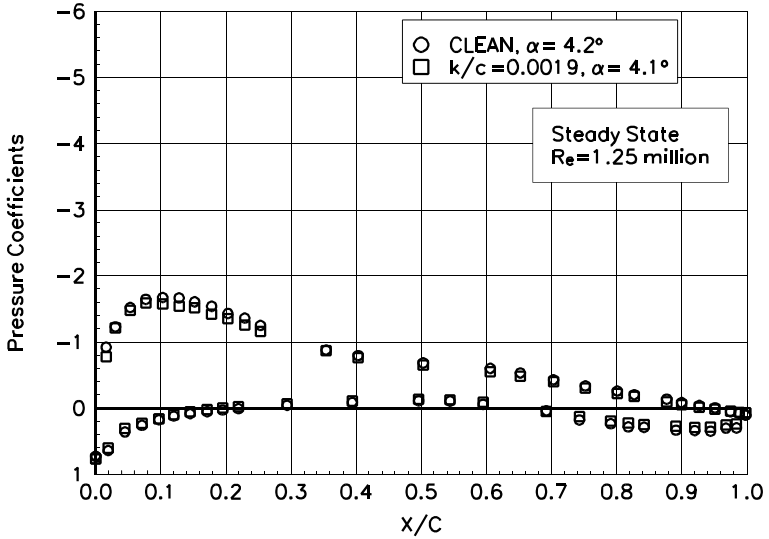

Figure B85. α = 4.2°

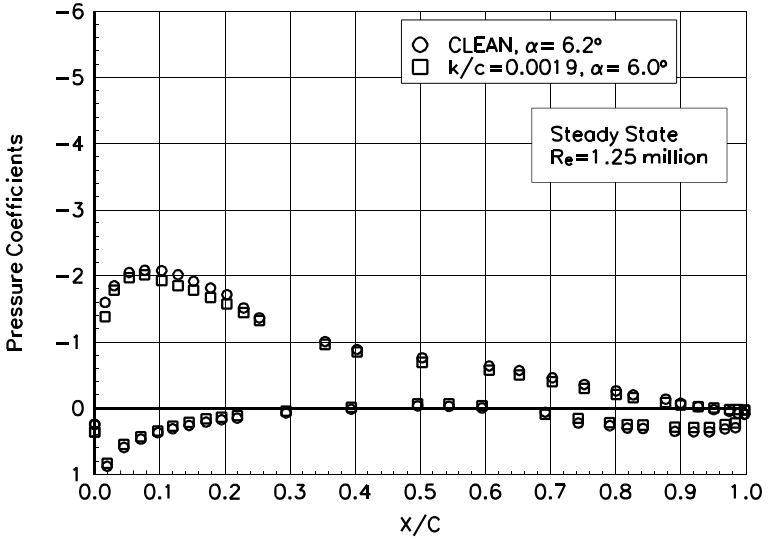

Figure B86. α = 6.2°

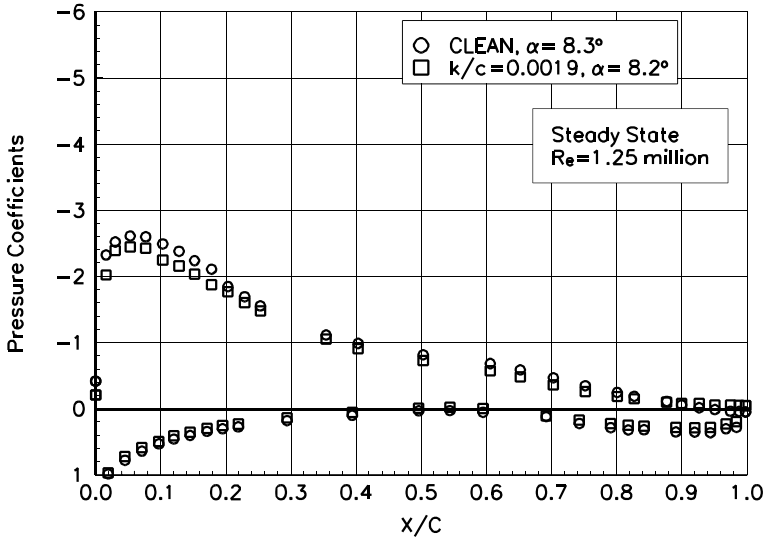

Figure B87. α = 8.3°

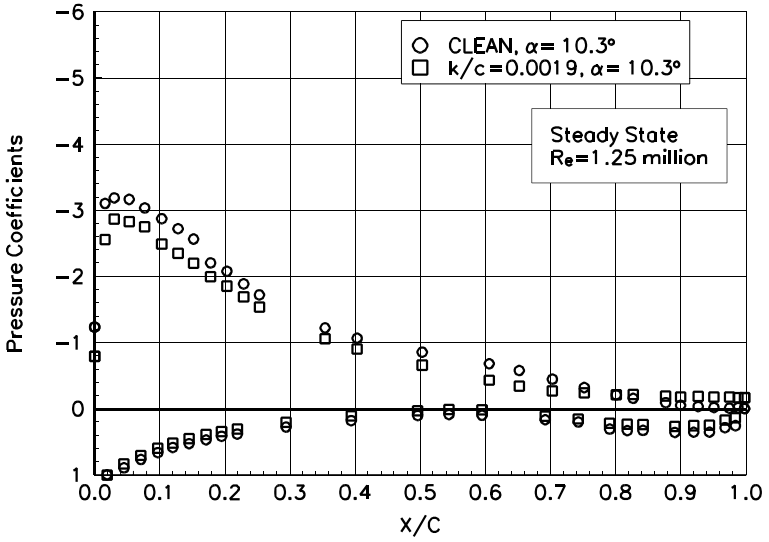

Figure B88. α = 10.3°

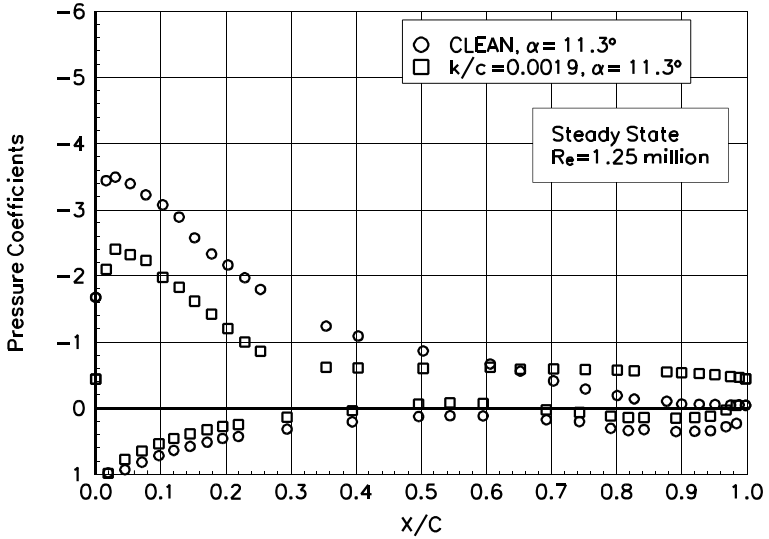

Figure B89. α = 11.3°

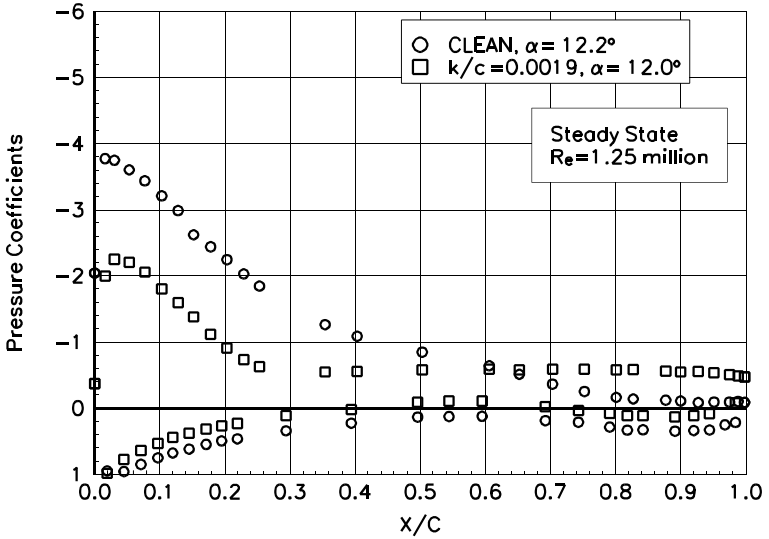

Figure B90. α = 12.2°

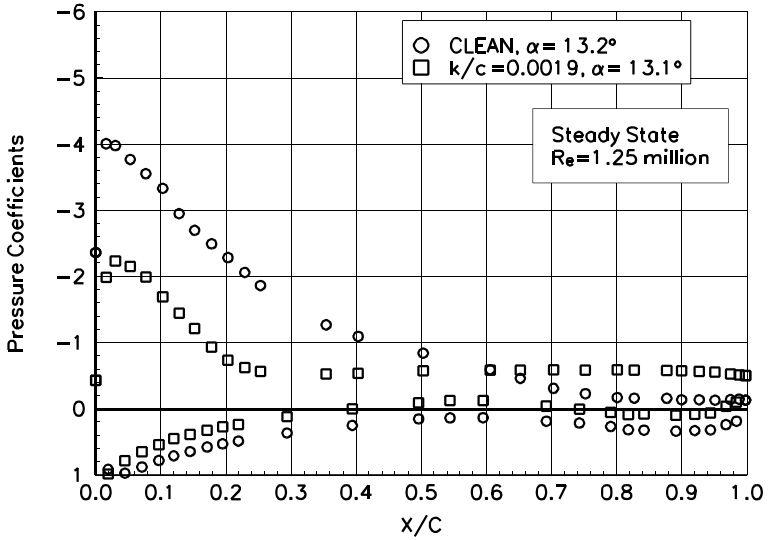

Figure B91. α = 13.2°

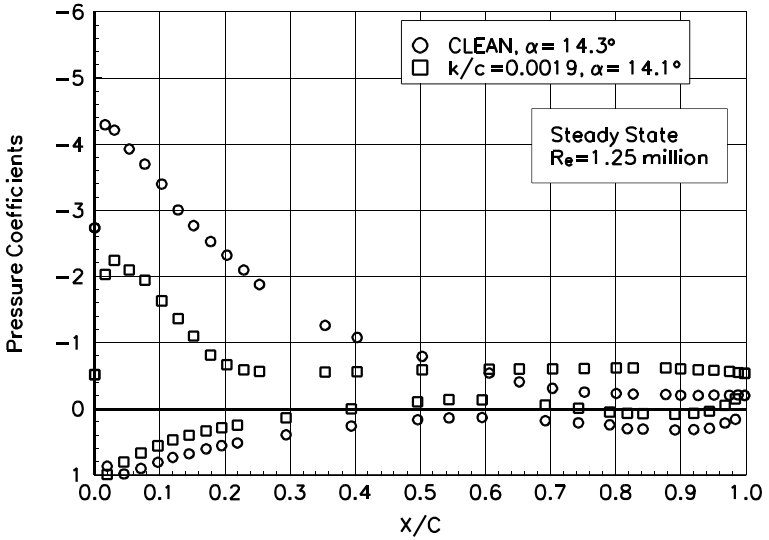

Figure B92. α = 14.3°

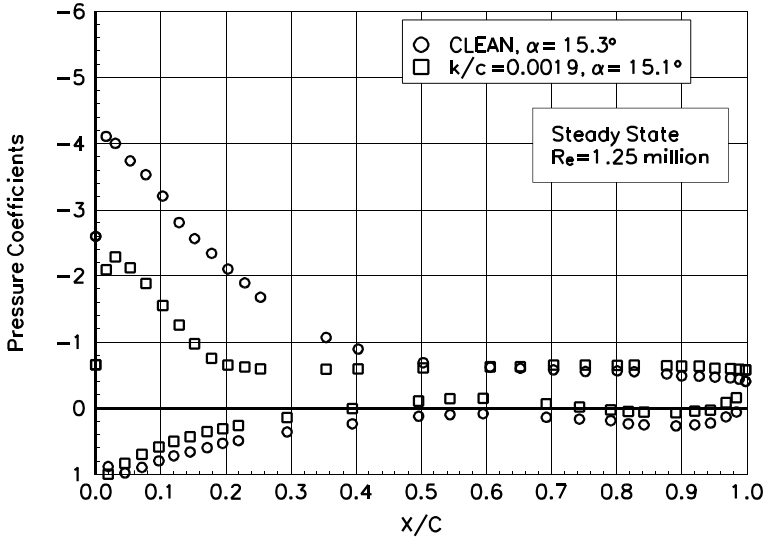

Figure B93. α = 15.3°

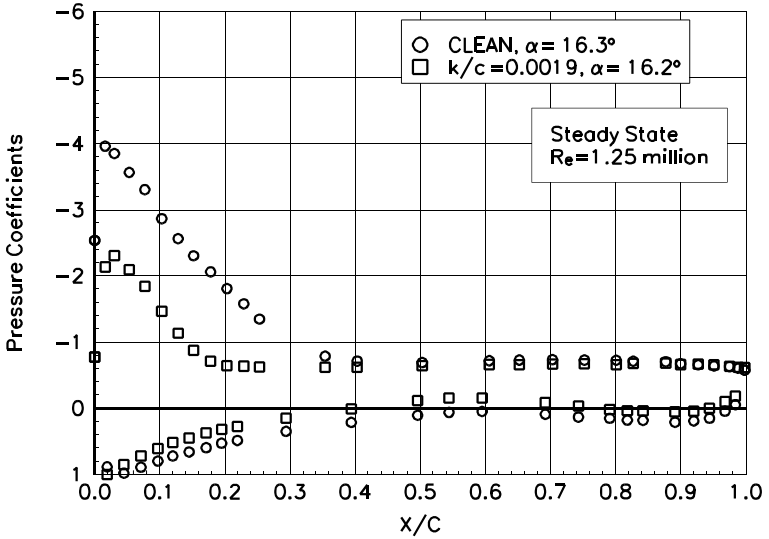

Figure B94. α = 16.3°

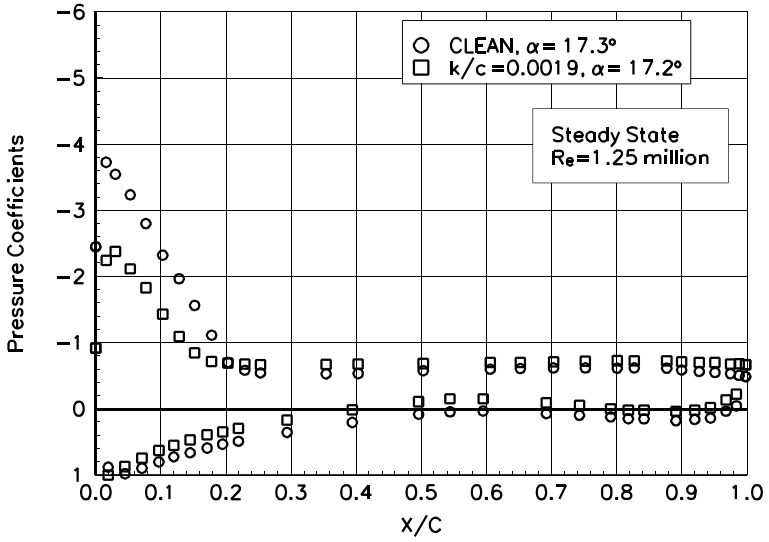

Figure B95. α = 17.3°

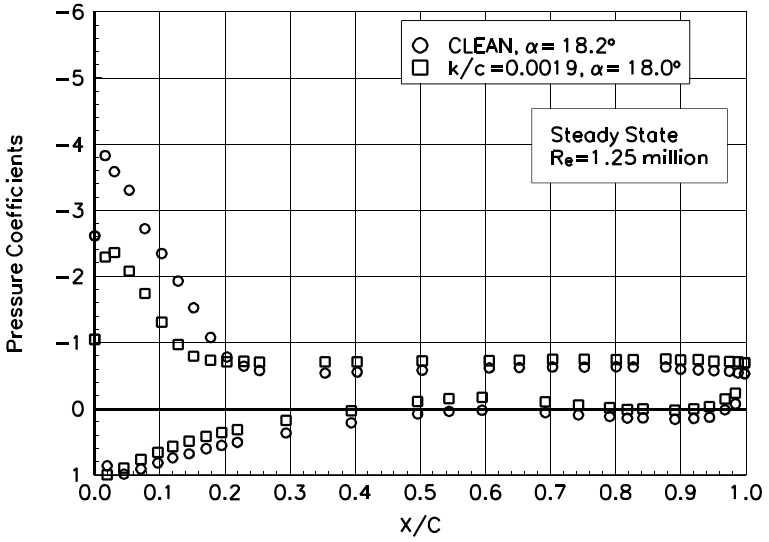

Figure B96. α = 18.2°

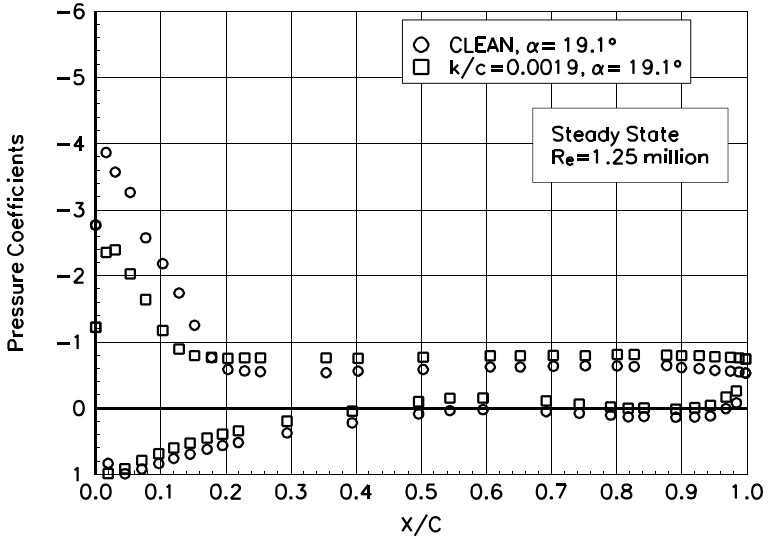

Figure B97. α = 19.1°

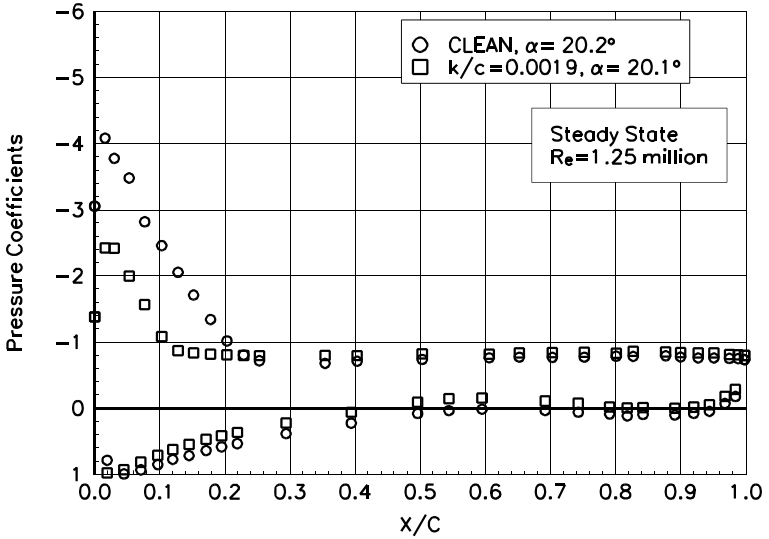

Figure B98. α = 20.2°

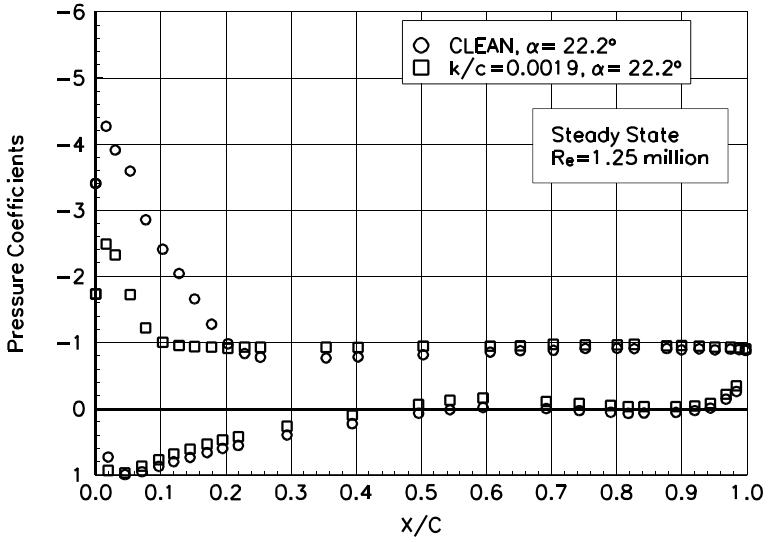

Figure B99. α = 22.2°

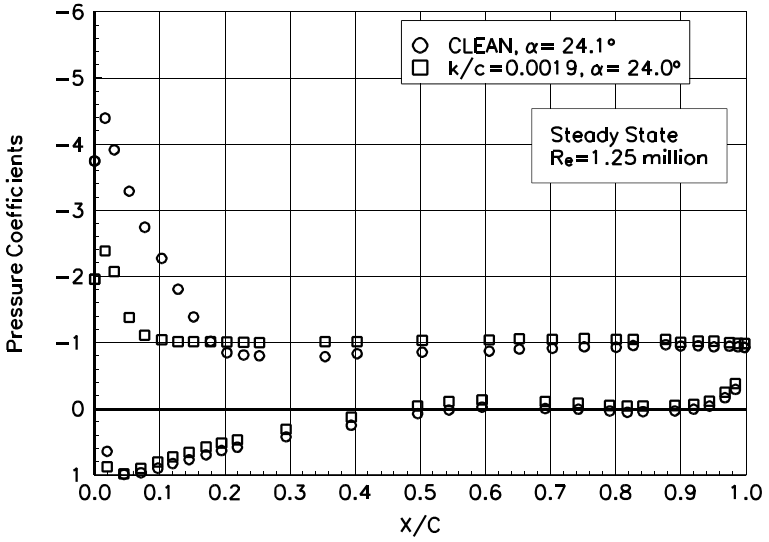

Figure B100. α = 24.1°

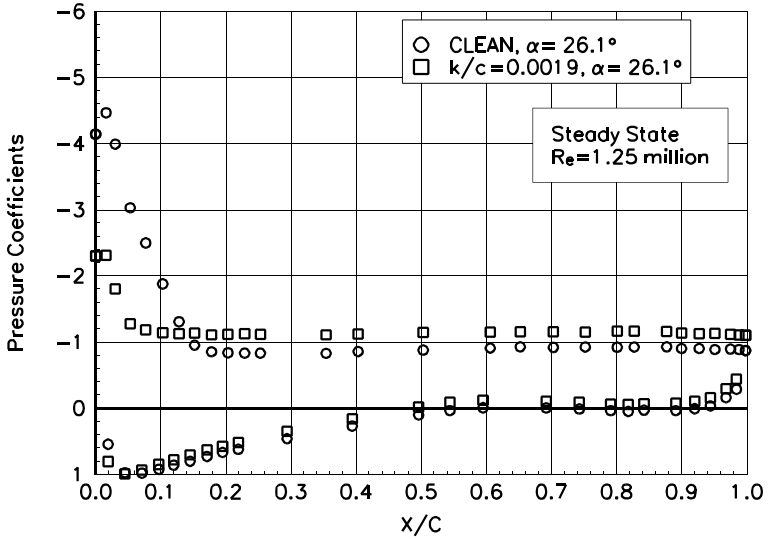

Figure B101. α = 26.1°

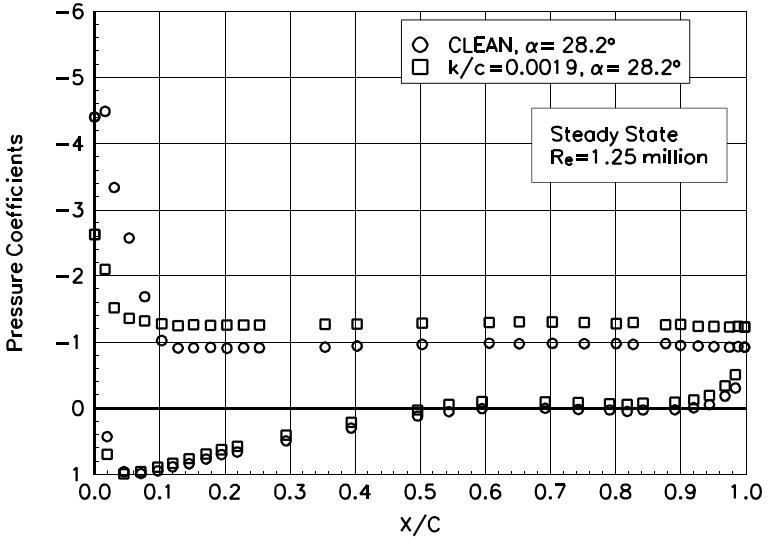

Figure B102. α = 28.2°

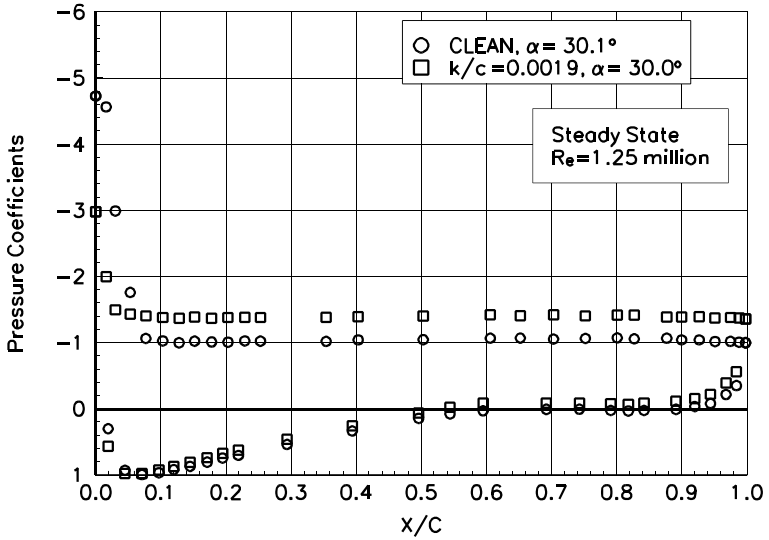

Figure B103. α = 30.1°

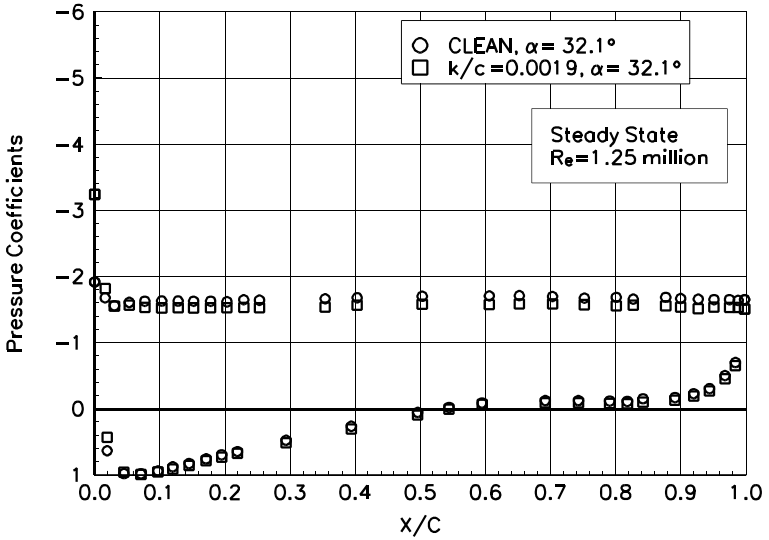

Figure B104. α = 32.1°

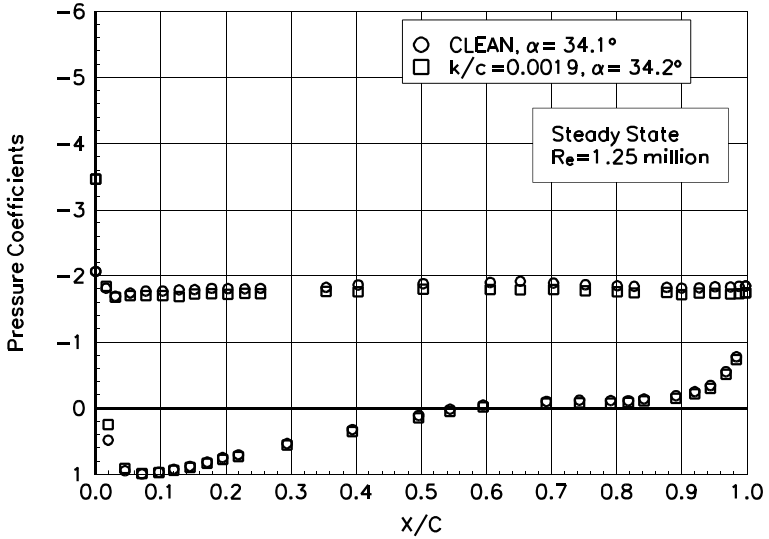

Figure B105. α = 34.1°

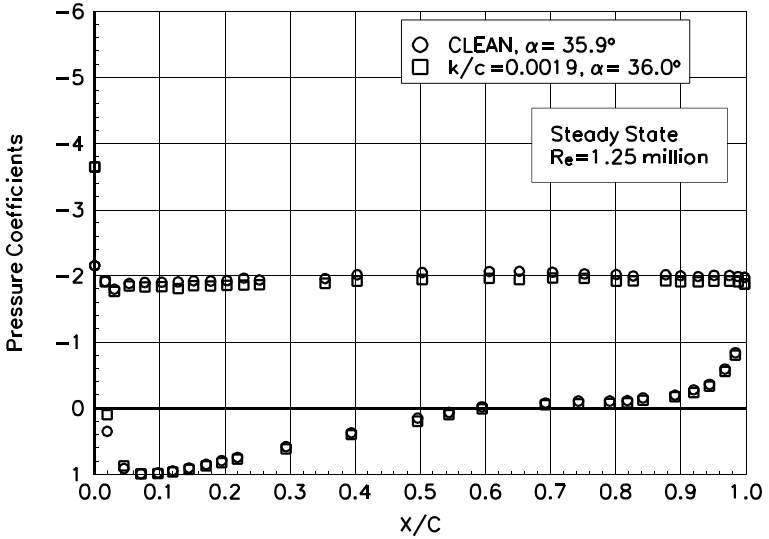

Figure B106. α = 35.9°

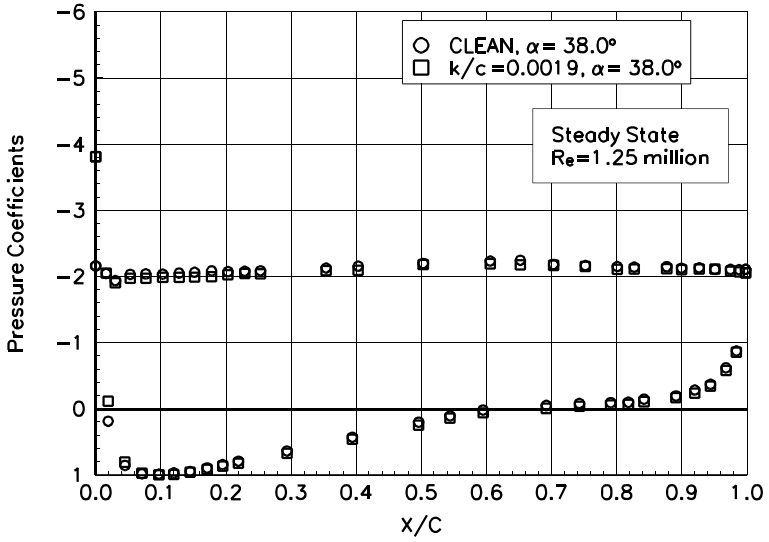

Figure B107. α = 38.0°

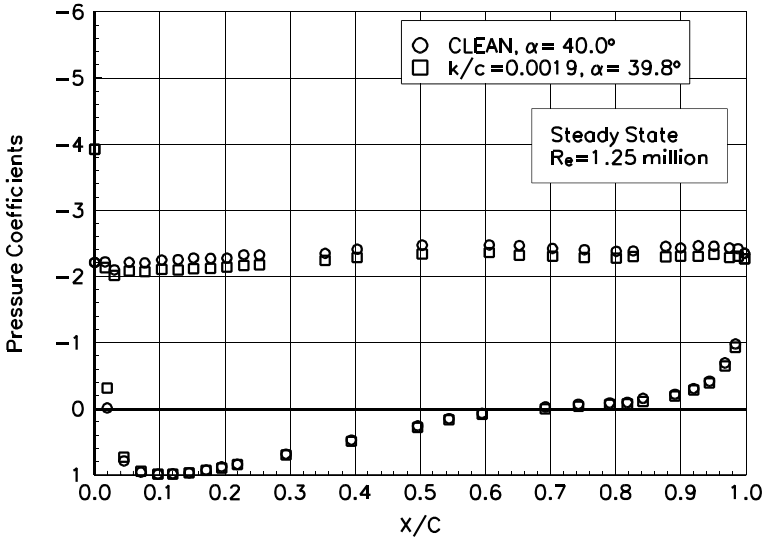

Figure B108. α = 40.0°

Steady State
Pressure Distributions
LS(1)-0417MOD

Re = 1.5 million

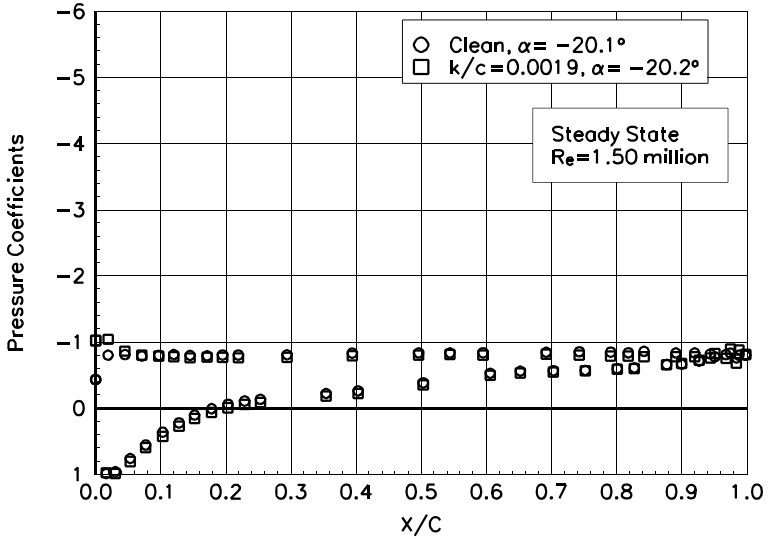

Figure B109. α = -20.1°

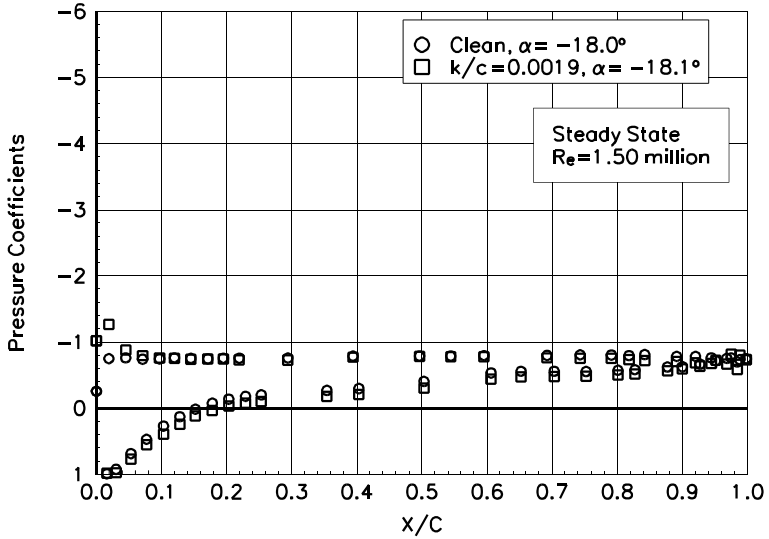

Figure B110. α = -18.0°

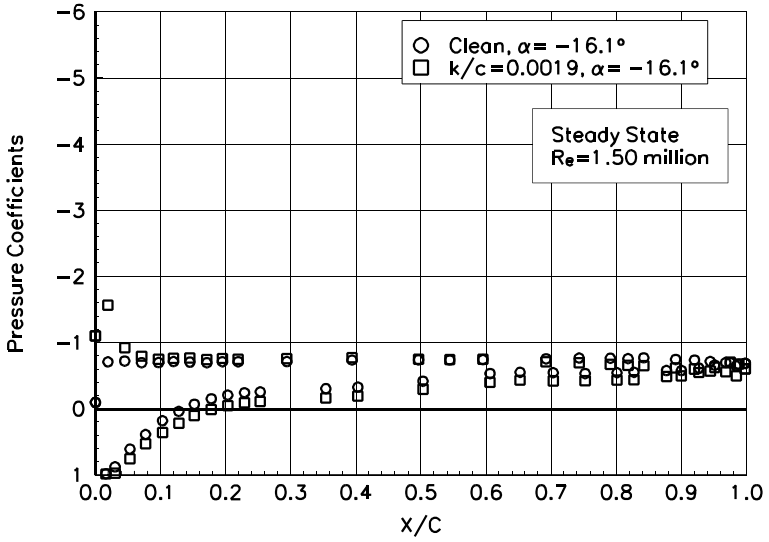

Figure B111. α = -16.1°

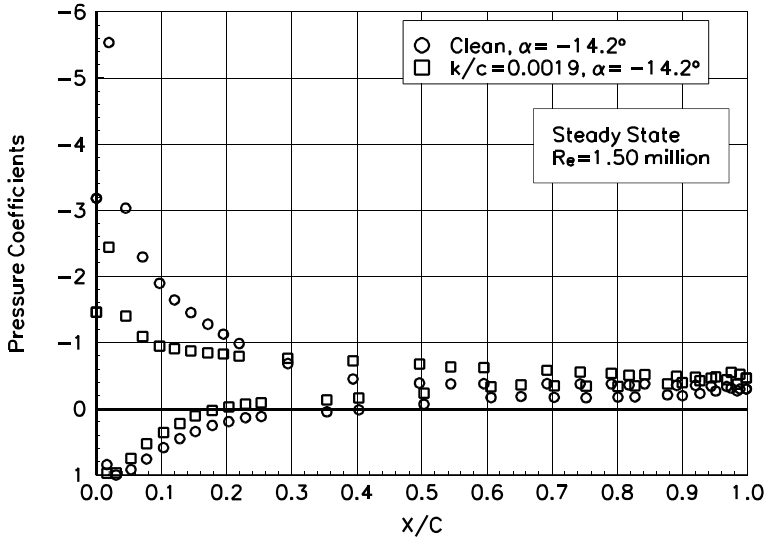

Figure B112. α = -14.2°

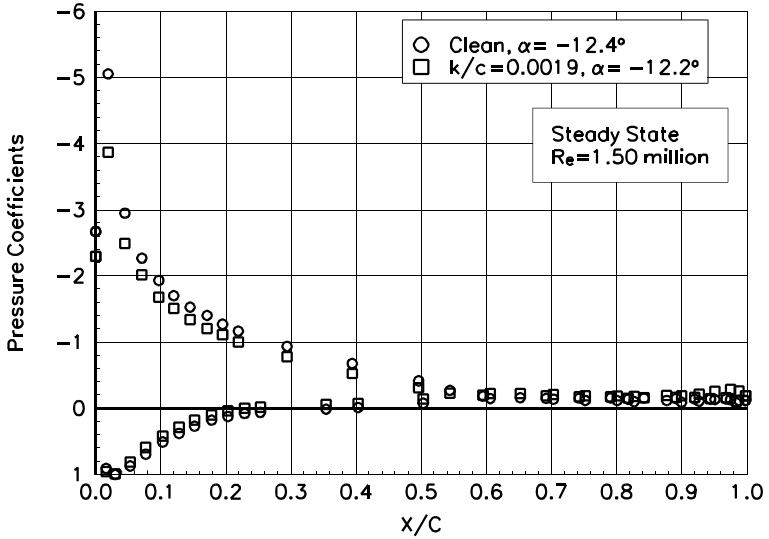

Figure B113. α = -12.4°

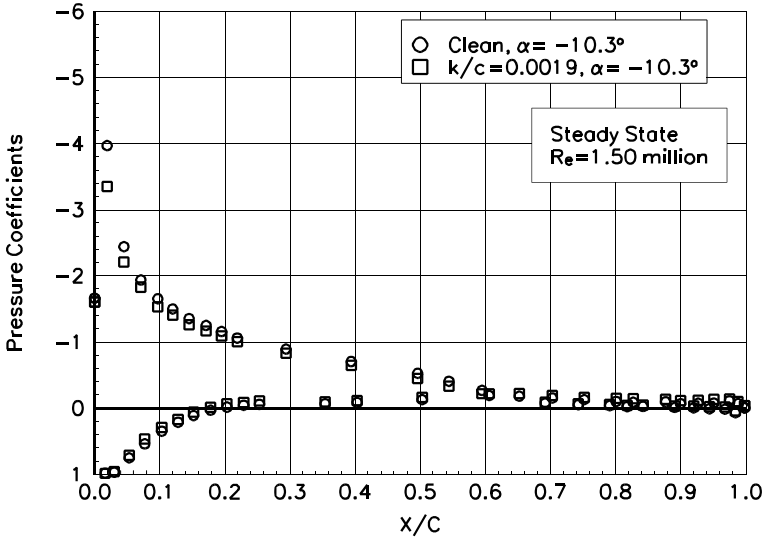

Figure B114. α = -10.3°

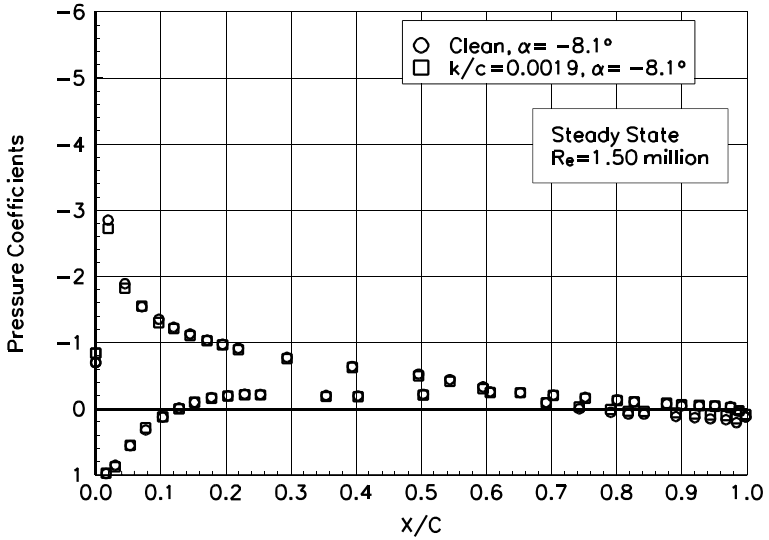

Figure B115. α = -8.1°

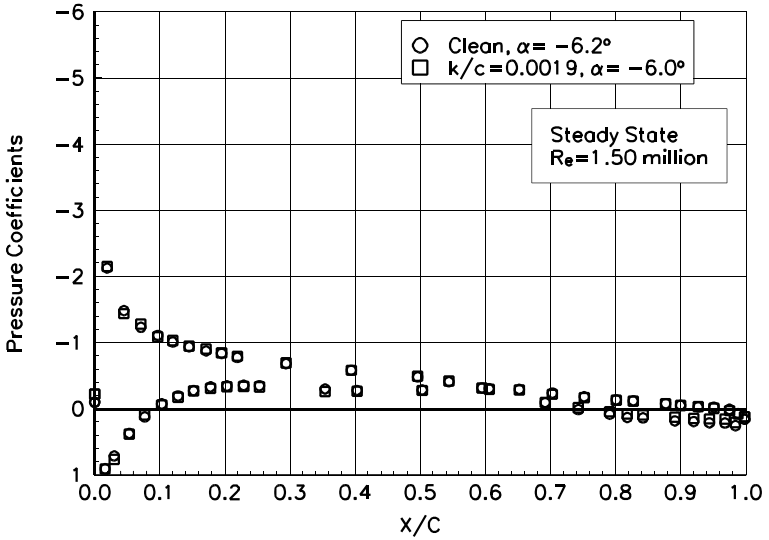

Figure B116. α = -6.2°

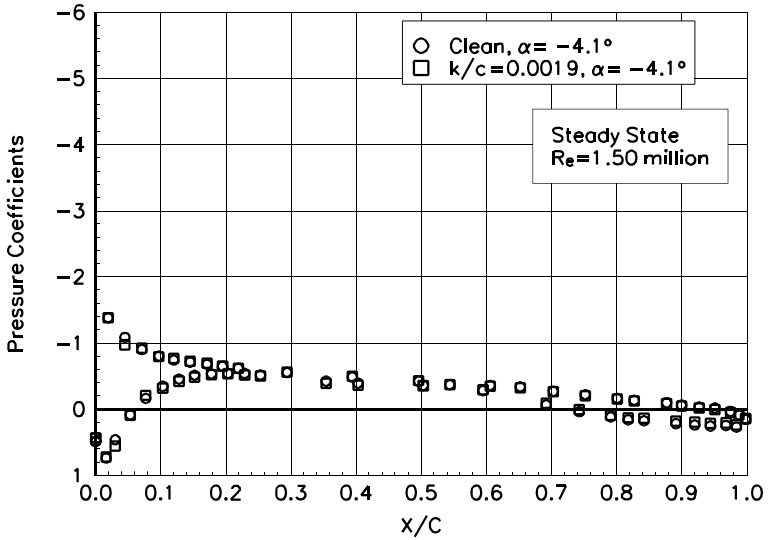

Figure B117. α = -4.1°

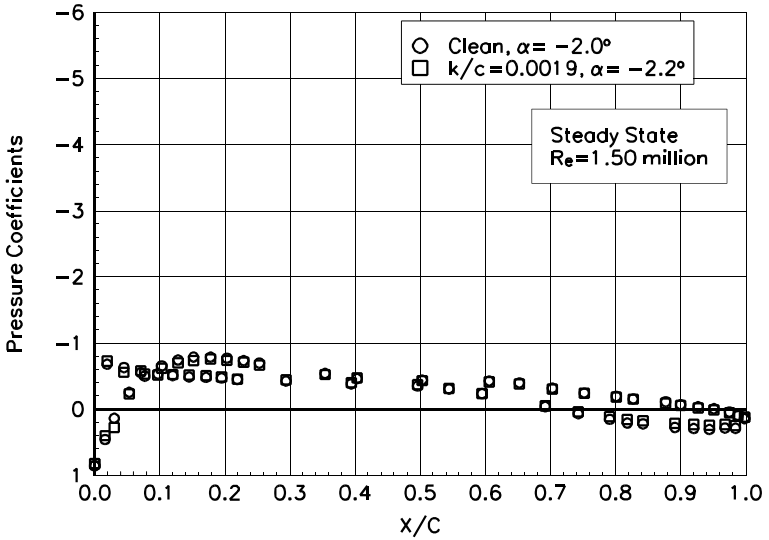

Figure B118. α = -2.0°

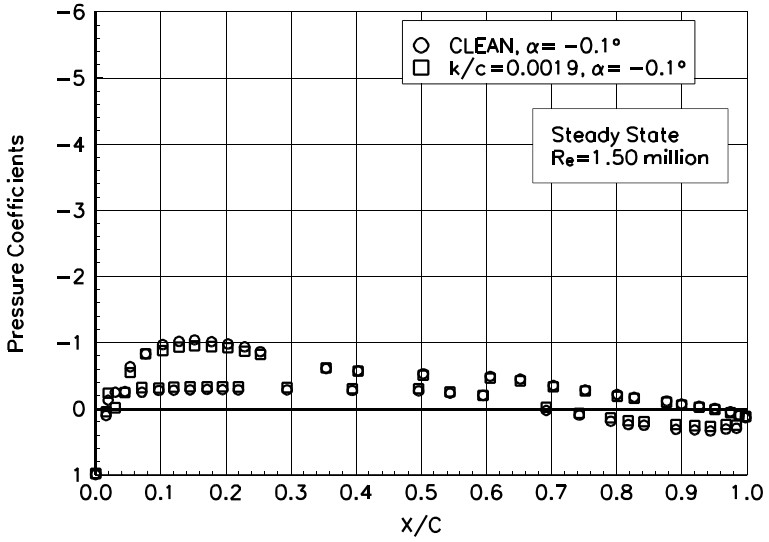

Figure B119. α = -0.1°

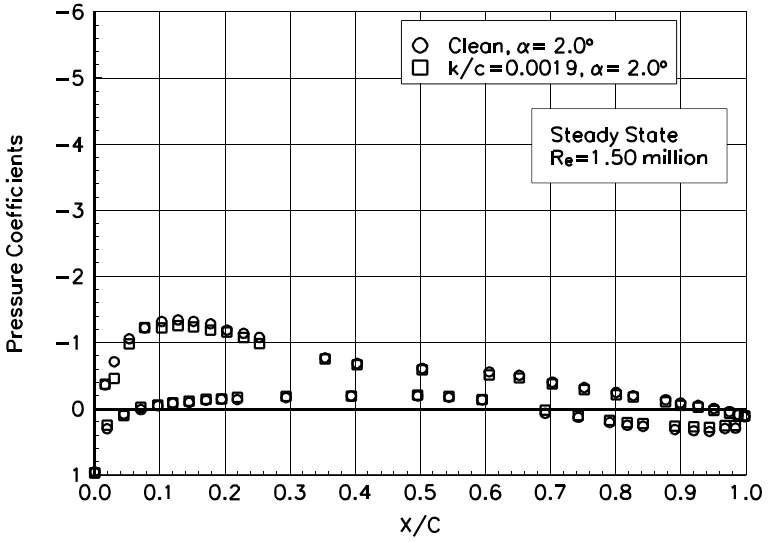

Figure B120. α = 2.0°

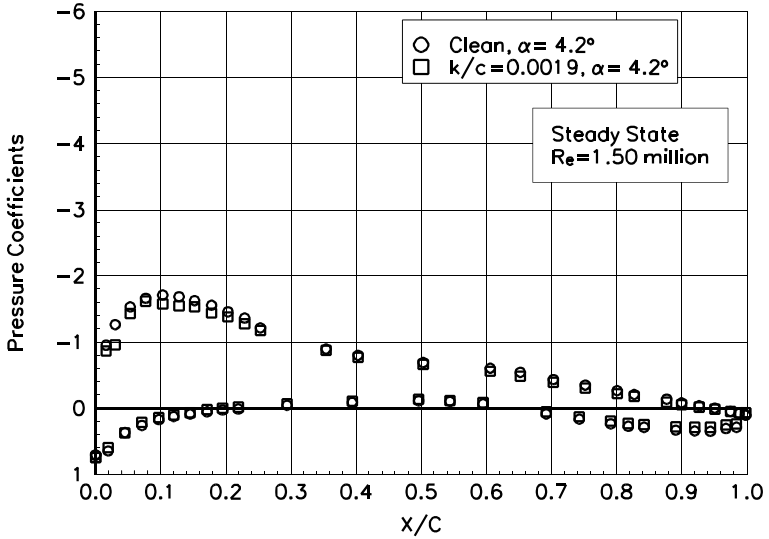

Figure B121. α = 4.2°

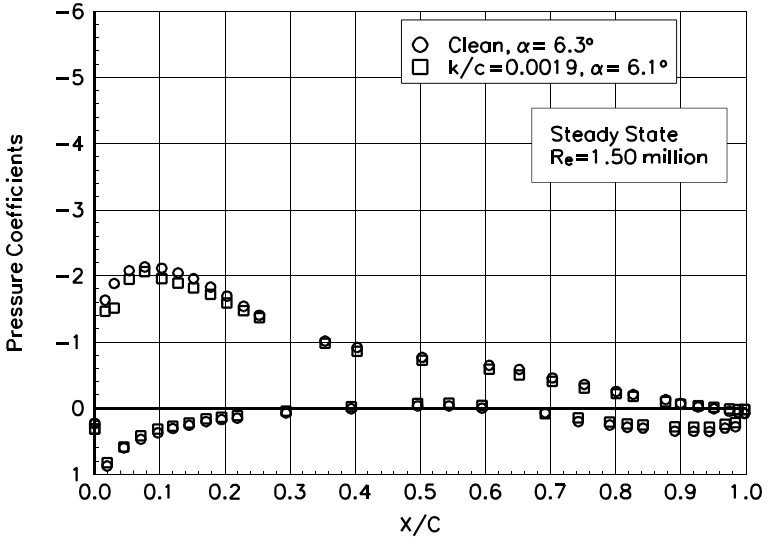

Figure B122. α = 6.3°

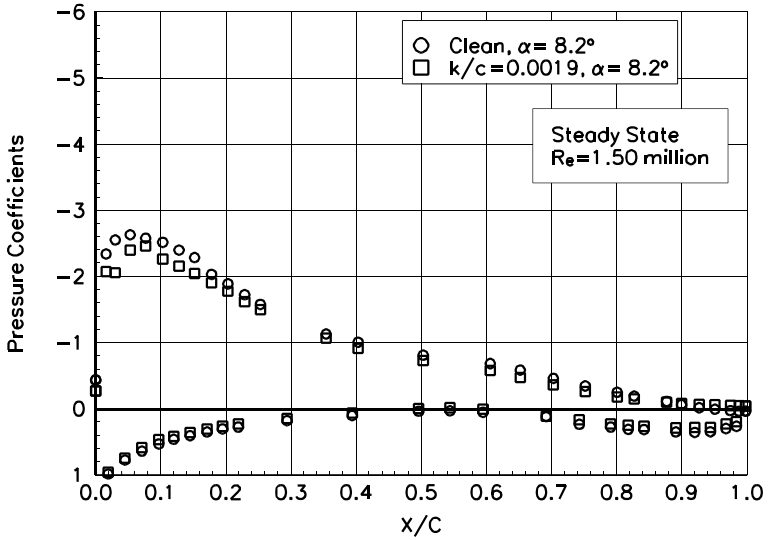

Figure B123. α = 8.2°

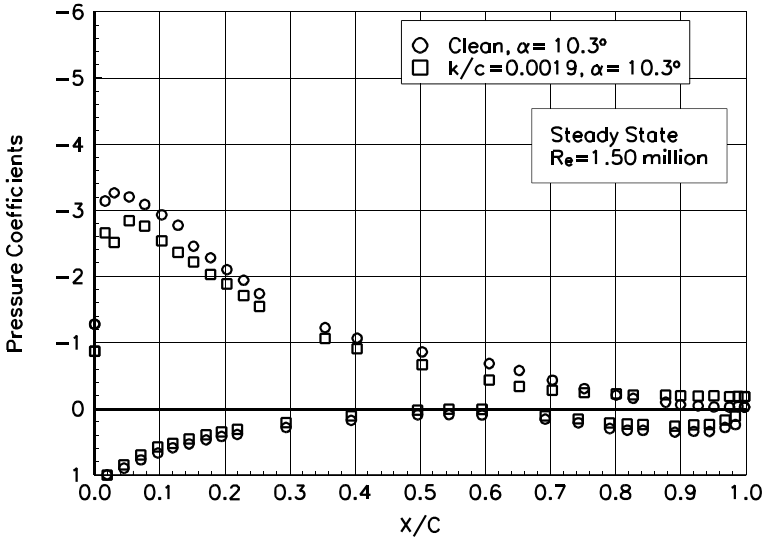

Figure B124. α = 10.3°

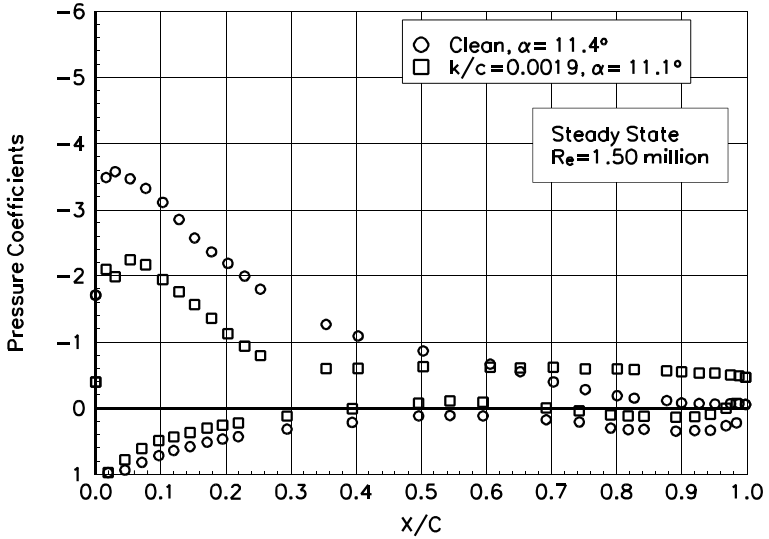

Figure B125. α = 11.4°

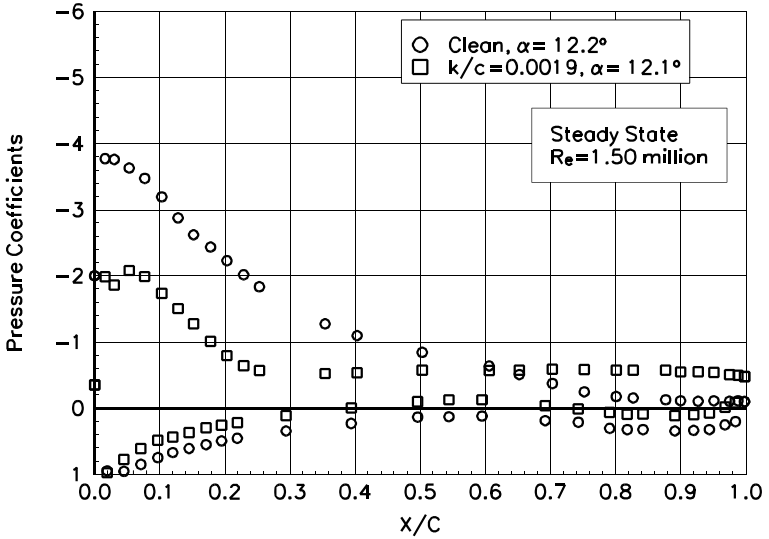

Figure B126. α = 12.2°

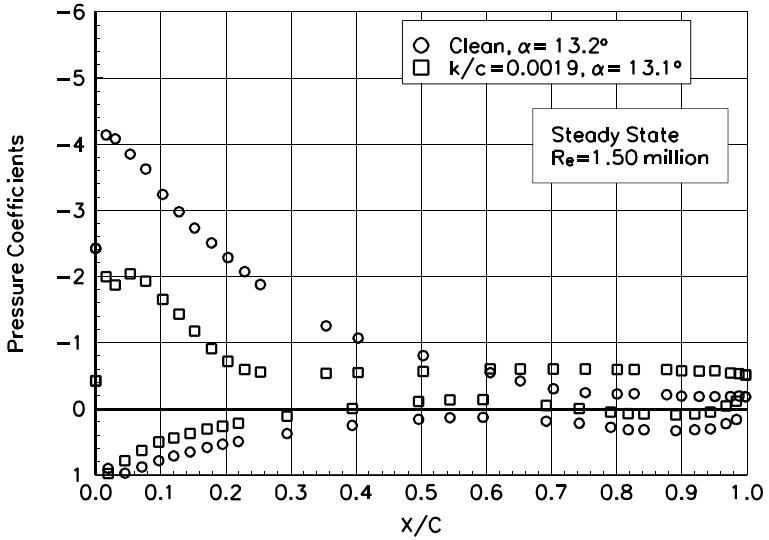

Figure B127. α = 13.2°

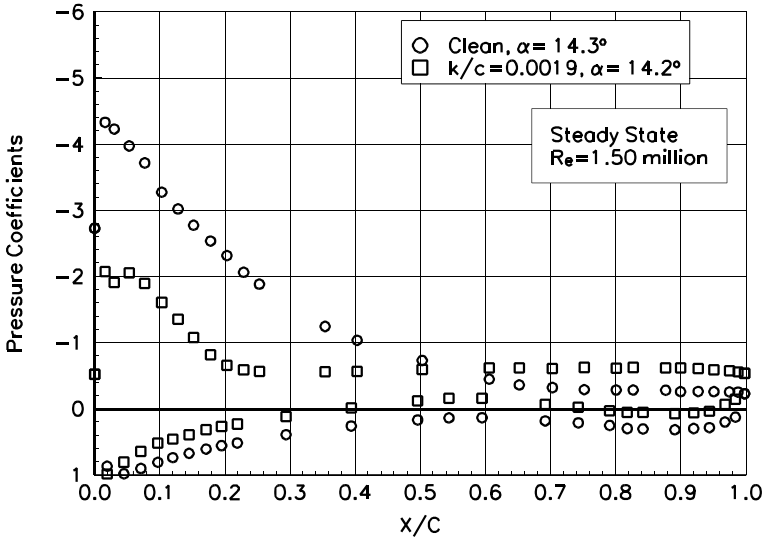

Figure B128. α = 14.3°

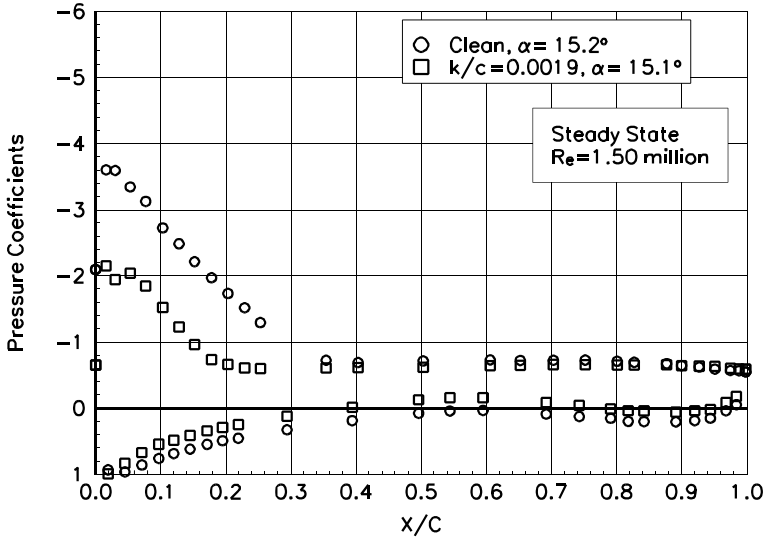

Figure B129. α = 15.2°

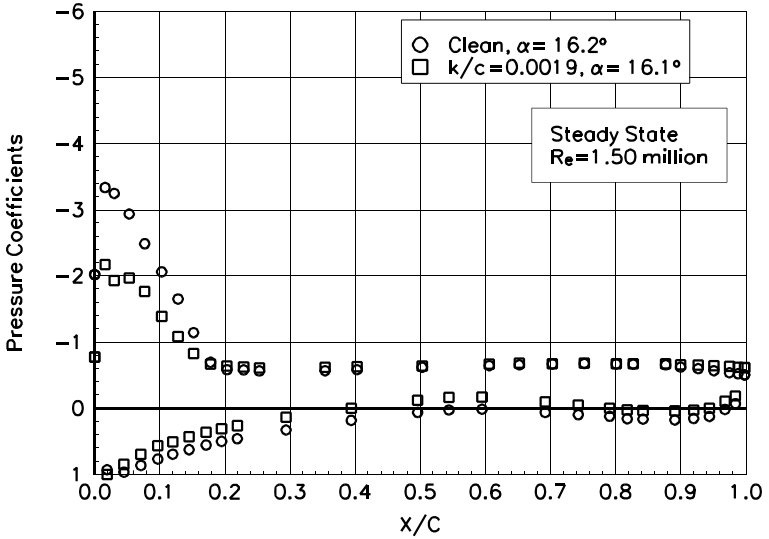

Figure B130. α = 16.2°

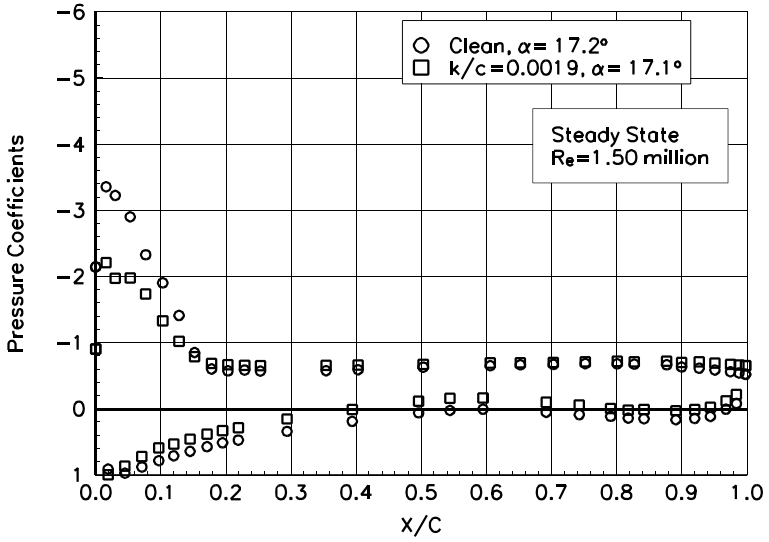

Figure B131. α = 17.2°

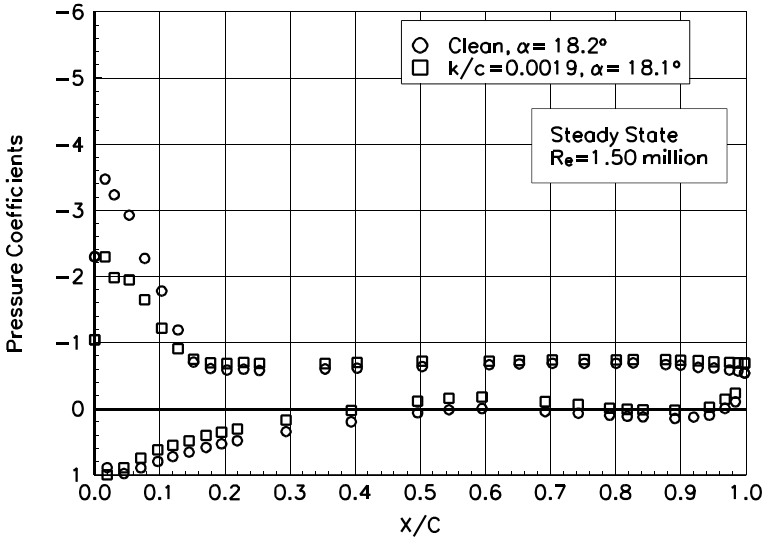

Figure B132. α = 18.2°

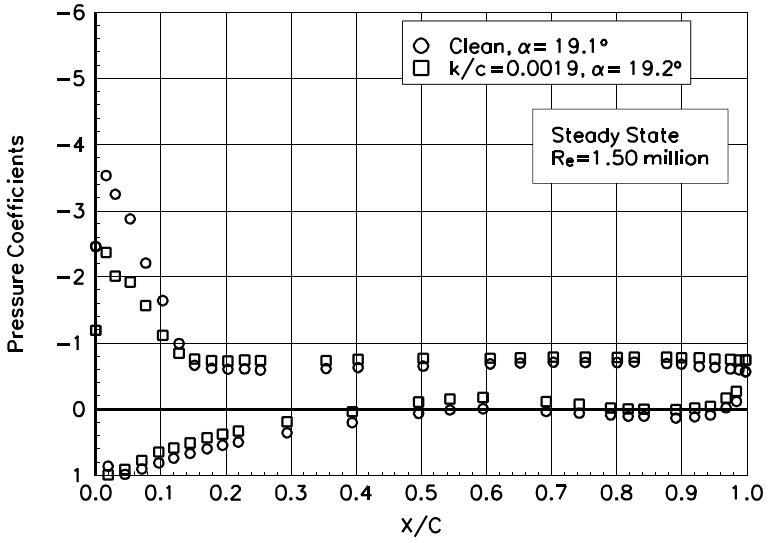

Figure B133. α = 19.1°

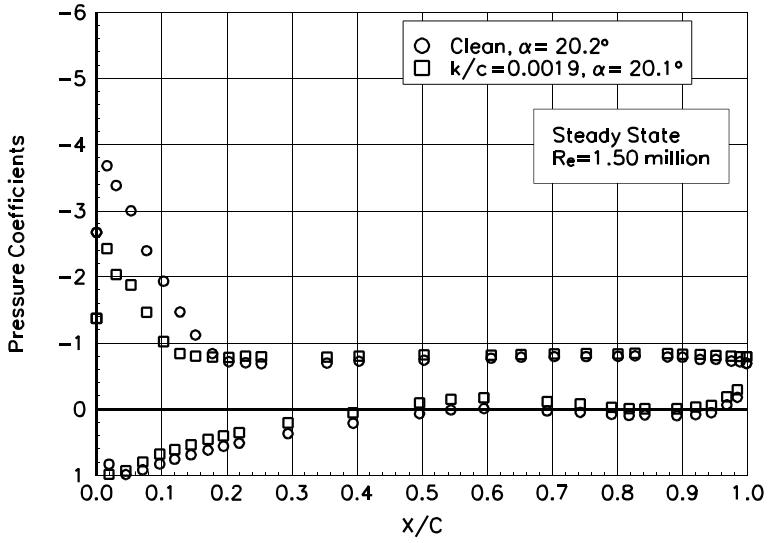

Figure B134. α = 20.2°

Appendix C: Unsteady Integrated Coefficients

List of Figures Page

Unsteady Airfoil Characteristics

±5.5° Sine, Re = 0.75 million

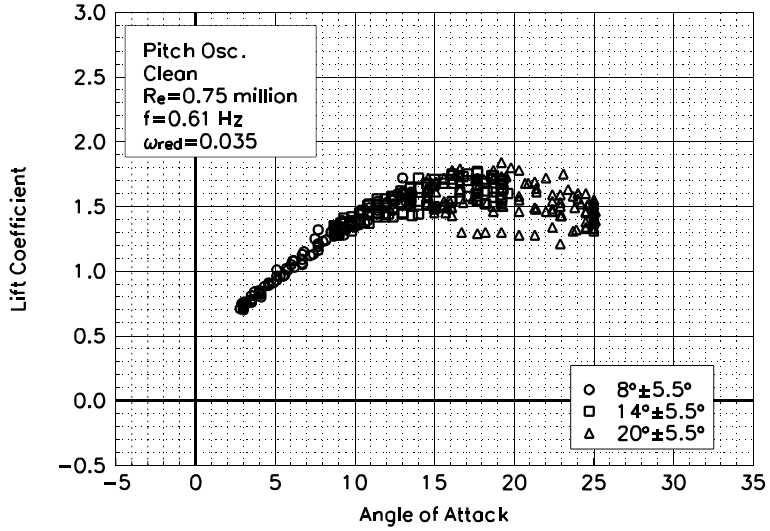

Figure C1. Lift coefficient vs α.

LS(1)-0417MOD
Clean
Re=0.75 million
$\omega_{reduced}$=0.035

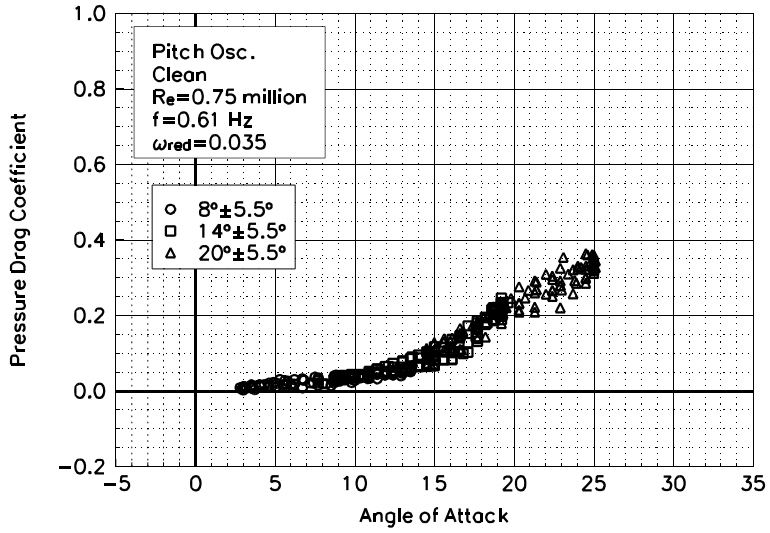

Figure C2. Pressure drag coefficient vs α.

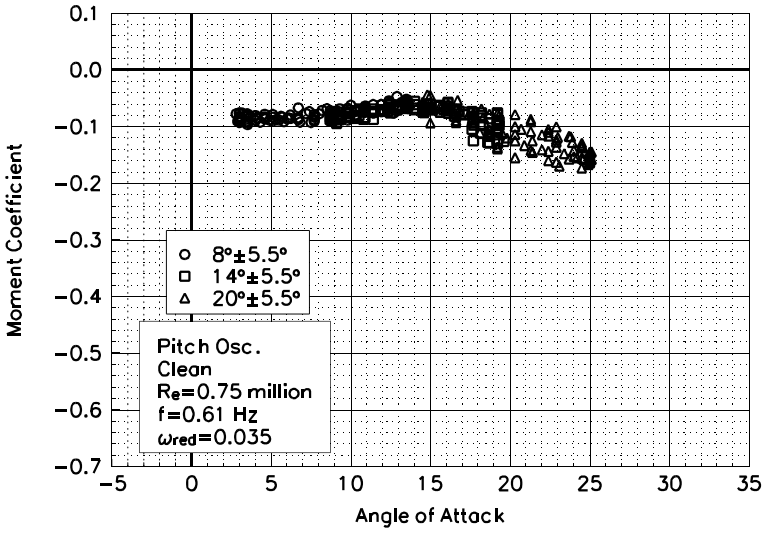

Figure C3. Moment coefficient vs α.

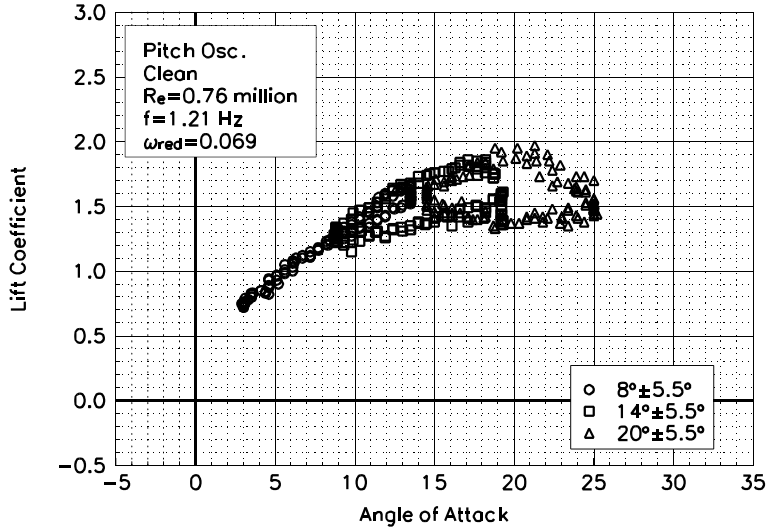

Figure C4. Lift coefficient vs α.

LS(1)-0417MOD
Clean
Re=0.76 million
$\omega_{reduced}$=0.069

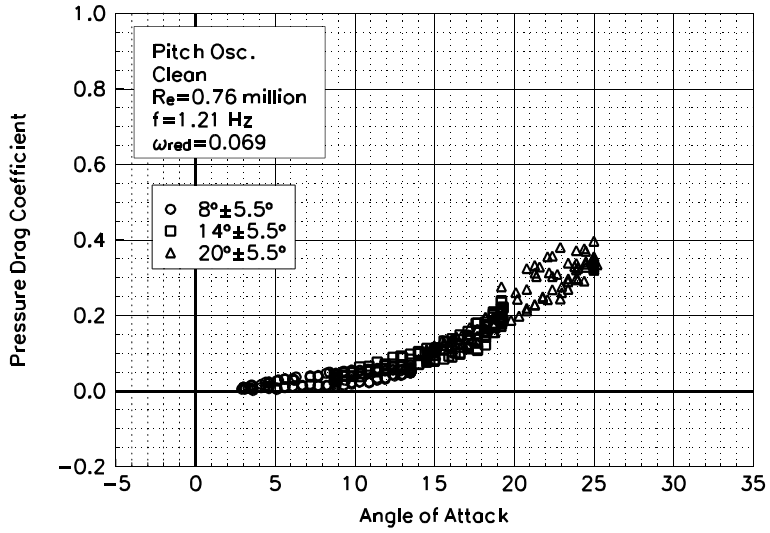

Figure C5. Pressure drag coefficient vs α.

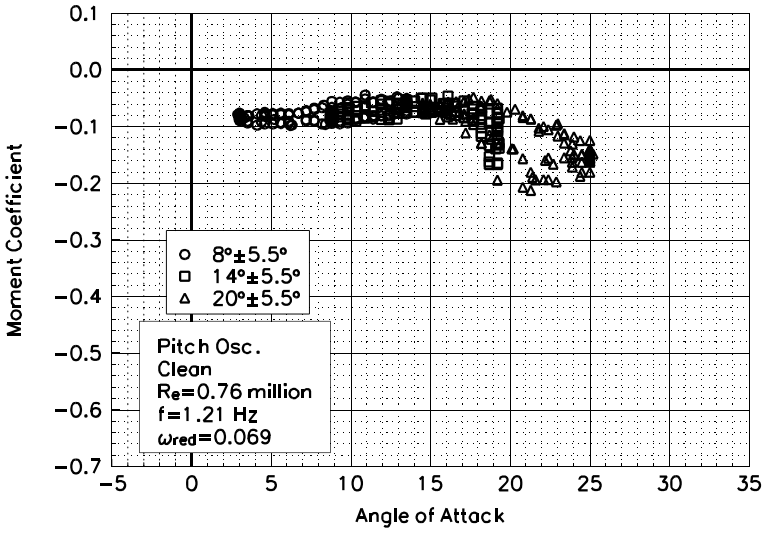

Figure C6. Moment coefficient vs α.

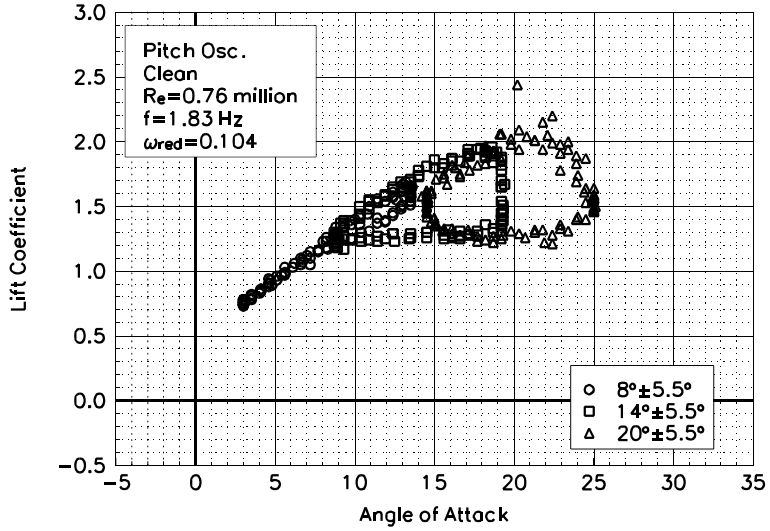

Figure C7. Lift coefficient vs α.

LS(1)-0417MOD
Clean
Re=0.76 million
$\omega_{reduced}$=0.104

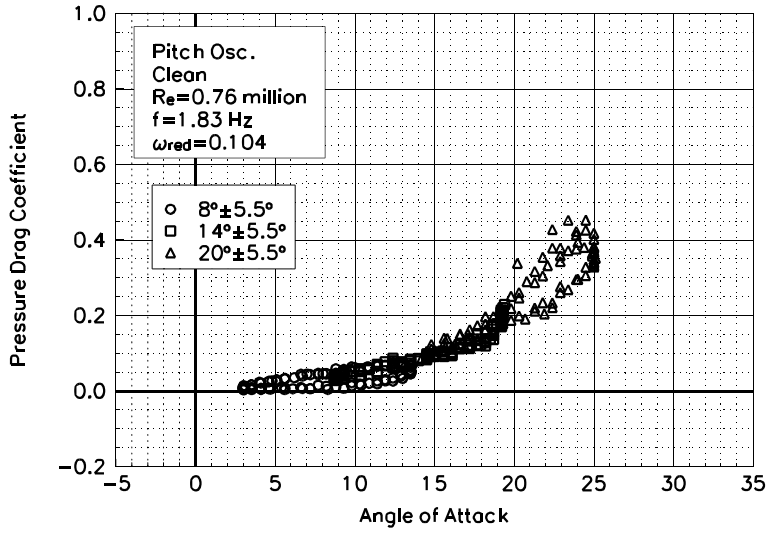

Figure C8. Pressure drag coefficient vs α.

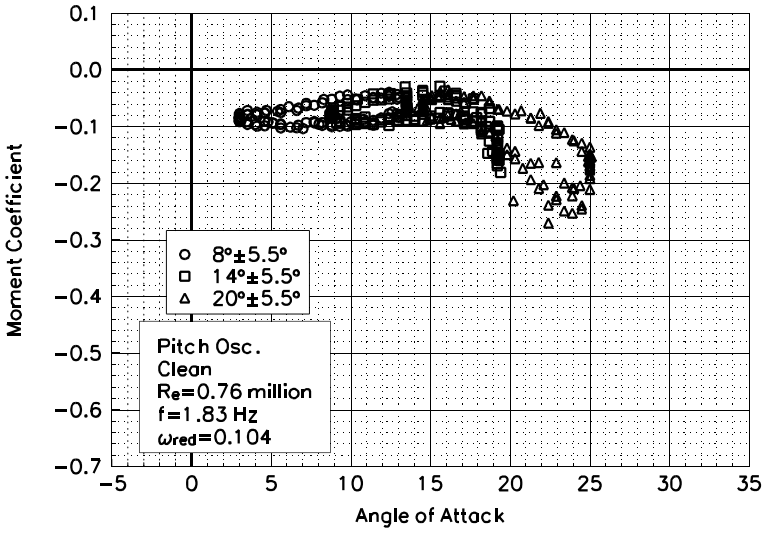

Figure C9. Moment coefficient vs α.

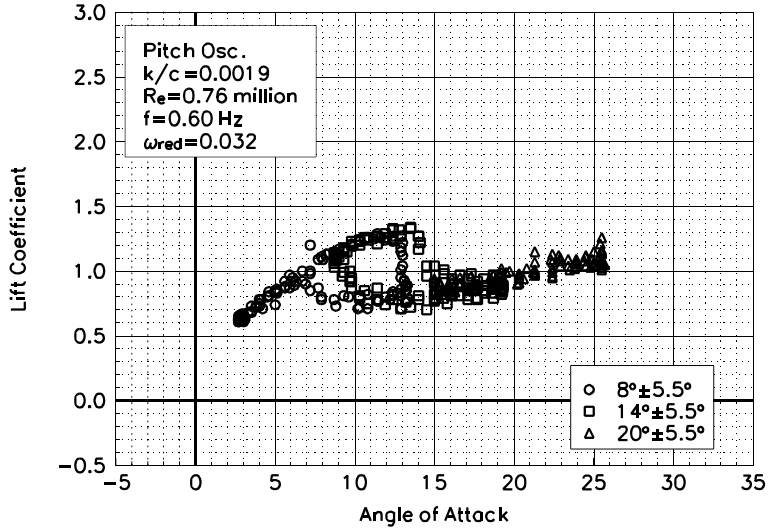

Figure C10. Lift coefficient vs α.

LS(1)-0417MOD
LEGR
Re=0.76 million
$\omega_{reduced}$=0.032

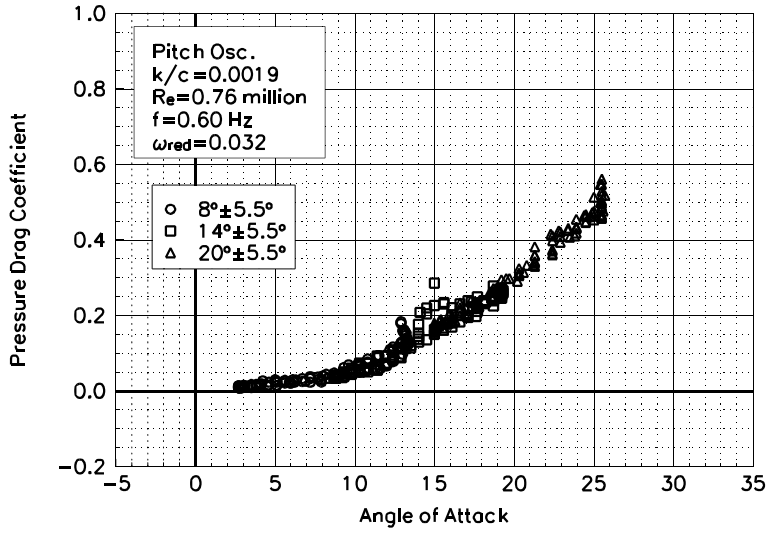

Figure C11. Pressure drag coefficient vs α.

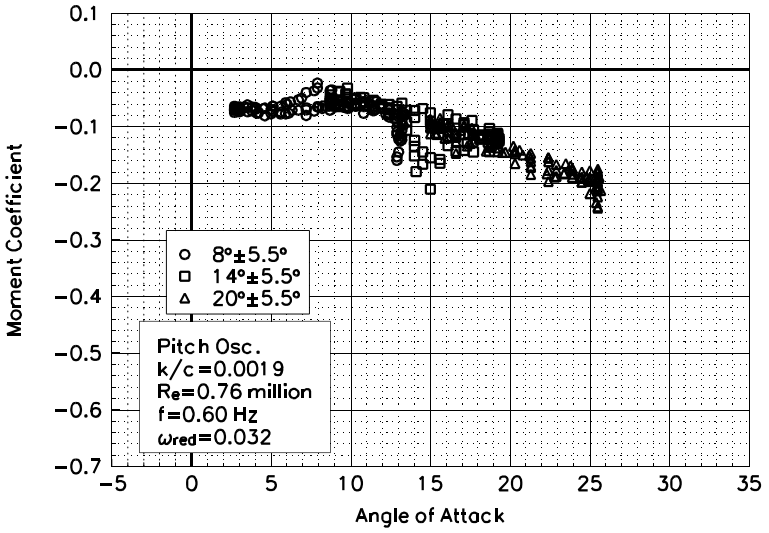

Figure C12. Moment coefficient vs α.

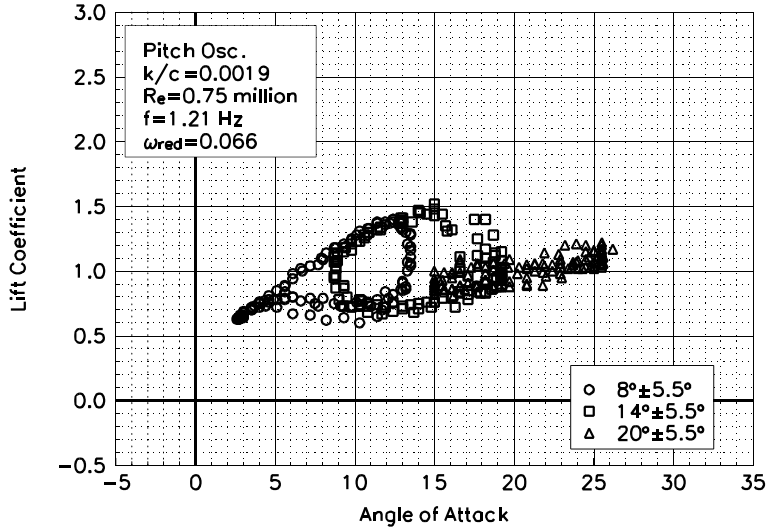

Figure C13. Lift coefficient vs α.

LS(1)-0417MOD
LEGR
Re=0.75 million
$\omega_{reduced}$=0.066

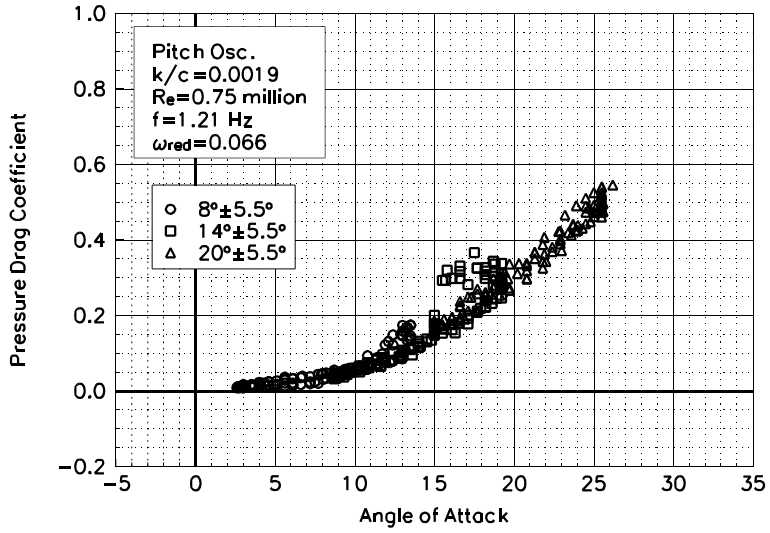

Figure C14. Pressure drag coefficient vs α.

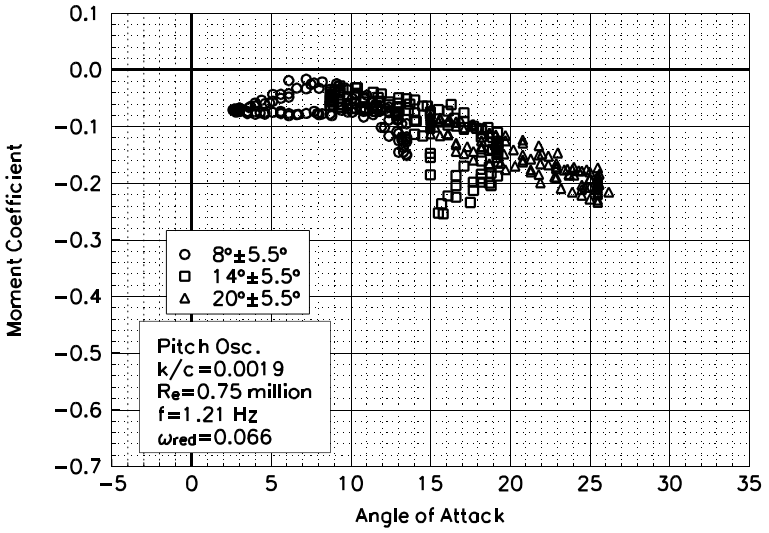

Figure C15. Moment coefficient vs α.

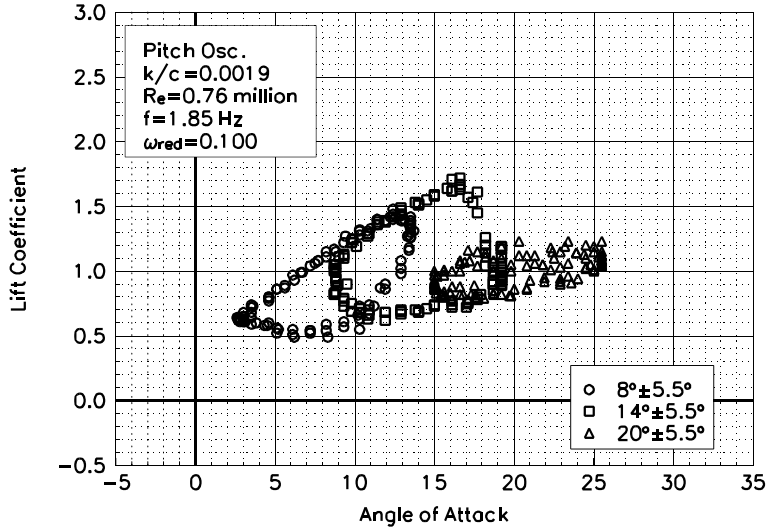

Figure C16. Lift coefficient vs α.

LS(1)-0417MOD
LEGR
Re=0.76 million
$\omega_{reduced}$=0.100

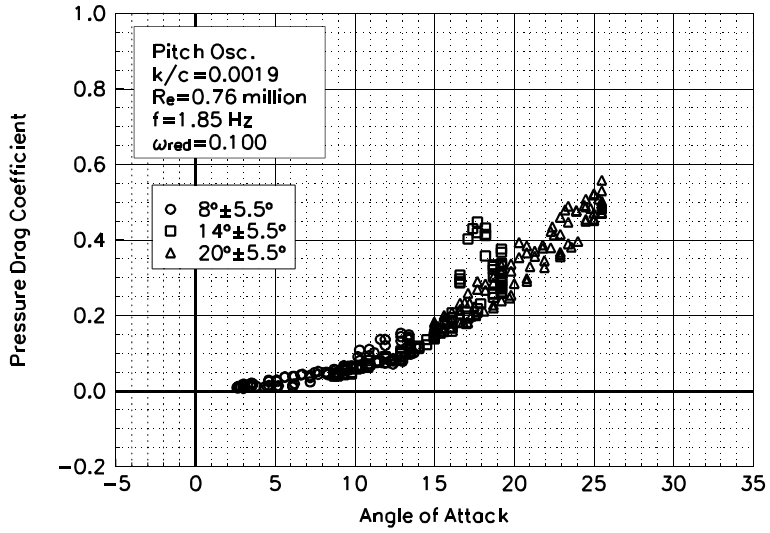

Figure C17. Pressure drag coefficient vs α.

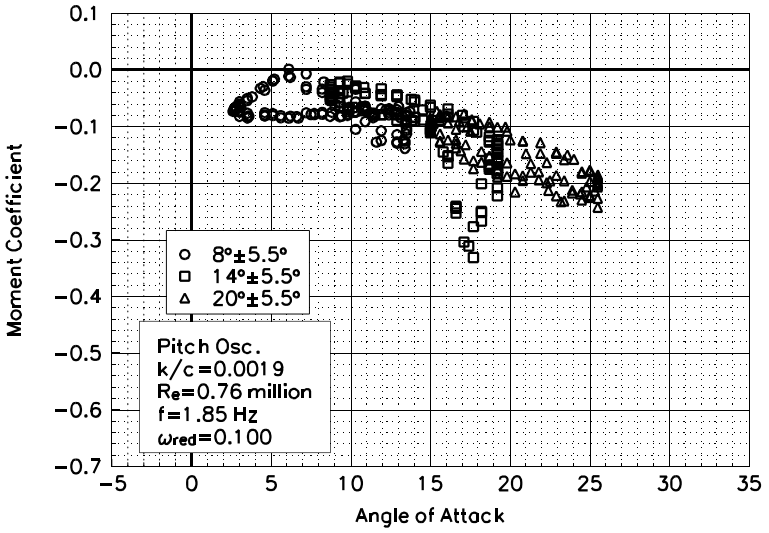

Figure C18. Moment coefficient vs α.

Unsteady Airfoil Characteristics

±5.5° Sine, Re = 1 million

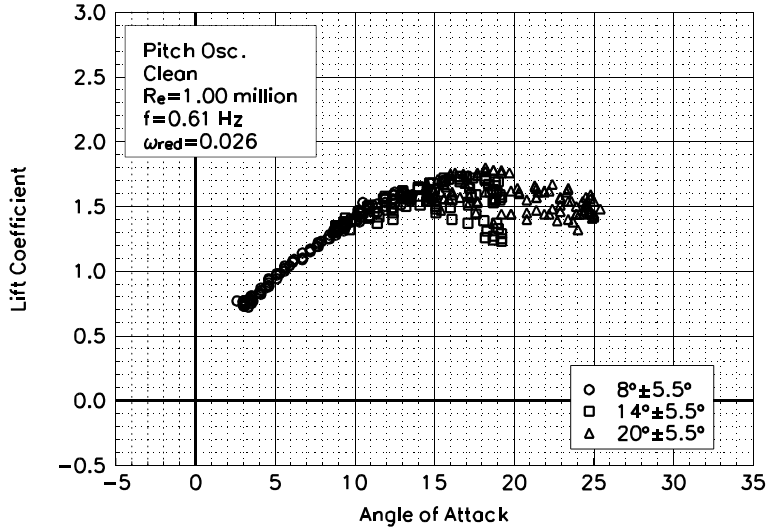

Figure C19. Lift coefficient vs α.

LS(1)-0417MOD
Clean
Re=1.00 million
$\omega_{reduced}$=0.026

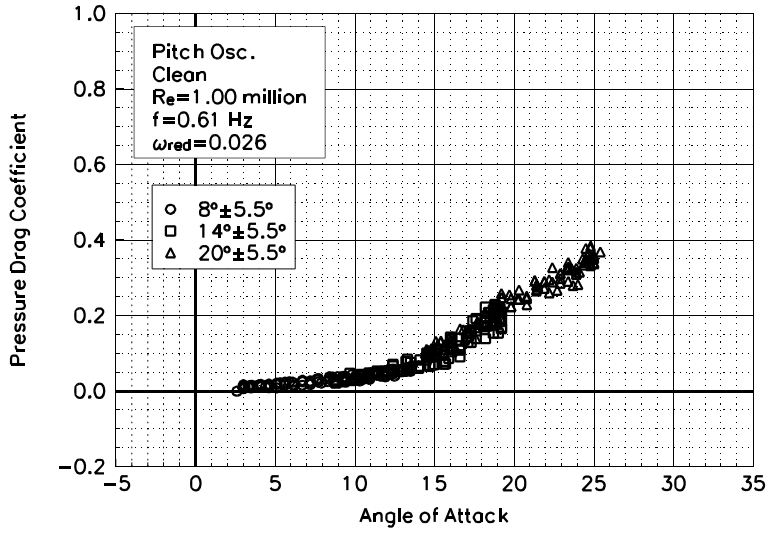

Figure C20. Pressure drag coefficient vs α.

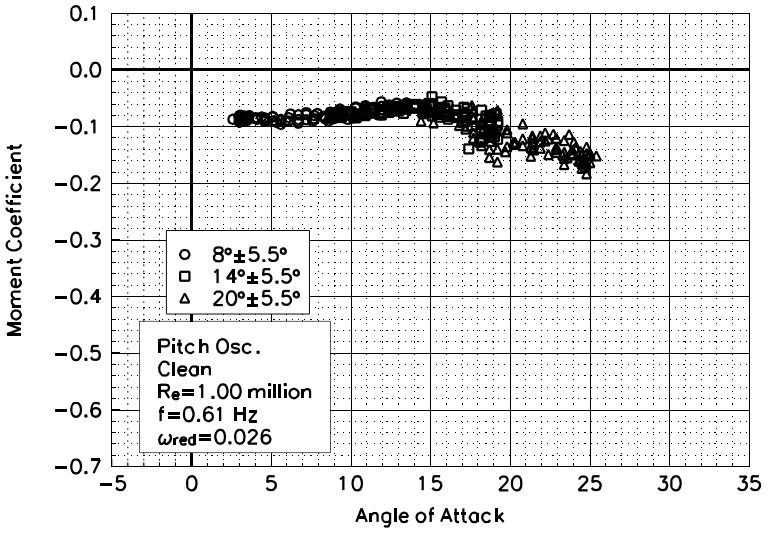

Figure C21. Moment coefficient vs α.

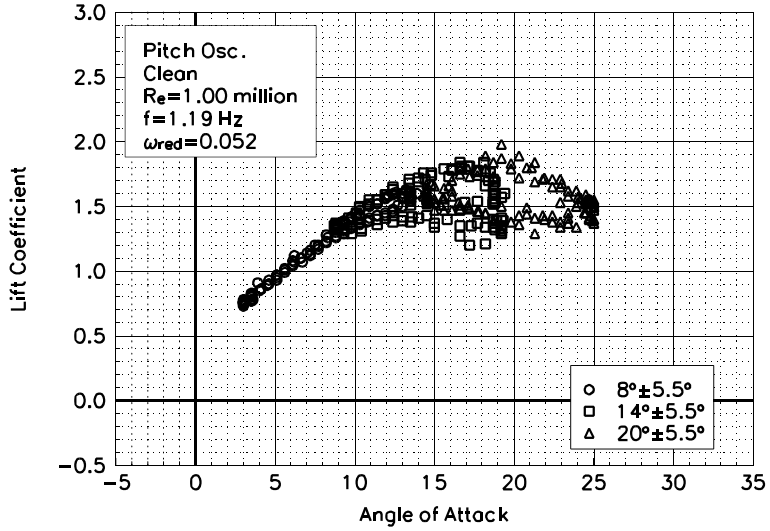

Figure C22. Lift coefficient vs α.

LS(1)-0417MOD
Clean
Re=1.00 million
$\omega_{reduced}$=0.052

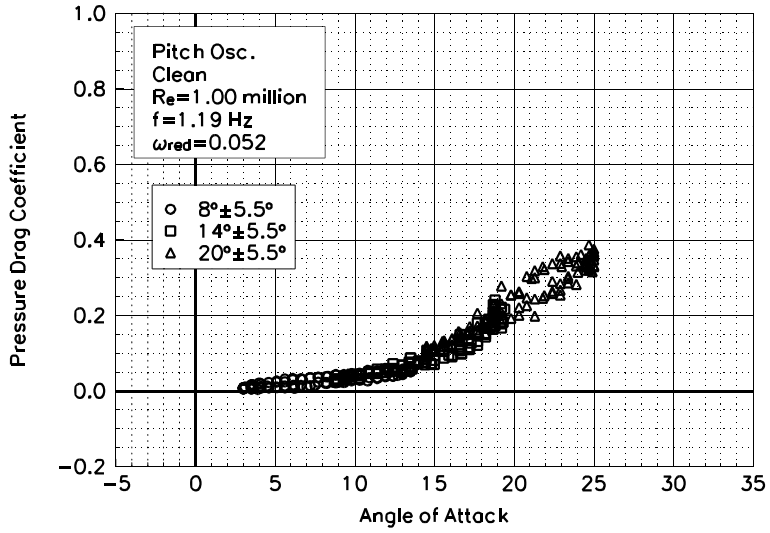

Figure C23. Pressure drag coefficient vs α.

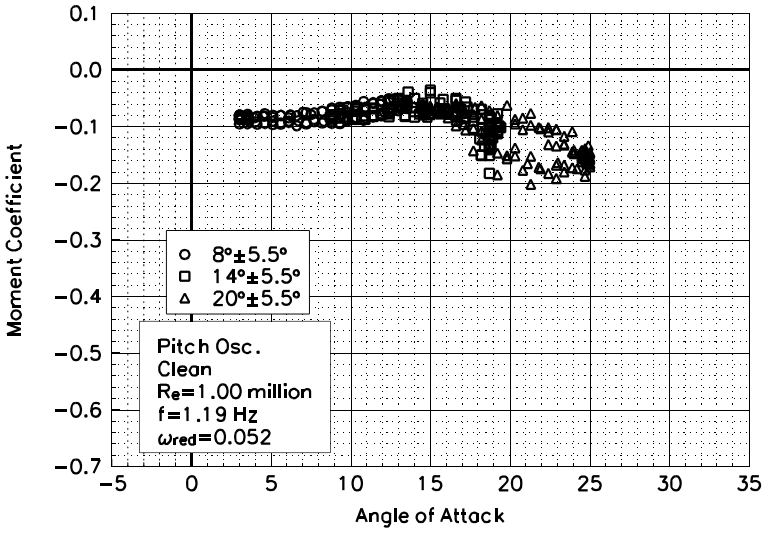

Figure C24. Moment coefficient vs α.

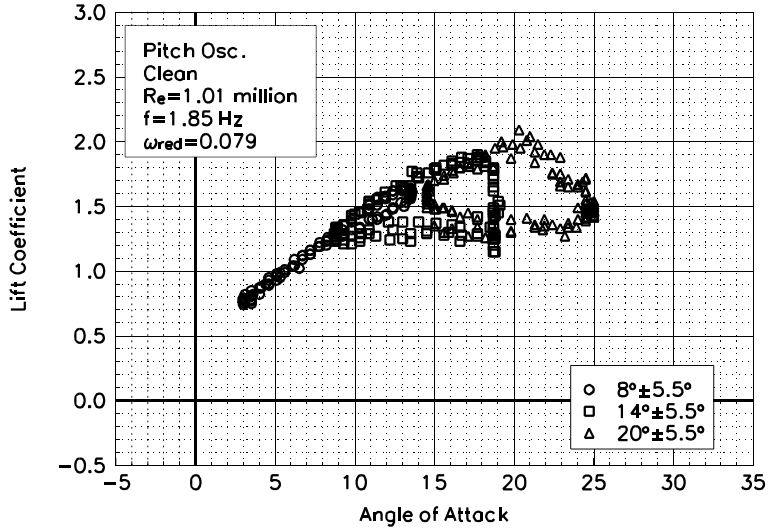

Figure C25. Lift coefficient vs α.

LS(1)-0417MOD
Clean
Re=1.01 million
$\omega_{reduced}$=0.079

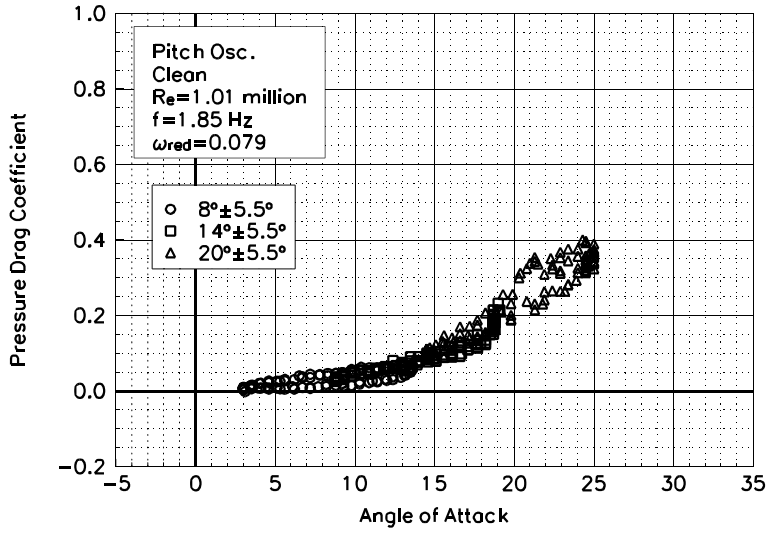

Figure C26. Pressure drag coefficient vs α.

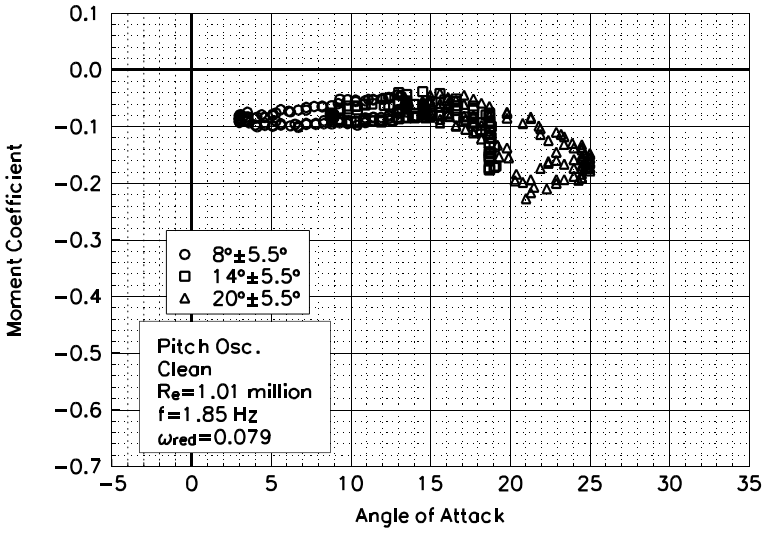

Figure C27. Moment coefficient vs α.

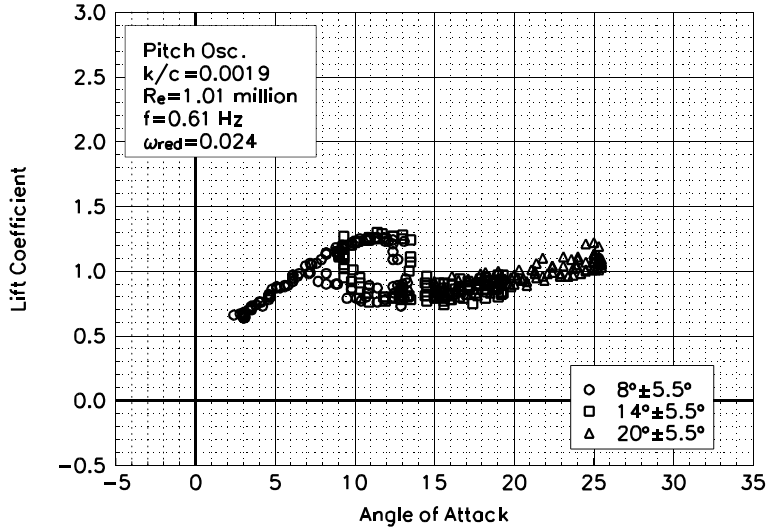

Figure C28. Lift coefficient vs α.

LS(1)-0417MOD
LEGR
Re=1.01 million
$\omega_{reduced}$=0.024

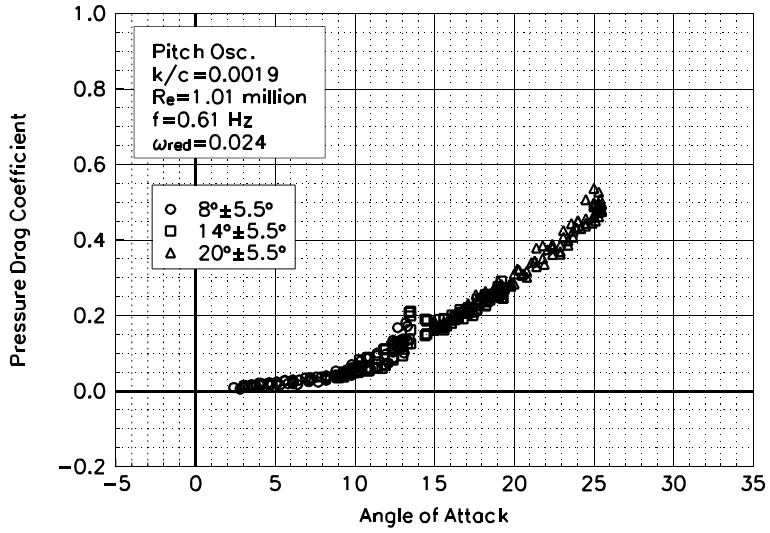

Figure C29. Pressure drag coefficient vs α.

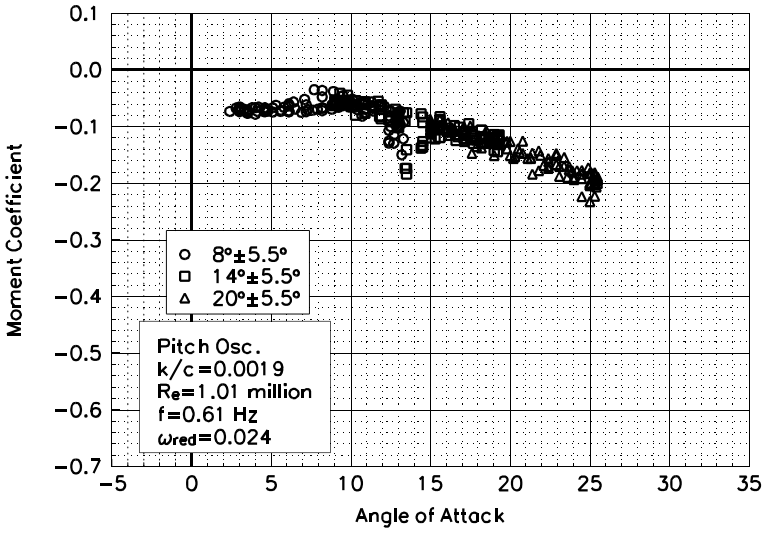

Figure C30. Moment coefficient vs α.

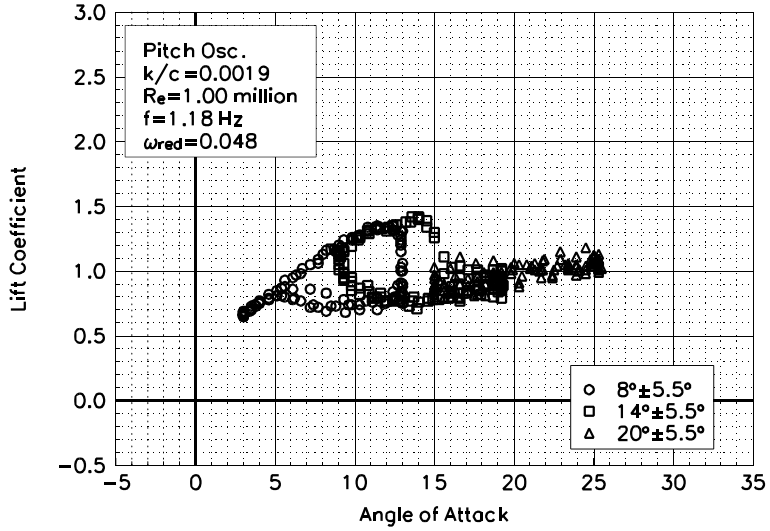

Figure C31. Lift coefficient vs α.

LS(1)-0417MOD
LEGR
Re=1.00 million
$\omega_{reduced}$=0.048

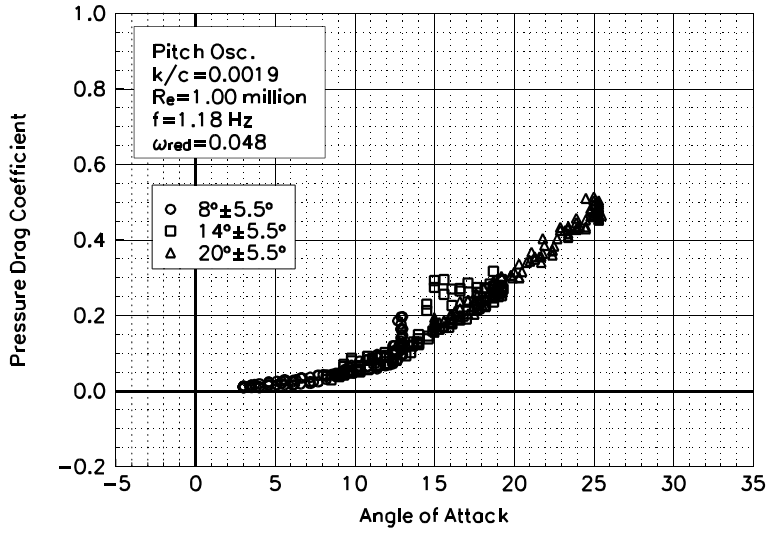

Figure C32. Pressure drag coefficient vs α.

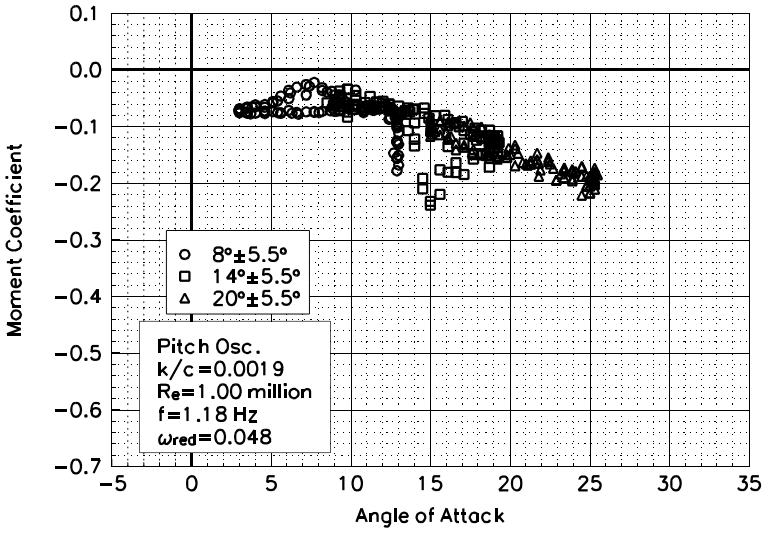

Figure C33. Moment coefficient vs α.

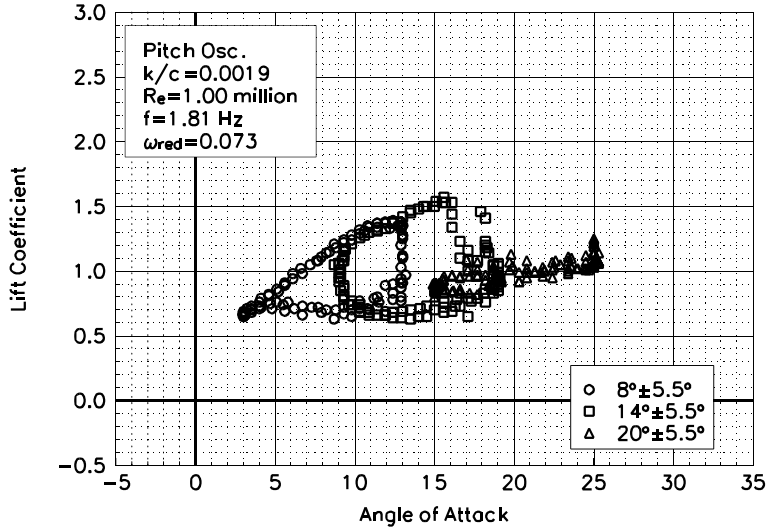

Figure C34. Lift coefficient vs α.

LS(1)-0417MOD
LEGR
Re=1.00 million
$\omega_{reduced}$=0.073

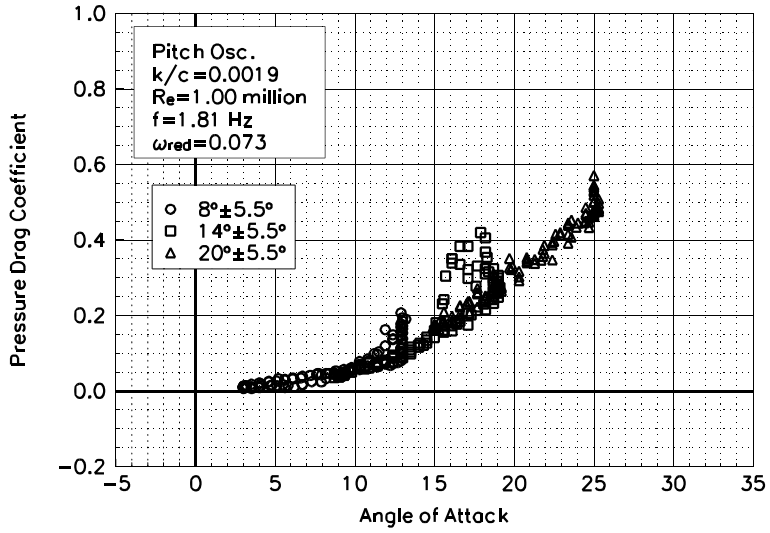

Figure C35. Pressure drag coefficient vs α.

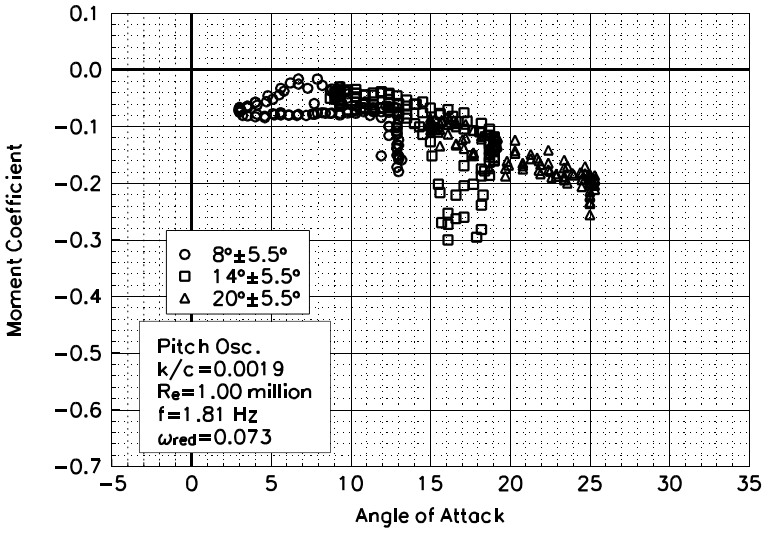

Figure C36. Moment coefficient vs α.

Unsteady Airfoil Characteristics

±5.5° Sine, Re= 1.25 million

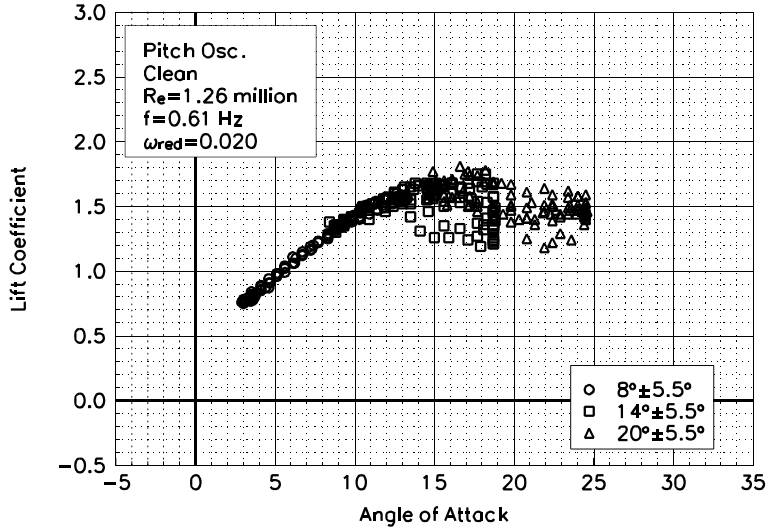

Figure C37. Lift coefficient vs α.

LS(1)-0417MOD
Clean
Re=1.26 million
$\omega_{reduced}$=0.020

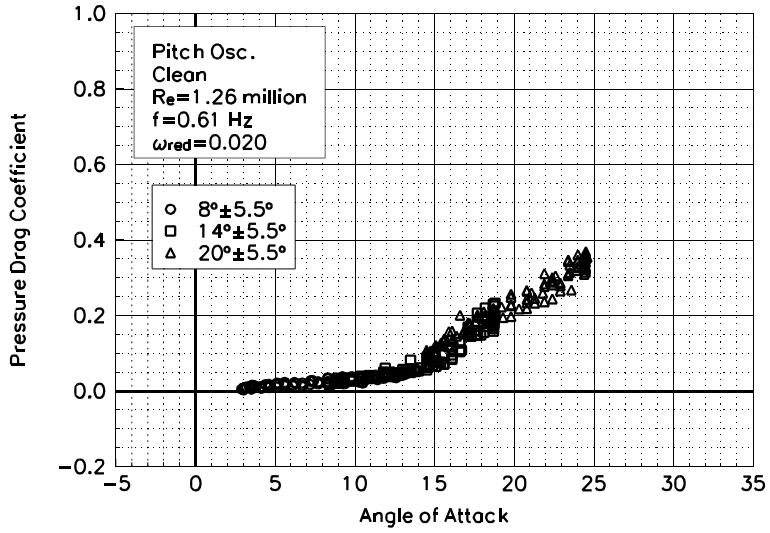

Figure C38. Pressure drag coefficient vs α.

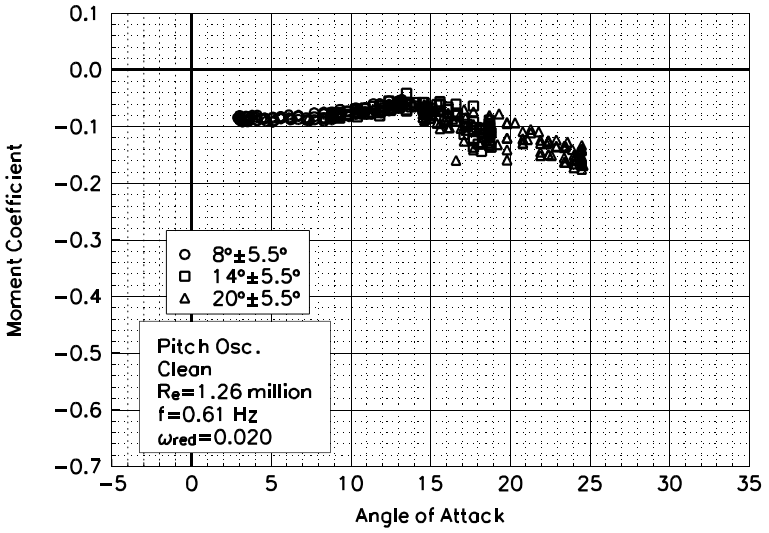

Figure C39. Moment coefficient vs α.

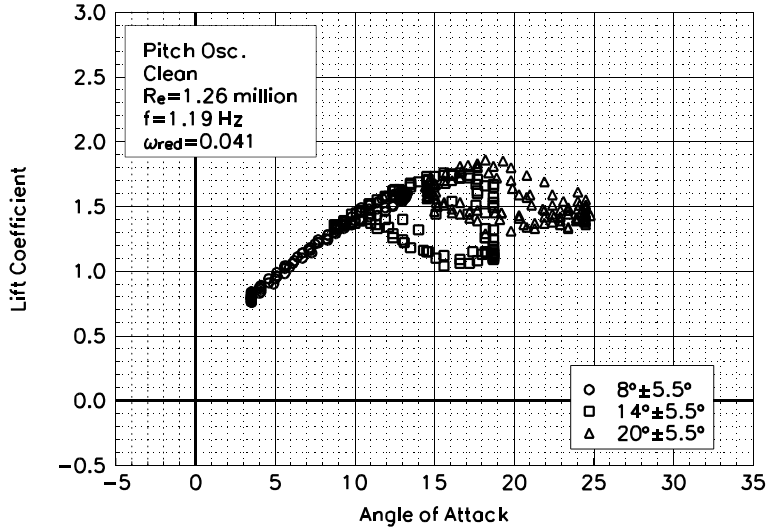

Figure C40. Lift coefficient vs α.

LS(1)-0417MOD
Clean
Re=1.26 million
$\omega_{reduced}$=0.041

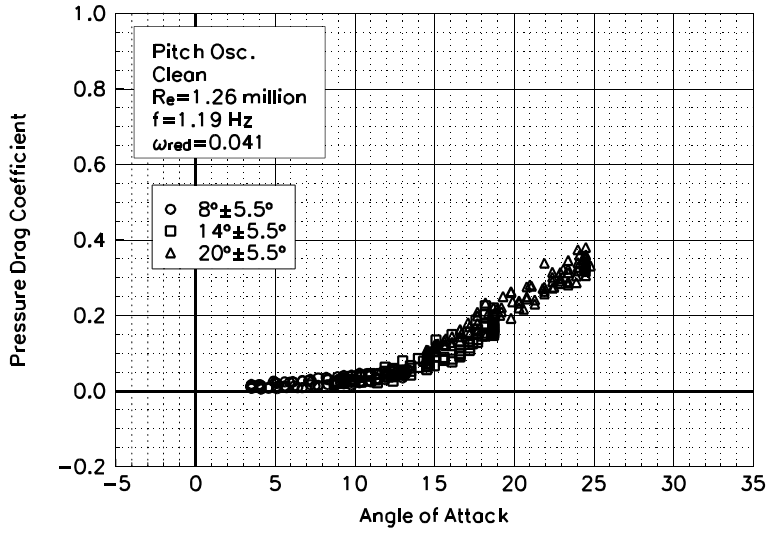

Figure C41. Pressure drag coefficient vs α.

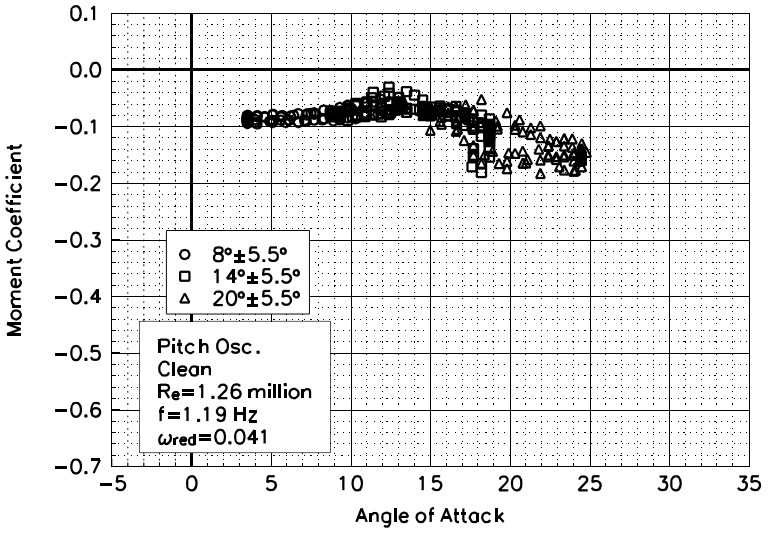

Figure C42. Moment coefficient vs α.

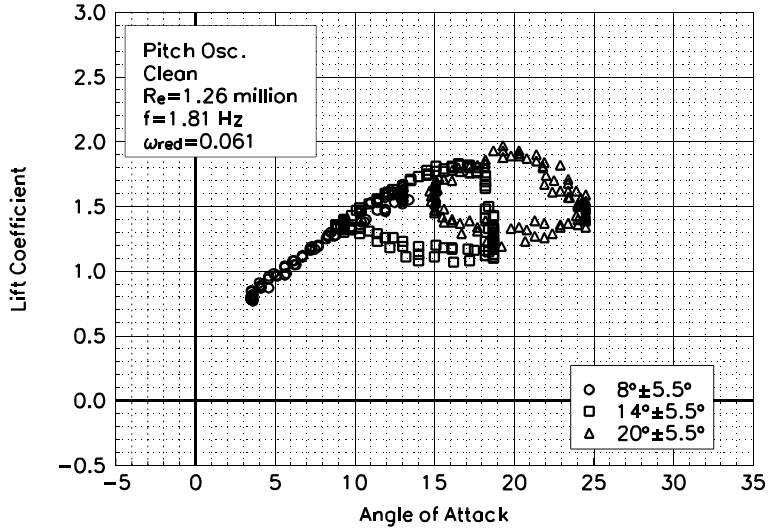

Figure C43. Lift coefficient vs α.

LS(1)-0417MOD
Clean
Re=1.26 million
$\omega_{reduced}$=0.061

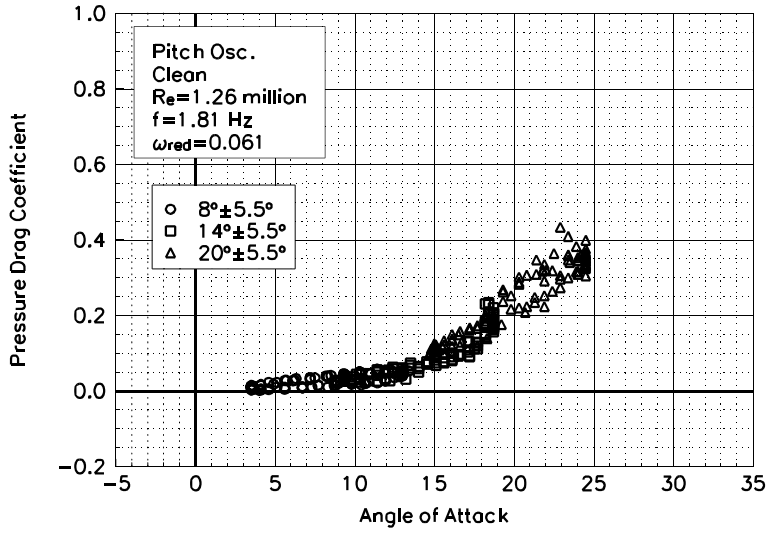

Figure C44. Pressure drag coefficient vs α.

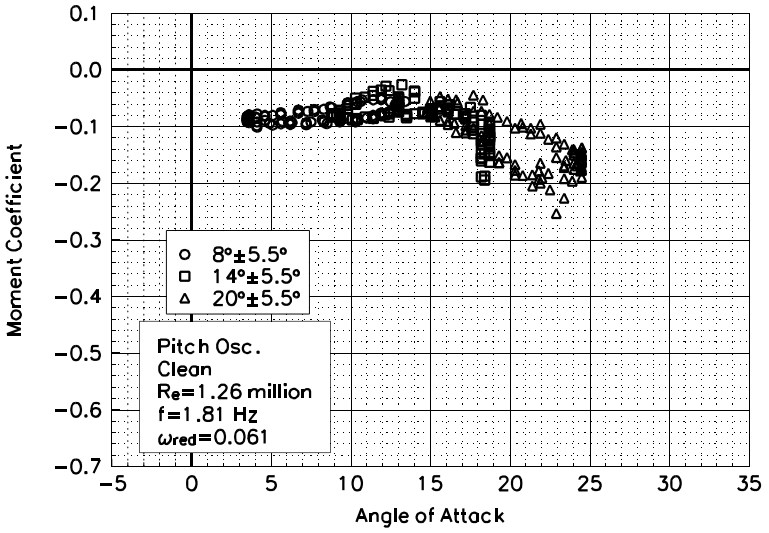

Figure C45. Moment coefficient vs α.

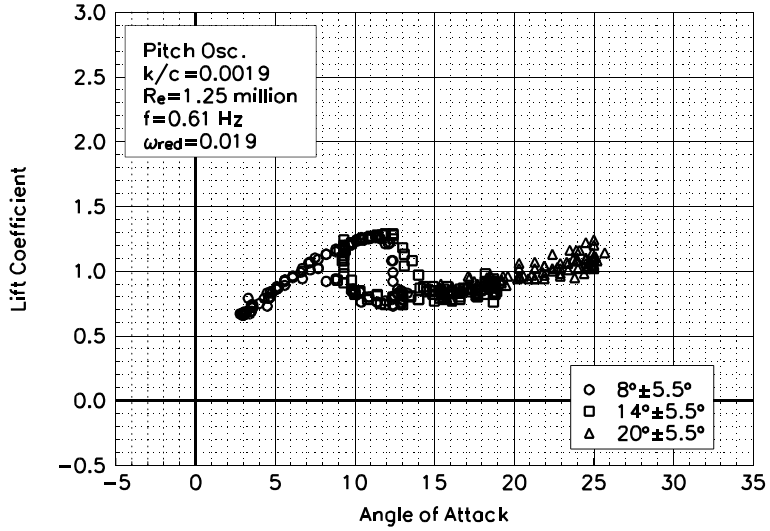

Figure C46. Lift coefficient vs α.

LS(1)-0417MOD
LEGR
Re=1.25 million
$\omega_{reduced}$=0.019

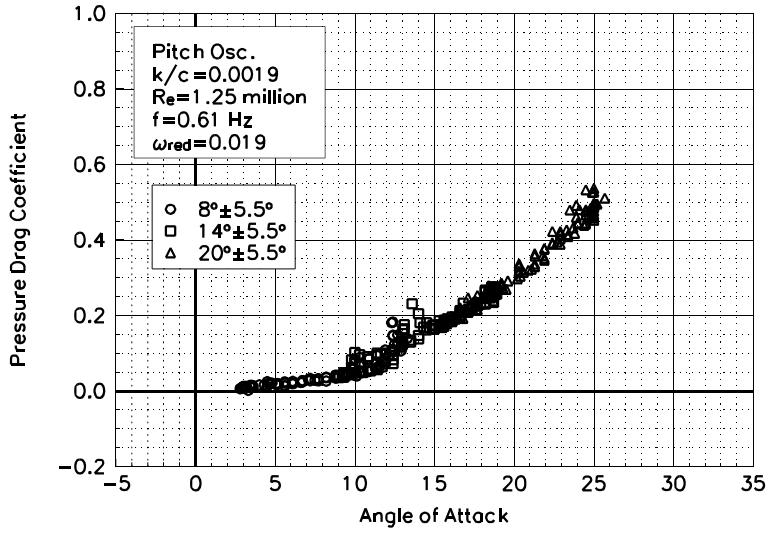

Figure C47. Pressure drag coefficient vs α.

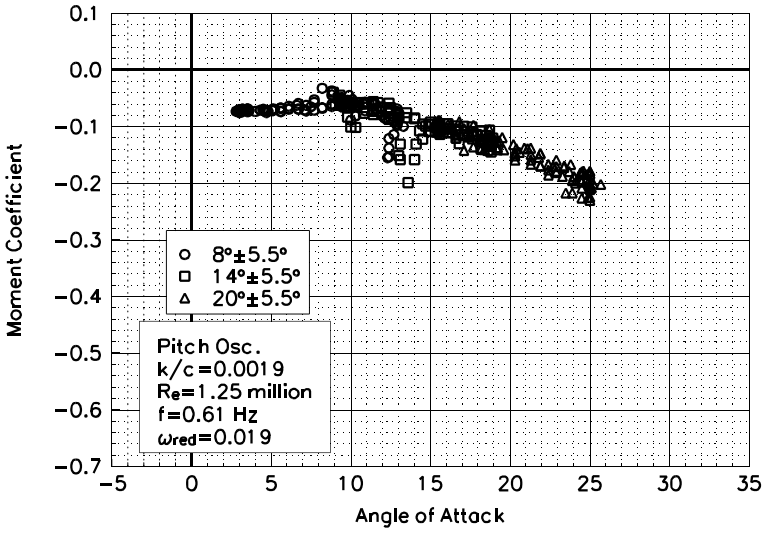

Figure C48. Moment coefficient vs α.

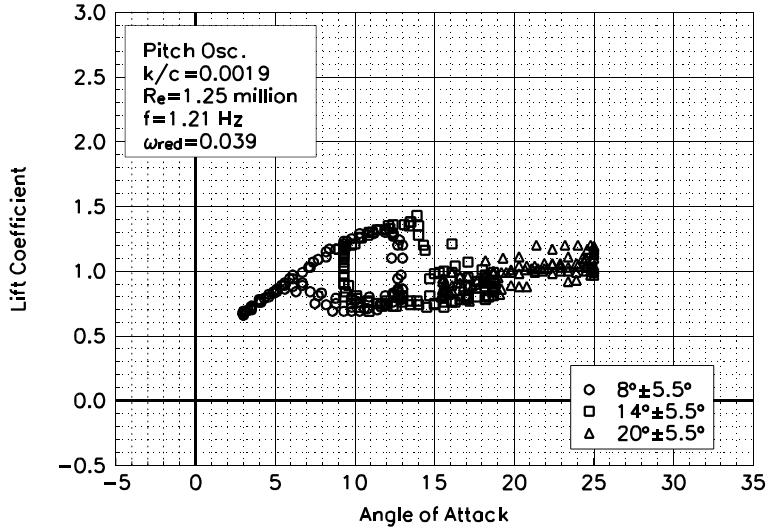

Figure C49. Lift coefficient vs α.

LS(1)-0417MOD
LEGR
Re=1.25 million
$\omega_{reduced}$=0.039

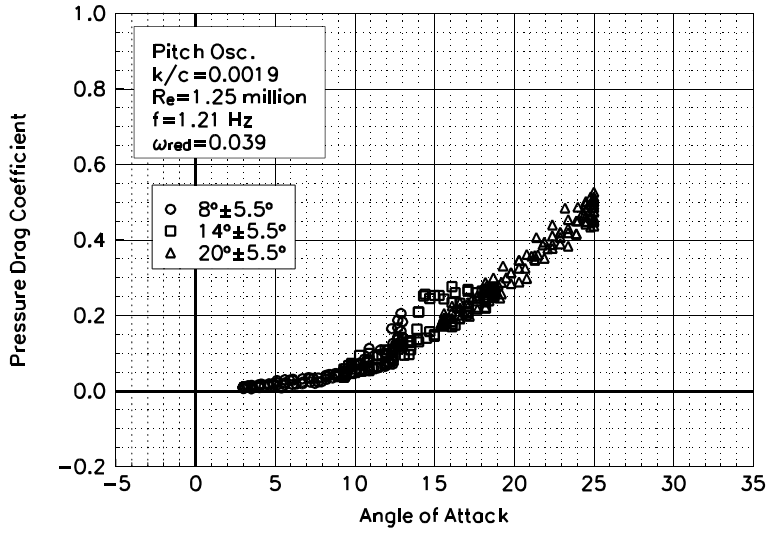

Figure C50. Pressure drag coefficient vs α.

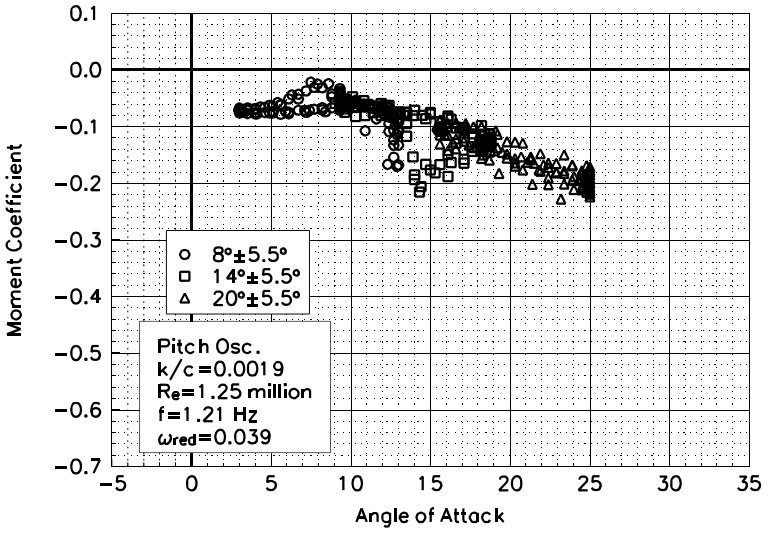

Figure C51. Moment coefficient vs α.

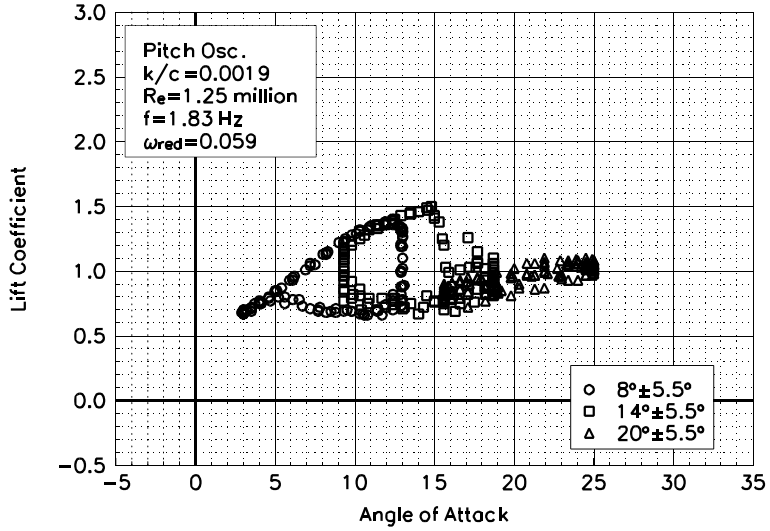

Figure C52. Lift coefficient vs α.

LS(1)-0417MOD
LEGR
Re=1.25 million
$\omega_{reduced}$=0.059

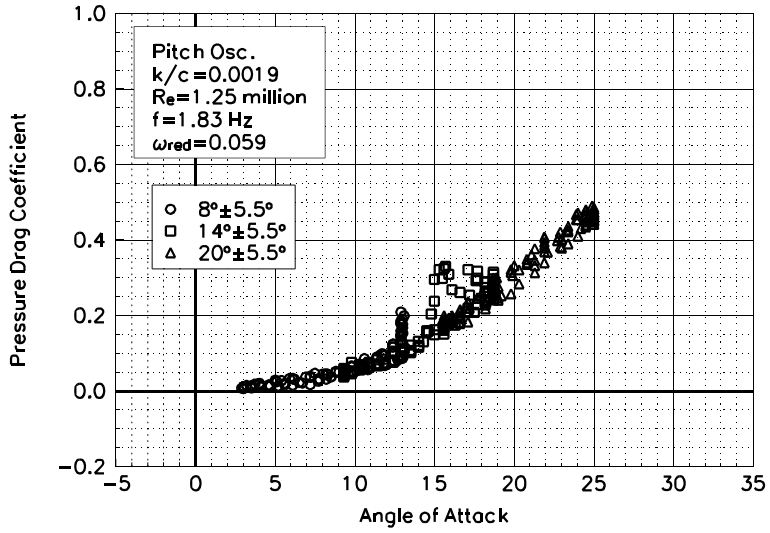

Figure C53. Pressure drag coefficient vs α.

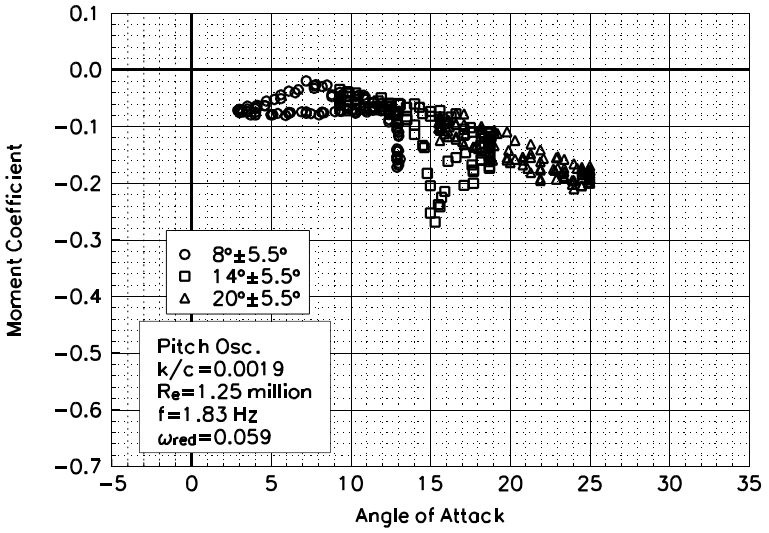

Figure C54. Moment coefficient vs α.

Unsteady Airfoil Characteristics

±5.5° Sine, Re = 1.5 million

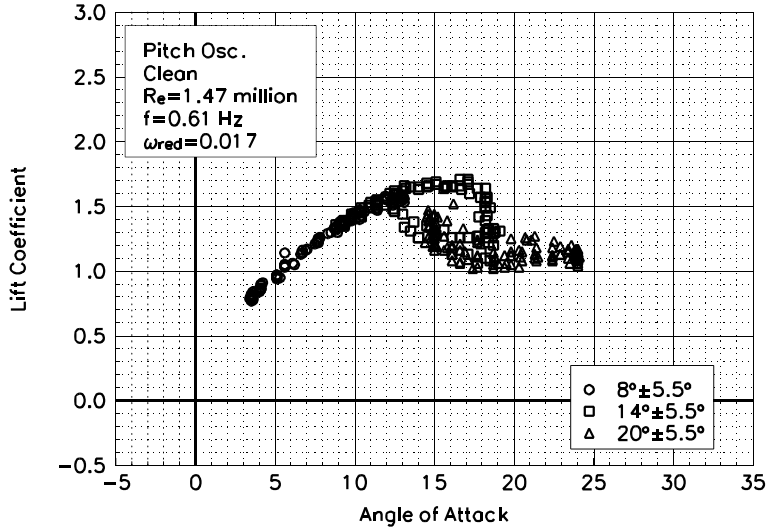

Figure C55. Lift coefficient vs α.

LS(1)-0417MOD
Clean
Re=1.47 million
$\omega_{reduced}$=0.017

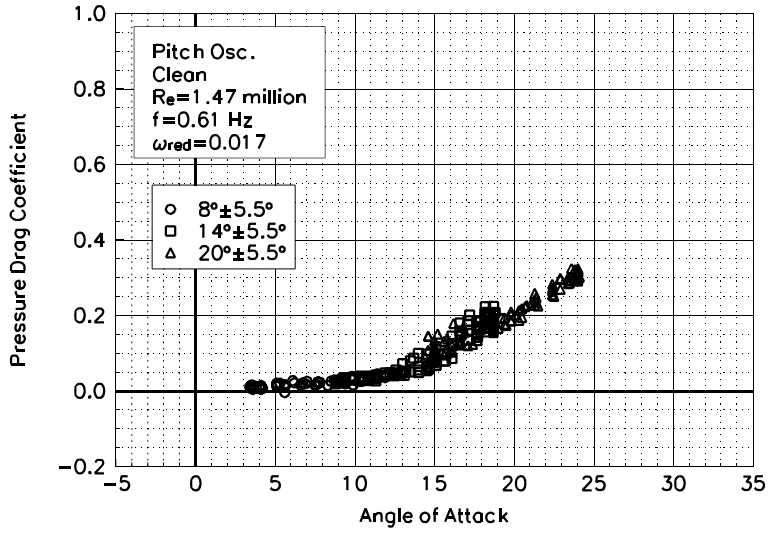

Figure C56. Pressure drag coefficient vs α.

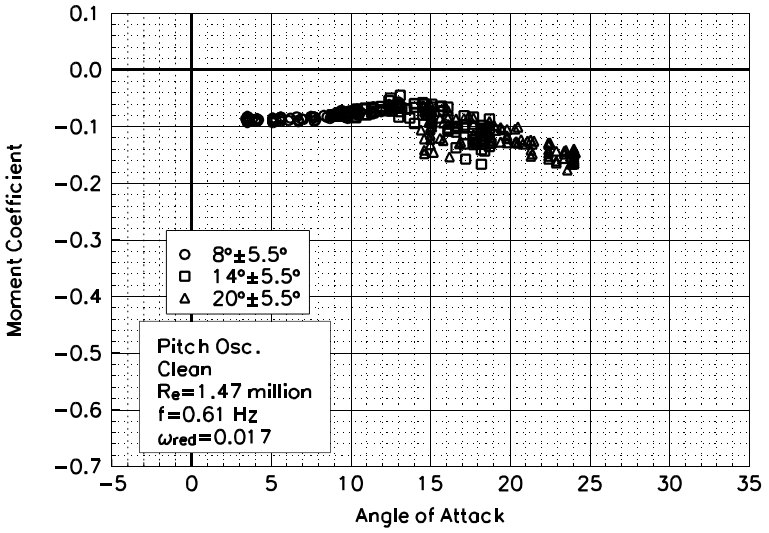

Figure C57. Moment coefficient vs α.

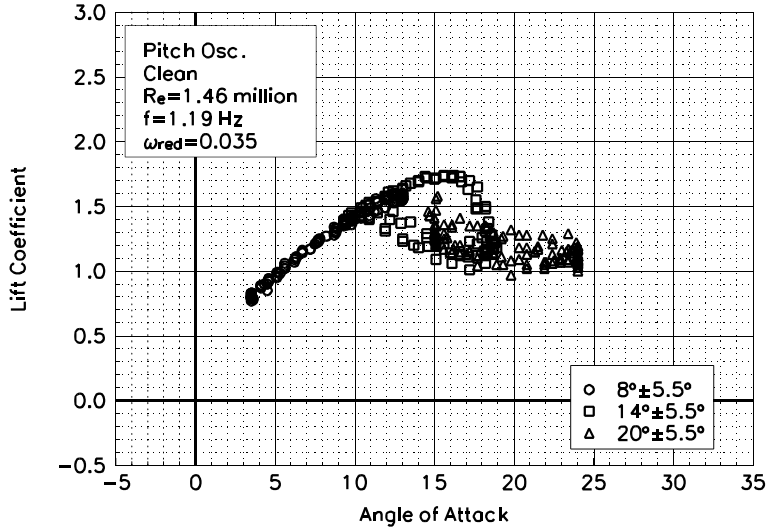

Figure C58. Lift coefficient vs α.

LS(1)-0417MOD
Clean
Re=1.46 million
$\omega_{reduced}$=0.035

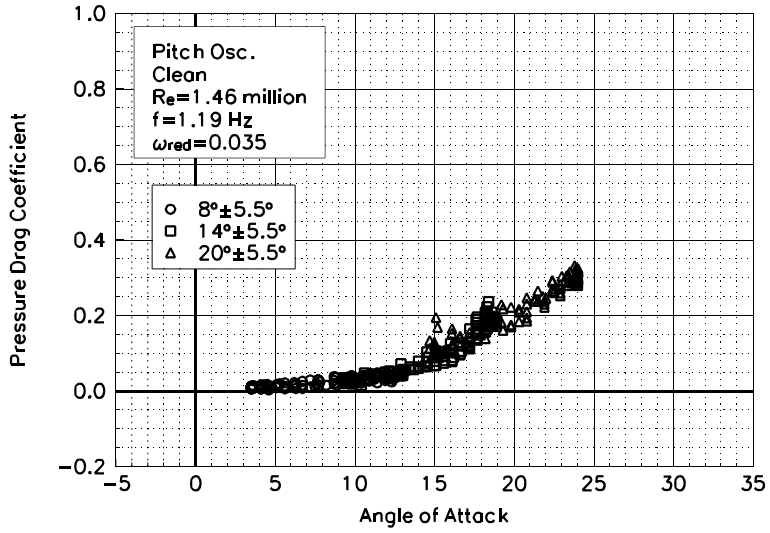

Figure C59. Pressure drag coefficient vs α.

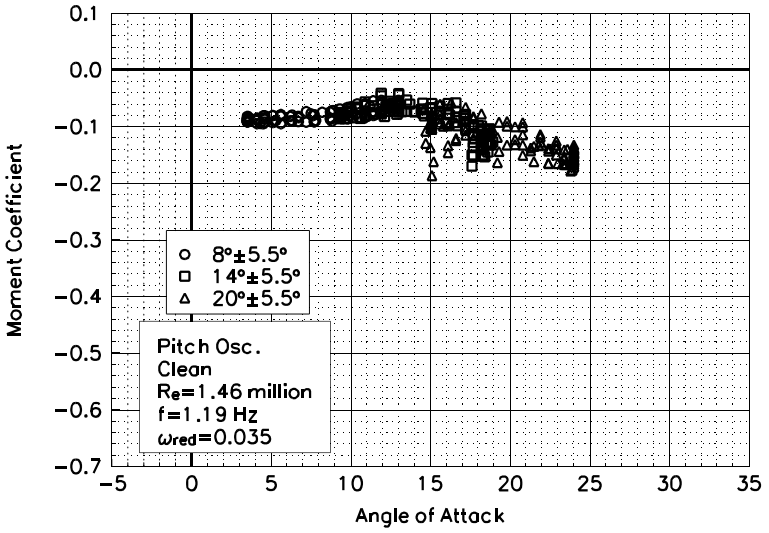

Figure C60. Moment coefficient vs α.

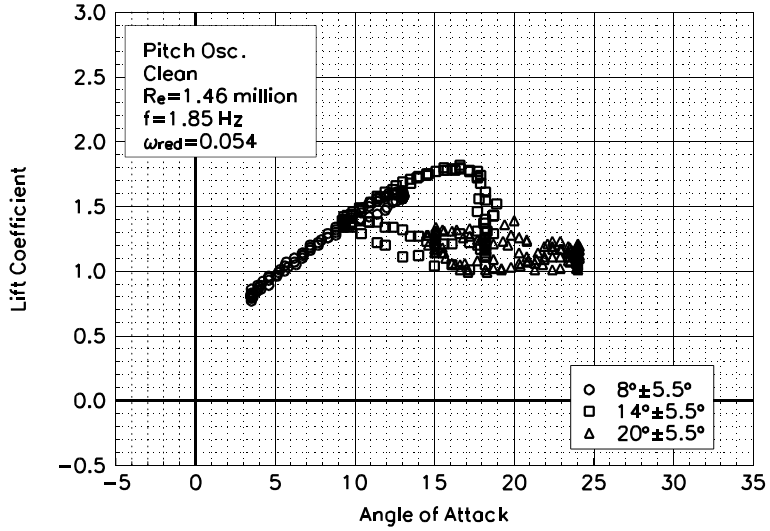

Figure C61. Lift coefficient vs α.

LS(1)-0417MOD
Clean
Re=1.46 million
$\omega_{reduced}$=0.054

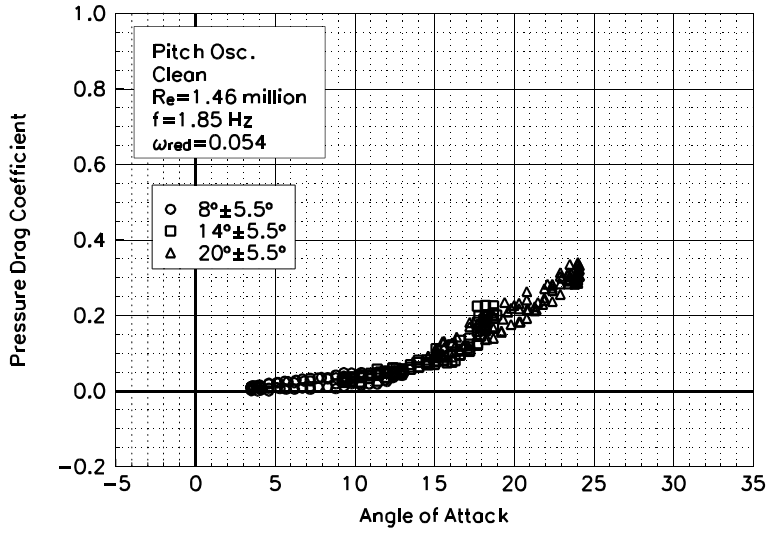

Figure C62. Pressure drag coefficient vs α.

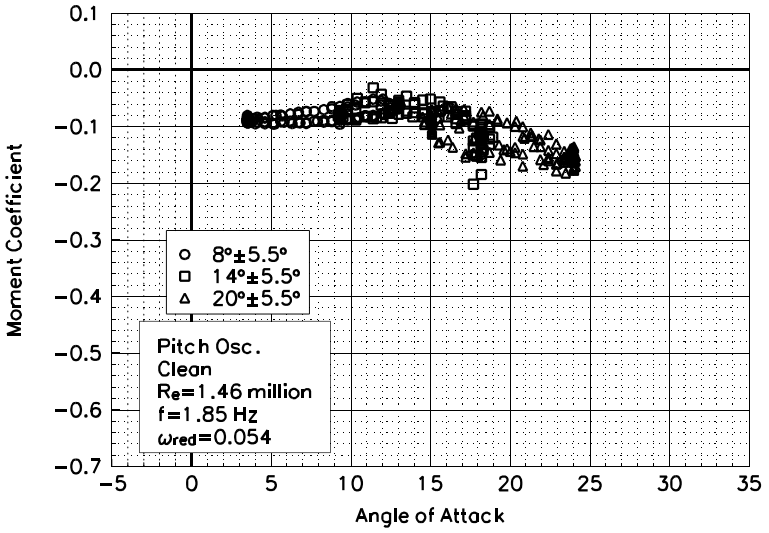

Figure C63. Moment coefficient vs α.

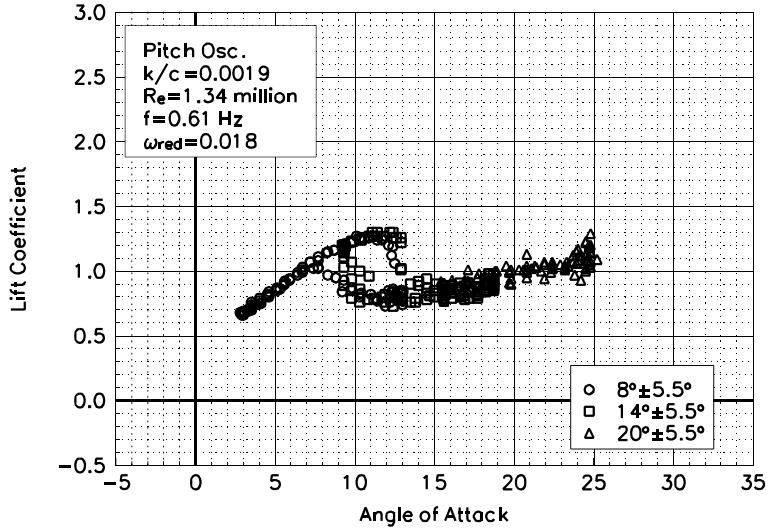

Figure C64. Lift coefficient vs α.

LS(1)-0417MOD
LEGR
Re=1.34 million
$\omega_{reduced}$=0.018

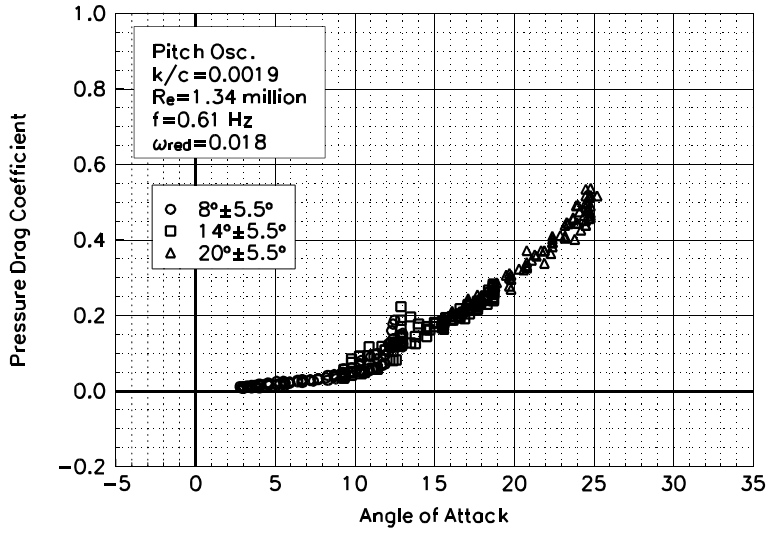

Figure C65. Pressure drag coefficient vs α.

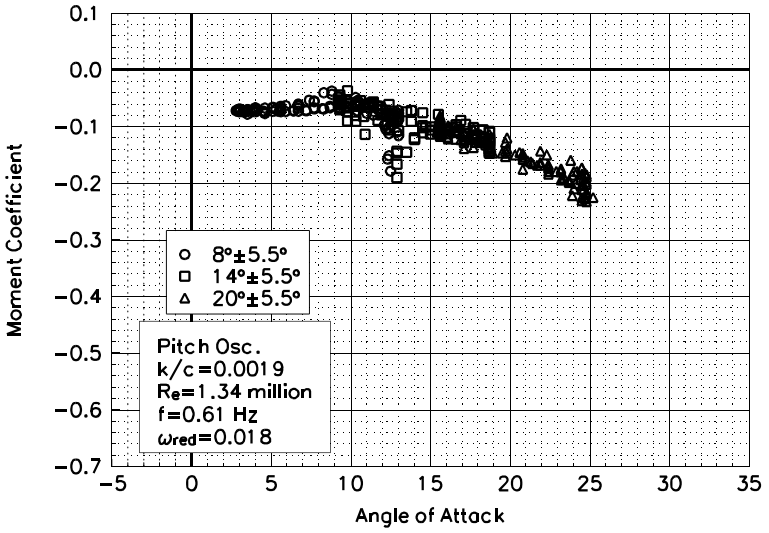

Figure C66. Moment coefficient vs α.

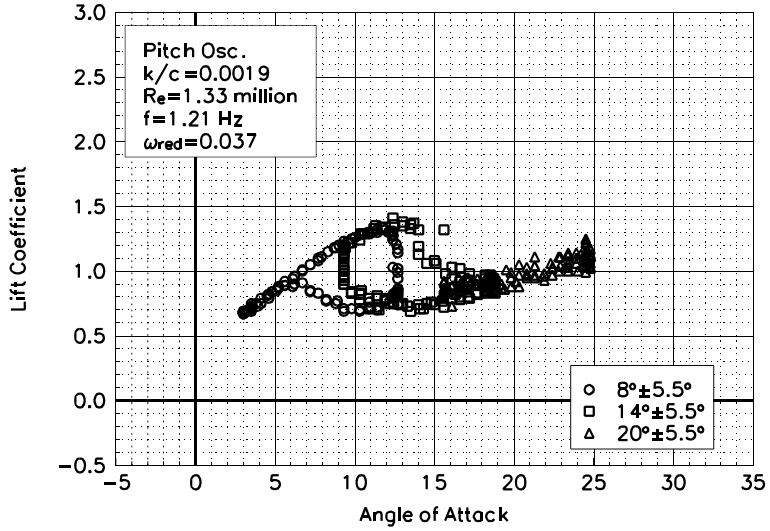

Figure C67. Lift coefficient vs α.

LS(1)-0417MOD
LEGR
Re=1.33 million
$\omega_{reduced}$=0.037

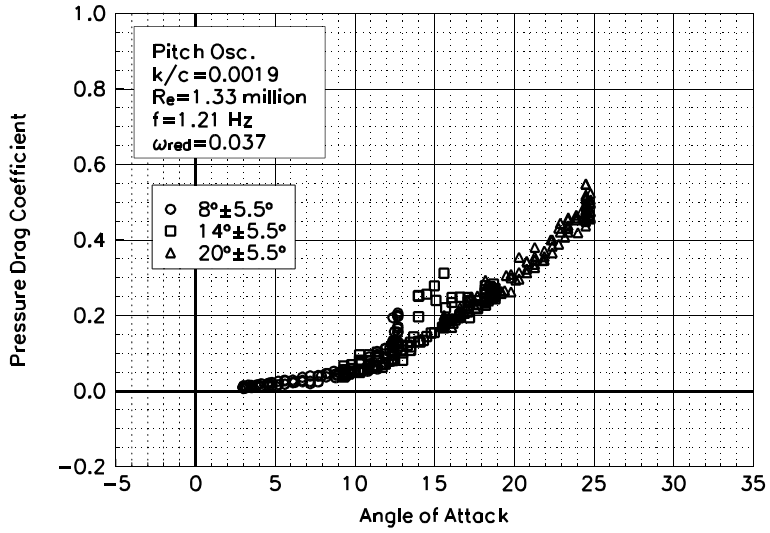

Figure C68. Pressure drag coefficient vs α.

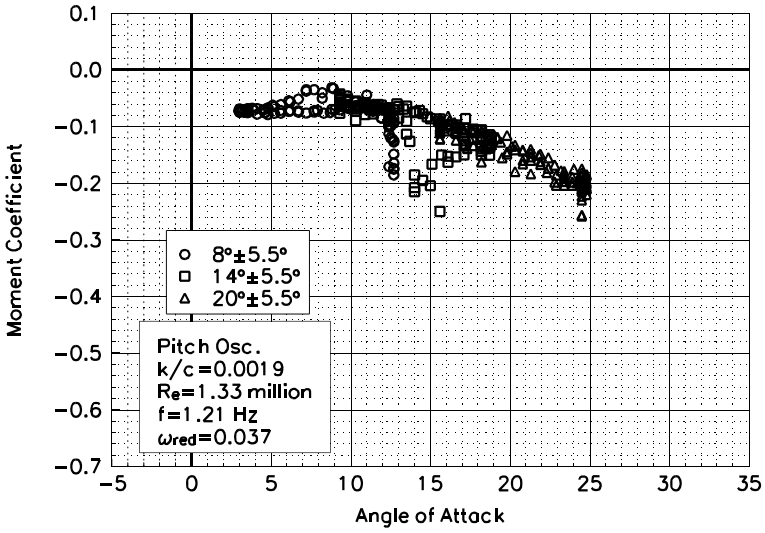

Figure C69. Moment coefficient vs α.

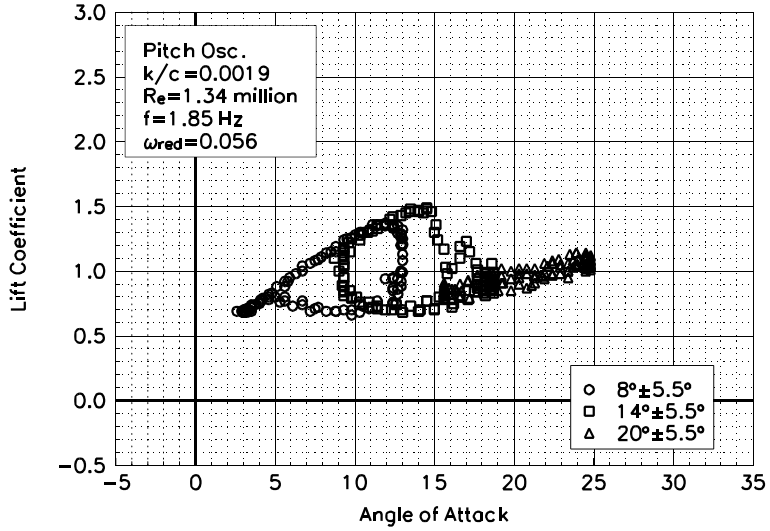

Figure C70. Lift coefficient vs α.

LS(1)-0417MOD
LEGR
Re=1.34 million
$\omega_{reduced}$=0.056

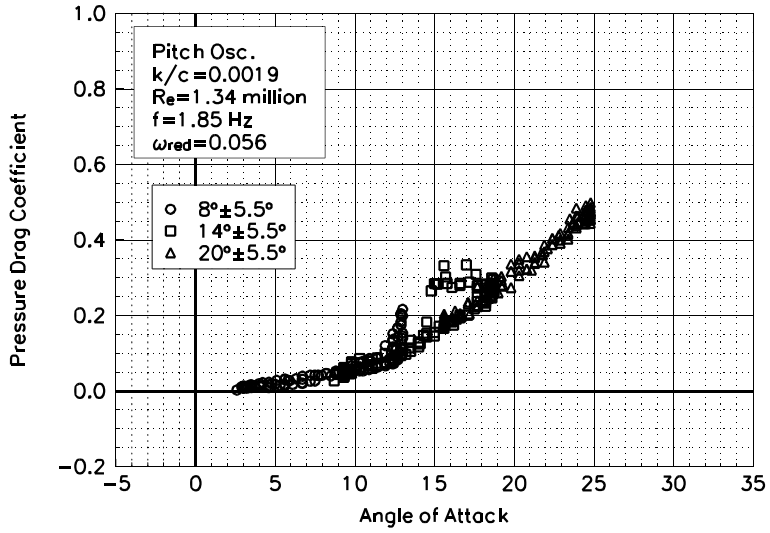

Figure C71. Pressure drag coefficient vs α.

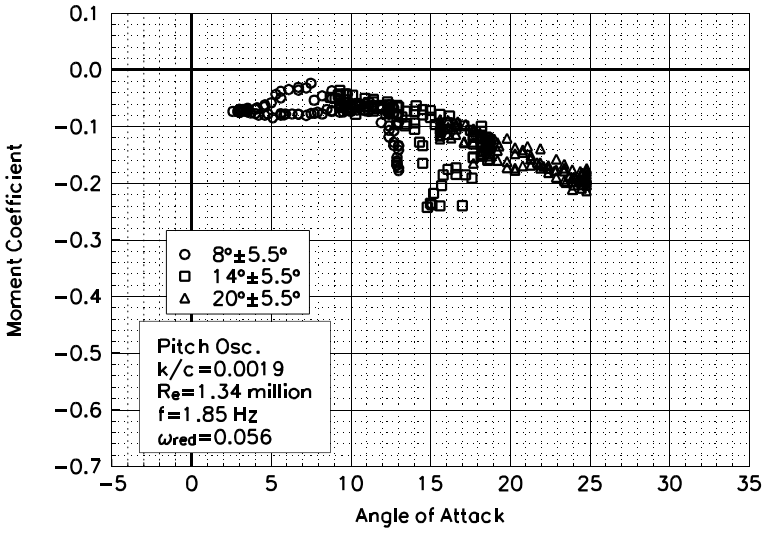

Figure C72. Moment coefficient vs α.

Unsteady Airfoil Characteristics

±10° Sine, Re = 0.75 million

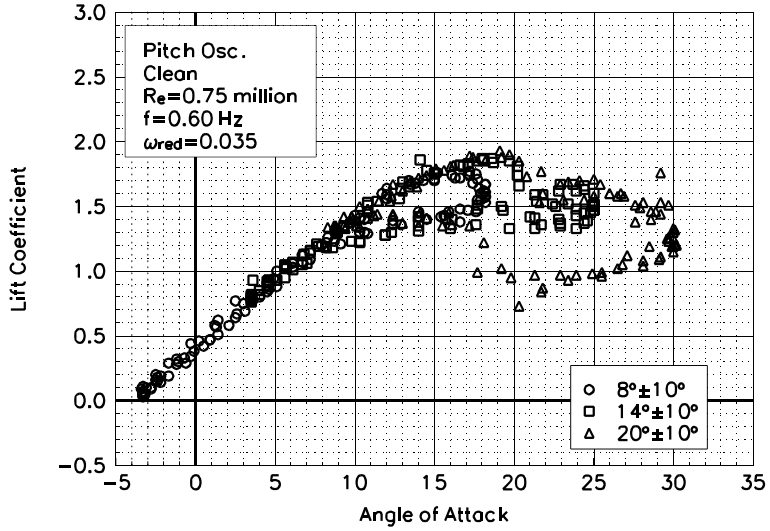

Figure C73. Lift coefficient vs α.

LS(1)-0417MOD
Clean
Re=0.75 million
$\omega_{reduced}$=0.035

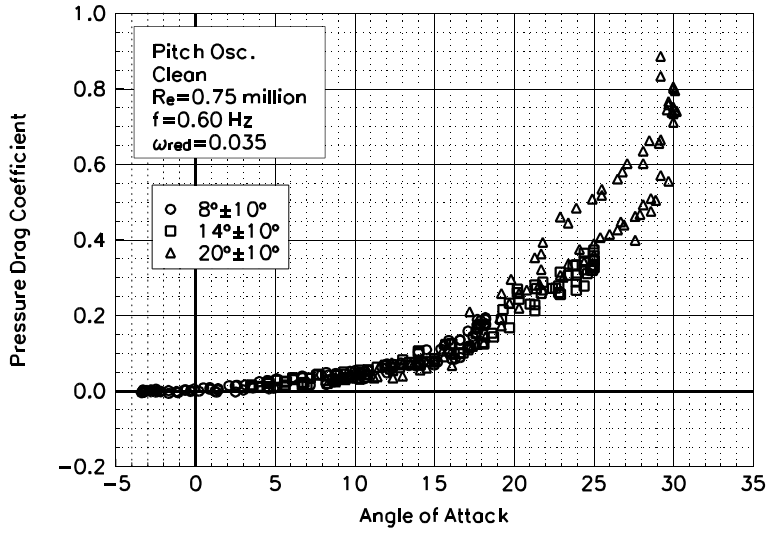

Figure C74. Pressure drag coefficient vs α.

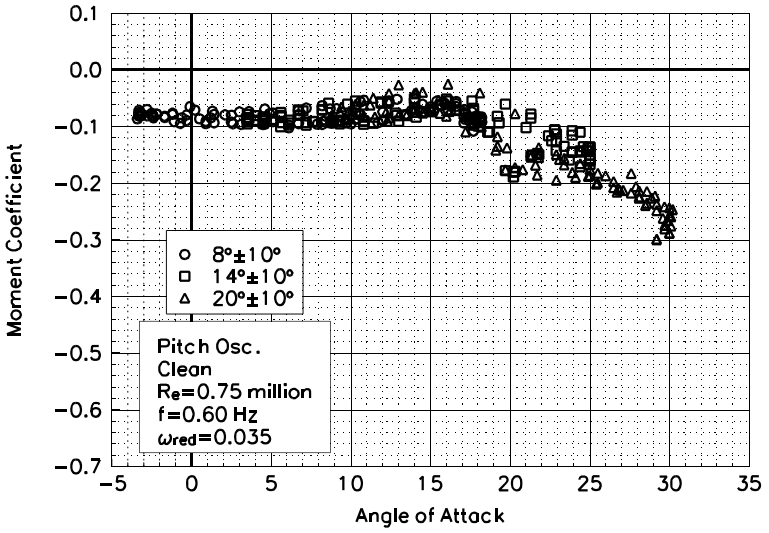

Figure C75. Moment coefficient vs α.

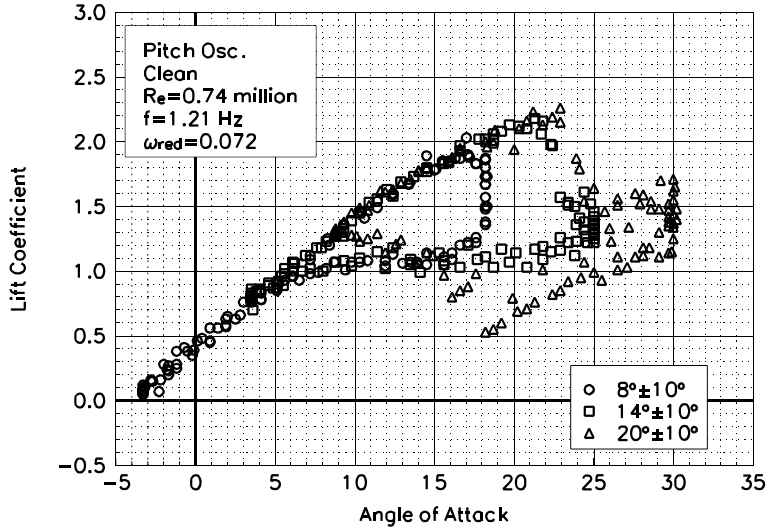

Figure C76. Lift coefficient vs α.

LS(1)-0417MOD
Clean
Re=0.74 million
$\omega_{reduced}$=0.072

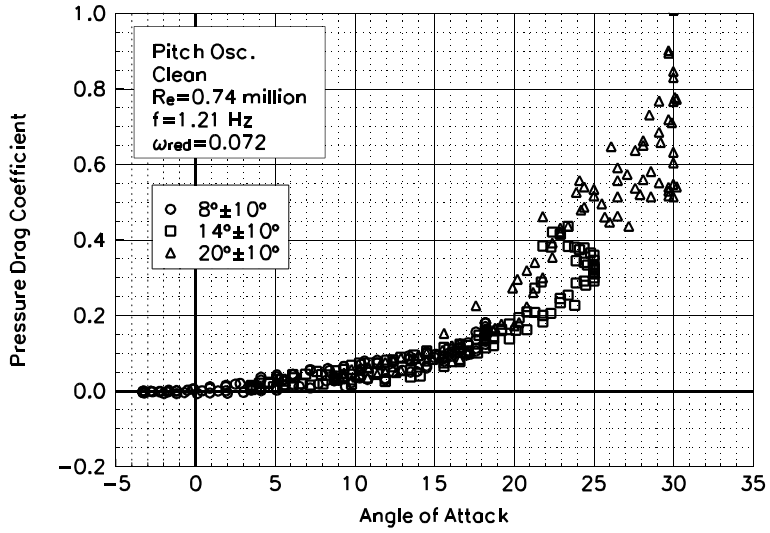

Figure C77. Pressure drag coefficient vs α.

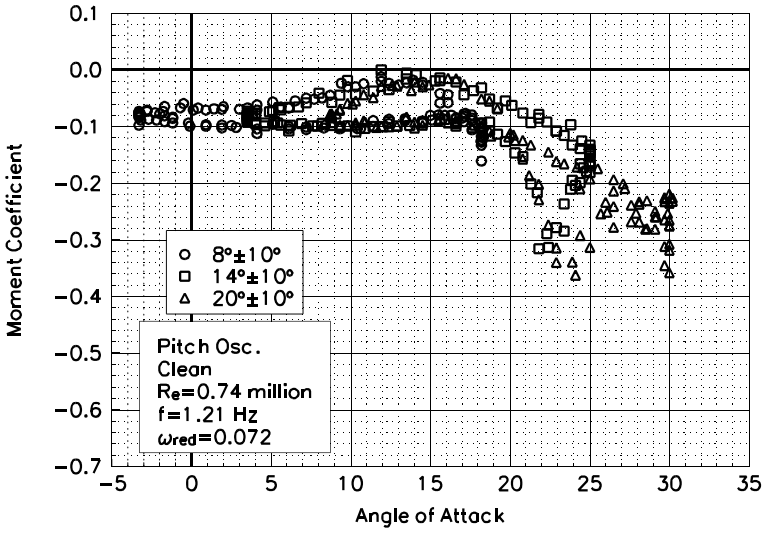

Figure C78. Moment coefficient vs α.

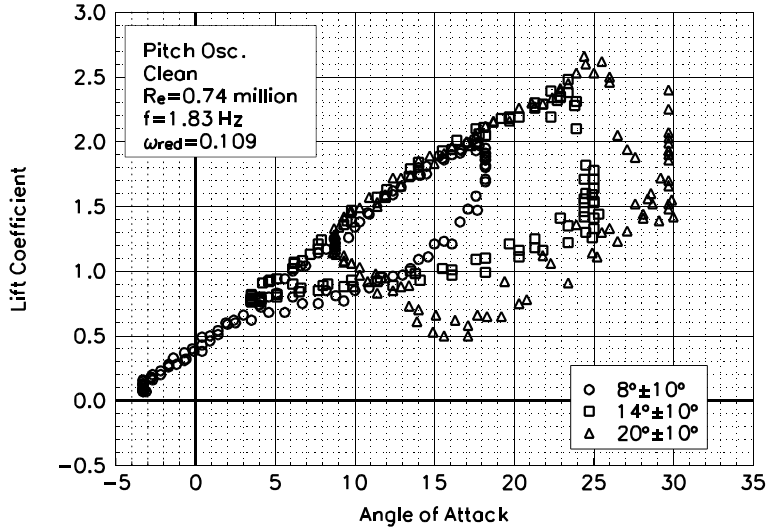

Figure C79. Lift coefficient vs α.

LS(1)-0417MOD
Clean
Re=0.74 million
$\omega_{reduced}$=0.109

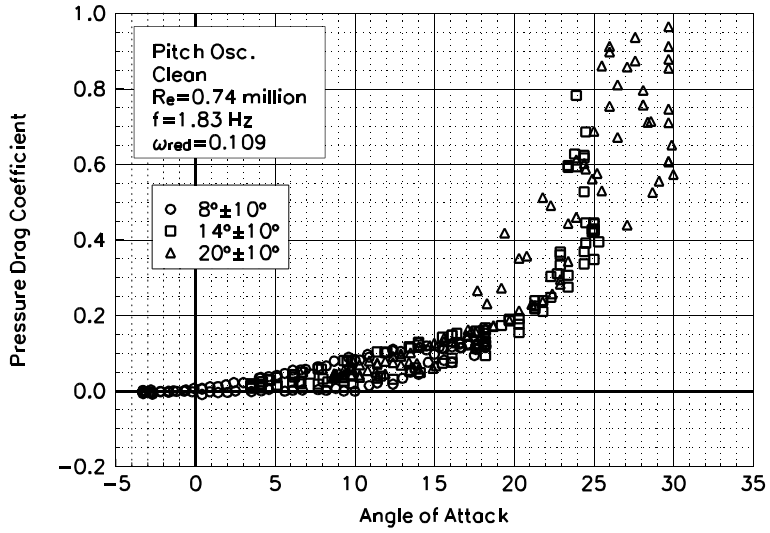

Figure C80. Pressure drag coefficient vs α.

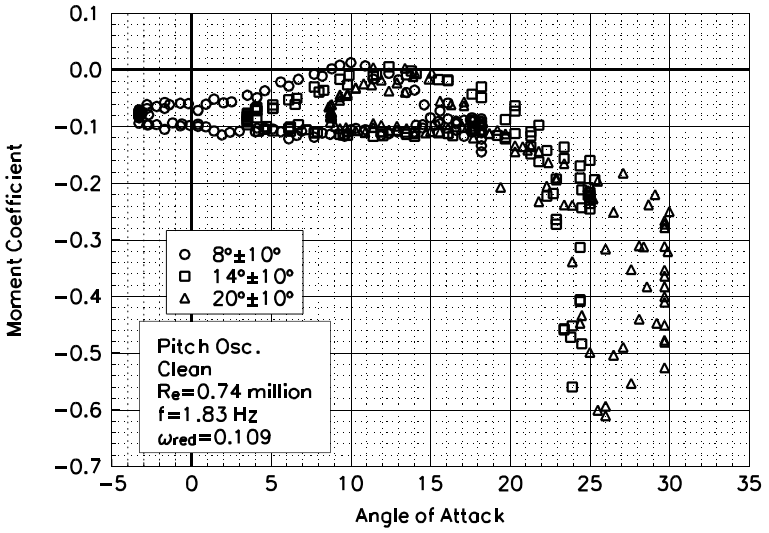

Figure C81. Moment coefficient vs α.

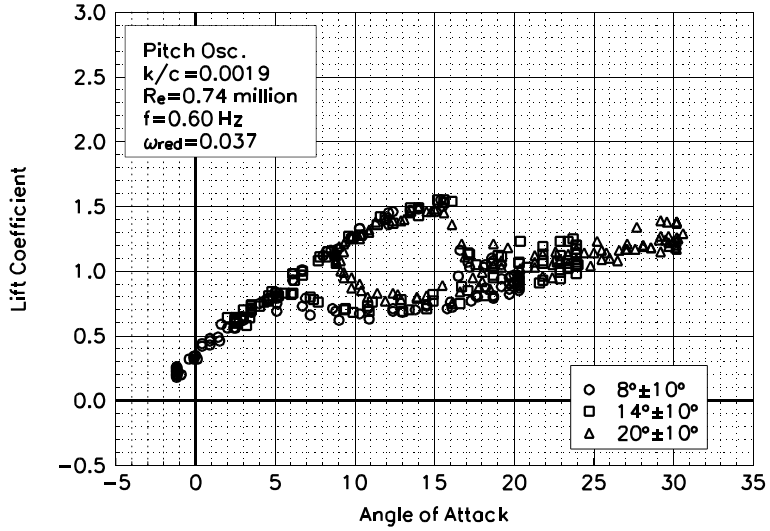

Figure C82. Lift coefficient vs α.

LS(1)-0417MOD
LEGR
Re=0.74 million
$\omega_{reduced}$=0.037

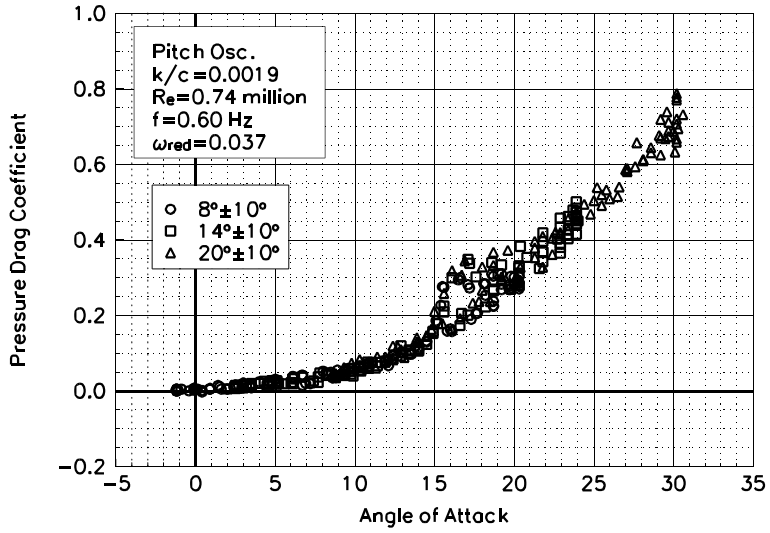

Figure C83. Pressure drag coefficient vs α.

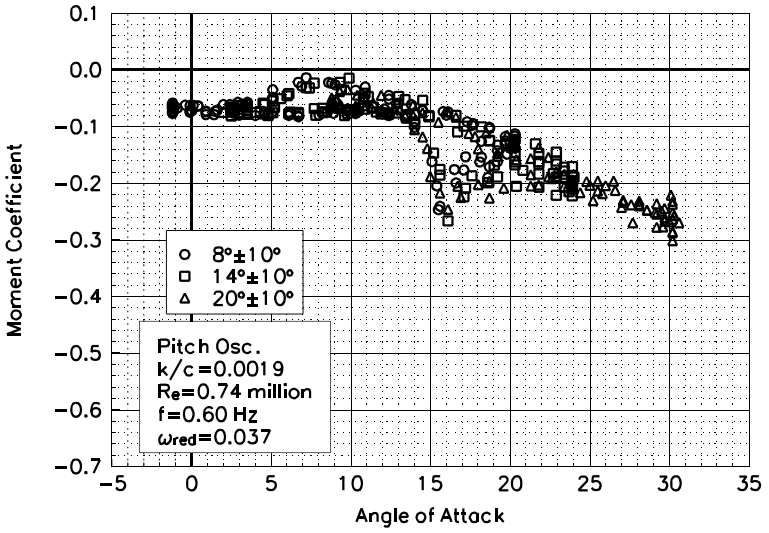

Figure C84. Moment coefficient vs α.

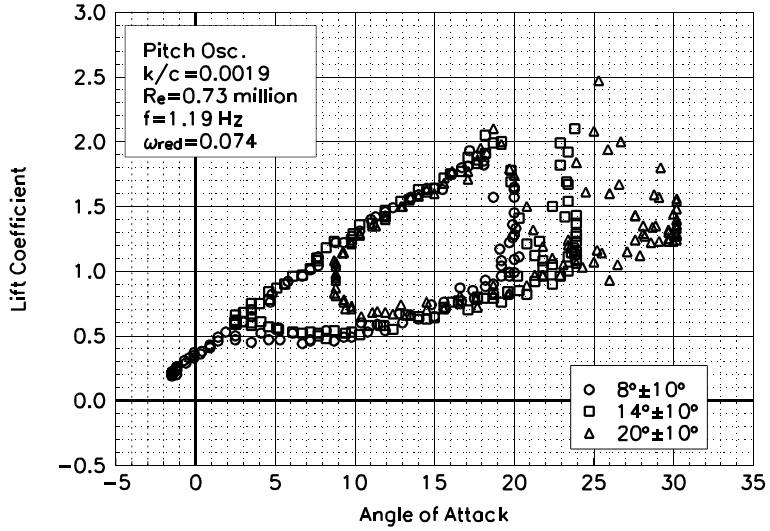

Figure C85. Lift coefficient vs α.

LS(1)-0417MOD
LEGR
Re=0.73 million
$\omega_{reduced}$=0.074

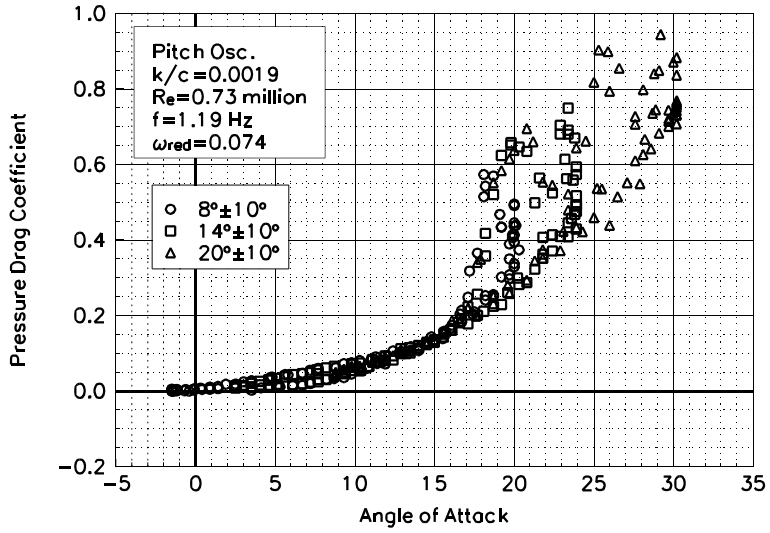

Figure C86. Pressure drag coefficient vs α.

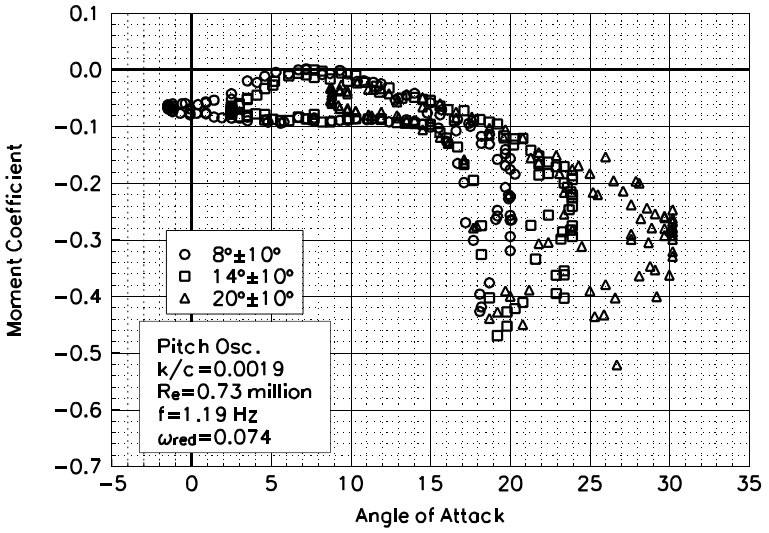

Figure C87. Moment coefficient vs α.

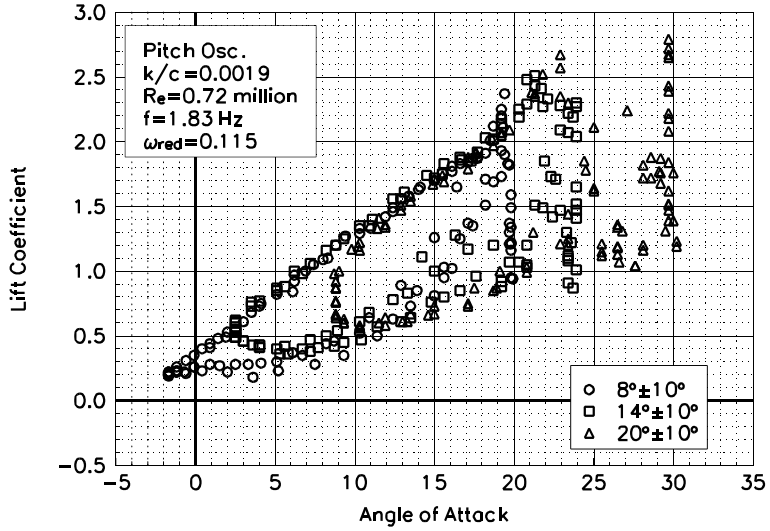

Figure C88. Lift coefficient vs α.

LS(1)-0417MOD
LEGR
Re=0.72 million
$\omega_{reduced}$=0.115

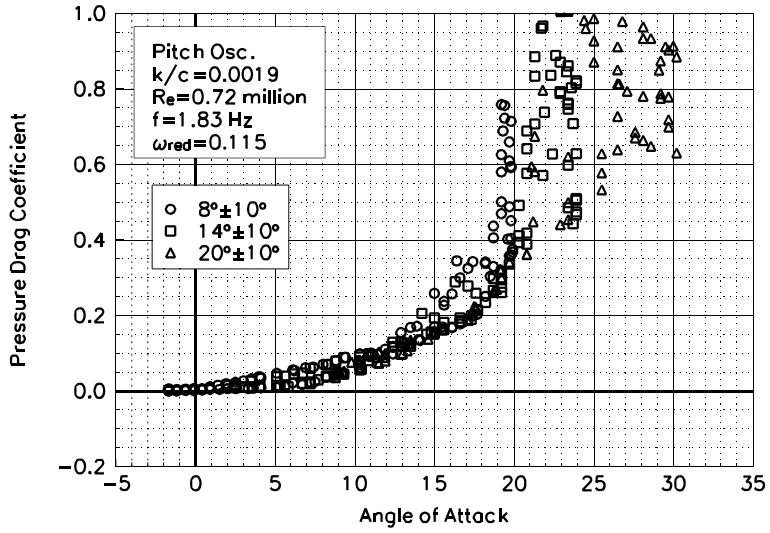

Figure C89. Pressure drag coefficient vs α.

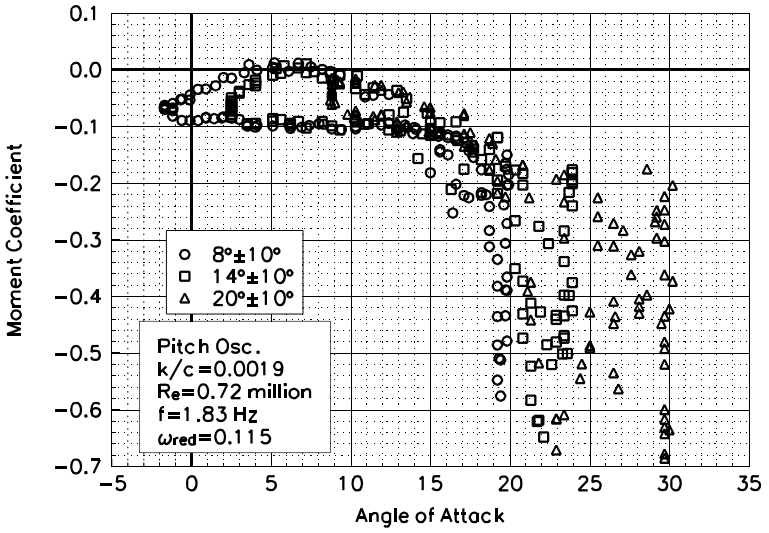

Figure C90. Moment coefficient vs α.

Unsteady Airfoil Characteristics

±10° Sine, Re = 1 million

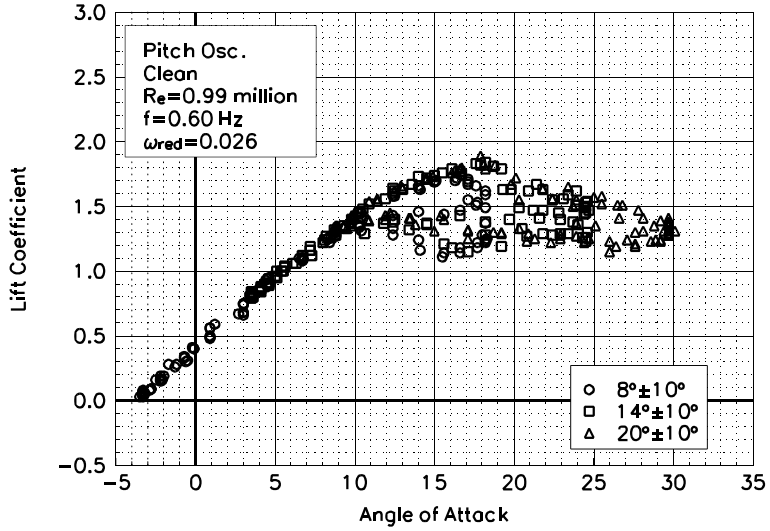

Figure C91. Lift coefficient vs α.

LS(1)-0417MOD
Clean
Re=0.99 million
$\omega_{reduced}$=0.026

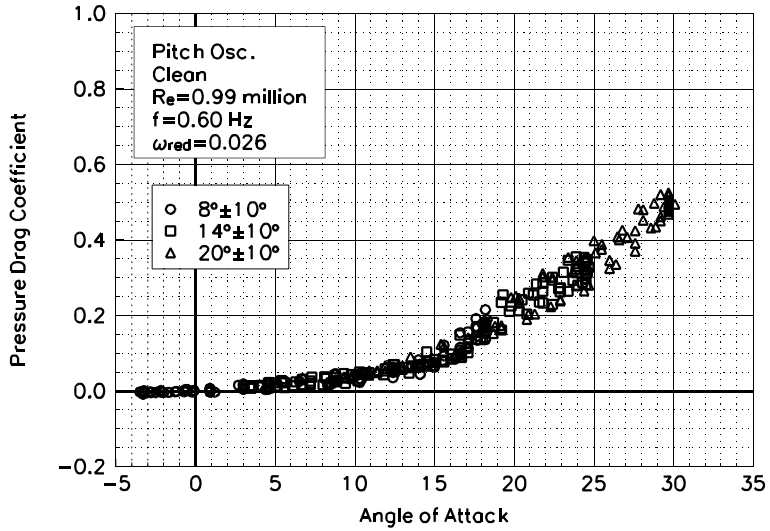

Figure C92. Pressure drag coefficient vs α.

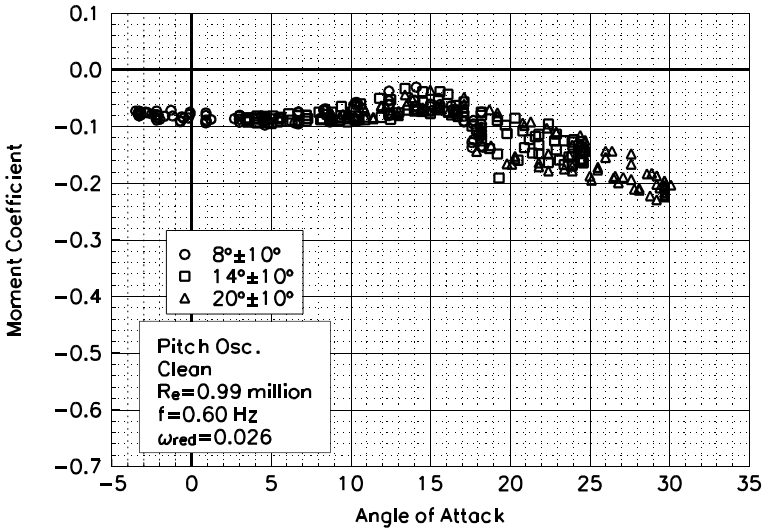

Figure C93. Moment coefficient vs α.

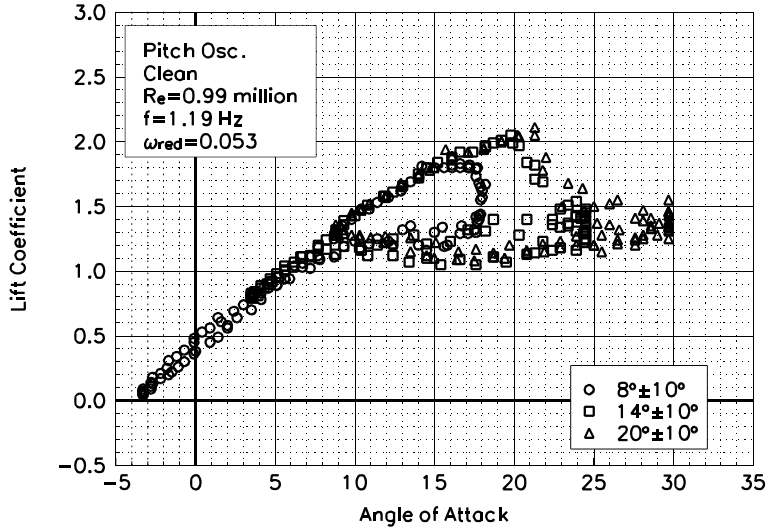

Figure C94. Lift coefficient vs α.

LS(1)-0417MOD
Clean
Re=0.99 million
$\omega_{reduced}$=0.053

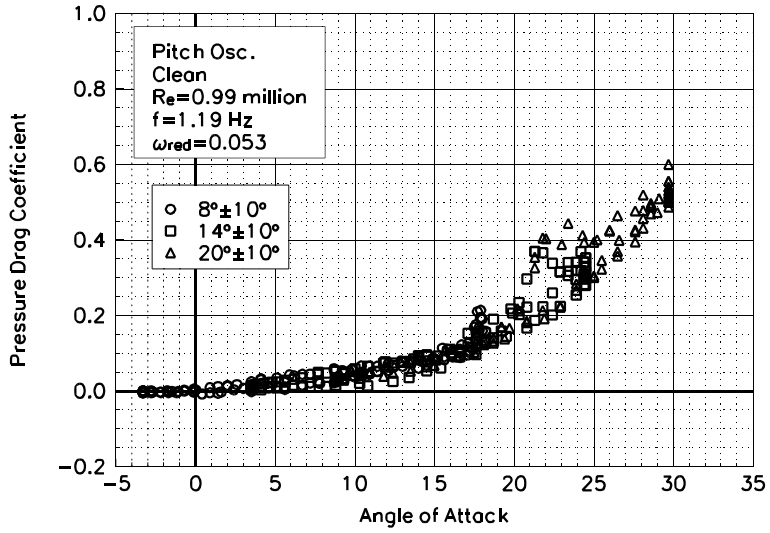

Figure C95. Pressure drag coefficient vs α.

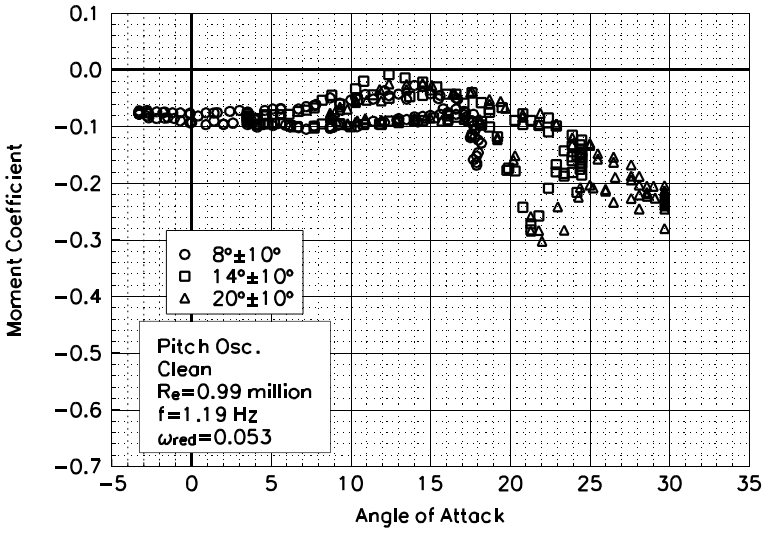

Figure C96. Moment coefficient vs α.

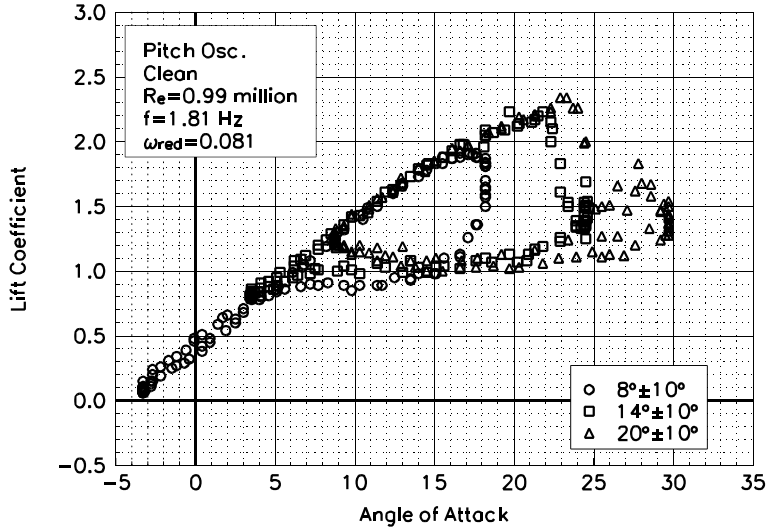

Figure C97. Lift coefficient vs α.

LS(1)-0417MOD
Clean
Re=0.99 million
$\omega_{reduced}$=0.081

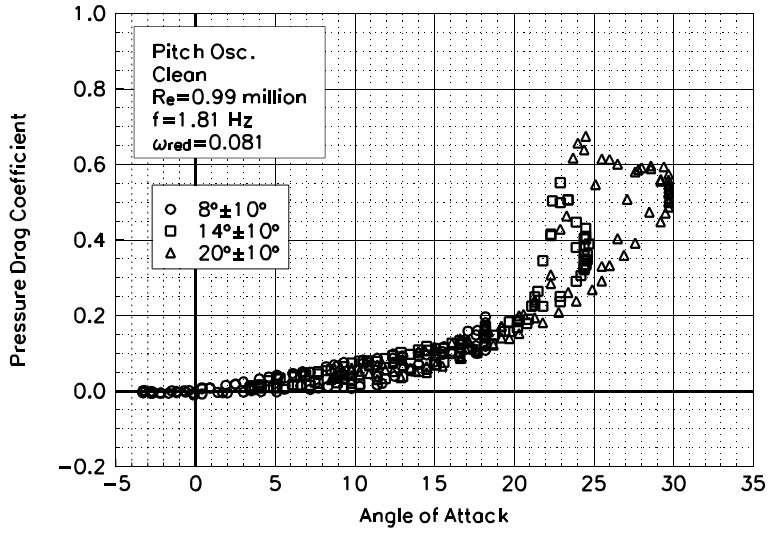

Figure C98. Pressure drag coefficient vs α.

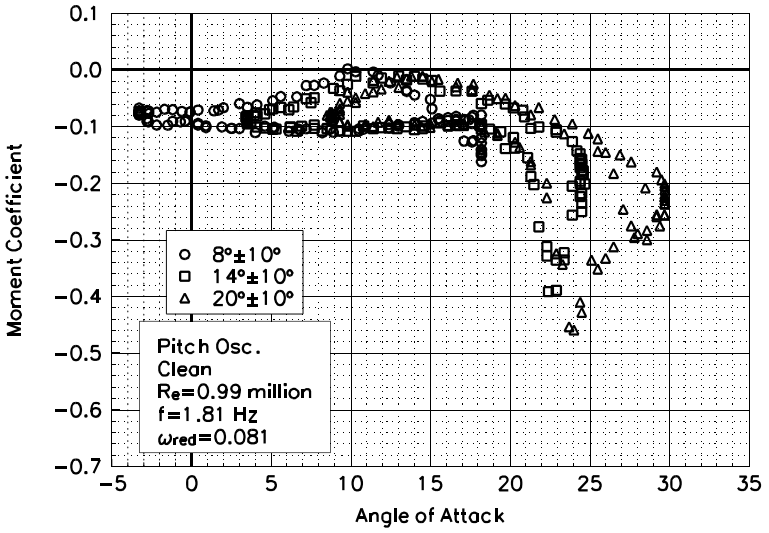

Figure C99. Moment coefficient vs α.

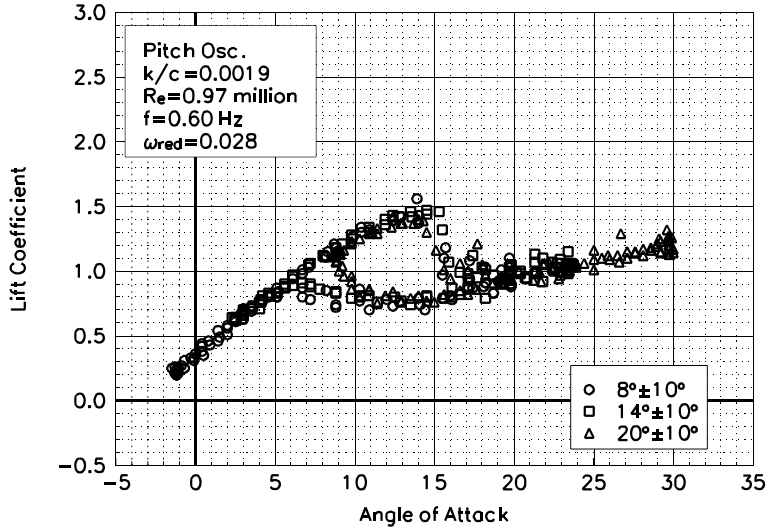

Figure C100. Lift coefficient vs α.

LS(1)-0417MOD
LEGR
Re=0.97 million
$\omega_{reduced}$=0.028

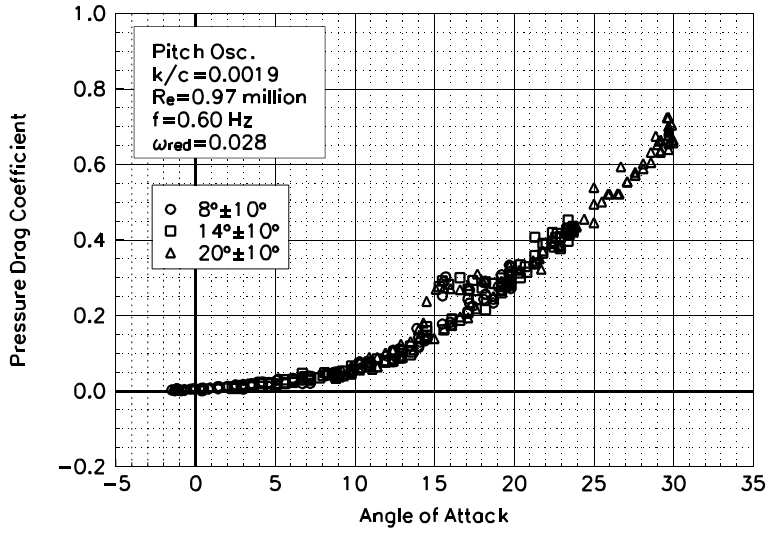

Figure C101. Pressure drag coefficient vs α.

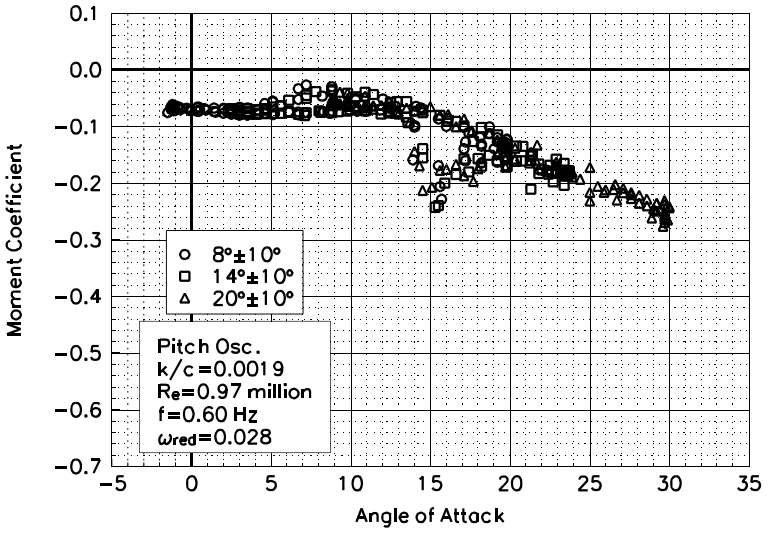

Figure C102. Moment coefficient vs α.

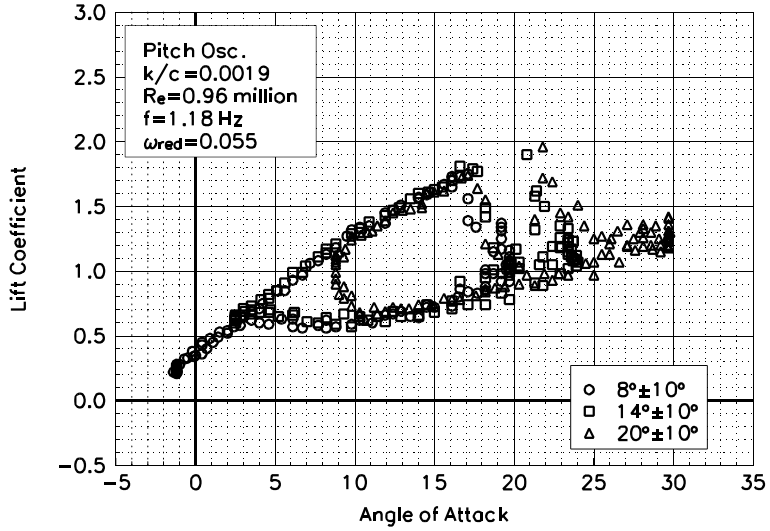

Figure C103. Lift coefficient vs α.

LS(1)-0417MOD
LEGR
Re=0.96 million
$\omega_{reduced}$=0.055

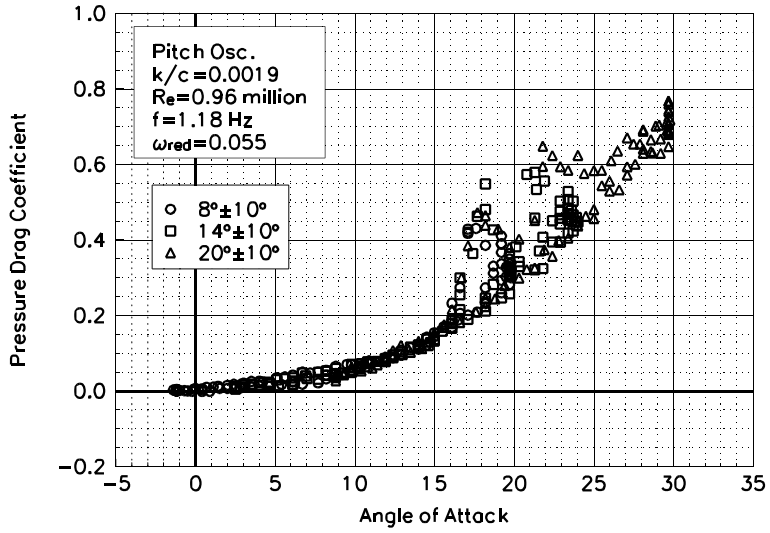

Figure C104. Pressure drag coefficient vs α.

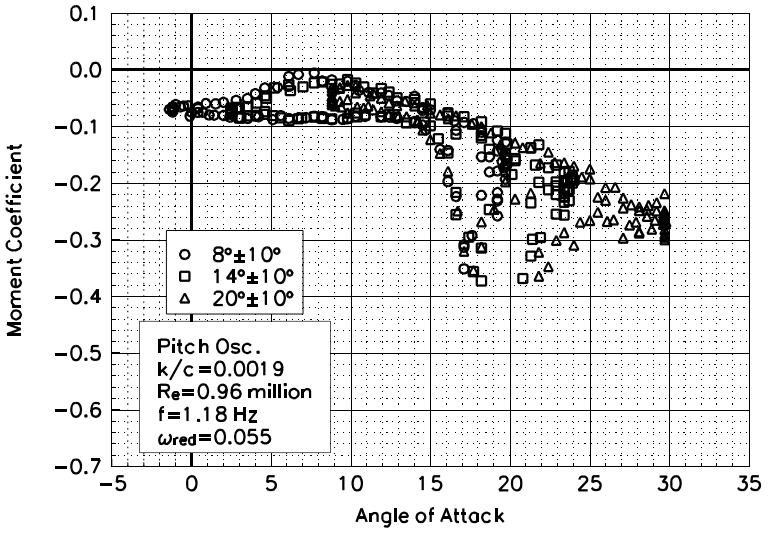

Figure C105. Moment coefficient vs α.

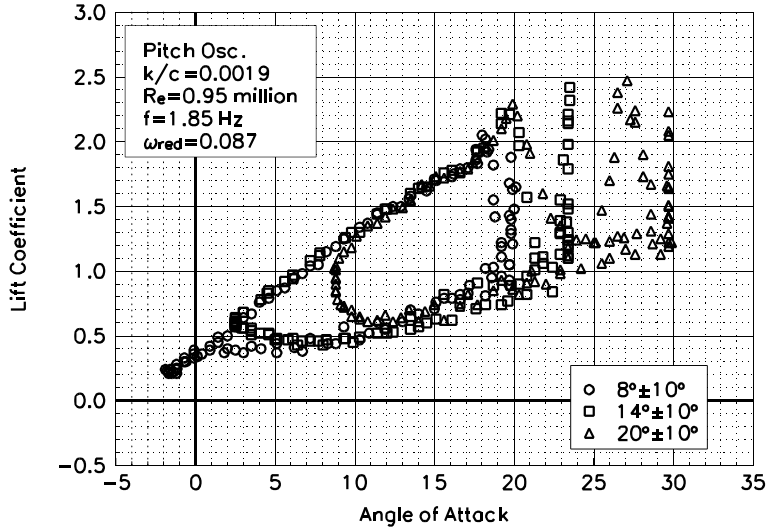

Figure C106. Lift coefficient vs α.

LS(1)-0417MOD
LEGR
Re=0.95 million
$\omega_{reduced}$=0.087

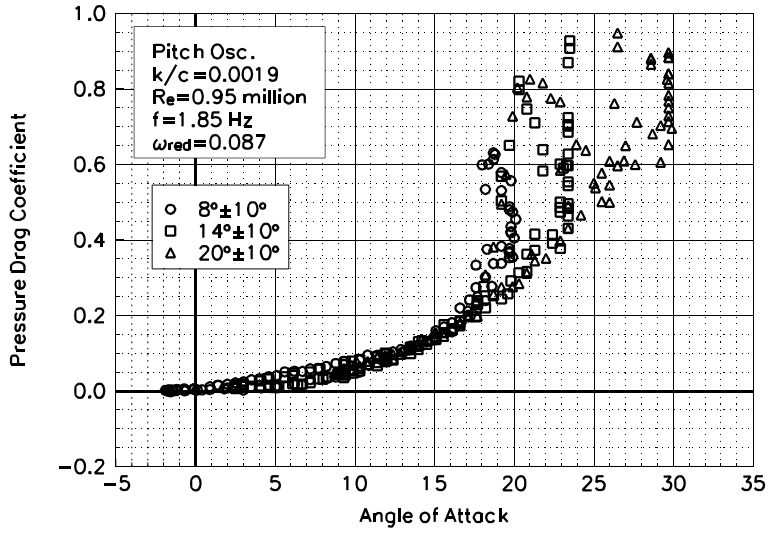

Figure C107. Pressure drag coefficient vs α.

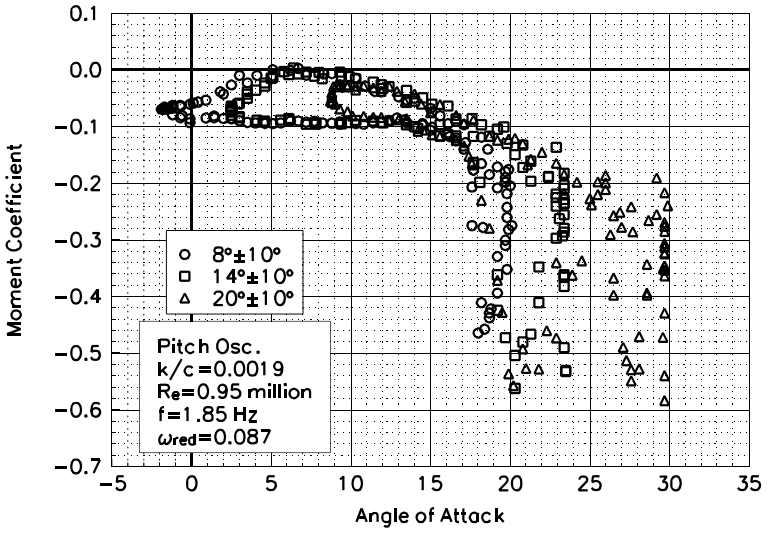

Figure C108. Moment coefficient vs α.

Unsteady Airfoil Characteristics

±10° Sine, Re = 1.25 million

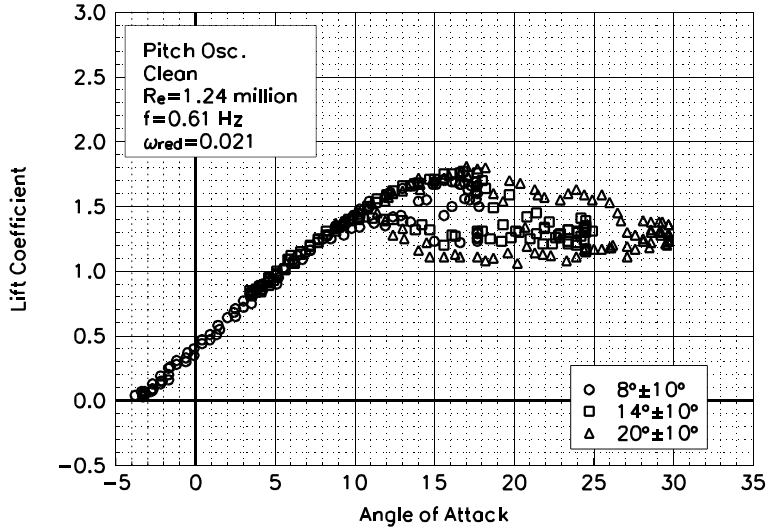

Figure C109. Lift coefficient vs α.

LS(1)-0417MOD
Clean
Re=1.24 million
$\omega_{reduced}$=0.021

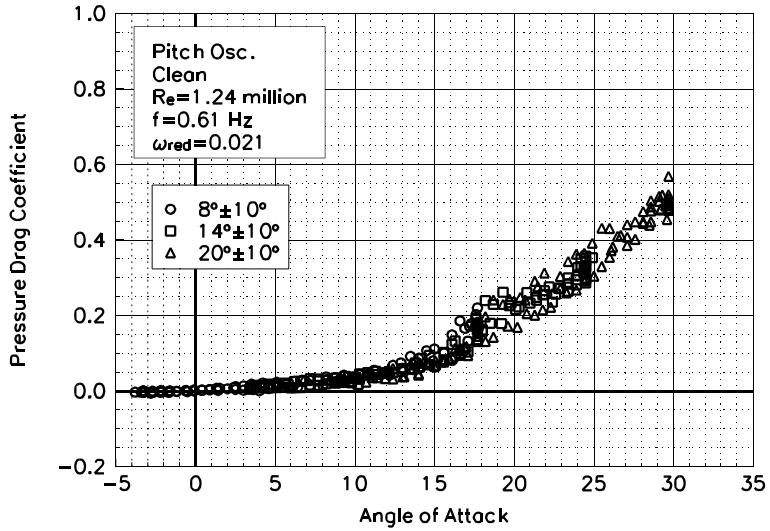

Figure C110. Pressure drag coefficient vs α.

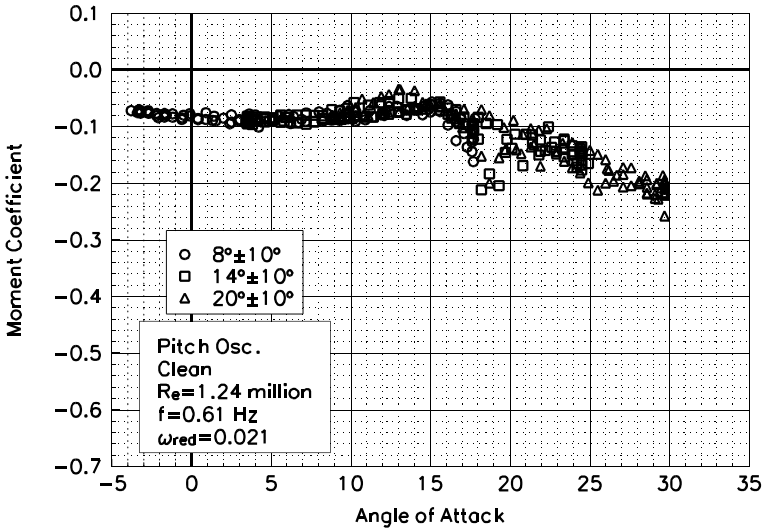

Figure C111. Moment coefficient vs α.

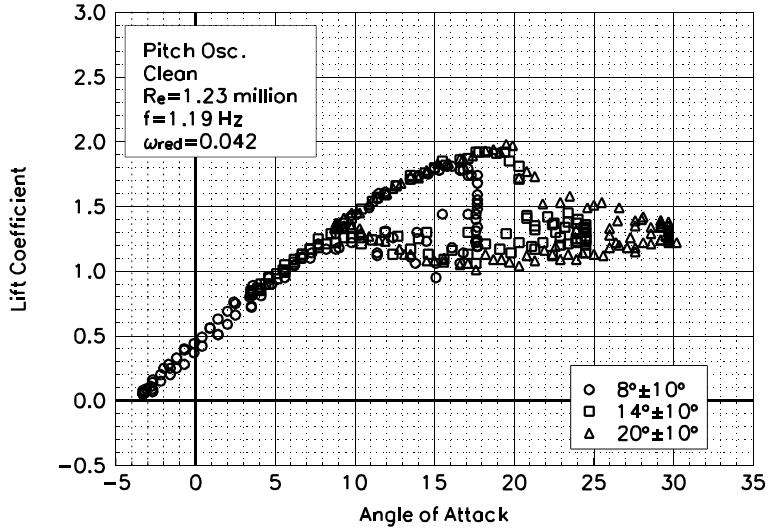

Figure C112. Lift coefficient vs α.

LS(1)-0417MOD
Clean
Re=1.23 million
$\omega_{reduced}$=0.042

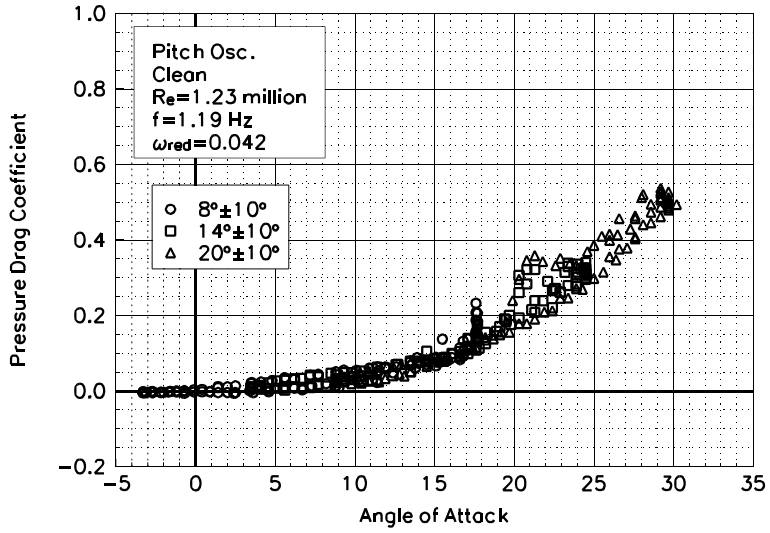

Figure C113. Pressure drag coefficient vs α.

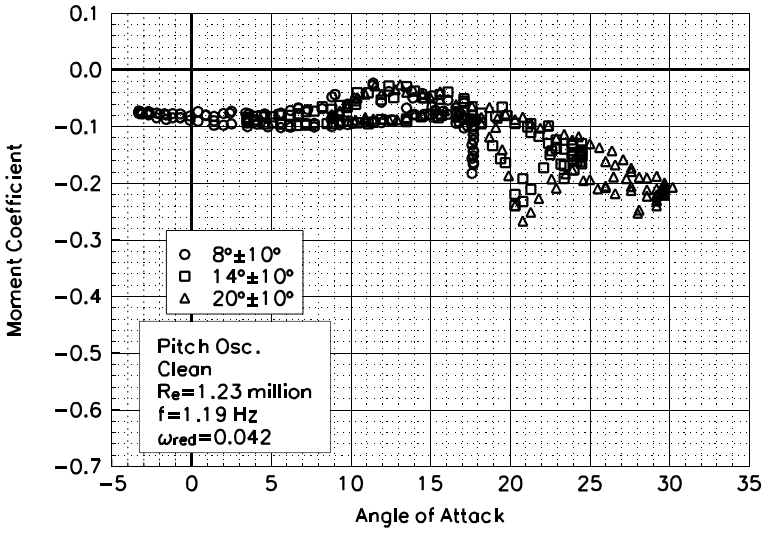

Figure C114. Moment coefficient vs α.

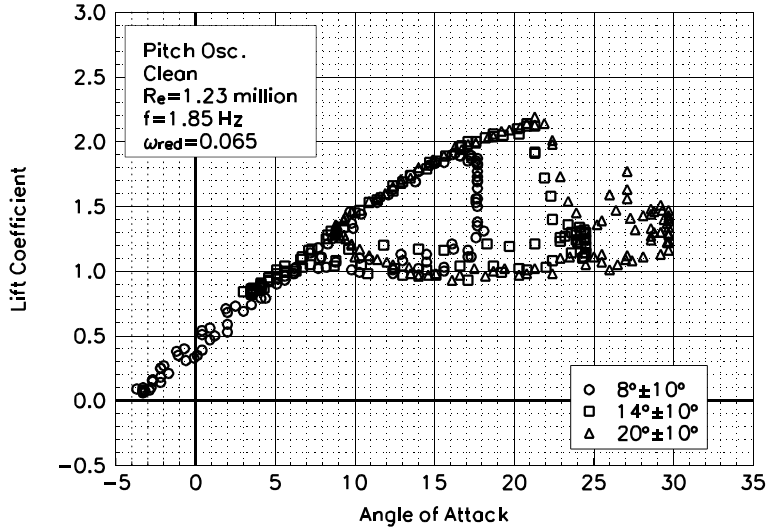

Figure C115. Lift coefficient vs α.

LS(1)-0417MOD
Clean
Re=1.23 million
$\omega_{reduced}$=0.065

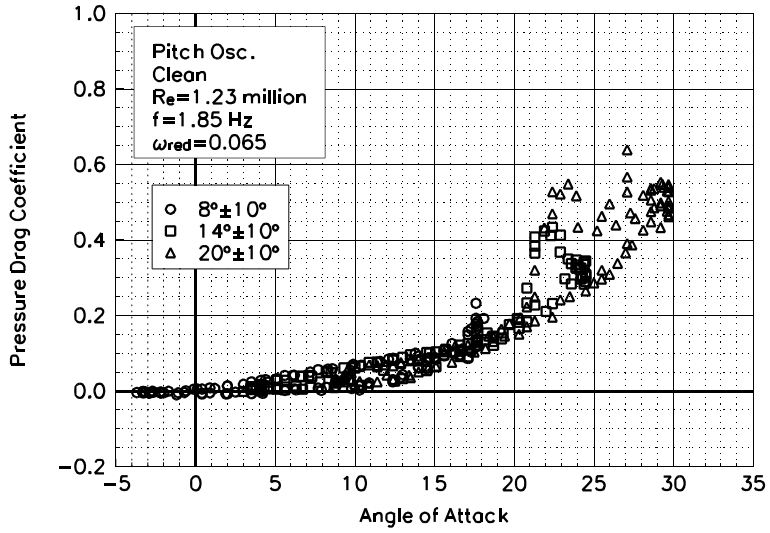

Figure C116. Pressure drag coefficient vs α.

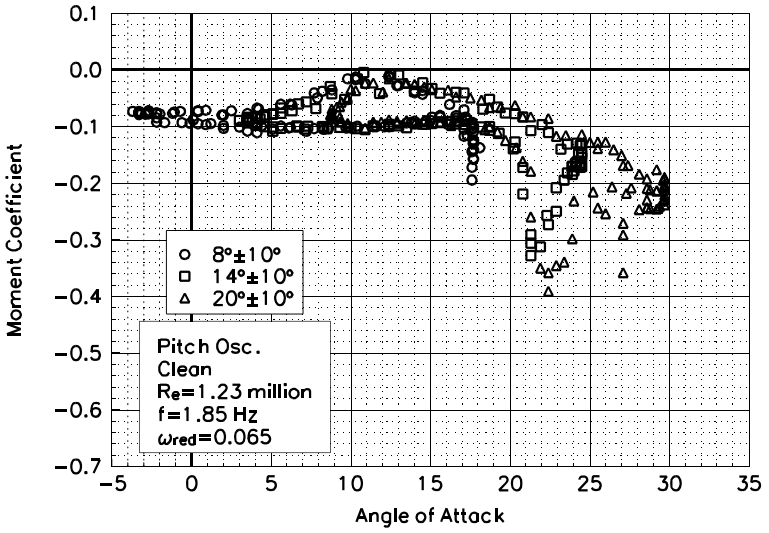

Figure C117. Moment coefficient vs α.

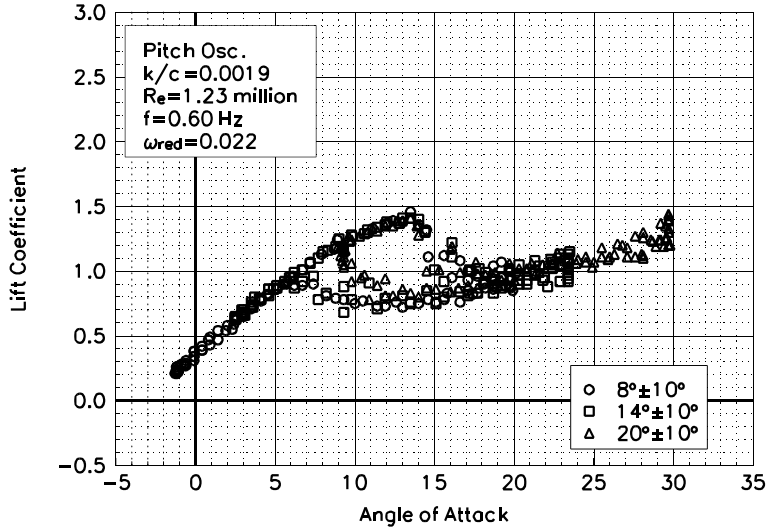

Figure C118. Lift coefficient vs α.

LS(1)-0417MOD
LEGR
Re=1.23 million
$\omega_{reduced}$=0.022

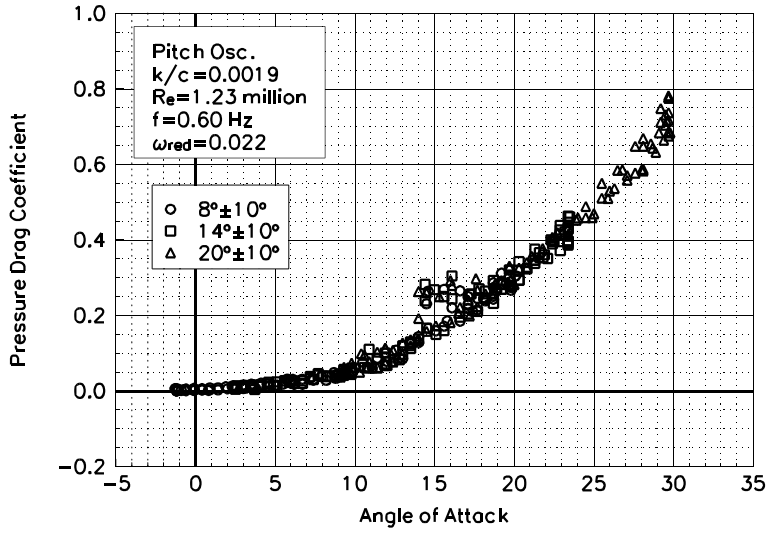

Figure C119. Pressure drag coefficient vs α.

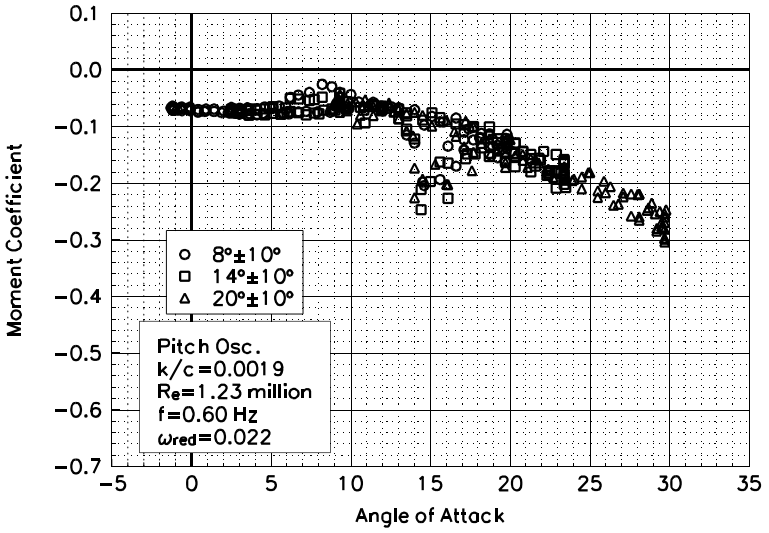

Figure C120. Moment coefficient vs α.

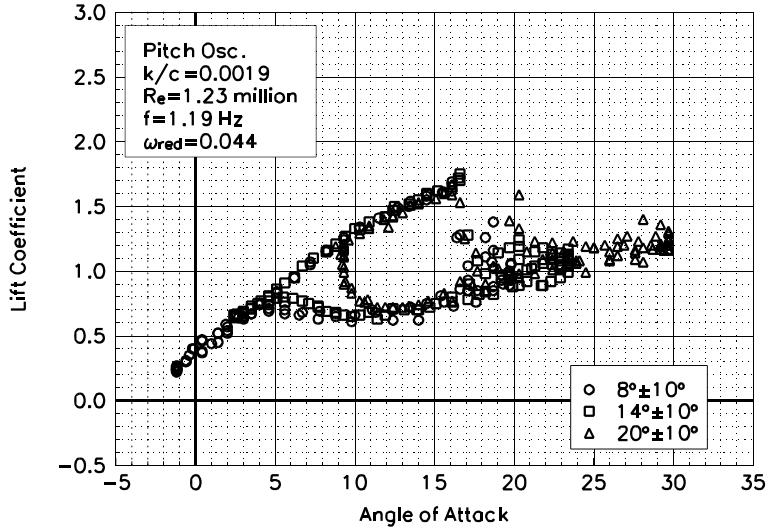

Figure C121. Lift coefficient vs α.

LS(1)-0417MOD
LEGR
Re=1.23 million
$\omega_{reduced}$=0.044

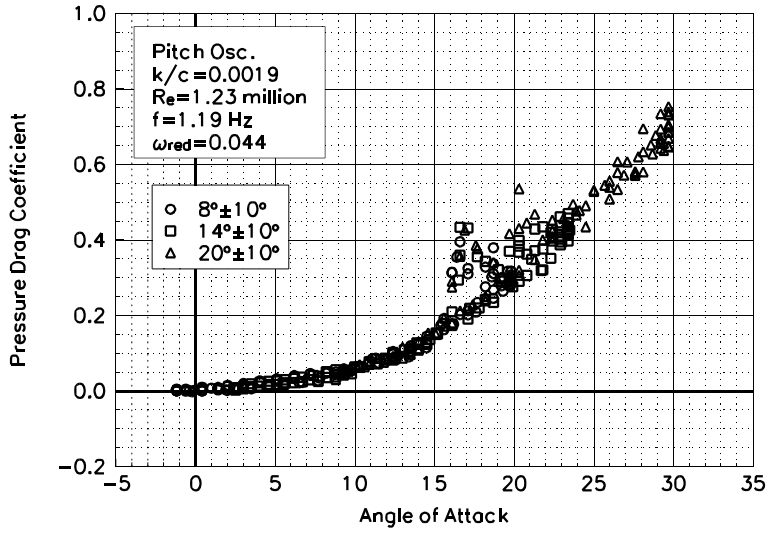

Figure C122. Pressure drag coefficient vs α.

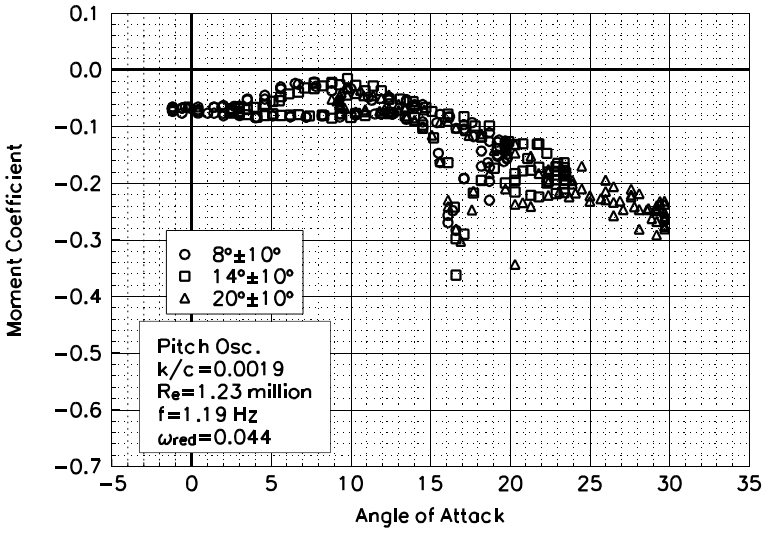

Figure C123. Moment coefficient vs α.

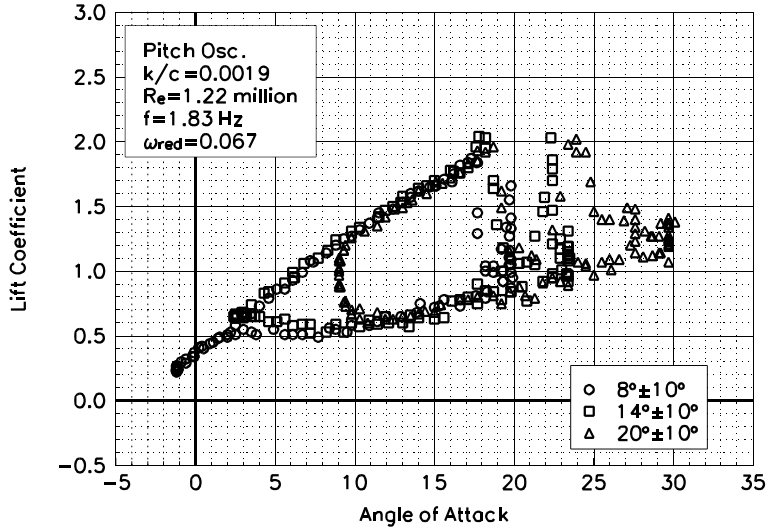

Figure C124. Lift coefficient vs α.

LS(1)-0417MOD
LEGR
Re=1.22 million
$\omega_{reduced}$=0.067

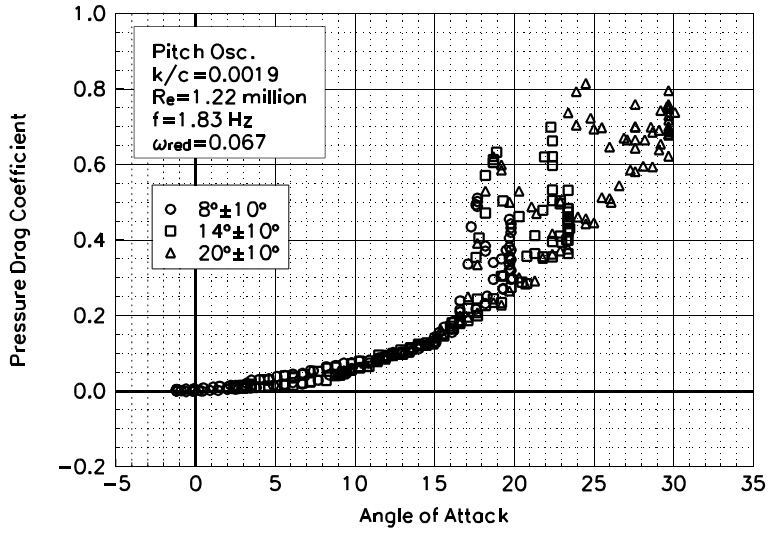

Figure C125. Pressure drag coefficient vs α.

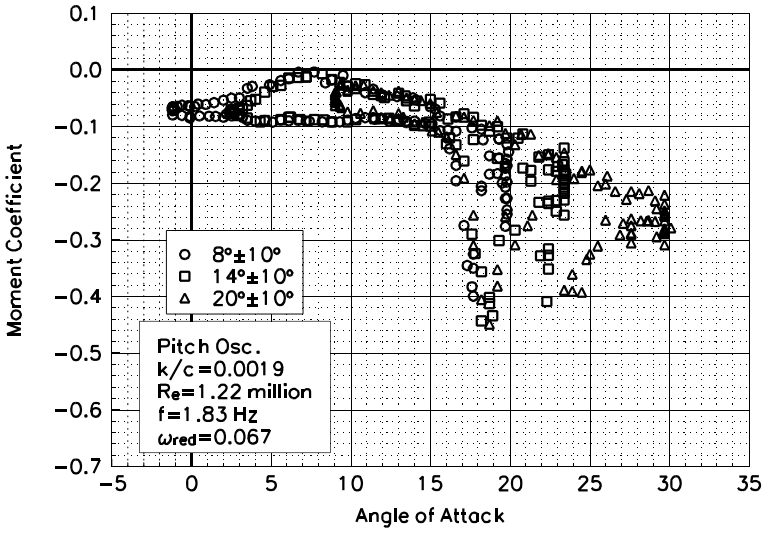

Figure C126. Moment coefficient vs α.

Unsteady Airfoil Characteristics

±10° Sine, Re = 1.5 million

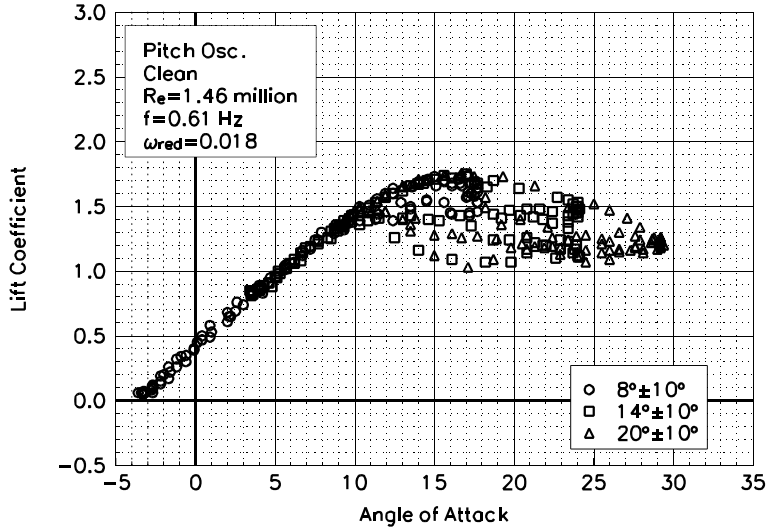

Figure C127. Lift coefficient vs α.

LS(1)-0417MOD
Clean
Re=1.46 million
$\omega_{reduced}$=0.018

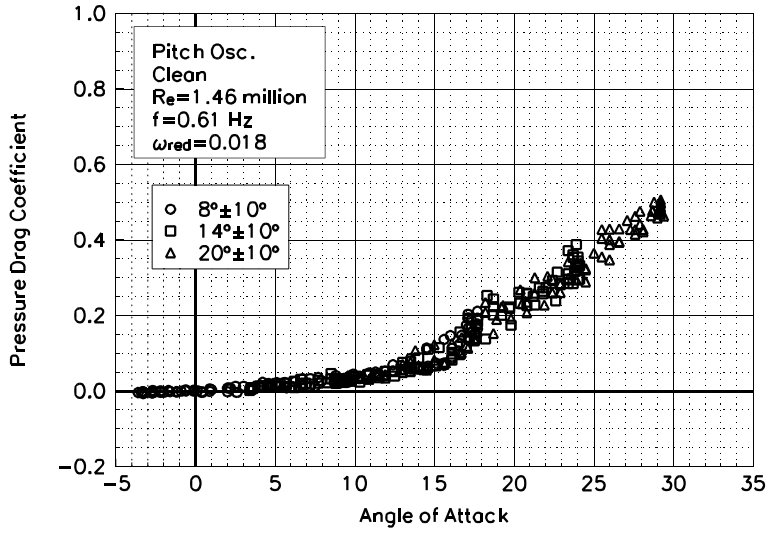

Figure C128. Pressure drag coefficient vs α.

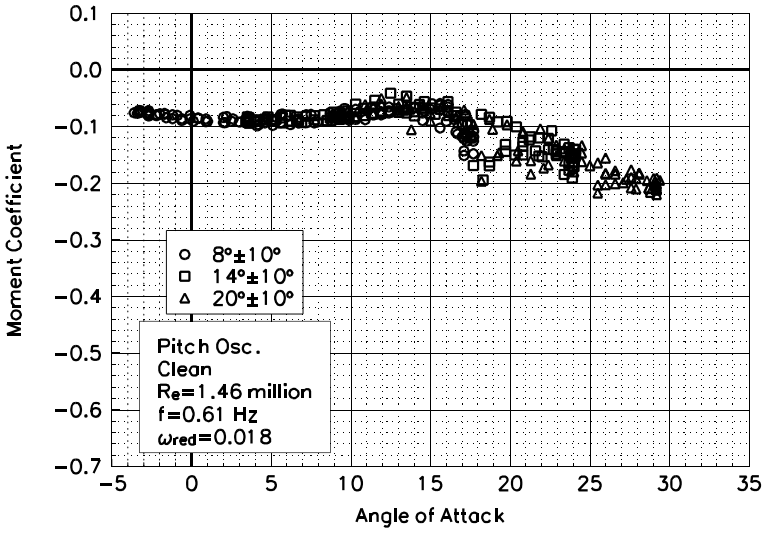

Figure C129. Moment coefficient vs α.

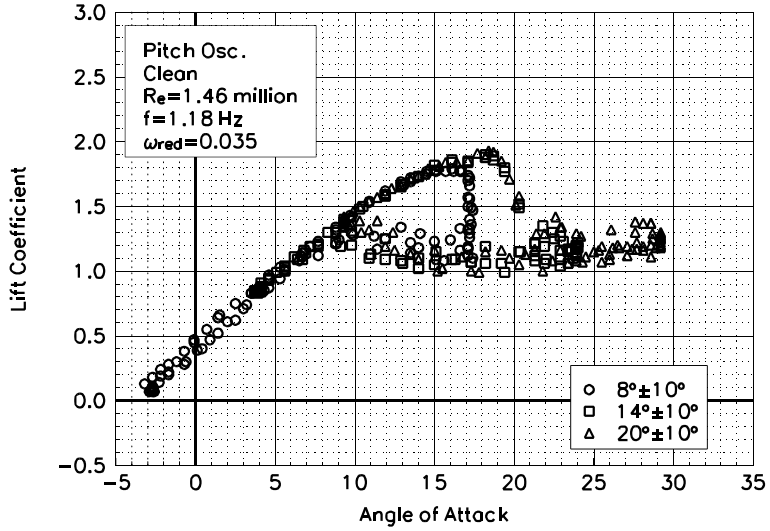

Figure C130. Lift coefficient vs α.

LS(1)-0417MOD
Clean
Re=1.46 million
$\omega_{reduced}$=0.035

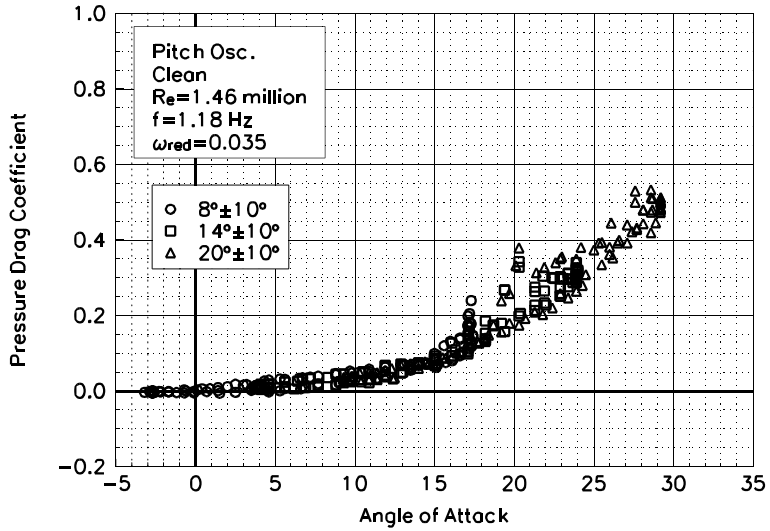

Figure C131. Pressure drag coefficient vs α.

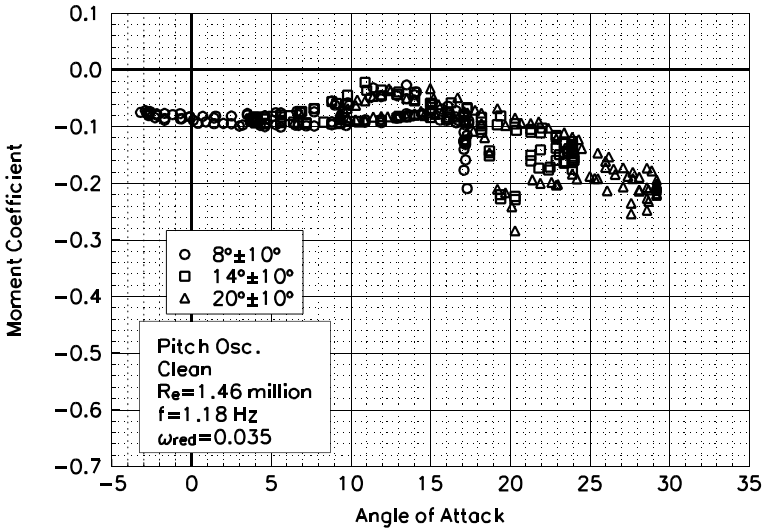

Figure C132. Moment coefficient vs α.

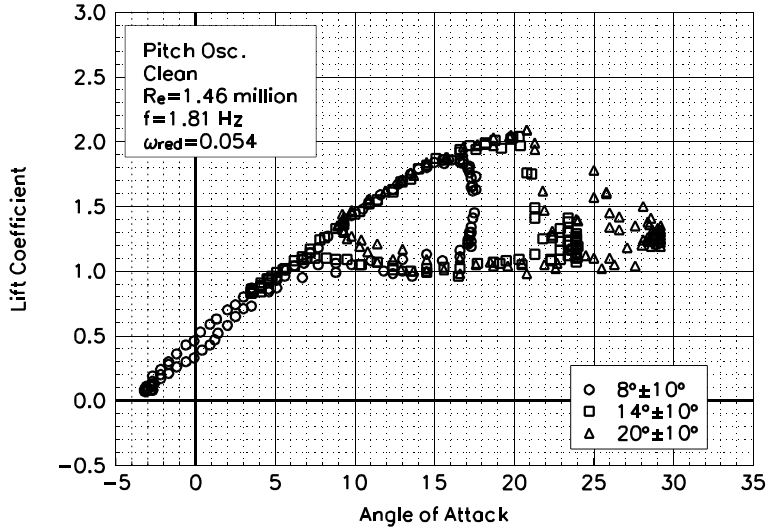

Figure C133. Lift coefficient vs α.

LS(1)-0417MOD
Clean
Re=1.46 million
$\omega_{reduced}$=0.054

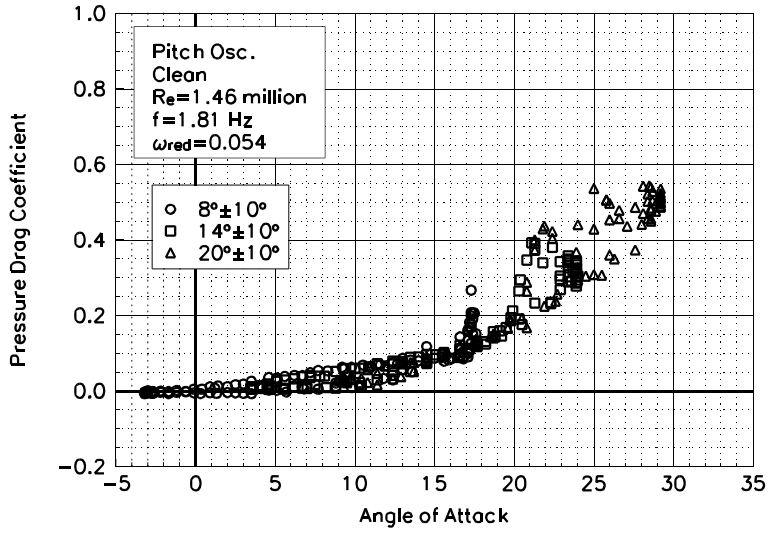

Figure C134. Pressure drag coefficient vs α.

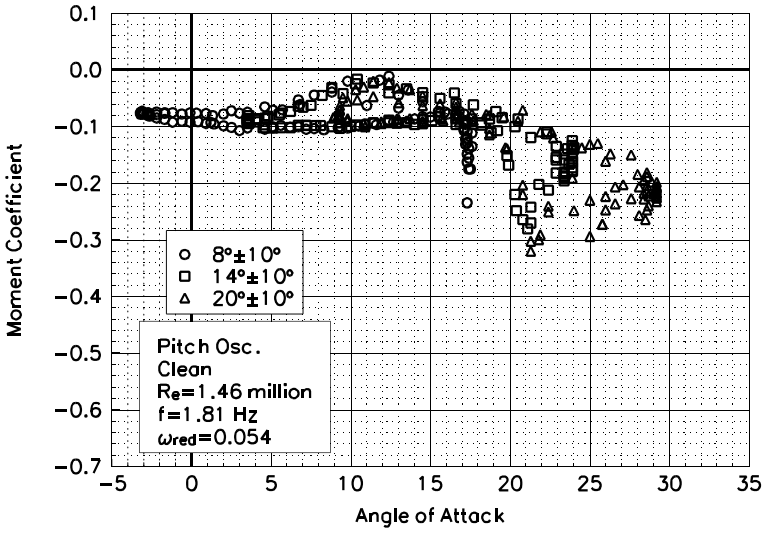

Figure C135. Moment coefficient vs α.

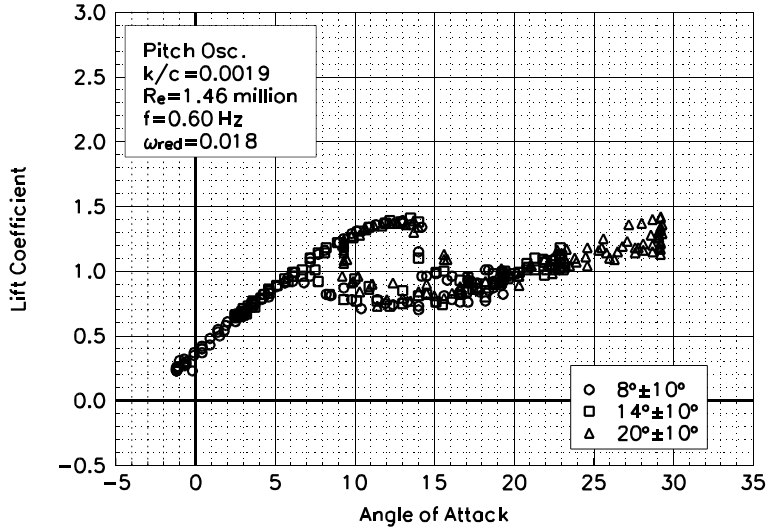

Figure C136. Lift coefficient vs α.

LS(1)-0417MOD
LEGR
Re=1.46 million
$\omega_{reduced}$=0.018

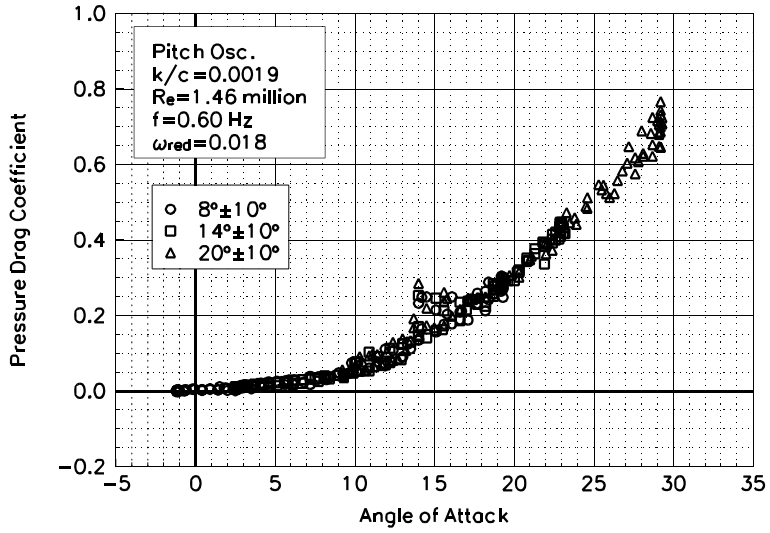

Figure C137. Pressure drag coefficient vs α.

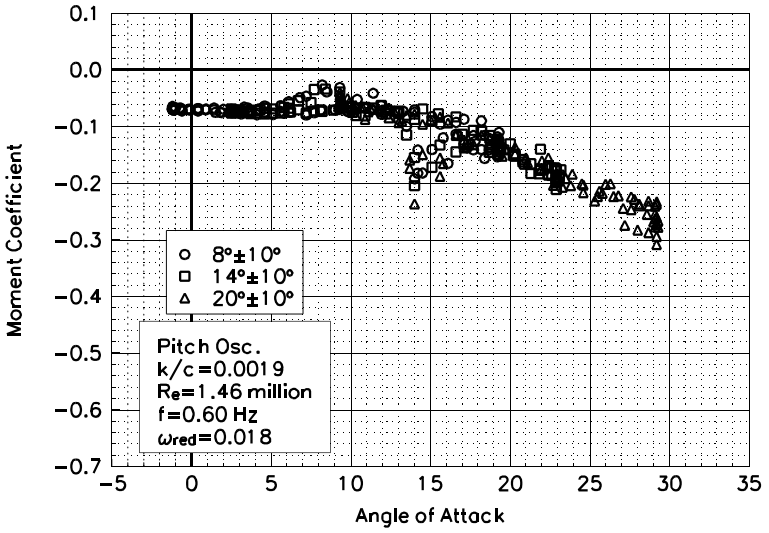

Figure C138. Moment coefficient vs α.

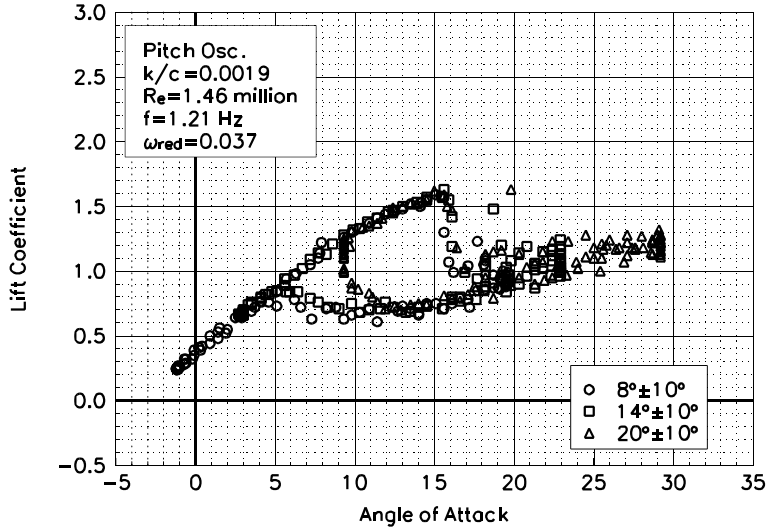

Figure C139. Lift coefficient vs α.

LS(1)-0417MOD
LEGR
Re=1.46 million
$\omega_{reduced}$=0.037

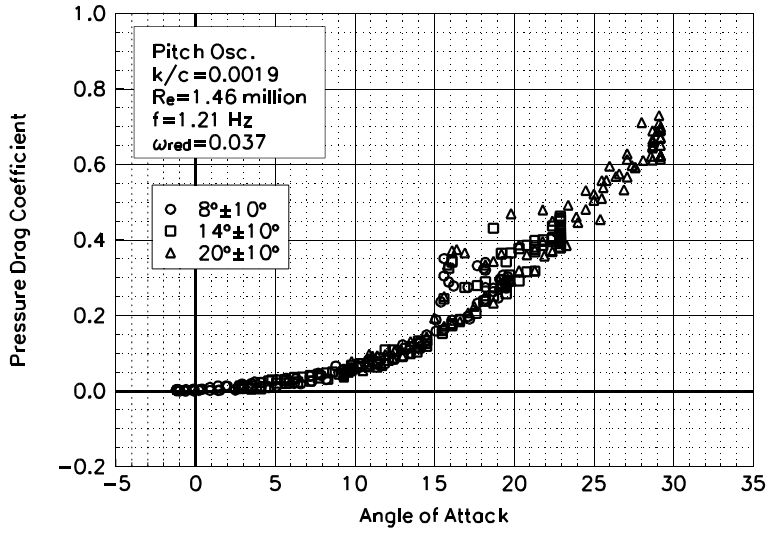

Figure C140. Pressure drag coefficient vs α.

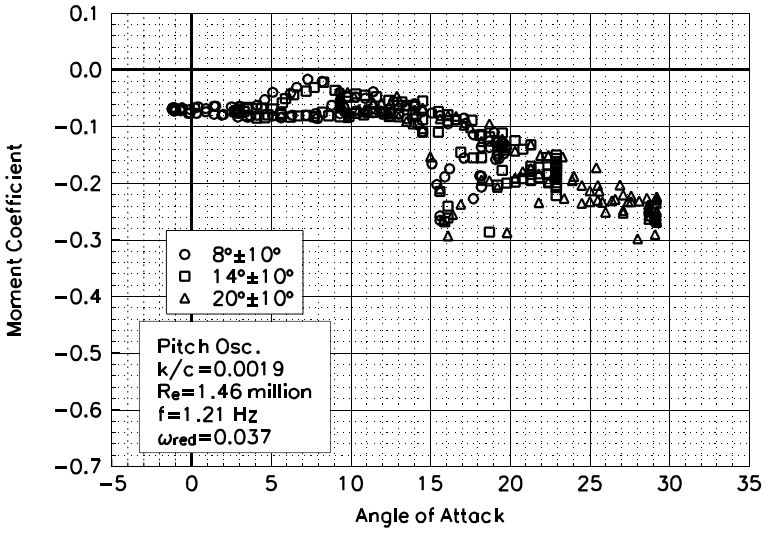

Figure C141. Moment coefficient vs α.

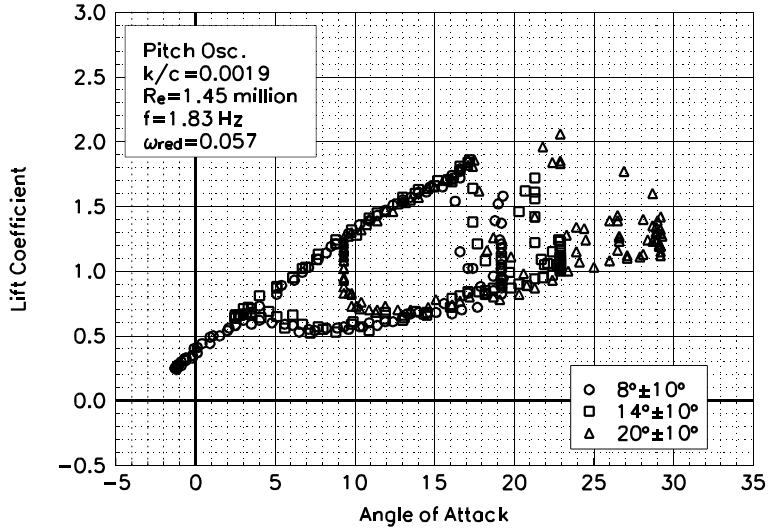

Figure C142. Lift coefficient vs α.

LS(1)-0417MOD
LEGR
Re=1.45 million
$\omega_{reduced}$=0.057

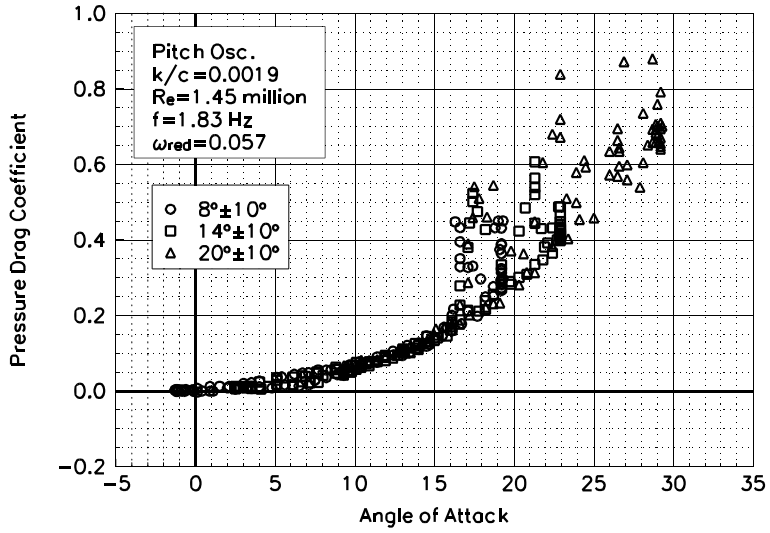

Figure C143. Pressure drag coefficient vs α.

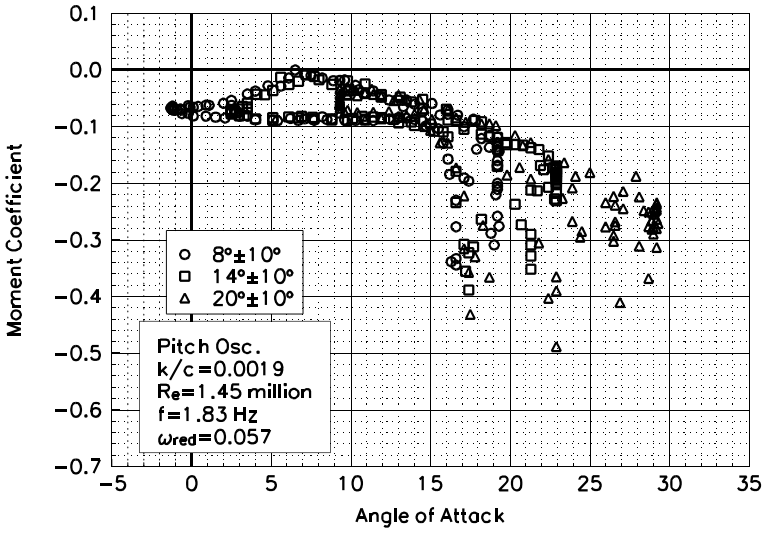

Figure C144. Moment coefficient vs α.